Search for Supersymmetry in Final States with a Single Lepton, B-Quark Jets, and Missing Transverse Energy at the CMS Experiment

Dissertation

zur Erlangung des Doktorgrades

des Department Physik

der Universität Hamburg

vorgelegt von

Niklas Pietsch

aus Hamburg

Hamburg

2014

Gutachter der Dissertation:	Dr. Isabell Melzer-Pellmann Prof. Dr. Peter Schleper
Gutachter der Disputation:	Dr. Isabell Melzer-Pellmann Jun.-Prof. Dr. Christian Sander
Datum der Disputation:	18.09.2014
Vorsitzender des Prüfungsausschusses:	Dr. Georg Steinbrück
Vorsitzender des Promotionsausschusses:	Prof. Dr. Daniela Pfannkuche
Leiterin des Fachbereichs Physik:	Prof. Dr. Peter Hauschildt
Dekan der Fakultät für Mathematik, Informatik und Naturwissenschaften:	Prof. Dr. Heinrich Graener

Abstract

Supersymmetry constitutes an attractive extension of the Standard Model of particle physics. It provides a natural Dark Matter candidate and is able to resolve the hierarchy problem. If Supersymmetry is a natural solution of the hierarchy problem, the supersymmetric partner particles of the top and the bottom quark may be copiously produced in proton-proton collisions at the Large Hadron Collider, resulting in final states with isolated leptons, jets, some of which originate from a bottom quark, and missing transverse energy.

In this thesis, the first search for Supersymmetry in events with a single lepton, bottom quark-jets, and missing transverse energy at the Compact Muon Solenoid experiment is presented. This search is one of the worldwide first analyses that directly probe natural Supersymmetry. The search is performed with proton-proton collision data recorded at a center-of-mass energy of 7 TeV during 2011, corresponding to an integrated luminosity of $4.98\,\mathrm{fb}^{-1}$. To minimize the systematic uncertainties of the measurement, the expected background from Standard Model processes is modeled with a data-driven method. No significant deviation from the Standard Model prediction is observed. Therefore, the results are interpreted as exclusion limits upon the parameters of the Constrained Minimal Supersymmetric Standard Model and a simplified model with four top quarks in the final state. In preparation of the next data-taking periods, where proton-proton collisions at envisaged center-of-mass energies of 13 and 14 TeV will open up new kinematic regions with a large discovery potential for physics beyond the Standard Model, prospects of measuring dijet-mass endpoints resulting from gluino decays are investigated.

Kurzfassung

Supersymmetrie stellt eine attraktive Erweiterung des Standard Modells der Teilchenphysik dar. Sie beinhaltet einen Kandidaten für Dunkle Materie und ermöglicht eine Lösung des Hierarchieproblems. Wenn Supersymmetrie eine natürliche Lösung des Hierarchieproblems ist, kann es in Proton-Proton-Kollisionen am Large Hadron Collider zu einer umfassenden Produktion der supersymmetrischen Partnerteilchen von Top- und Bottom-Quark kommen. Diese wäre durch Endzustände mit isolierten Leptonen, Teilchenjets, von denen einige durch ein Bottom-Quark initiiert sind, sowie fehlender transversaler Energie gekennzeichnet.

In dieser Arbeit wird die erste Suche nach Supersymmetrie in Ereignissen mit einem einzelnen Lepton, Bottom-Quark-Jets und fehlender transversaler Energie am Compact-Muon-Solenoid-Experiment vorgestellt. Die Suche basiert auf Daten, die während Proton-Proton-Kollisionen bei einer Schwerpunktsenergie von 7 TeV im Jahr 2011 aufgezeichnet wurden und einer integrierten Luminosität von $4.98\,\mathrm{fb}^{-1}$ entsprechen. Um die systematischen Unsicherheiten der Messung zu minimieren, wird der erwartete Untergrund von Standard-Modell-Prozessen mithilfe einer Datengetriebenen Methode modelliert. Es wird keine signifikante Abweichung zur Standard-Modell-Vorhersage beobachtet. Daher werden Ausschlussgrenzen auf die Parameter des Constrained Minimal Supersymmetric Standard Model und eines vereinfachten Modells mit vier Top-Quarks im Endzustand gesetzt. In Vorbereitung auf die nächsten Datennahme-Perioden, in denen Proton-Proton-Kollisionen bei geplanten Schwerpunktsenergien von 13 und 14 TeV neue kinematische Regionen mit einem großen Entdeckungspotential für Physik jenseits des Standard Modells eröffnen, wird die Möglichkeit untersucht, Zweijet-Massen-Endpunkte, die von Gluino-Zerfällen resultieren, zu messen.

Contents

1. Introduction

Natural science aims to deduce hypotheses about the external world from observations. These hypotheses, in turn, allow for the prediction of further observations. Conflicts between predictions and observations require the revision of hypotheses. Which hypotheses are to be revised in such a case? Following the epistemological holism argued by P. Duhem [1] and W.V.O. Quine [2], our statements about the external world cannot be tested individually, but "face the tribunal of sense experience [...] as a corporate body" (Quine). Neither the single hypothesis, nor the single theory, but the whole of science has to be regarded as unit of empirical significance. Hence, empirical evidence cannot force the revision of any particular hypothesis or theory. Instead, any statement or subset of statements can be re-evaluated. Quine concludes that in kind of epistemological footing, physics does therefore not differ from e.g. the ancient Greek gods. Which criteria are to be applied then? A consequence of the epistemological holism is a shift towards pragmatism. According to Quine, the ultimate objective of science is the degree to which our so-called knowledge allows us to deal with experience. In this view, physics is indeed epistemologically superior to e.g. the Greek gods because it proves more efficiency as "a device for working a manageable structure into the flux of experience".

An efficient device for working a structure into the flux of physical observations is the concept of symmetry. Whether symmetry is an intrinsic feature of nature or not (from a pragmatic point of view this is not relevant), physics is largely grounded in symmetries. According to Noether's Theorem [3], invariance under continuous symmetry transformations yields laws of conservation, based on which physical theories are built. In particle physics, the assumptions of local gauge symmetries and global Poincaré symmetry allow for a precise description of observations over an energy range of more than twelve orders of magnitude. However, despite this remarkable success, which recently has been magnified by the discovery of a Higgs boson, several questions remain open. These have inspired for numerous extensions of the Standard Model. Among these are supersymmetric models.

"Supersymmetry" names the invariance under transformations that turn fermionic in bosonic states and vice versa. Invariance under global Supersymmetry transformations requires to introduce for each Standard Model particle at least one partner particle (referred to as "sparticle") with identical gauge quantum numbers, but a spin differing by 1/2 a unit. Following Quine's line of reasoning, Supersymmetry can be considered an attractive extension of the Standard Model. In regard of symmetry as a device for dealing with physical observations, Supersymmetry constitutes

the most natural extension of the Standard Model in that it is the only non-trivial extension of Poincaré symmetry that is consistent with relativistic quantum field theory [4]. And in fact, Supersymmetry can resolve conflicts between physical observations and predictions. Furthermore, it allows for solutions of several conceptional problems.

Importantly for this thesis, Supersymmetry is able to resolve the hierarchy problem and can provide a natural Dark Matter candidate. In the Standard Model, radiative corrections to the squared Higgs-boson mass diverge quadratically with the energy scale. Although these divergences can be canceled by means of renormalization, this requires an enormous amount of fine-tuning of the underlying parameters, which is usually regarded as very unnatural. In supersymmetric models, the quadratic divergences automatically cancel out. However, in order not to introduce a further hierarchy, the top and the bottom squark, which are the partner particles of the top and the bottom quark, respectively, must be relatively light [5]. To a lesser extent this does also apply for the gluino, which is the partner particle of the gluon. Cosmological observations found that ordinary matter only constitutes 5% of the total energy in the universe [6]. About 95% is composed by Dark Energy and Dark Matter, both of which cannot be explained by the Standard Model. In many supersymmetric models, the lightest supersymmetric particle is a heavy, electrically neutral, weakly interacting particle. Assuming this particle to be protected from decay by a discrete symmetry, it is a viable Dark Matter candidate.

At the Large Hadron Collider, proton-proton collisions enable to probe physics beyond the Standard Model at the TeV scale. If Supersymmetry is a natural solution of the hierarchy problem, top and bottom squarks may be copiously produced. This may happen by direct pair production or the production of gluinos that subsequently decay into top and bottom squarks, resulting in final states with a large multiplicity of isolated leptons and quark-jets, some of the latter can be identified as originating from a bottom quark. Since mainly colored particles will be produced in proton-proton collisions, the top and the bottom squark and the gluino may even be the only sparticles that are experimentally accessible during the first data-taking period at the Large Hadron Collider.[1] Assuming the decay chains of top and bottom squarks to terminate with a lightest supersymmetric particle that escapes detection, final states will be characterized by a significant imbalance of the visible transverse momentum in addition. Possible signals of Supersymmetry at the Large Hadron Collider can be detected by two multipurpose experiments, which are installed around the interaction points. One of these is the Compact Muon Solenoid experiment, whose primary tasks are the discovery of the Higgs boson and the search for physics beyond the Standard Model.

[1] Although natural Supersymmetry suggests that the partner particles of the electroweak gauge bosons and the Higgs boson are light - even lighter than top and bottom squarks - they are hardly directly accessible in early data, because their production cross section is several orders of magnitude smaller than that for colored sparticles.

In this thesis, the first search for Supersymmetry in final states with a single lepton, bottom-quark jets, and missing transverse energy at the Compact Muon Solenoid experiment is presented. This search is one of the worldwide first analyses that directly probe natural Supersymmetry. The search is based on proton-proton collision data recorded at a center-of-mass energy of 7 TeV during 2011, corresponding to an integrated luminosity of $4.98\,\mathrm{fb}^{-1}$. In Section 2, the Standard Model of particle physics and possible extensions are outlined. Based on the above-mentioned assumptions, signatures of Supersymmetry with light top and bottom squarks at the Large Hadron Collider are deduced. In Section 3, a brief overview of the Large Hadron Collider and the Compact Muon Solenoid experiment is given. In order to compare theoretical predictions and experimental data, signal and background processes are simulated, which is described in Section 4. In Section 5, the reconstruction of elementary particles from the detector response is outlined. The selection of possible signal events from the huge amount of accumulated data is discussed in more detail in Section 6. Especially in those regions of the phase space where a potential signal is expected, the Standard Model prediction from the event simulation suffers from large systematic uncertainties. Therefore, the expected background from Standard Model processes is modeled with a data-driven method, as described in Section 7. The advantage of this method is that the systematic uncertainties largely cancel out, which is discussed in Section 8. The obtained results are presented in Section 9. Since no significant deviation from the Standard Model prediction is observed, limits upon the parameters of the Constrained Supersymmetric Standard Model and a simplified model are set. Despite extensive searches in various production and decay channels, so far no significant deviation from the Standard Model expectation has been observed at the Large Hadron Collider. During the next data-taking periods, proton-proton collisions at envisaged center-of-mass energies of 13 and 14 TeV will open up new kinematic regions with a large discovery potential for physics beyond the Standard Model. In the case of a discovery of Supersymmetry, the measurement of sparticle properties will become the next important task. In Section 10, prospects of measuring dijet-mass endpoints resulting from gluino decays are investigated. This study is based on the simulation of proton-proton collisions at a center-of-mass energy of 14 TeV and corresponds to an integrated luminosity of $300\,\mathrm{fb}^{-1}$. Finally, a summary and an outlook are given in Section 11. The results presented in this thesis are mostly published in [7] and [8].

2. Theoretical Framework

The present knowledge of particle physics is mainly encompassed by the *Standard Model* (SM) [9–11], which describes the observed elementary particles and three of the four known interactions between them. The Standard Model is a quantum field theory that essentially arises from local *gauge symmetries* and global *Poincaré symmetry*. Based on the posit of fundamental fermions, invariance under local gauge transformations requires the introduction of boson fields that mediate the electromagnetic, weak, and strong interactions[1]. Invariance under translations in spacetime and *Lorentz transformations* yields the conservation of four-momentum and the covariance of field equations, respectively. Along with the experimentally determined values of 19 free parameters that correspond to mass and coupling terms, these symmetries allow for a precise description of physical observations over a large energy range, as outlined in Section 2.1. Despite this remarkable success, which recently has been increased by the discovery of a Higgs boson that is compatible with the Standard Model expectation, the SM suffers from several shortcomings. These have inspired for various extensions of the SM. Among these is *Supersymmetry* (SUSY) [12,13], which yields the only non-trivial extension of Poincaré symmetry that is consistent with relativistic quantum field theory. Besides such aesthetic considerations, SUSY is first of all motivated by phenomenologically driven arguments: SUSY may provide a *Dark Matter* candidate, can resolve the *hierarchy problem*, and allows for the *unification of gauge couplings*. However, in order for quadratic divergences to the squared Higgs-boson mass to cancel in a way that no further hierarchy is introduced, the *superpartners* of top and bottom quarks must be relatively light, which may result in an enhanced production of final states with isolated leptons, bottom-quark jets, and missing transverse energy at the Large Hadron Collider (LHC). An introduction to Supersymmetry that emphasizes this possibility is given in Section 2.2. Other extensions of the Standard Model that may involve similar signatures are addressed in Section 2.3.

Following the conventions in high energy physics, units are redefined such that the speed of light c, the reduced Planck constant $\hbar$, and the vacuum permittivity ϵ_0 equal one: $c = 1$, $\hbar = 1$, $\epsilon_0 = 1$. The components of four-vectors and field tensors are indicated by Greek letters, and the Einstein summation convention is assumed. Three-vectors are represented in bold print.

[1] The fourth known interaction, gravity, is subject of the *general theory of relativity*. However, since its strength is many orders of magnitude smaller compared to the strengths of the other interactions, gravity is not relevant within this thesis.

2.1. The Standard Model of Particle Physics

In the Standard Model, the fundamental constituents of matter are leptons and quarks. Up to now, three *generations* that comprise twelve different *flavors* have been observed. The lepton generations consist of three electron-type leptons comprising the electron (e), the muon (μ), and the tau (τ), and three neutrinos, which are the electron neutrino (ν_e), the muon neutrino (ν_μ), and the tau neutrino (ν_τ). The quark generations are constituted by the up (u), the charm (c), and the top (t) quark, which are referred to as "up-type" quarks, and the down (d), the strange (s), and the bottom (b) quark, which are named "down-type". Leptons and quarks carry spin 1/2 and can be described by positive-energy solutions of the Dirac equation

$$(i\gamma^\mu \partial_\mu - m)\,\Psi = 0, \tag{2.1}$$

where γ^μ indicates the gamma matrices (cf. Appendix A) and m the fermion's mass. For each lepton and quark, an *antiparticle* (denoted by a bar above the particle's symbol) exists with the same spin and mass. *Antileptons* and *antiquarks* are described by negative-energy solutions of Eq. (2.1), which obtain a physical meaning when interpreted as particles with a positive energy that propagate backwards in time [14]. The solutions Ψ of Eq. (2.1) are four-component spinors (cf. Appendix A) called "Dirac spinors".

Besides spin and mass, the Standard Model fermions are characterized by their *gauge charges*. These define their couplings to the *gauge bosons*, which arise from the assumption of a local gauge symmetry. Invariance under local isospin and phase transformations requires the introduction of bosons that mediate the electromagnetic and weak interactions, which are unified within the theory of electroweak interaction, as outlined in Section 2.1.1. However, in order for the electroweak gauge bosons to obtain masses, the electroweak symmetry must be broken. This is explained by a mechanism of *spontaneous symmetry breaking*, as described in Section 2.1.2. Invariance under local color transformations yields the strong interaction, as outlined in Section 2.1.3. The computation of observables from the Standard Model *Lagrangian* by means of perturbation theory is addressed in Section 2.1.4. Finally, shortcomings of the SM are discussed in Section 2.1.5.

2.1.1. Electroweak Interaction

To illustrate the concept of local gauge symmetry, the electromagnetic interaction is introduced on the level of field equations. The unification of electromagnetic and weak interactions is then described using the *Lagrangian formalism*: In generalization of classical mechanics, where a system of particles is described by a scalar function $L(\mathrm{q}_i, \dot{\mathrm{q}}_i, t)$ (*Lagrange function*) of the generalized coordinates q_i, the generalized velocities $\dot{\mathrm{q}}_i$, and the time parameter t, elementary particles are described

by a scalar function $\mathcal{L}(\Phi_i, \partial_\mu \Phi_i)$ (*Lagrangian density* or *Lagrangian*) of the fields Φ_i and their four-gradients $\partial_\mu \Phi_i$. Field equations can be derived from the Lagrangian by solving the *Euler-Lagrange equations* given in Appendix A.

Electromagnetic Interaction

Physics is assumed to be invariant under local phase transformations

$$\Psi \to \Psi' = \exp\left(iq\chi(x)\right)\, \Psi, \tag{2.2}$$

where Ψ denotes a solution of Eq. (2.1), q the electric charge, and $\chi(x)$ any scalar function. These transformations constitute a U(1) Lie group with the generator q referred to as "$\mathrm{U(1)_q}$" in the following. Invariance under $\mathrm{U(1)_q}$ transformations requires the introduction of a spin-1 field A^μ in Eq. (2.1) and to perform the following gauge transformation simultaneously to any $\mathrm{U(1)_q}$ transformation:

$$A^\mu \to A'^\mu = A^\mu - \partial^\mu \chi(x). \tag{2.3}$$

The field A^μ is identified with the electromagnetic four-potential, which yields the Dirac equation for a fermion field interacting with the electromagnetic field:

$$\left(i\gamma^\mu \partial_\mu - m\right) \Psi = q\gamma^\mu A_\mu \Psi\,. \tag{2.4}$$

The equation of motion for A^μ is the Proca equation for massless particles

$$\Box A^\mu - \partial^\mu \left(\partial_\nu A^\nu\right) = j^\mu \tag{2.5}$$

and known from classical electrodynamics as Maxwell equations. Here, j^μ denotes the four-current $(\rho, \boldsymbol{j})$, which consists of the electric charge density ρ and the electric current density $\boldsymbol{j}$. The coupling of a fermion to the electromagnetic field is proportional to its electric charge. Since U(1) is Abelian, fermions may carry different electric charges. Electron-type leptons carry an electric charge of $q = -e$, up-type quarks a charge of $q = \frac{2}{3}\, e$, and down-type quarks a charge of $q = -\frac{1}{3}\, e$, where e denotes the elementary charge. Their antiparticles carry electric charges of opposite sign. Since the neutrinos do not carry electric charge, they do not couple to the electromagnetic field. A further characteristic of an Abelian gauge theory is that there exists no gauge-boson self-coupling. Thus, an electric charge of $q = 0$ has to be assigned to the photon (γ).

Electroweak Unification

In the Standard Model, the electromagnetic and weak interactions are unified within the theory of electroweak interaction, which was developed by S. L. Glashow, A. Salam, and S. Weinberg [15–17], hereafter named *GSW theory*. In order to formally

account for the violation of invariance under parity transformations $\vec{x} \to -\vec{x}$ (*parity violation*) in the weak interaction, the *chirality* or *handedness* operator γ^5 (cf. Appendix A) is introduced. Each solution Ψ of the Dirac equation (2.1) then can be written as sum of the *left-handed component* $\Psi_L = \frac{1}{2}(1-\gamma^5)\,\Psi$, which is an eigenstate of the chirality operator with eigenvalue $\lambda = -1$, and the *right-handed component* $\Psi_R = \frac{1}{2}(1+\gamma^5)\,\Psi$, which is an eigenstate with the eigenvalue $\lambda = +1$. Fermions are divided into *left-handed* and *right-handed* particles, which are described by Ψ_L and Ψ_R, respectively.[2] Left-handed leptons and quarks (denoted by the index "L") are grouped into doublets as shown in Table 2.1, where d'_L, s'_L, and b'_L denote superpositions of the mass eigenstates d_L, s_L, and b_L.

Table 2.1.: Leptons and quarks in the GSW theory. Left-handed fermions are grouped into isospin doublets, right-handed fermions into isospin singlets. Right-handed neutrinos are not predicted in the Standard Model.

	1. generation	2. generation	3. generation
leptons	$\begin{pmatrix}\nu_{e,L}\\ e_L\end{pmatrix}$, e_R	$\begin{pmatrix}\nu_{\mu,L}\\ \mu_L\end{pmatrix}$, μ_R	$\begin{pmatrix}\nu_{\tau,L}\\ \tau_L\end{pmatrix}$, τ_R
quarks	$\begin{pmatrix}u_L\\ d'_L\end{pmatrix}$, u_R, d_R	$\begin{pmatrix}c_L\\ s'_L\end{pmatrix}$, c_R, s_R	$\begin{pmatrix}t_L\\ b'_L\end{pmatrix}$, t_R, b_R

The fermions of each doublet are interpreted as eigenstates of the third component $\hat{I}_3$ of the weak isospin operator $\hat{\boldsymbol{I}}$. The eigenvalue $I_3 = \frac{1}{2}$ is assigned to neutrinos and up-type quarks, the eigenvalue $I_3 = -\frac{1}{2}$ is assigned to electron-type leptons and down-type quarks. In the following, the corresponding fields are denoted by $\Psi_{L\uparrow}$ and $\Psi_{L\downarrow}$. A weak isospin of $I = 0$ is assigned to all right-handed electron-type leptons and quarks (denoted by the index "R"), which appear in singlets. Right-handed neutrinos are not predicted in the SM. Right-handed antileptons and antiquarks carry the same isospin as left-handed leptons and quarks, but with opposite signs. Left-handed antiquarks and electron-type leptons carry isospin 0. The Lagrangian of a fermion field reads

$$\mathcal{L}_{\text{Dirac}} = \overline{\Psi}(i\gamma^\mu\partial_\mu - m)\Psi\,, \tag{2.6}$$

where $\overline{\Psi}$ denotes the adjunct spinor $\Psi^\dagger\gamma^0$ with the Hermitean adjoint $\Psi^\dagger$.

[2] This naming is a bit misleading, as it suggests that left- and right-handedness are intrinsic properties of elementary particles. However the handedness of massive particles is not a conserved quantity. In general, solutions of the Dirac equation (2.1) are not eigenstates of the handedness operator. Nevertheless, it is convenient to refer to particles as "left-handed" and "right-handed", as this allows to "absorb" the projection operators $\frac{1}{2}(1\pm\gamma^5)$ into the naming.

Physics is assumed to be invariant under local phase transformations

$$\begin{aligned} \begin{pmatrix} \Psi_{L\uparrow} \\ \Psi_{L\downarrow} \end{pmatrix} \rightarrow \begin{pmatrix} \Psi'_{L\uparrow} \\ \Psi'_{L\downarrow} \end{pmatrix} &= \exp\left(\frac{1}{2} i g' Y \chi(x)\right) \begin{pmatrix} \Psi_{L\uparrow} \\ \Psi_{L\downarrow} \end{pmatrix}, \\ \Psi_R \quad \rightarrow \quad \Psi'_R \quad &= \exp\left(\frac{1}{2} i g' Y \chi(x)\right) \quad \Psi_R \,, \end{aligned} \tag{2.7}$$

and local isospin transformations

$$\begin{pmatrix} \Psi_{L\uparrow} \\ \Psi_{L\downarrow} \end{pmatrix} \rightarrow \begin{pmatrix} \Psi'_{L\uparrow} \\ \Psi'_{L\downarrow} \end{pmatrix} = \exp\left(i \frac{g}{2} \tau^j \lambda_j(x)\right) \begin{pmatrix} \Psi_{L\uparrow} \\ \Psi_{L\downarrow} \end{pmatrix}, \tag{2.8}$$

where $\chi(x)$ and $\lambda_j(x)$ $(j = 1, 2, 3)$ are any scalar functions. As generators for the transformations (2.7) and (2.8) the weak hypercharge $Y \equiv q - I_3$ and the Pauli matrices (cf. Appendix A) are chosen. The coupling constants g and g' are free parameters and subject of experimental measurement. The transformations (2.7) and (2.8) constitute an $\mathrm{SU}(2) \times \mathrm{U}(1)$ Lie group referred to as "$\mathrm{SU}(2)_\mathrm{L} \times \mathrm{U}(1)_\mathrm{Y}$" in the following. Invariance under $\mathrm{SU}(2)_\mathrm{L} \times \mathrm{U}(1)_\mathrm{Y}$ transformations requires the introduction of four spin-1 fields W_1^μ, W_2^μ, W_3^μ, and B^μ in the Lagrangian density of the Dirac field (2.6) by replacing ∂_μ by the covariant derivative

$$D_\mu = \partial_\mu + i \frac{g}{2} \tau^j W_{j\mu} + i \frac{g'}{2} Y B_\mu. \tag{2.9}$$

This yields the Lagrangian density for a fermion field interacting with the electroweak gauge bosons. Since SU(2) is non-Abelian, all fermion fields couple with the same strength to W_1^μ, W_2^μ, and W_3^μ, whereas their couplings to B^μ depend on their weak hypercharges. Simultaneously to any $\mathrm{SU}(2)_\mathrm{L} \times \mathrm{U}(1)_\mathrm{Y}$ transformation the following gauge transformations have to be performed:

$$B^\mu \rightarrow B'^\mu = B^\mu - \partial^\mu \chi(x), \tag{2.10}$$

$$W_i^\mu \rightarrow W'^\mu_i = W_i^\mu - \partial^\mu \lambda_i(x) - g\, \epsilon_{ijk} \lambda_j W_k^\mu, \qquad i, j, k = 1, 2, 3, \tag{2.11}$$

Here, ϵ_{ijk} denotes the totally antisymmetric epsilon tensor (cf. Appendix A). The Lagrangian density of the gauge fields is introduced as

$$\mathcal{L}_\mathrm{EW} = -\frac{1}{4} F^a_{\mu\nu} F_a^{\mu\nu}, \qquad a = 1, 2, 3, 4, \tag{2.12}$$

where $F_a^{\mu\nu}$ denotes the field tensors

$$F_i^{\mu\nu} = \partial^\mu W_i^\nu - \partial^\nu W_i^\mu - g\, \epsilon_{ijk}\, W_j^\mu W_k^\nu, \qquad i, j, k = 1, 2, 3, \tag{2.13}$$

$$F_4^{\mu\nu} = \partial^\mu B^\nu - \partial^\nu B^\mu. \tag{2.14}$$

The last term in (2.13) is characteristic for non-Abelian gauge theories and implies triple and quartic self-coupling of the W bosons. Thus, they have to carry electroweak charge as well. In contrast to this, there is no self-coupling of the B boson and an electroweak hypercharge of $Y = 0$ has to be assigned to it.

However, the introduced fields cannot be identified with the physical gauge fields. Superpositions of W_1^μ and W_2^μ constitute the fields $W^{\pm\mu} = \frac{1}{\sqrt{2}}\,(\,W_1^\mu \pm W_2^\mu\,)$. These are related to transitions between states within one isospin doublet. For example, a left-handed muon turns into a left-handed muon neutrino by the emission of a W^- boson. Vice versa, a right-handed antimuon transforms into a right-handed antimuon neutrino emitting a W^+ boson.[3] As the eigenstates d', s', and b' of the electroweak interaction are superpositions of the mass eigenstates d, s, and b, the electroweak charged interaction allows for quark-flavor transitions between different generations. The probability amplitudes for such transitions are given by the elements of the CKM matrix [18, 19], which is a 3×3 unitary matrix that can be parametrized by four free parameters. These are three angles and one complex phase, which causes the observed violation of invariance under combined charge conjugation and parity transformation (*CP violation*). Values for the CKM matrix elements that are obtained from combining results of independent measurements in a global fit are given in Appendix A. Importantly for this thesis, b' is almost purely composed by b, which has the following two phenomenological consequences: First, the top quark decays almost exclusively into a W boson and a bottom quark. Secondly, bound states including a bottom quark (*B-hadrons*) have a comparatively long life-time, which allows to identify initially produced bottom quarks at the LHC experiments by the reconstruction of displaced decay vertices (cf. Section 5.6).

The photon and the Z field are identified with the rotated states A^μ and Z^μ, respectively, which in matrix form are given by

$$\begin{pmatrix} A^\mu \\ Z^\mu \end{pmatrix} = \begin{pmatrix} \cos\theta_W & \sin\theta_W \\ -\sin\theta_W & \cos\theta_W \end{pmatrix} \begin{pmatrix} B^\mu \\ W_3^\mu \end{pmatrix}. \tag{2.15}$$

The mixing angle θ_W (*Weinberg angle*) is defined by $\cos\theta_W = g/\sqrt{g^2 + g'^2}$ with $\sin^2\theta_W \approx 0.23$. As result of the mixing, the Z boson couples with the strength $g_z \neq g$ to a particle-dependent superposition of the left- and right-handed components, while the coupling of the photon to fermions appears as described in the beginning of this Section. As W_3^μ and B^μ do not carry weak isospin and weak hypercharge, respectively, both the photon and the Z boson mediate neutral currents that do not change the lepton or the quark flavor. As further consequence of the mixing, the triple and quartic self-coupling inherited from the structure of the field tensors (2.13) include all physical gauge bosons, W^+, W^-, Z, and γ.

[3] If not explicitly stated differently, possible charge-conjugated processes are always implied when discussing interaction processes in the following.

2.1.2. Electroweak Symmetry Breaking

Invariance under $\mathrm{SU(2)_L} \times \mathrm{U(1)_Y}$ transformations requires the electroweak gauge bosons to be massless and the fermions of each isospin doublet to have the same mass. Therefore, in Section 2.1.1 no mass terms have been introduced in the Lagrangian density of the electroweak gauge fields and no concrete assumption about the fermion masses (so far represented by the parameter m) has been done. However, among the electroweak gauge bosons, only the photon is massless. The masses of $W^{\pm}$ and and Z amount to $m_{W^{\pm}} = 80.385 \pm 0.015$ GeV and $m_Z = 91.1876 \pm 0.0021$ GeV [20], respectively. The fermion mass spectrum comprises masses in the order of 0.1 eV (neutrinos), 511 keV (e), a few MeV (u, d), ca. 100 MeV (s, μ), a few GeV (c, τ, b), and the top-quark mass, which amounts to $173.3 \pm 0.05 \pm 1.3$ GeV [21]. Thus, the electroweak symmetry must be broken. In the Standard Model, this is achieved by a mechanism of spontaneous symmetry breaking proposed by P. Higgs and others [22–24], in the following referred to as "Higgs mechanism".

In its simplest structure, a charged (ϕ^+) and a neutral (ϕ^0) complex scalar field are introduced. Like left-handed leptons and quarks, these are grouped into an isospin doublet (*Higgs doublet*)

$$\Phi = \begin{pmatrix} \phi^+ \\ \phi^0 \end{pmatrix} , \tag{2.16}$$

where the eigenvalue $I_3 = \frac{1}{2}$ ($I_3 = -\frac{1}{2}$) is assigned to ϕ^+ (ϕ^0). The Lagrangian density of the Higgs doublet is introduced as

$$\mathcal{L}_{\mathrm{Higgs}} = (\partial^\mu \Phi)^\dagger (\partial_\mu \Phi) - V(\Phi^\dagger \Phi) \tag{2.17}$$

with $V(\Phi^\dagger\Phi) = \mu^2 \Phi^\dagger \Phi + \lambda (\Phi^\dagger \Phi)^2$ the *Higgs potential*. By this, two additional parameters $\mu^2 < 0$ and λ, real and positive, enter the theory. The total Lagrangian density of the electroweak gauge fields and the Higgs doublet then reads

$$\mathcal{L}_{\mathrm{EW+Higgs}} = -\frac{1}{4} F^a_{\mu\nu} F_a^{\mu\nu} + (D^\mu \Phi)^\dagger (D_\mu \Phi) - V(\Phi^\dagger \Phi), \tag{2.18}$$

where D^μ denotes the covariant derivative (2.9). The Higgs potential has degenerate minima defined by

$$|\Phi_0| = v = \sqrt{\frac{-\mu^2}{2\lambda}} \, . \tag{2.19}$$

The Lagrangian density (2.18) is invariant under $\mathrm{SU(2)_L} \times \mathrm{U(1)_Y}$ transformations, whereas any particular choice of a ground state defined by (2.19) violates gauge invariance. In this sense, the electroweak symmetry is *spontaneously* broken. Without loss of generality

$$\Phi_0 = \frac{1}{\sqrt{2}} \begin{pmatrix} 0 \\ v \end{pmatrix} \tag{2.20}$$

can be chosen as ground state. Expanding Φ around its ground state allows to separate the latter by redefining the Higgs doublet as

$$\Phi = \exp\left(\frac{i\zeta_j \tau^j}{2v}\right) \frac{1}{\sqrt{2}} \begin{pmatrix} 0 \\ v + H \end{pmatrix} . \tag{2.21}$$

Here, τ^j represents the Pauli-matrices ($j = 1, 2, 3$) and ζ_j and H denote real scalar fields with vanishing vacuum expectation values. The *Goldstone bosons* [25] described by ζ_j are massless, while the Higgs boson described by H obtains a mass of $m_H = \sqrt{2}\mu$. Obviously, the Goldstone-boson fields vanish when performing an appropriate gauge transformation. Not obvious from the Lagrangian density (2.18), such a gauge transformation yields terms of the form $W_{j\mu} W_j^{\mu}$, $j = 1, 2, 3$. These terms are related to the masses of $W^{\pm}$ and Z, which are given by

$$m_{W^{\pm}} = \frac{1}{2} g v \,, \tag{2.22}$$

$$m_Z = \frac{m_{W^{\pm}}}{\cos\theta_W} \,, \tag{2.23}$$

respectively. The number of degrees of freedom is conserved, because W^+, W^-, and Z may now appear in a state with a helicity of $\lambda = 0$, which is forbidden for massless spin-1 particles like the photon.

The masses of charged leptons and quarks are generated by *Yukawa coupling* in terms of the form

$$\mathcal{L} = -y_f \left(\overline{L}\, \Phi_c\, \Psi_R + \overline{\Psi}_R\, \Phi_c^{\dagger}\, L\right) , \tag{2.24}$$

where L denotes a left-handed SU(2) doublet and Φ_c the charged conjugated Higgs doublet. In the Standard Model, the neutrinos are assumed to be massless and not to couple to the Higgs boson. By this, three coupling constants y_f are introduced for each fermion generation. Substitution of the Higgs doublet Φ in (2.24) by its ground state Φ_0 results in the following expression for the masses m_f of charged leptons and quarks:

$$m_f = \frac{v}{\sqrt{2}}\, y_f \,. \tag{2.25}$$

Since the Yukawa coupling constants y_f are proportional to the fermion masses ($y_f \propto m_f$), the Higgs boson predominantly couples to the top quark and, to a lesser extent, to the bottom quark and the tau. Besides the massive electroweak gauge bosons, the third generation of fermions therefore plays an important role in Higgs-boson analyses at the LHC. Over the whole range of considered masses, the gluon induced process $gg \to H$ dominates the Higgs-boson-production cross section [26].

Since the gluon does not couple directly to the Higgs boson, this process involves intermediate quarks. By far the largest contribution to this process originates from the top quark mediated production, which is represented by the *Feynman diagram*[4] in Fig. 2.1(a).

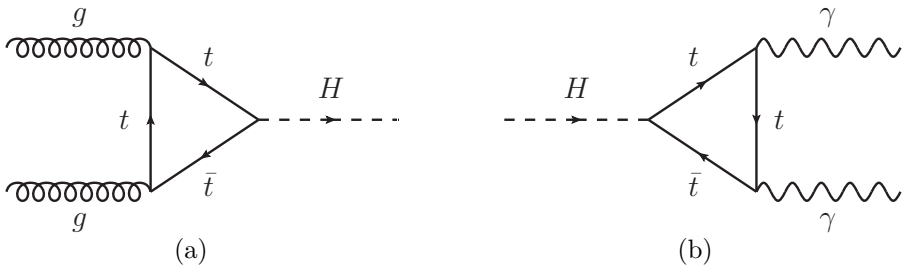

Figure 2.1.: Top-quark-mediated Higgs-boson production (a) and decay into two photons (b).

Similarly, the Higgs-boson decay into two photons can be mediated by top quarks, as illustrated in Fig. 2.1(b). However, a larger contribution to this process originates from the decay that is mediated by W bosons. Though its branching ratio is in the order of 10^{-3} [27], the Higgs-boson decay into two photons in the region of low masses is of major relevance. Since photons can be reconstructed very well, this channel enables a mass reconstruction with a high resolution ($\mathcal{O}(1-2\%)$). Both the ATLAS and the CMS experiment observe a significant excess of events in the invariant diphoton mass at $m_{\gamma\gamma} = 126.8$ GeV and $m_{\gamma\gamma} = 125.7$ GeV, respectively [28, 29]. The distribution of the invariant diphoton mass reconstructed from data recorded at the ATLAS experiment is shown in Fig. 2.2(a). The dashed red line represents the distribution of background events, which is obtained from fitting a fourth-order polynomial to the data in the region 100 GeV $< m_{\gamma\gamma} <$ 160 GeV. The combined signal and background fit is represented by the solid red line.

An even more striking signature results from the Higgs boson decay into two Z bosons with the subsequent decay of each Z into a e^-e^+ or $\mu^-\mu^+$ pair. Besides a high mass resolution ($\mathcal{O}(1-2\%)$), this channel in addition profits from a small irreducible background. Compared to the $H \to \gamma\gamma$ channel, the limiting factor is rather the small number of selected events. The distribution of the invariant four-lepton mass m_{4l} reconstructed from data recorded at the CMS experiment is shown in Fig. 2.2(b). The four-lepton mass is calculated from two pairs of opposite-sign same-flavor leptons (e^-e^+ or $\mu^-\mu^+$), one of which can be identified as originating from the decay of a non-virtual[5] Z boson.

[4] Within this thesis, Feynman diagrams are always presented such that the horizontal can be identified with the time-axis.

[5] A particle is referred to as "virtual" or "off-shell" if it is not fixed to its mass-shell, i.e. $E^2 - p^2 \neq m^2$. Virtual particles are denoted by a star right to the particle's symbol, e.g. Z^*.

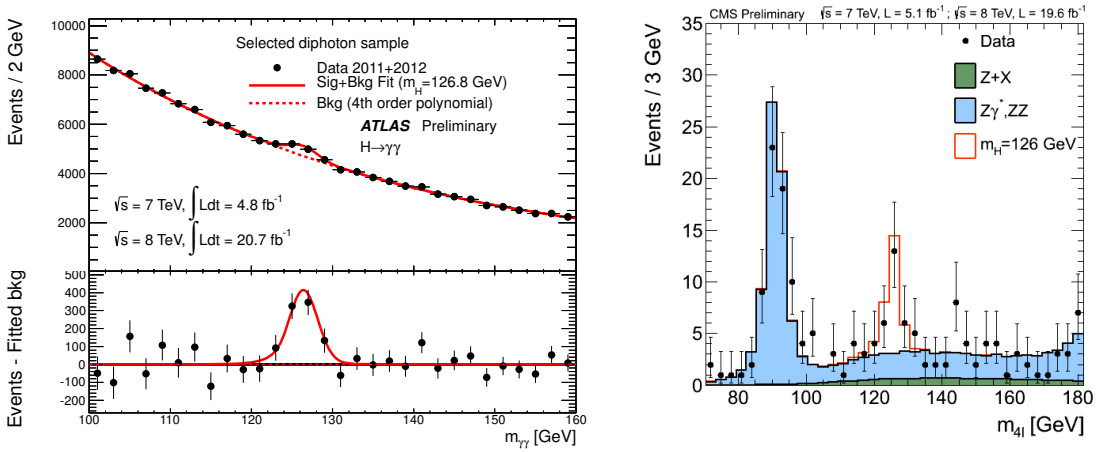

(a) (b)

Figure 2.2.: Invariant diphoton mass (a) and invariant four-lepton mass (b) reconstructed from data recorded at the ATLAS and the CMS experiment, respectively. The results correspond to the full set of data recorded into 2011 and 2012. Figures taken from [28] and [30].

In the region $m_{4l} < 2m_Z$, the other Z boson is produced off-shell. As can bee seen in Fig. 2.2(b), a significant excess of events at $m_{4l} = 126$ GeV is visible.

Further Higgs boson decays of relevance are the decays $H \to WW^* \to 2l2\nu$, $H \to b\bar{b}$, and $H \to \tau\bar{\tau}$. The latter two are of special interest as they enable to directly probe the coupling of the Higgs boson to fermions. However, mainly due to a worse mass resolution, the excesses in these channels are less significant [29, 31]. The observed and expected significances combined for the individual channels at the CMS experiment amount 9.4 and 10.1, respectively.

The compatibility of the observed excesses with the SM Higgs-boson hypothesis are quantified by the signal strength $\hat{\mu} = \hat{\sigma}/\sigma_{\mathrm{SM}}$ with $\hat{\sigma}$ the observed and σ_{SM} the expected Higgs-boson-production cross section. The signal strengths for the individual decay channels are presented in Fig. 2.3. The signal strengths combined for the individual decay channels at the ATLAS and the CMS experiment amount $\hat{\mu}_{\mathrm{ATLAS}} = 1.43 \pm 0.21$ and $\hat{\mu}_{\mathrm{CMS}} = 0.80 \pm 0.14$, respectively. In total, no significant deviation from the SM expectation is observed. In the context of searches for physics beyond the Standard Model, such deviations are of interest, because they might hint at the existence of new elementary particles (see also Sections 2.2 and 2.3). In supersymmetric models these might be the superpartners of the top quark. Since Supersymmetry requires that quarks have identical gauge-quantum numbers and Higgs coupling constants as their scalar partners (squarks), especially light top squarks might contribute to a deviation from the gluon-induced production of neutral Higgs bosons and, to a lesser extent, to the branching ratio for the decay into two photons.

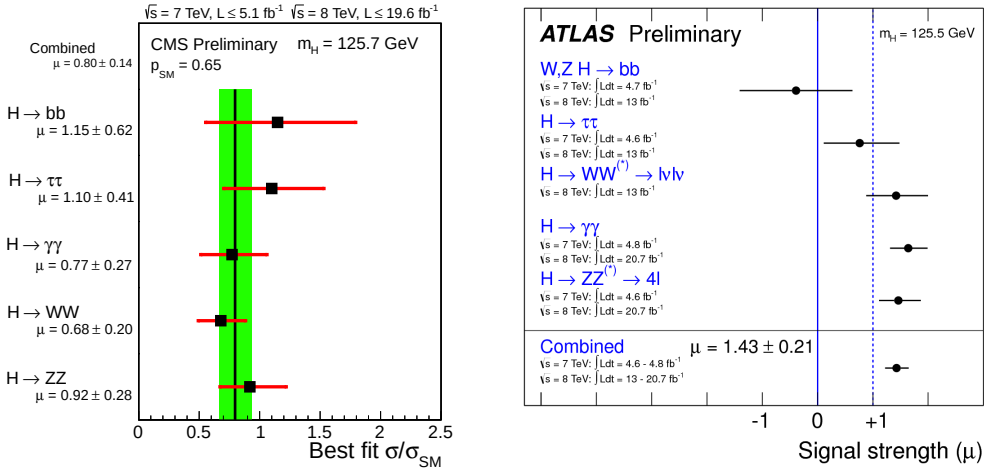

Figure 2.3.: Signal strengths for the excesses observed in the individual decay channels at the ATLAS (left) and the CMS (right) experiment. Figures taken from [29] and [32].

2.1.3. Strong Interaction

Several experimental observations suggest that quarks occur in three different states [11]. Therefore, an inner degree of freedom, which is called "color", is assigned to them. Quarks are assumed to occur in the color states *red*, *blue*, and *green*, which are represented by three-vectors. The colors *anti-red*, *anti-blue*, and *anti-green* are assigned to antiquarks. Formally, this is taken into account by multiplying Ψ in the Lagrangian density of the Dirac fields (2.6) with a three-component color vector Ψ_c. Physics is assumed to be invariant under local color transformations

$$\Psi_\mathrm{c} \to \Psi'_\mathrm{c} = \exp\left(\frac{1}{2} i g_s \lambda^k \beta_k(x)\right) \Psi_\mathrm{c}\,, \tag{2.26}$$

where $\beta_k(x)$ are any scalar functions with k running from $k = 1$ to 8 and g_s denotes the strong coupling constant, which is a further free parameter of the SM. As generators λ^k of local color transformations, the Gell-Mann matrices (cf. Appendix A) can be chosen. The local color transformations constitute an SU(3) Lie group referred to as "$\mathrm{SU(3)_C}$" in the following. Invariance under local color transformations requires the introduction of eight gauge fields G_k^μ that gauge transform similarly as the electroweak gauge fields W_1^μ, W_2^μ, and W_3^μ introduced in Section 2.1.1. The couplings of fermions to the gauge bosons, the gluons, is introduced by replacing ∂_μ by the covariant derivative

$$D_\mu = \partial_\mu + i\frac{g_s}{2}\lambda^k G_{k\mu} \tag{2.27}$$

in the Lagrangian density of the Dirac field (2.6). As SU(3) is non-Abelian, all quarks couple with the same strength g_s to the gluons. The Lagrangian density of the latter is introduced as

$$\mathcal{L}_{\mathrm{QCD}} = -\frac{1}{4}F^a_{\mu\nu}F^{\mu\nu}_a, \tag{2.28}$$

where $F^{\mu\nu}_a$ denotes field tensors that are similarly defined as those in Eq. (2.13). In analogy to the electroweak interaction, triple and quartic self-coupling of gluons follows from the structure of these tensors. Neither the leptons nor the electroweak gauge bosons carry color. Hence, they do not interact strongly.

Both the photon and the gluons are massless, but unlike the electromagnetic interaction the strong interaction is not of infinite reach. Since the color of a quark changes when a virtual gluon is emitted, the effective coupling of the strong interaction decreases as the distance r gets smaller. For $\mathrm{r} \to 0$ the coupling becomes zero, which is referred to as *asymptotic freedom*. The potential describing the strong interaction between a quark q and an antiquark $\bar{q}$ therefore increases as the distance r between them gets larger. At a certain distance the production of a new quark-antiquark pair between q and $\bar{q}$ is energetically favored. Due to this behavior, which is called *confinement*, quarks do not appear as individual partons, but in colorless bound states of quark-antiquark pairs (*mesons*) or three quarks or antiquarks (*baryons*). Among these are the proton and the neutron, which constitute the atomic nucleus. Mesons and baryons are called "hadrons". Except for the top quark, gluons and quarks produced at colliders fragment in hadrons, which is called *hadronization*, and show up as collimated bunches of particles referred to as "jet".

Since $m_t > m_b + m_W$, the top quark decays into a bottom quark and a non-virtual W boson before it can hadronize. Besides the fact that b' is almost a purely composed b state (cf. Section 2.1.1) and the large Yukawa coupling constants of top and bottom quarks (cf. Section 2.1.2), this may be regarded as further important feature of the third generation of quarks: First, it allows for the kinematic reconstruction of top quarks using a W-boson mass constraint. Secondly, it enables the distinction between $t\bar{t}$ production and other processes using variables that involve a kinematic edge. Prominent examples for the latter are the transverse W-boson mass and the invariant lepton-b-quark mass, both of which are exploited in top-quark and Higgs-boson analyses as well as searches for physics beyond the SM at the ATLAS and the CMS experiment, see e.g. [33–37]. If the W boson was produced off-shell, as in the decays of all other quarks, such variables would either involve a kinematic endpoint, which is less striking than a kinematic edge, or no edge or endpoint at all. Also, the usage of a W-boson mass constraint would not be possible.

Parton Distribution Functions

The proton is a bound state of two up quarks and one down quark. These *valence quarks* steadily radiate gluons, which, in turn, further emit gluons or split into pairs of a quark and an antiquark (*sea quarks*) and so forth. Hence, also gluons and quarks of flavors other than up and down are found inside the proton. The probabilities of finding a parton that carries the fraction x of the proton momentum is parametrized by the parton distribution functions (PDFs), which have been experimentally determined using data from the H1 and the ZEUS experiment [38] and fixed target experiments. At high momentum fractions the contributions from the valence quark PDFs dominate, as can be seen in Fig. 2.4.

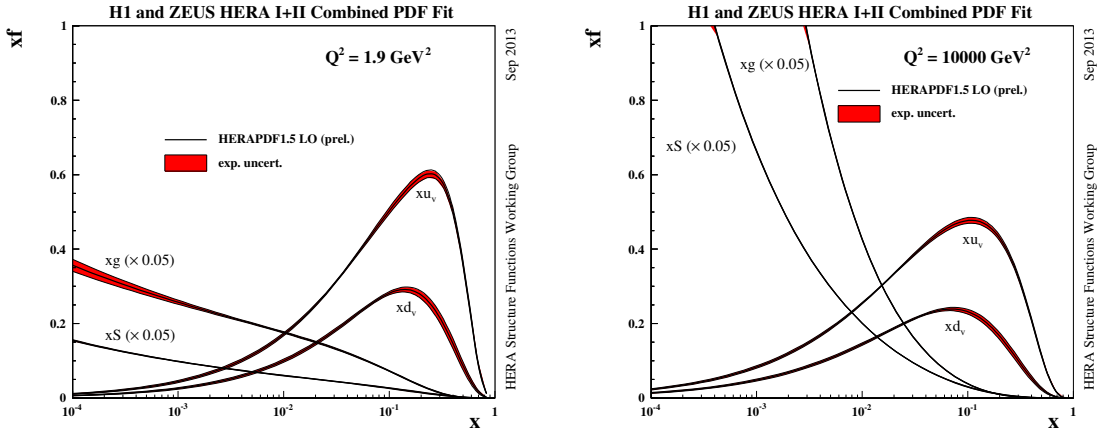

Figure 2.4.: Distribution of valence quarks (u_v and d_v), gluons (g), and sea quarks (S) multiplied by the fraction x of the proton momentum as a function of x for $Q^2 = 1.9$ GeV^2 and $Q^2 = 10000$ GeV^2. The distributions for gluons and sea quarks are scaled down by a factor of 20. Figure taken from [39]. Note the logarithmic x-axis scale.

With decreasing x, this contribution falls off, while the probability of finding gluons and sea quarks increases. Since charm and bottom sea-quarks are produced with a higher virtuality, their production is suppressed with regard to the production of light-flavor sea quarks. Top quarks are not found inside the proton. The probability of finding a parton with momentum fraction x also depends on the energy scale Q, i.e. the four-momentum exchange in the *hard scattering process*. This dependency can be understood as resolution effect: At low Q, the proton structure is dominated by the valence quarks. As can be seen in Fig. 2.4(a), the relative contribution to the total proton momentum from gluons and sea quarks is small At large Q, also the emission and splitting of gluons can be resolved. Hence, the relative contribution to the proton momentum from gluons and sea quarks gets larger (cf. Fig. 2.4(b)).

2.1.4. Perturbation Theory and Renormalization

The total Lagrangian of the Standard Model reads

$$\mathcal{L}_{\mathrm{SM}} = \sum_{\text{flavor}} \Psi(x)(i\gamma_\mu D^\mu)\Psi + (D^\mu\Phi)^\dagger(D_\mu\Phi) - V(\Phi^\dagger\Phi) - \frac{1}{4}F^a_{\mu\nu}F^{\mu\nu}_a + \mathcal{L}_{\text{Yukawa}}\,, \quad (2.29)$$

where $\mathcal{L}_{\text{Yukawa}}$ denotes the Lagrangian density of the Yukawa coupling between the fermions and the Higgs boson, $F^{\mu\nu}_a$ the field tensors of the gauge fields, and D_μ the covariant derivative

$$D_\mu = \partial_\mu + i\frac{g}{2}\tau^j W_{j\mu} + i\frac{g'}{2}B_\mu + i\frac{g_s}{2}\lambda^k G_{k\mu} \quad (2.30)$$

with $j = 1, 2, 3$ and k running from $k = 1$ to 8. The sum runs over all lepton and quark flavors.

In general, the field equations derived from the SM Lagrangian (2.29) cannot be solved analytically. However, it is possible to expand their solutions in orders of coupling constants. Each term in such a *perturbation series* can be associated with distinct physical processes that contribute to the total interaction. For example, the first non-trivial (*leading order*) term that contributes to the *exclusive* $t\bar{t}$ production induced by quark-antiquark annihilation corresponds to the process represented by the Feynman diagram in Fig. 2.5(a). This diagram contains two vertices (q-$\bar{q}$-g and g-t-$\bar{t}$), both of which involve a factor that is proportional to the strong coupling constant g_s. Hence, the leading order (LO) term is proportional to g_s^2. The next-to-leading order (NLO) contribution comprises processes like the process illustrated in Fig. 2.5(b) and is proportional to g_s^4. Diagrams that involve three and five vertex factors, as exemplifed in Fig. 2.5(c) and (d), are related to the exclusive gluon-associated $t\bar{t}$ production at leading and next-to-leading order, respectively. Within this thesis "leading order" and "next-to-leading order" are always defined with respect to a particular process. For example, if the *inclusive* $t\bar{t}$ production induced by quark-antiquark annihilation was considered, diagrams that involve three vertices would be related to the NLO term, while processes like that shown in Fig. 2.5(b) would constitute the next-to-next-to-leading order (NNLO) contribution.

Formally, the probability amplitude for the transition of an initial state Ψ_i into a final state Ψ_f is given by the matrix element

$$\mathcal{M} = \int d^3x\, \Psi_f^\dagger\, S\, \Psi_i\,, \quad (2.31)$$

where S denotes the *scattering matrix*, which is subject to the expansion addressed above. Technically, the matrix element is expanded in orders of coupling constants following the *Feynman Rules* [10, 11].

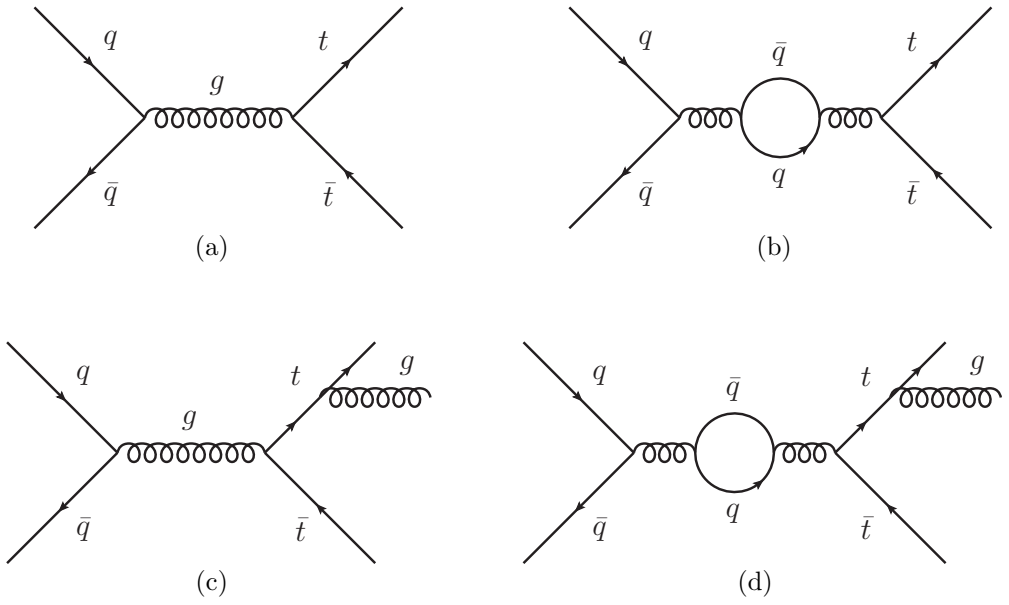

Figure 2.5.: Leading order (left) and next-to-leading order (right) contribution to the exclusive $t\bar{t}$ pair production (top) and the inclusive gluon-associated $t\bar{t}$ pair production (bottom) induced by quark-antiquark annihilation.

Importantly, according to these, the matrix element has to be calculated from all processes that involve the same initial- and final-state particles. Therefore, in principle also the processes $q\bar{q} \to Z^* \to t\bar{t}$ and $q\bar{q} \to \gamma^* \to t\bar{t}$ needed to be taken into account in the example discussed above. However, as the contributions from these processes are much smaller than those from the gluon-mediated production, they can be neglected.

Cross sections are calculated multiplying $|\mathcal{M}|^2$ with a factor that represents the available phase space of the final state Ψ_f. As the number of possible diagrams and the complexity of calculations rapidly increases with the order of coupling constants, cross sections are usually only known up to NLO or NNLO. The change of the NLO cross section σ_{NLO} with respect to the LO cross section σ_{LO} is usually expressed by a factor $K \equiv \sigma_{\mathrm{NLO}}/\sigma_{\mathrm{LO}}$ (*K factor*).

When calculating cross sections, difficulties arise from processes like that illustrated in 2.5(b), which involve divergent integrals. Such divergences need to be accommodated using *regularization* and *renormalization* techniques. In the first step, divergent integrals are split into finite and infinite terms by introducing a cut-off parameter that, in principle, has to be taken to infinity (regularization). In a second step, the "bare" coupling constants and masses are redefined such that the regularized divergences are included in their definitions (renormalization). This reflects the fact that coupling constants and masses are not infinite. If all divergent integrals can be

accommodated as described, the theory is called *renormalizable*. It has been proven that locally invariant gauge theories are renormalizable [40]. The remaining finite terms still depend on the energy scale Q at which the hard scattering process takes place. Therefore, effective coupling constants and masses that "absorb" the energy dependency and are consequently referred to as "running", are introduced. The scale at which coupling constants and masses are evaluated is called *renormalization scale*. Coupling constants and masses, measured e.g. at the electroweak scale m_Z, can be extrapolated to any other scale using the *renormalization group equations* [9]. If not explicitly stated differently, "coupling constant" and "mass" shall refer to the renormalized quantities evaluated at the electroweak scale in the following.

Non-Perturbative QCD

In the 1-loop approximation, the strong coupling constant $\alpha_s \equiv g^2/8\pi$ is given by the following expression:

$$\alpha_s(Q^2) = \frac{\alpha_s(\mu_\mathrm{R}^2)}{1 + (33 - 2\,n_f)\frac{\alpha_s(\mu_\mathrm{R}^2)}{(12\pi)}\,\ln\left(\frac{Q^2}{\mu_\mathrm{R}^2}\right)}\,. \tag{2.32}$$

Here, n_f denotes the number of active quark flavors at the energy scale Q and μ_R the renormalization scale. As already addressed in the context of asymptotic freedom in Section 2.1.3, the strong coupling constant decreases with increasing Q. Moving towards the other end of the energy scale, α_s becomes large. Below some energy scale Λ_QCD perturbation series diverge. In this region, strong interaction processes cannot be computed by means of perturbation theory anymore. Instead, phenomenological approaches are used to describe the observations.

2.1.5. Shortcomings of the Standard Model

Despite its remarkable success, the Standard Model involves various shortcomings. First, a number of experimental observations strongly suggests the existence of physics beyond the Standard Model. Secondly, different theoretical considerations indicate the incompleteness of the model.

The most striking experimental evidence for the existence of physics beyond the Standard Model originates from the missing incorporation of gravity. Though totally negligible at energy scales described by the SM, gravity is known to become relevant at the Planck scale $\Lambda_\mathrm{Pl} \sim 10^{18}$ GeV at the latest. Associated therewith, the Standard Model can also not explain the weakness of gravity relative to the other fundamental interactions. Additional experimental evidences for physics beyond the Standard Model stem from the observations of anisotropies in the cosmic microwave background [41, 42] and deviations from the expected rotational curves

of galaxies [43]. These are interpreted as a result of non-relativistic Dark Matter (*cold* Dark Matter), which cannot be accounted for in the Standard Model. Due to their ultrarelativistic nature, the SM neutrinos only constitute a candidate for *hot* Dark Matter. Also, the Standard Model cannot explain the observation of neutrino oscillations [44], which require non-vanishing neutrino masses and suggest that neutrinos may appear as right-handed particles as well. Within the Standard Model, there exists no mechanism that can generate neutrino masses.

Further indications for the incompleteness of the Standard Model originate from theoretical considerations. Contributions to the masses of fermions and gauge bosons from higher-order processes diverge logarithmically. As discussed in Section 2.1.4, this is taken into account by introducing a cut-off scale Λ_{UV}, which should be interpreted as at least the energy scale at which new physics enters to alter the high-energy behavior of the Standard Model. The corrections to the fermion and gauge boson mass parameter m becomes

$$\Delta m \propto m \ln \frac{\Lambda_{\mathrm{UV}}}{m} \,. \tag{2.33}$$

This does not involve a severe problem. Even if Λ_{UV} is in the order of the Planck scale, the observed masses remain close to the "bare" masses. However, contributions from fermion- and gauge-boson loops to the squared Higgs-boson mass diverge quadratically. The corrections to the Higgs-boson mass become

$$\Delta {m_H}^2 \propto \Lambda_{\mathrm{UV}}^2 + \mathcal{O}(\ln \Lambda_{\mathrm{UV}}) \,. \tag{2.34}$$

Though the quadratic divergences may be canceled by means of renormalization, this requires an enormous amount of "fine-tuning" and poses the question why there is such a large discrepancy (some 15 orders of magnitude) between the observed and the "bare" Higgs-boson mass. Since this *hierarchy problem* is related to the energy scale at which new physics becomes important, it is often not considered as a shortcoming of the Standard Model itself. Instead, it becomes relevant as soon as introducing new physics at higher energy scales. Another theoretical issue that receives much attention is the unification of gauge coupling strengths. The Standard Model does not allow the coincidence of the electroweak and strong coupling constants at any unification scale. Also, a unification of all four known interactions in terms of a renormalizable theory is still not achieved.

Finally, questions of a rather aesthetic kind remain. So far, there is no explanation for the particular choice of the SM gauge group, the existence of three generations of fermions, or their mass hierarchy.

2.2. Supersymmetry

Emphasizing the importance of symmetry in particle physics, a natural starting point to introduce Supersymmetry is the Haag-Łuposzański-Sohnius theorem [4]. According to this theorem SUSY is the only non-trivial extension of Poincaré symmetry that is consistent with relativistic quantum field theory. "Supersymmetry" names the invariance under transformations that turn fermionic in bosonic states and vice versa. These transformations are generated by N distinct pairs of spin-1/2 operators Q and $\bar{Q}$. However, only $N = 1$ Supersymmetry allows the construction of models that embed the Standard Model as an effective theory at low energies. For example, in models with $N > 1$ Supersymmetry, left- and right-handed fermions may transform similarly under local isospin and phase transformations, which contradicts the observed chirality of the electroweak interaction (cf. Section 2.1.1). Therefore, the following discussion of Supersymmetry is restricted to the case with $N = 1$.

Adding the generators of SUSY transformations to that of the Poincaré group yields the *Super-Poincaré algebra*, which includes the following anti-commutation relations:

$$\{Q_\alpha, \bar{Q}_{\dot{\alpha}}\} = 2\sigma^\mu_{\alpha\dot{\alpha}} P_\mu, \tag{2.35}$$

$$\{Q_\alpha, Q_\beta\} = \{\bar{Q}_{\dot{\alpha}}, \bar{Q}_{\dot{\beta}}\} = 0, \tag{2.36}$$

$$\{Q_\alpha, P_\mu\} = \{\bar{Q}_{\dot{\alpha}}, P_\mu\} = 0. \tag{2.37}$$

Here, P_μ represents the generator of space-time translations and $\alpha, \beta \in \{1, 2\}$ indicate the components of *Weyl spinors*[6]. Dotted indices denote the components of the corresponding complex conjugated spinors. Assuming invariance under global Supersymmetry transformations these relations imply that for each elementary particle there exists at least one partner particle (*superpartner*) with the identical gauge quantum numbers, Higgs coupling constant, and mass, but a spin differing by 1/2 a unit. As the SM does not contain any pair of superpartners, SUSY requires to introduce at least one superpartner for each SM particle, which is referred to as *sparticle*. In addition, a second Higgs doublet plus superpartners have to be introduced. These minimal requirements constitute the Minimal Supersymmetric Standard Model, which is outlined in Section 2.2.1. As no superpartner of any SM particle has been observed yet, sparticles must have larger masses, which can be explained by different SUSY-breaking models, one of which is described in Section 2.2.2. The phenomenology of light top- and bottom-quark superpartners at the LHC is discussed in detail in Section 2.2.3. In order to facilitate the interpretation of results, *simplified models* are commonly used at the ATLAS and CMS experiments. In Section 2.2.4, the simplified models examined in this thesis are presented.

[6] Weyl spinors are two-component spinors that represent solutions of the Dirac equation (2.1) with a defined handedness. When formulating supersymmetric theories, it is convenient to describe left- and right-handed fermions by Weyl spinors instead of left- and right-handed components of Dirac spinors.

2.2.1. Minimal Supersymmetric Standard Model

In the Minimal Supersymmetric Standard Model (MSSM) one superpartner (denoted by a tilde above the particle's symbol) is introduced for each SM particle.[7] The superpartners of the SM leptons and quarks are scalar particles named *sleptons* and *squarks*. Their antiparticles (denoted by a star right to the sparticle's symbol) are referred to as *antisleptons* and *antisquarks*.[8] The superpartners of left- and right-handed leptons and quarks are denoted by the indices "L" and "R". Though they carry spin 0 they are referred to as "left-handed" and "right-handed" as well. The superpartners of the SM gauge bosons carry spin 1/2 and are referred to as *gauginos*. In addition, a second Higgs doublet plus superpartners, which are named *higgsinos* and carry spin 1/2, have to be introduced. The particle content of the MSSM before electroweak symmetry breaking is given in Table 2.2.

Table 2.2.: Particle content of the Minimal Supersymmetric Standard Model before electroweak symmetry breaking.

	SM particle	Spin	Sparticle	Spin
Leptons, Sleptons	$\nu_{e,L}\,,\ e_L,\ e_R$	1/2	$\tilde{\nu}_{e,L}\,,\ \tilde{e}_L,\ \tilde{e}_R$	0
	$\nu_{\mu,L}\,,\ \mu_L,\ \mu_R$	1/2	$\tilde{\nu}_{\mu,L}\,,\ \tilde{\mu}_L,\ \tilde{\mu}_R$	0
	$\nu_{\tau,L}\,,\ \tau_L,\ \tau_R$	1/2	$\tilde{\nu}_{\tau,L}\,,\ \tilde{\tau}_L,\ \tilde{\tau}_R$	0
Quarks, Squarks	$u_L,\ u_R,\ d_L,\ d_R$	1/2	$\tilde{u}_L,\ \tilde{u}_R,\ \tilde{d}_L,\ \tilde{d}_R$	0
	$c_L,\ c_R,\ s_L,\ s_R$	1/2	$\tilde{c}_L,\ \tilde{c}_R,\ \tilde{s}_L,\ \tilde{s}_R$	0
	$t_L,\ t_R,\ b_L,\ b_R$	1/2	$\tilde{t}_L,\ \tilde{t}_R,\ \tilde{b}_L,\ \tilde{b}_R$	0
B boson, Bino	B	1	$\tilde{B}$	1/2
W bosons, Winos	W^1, W^2, W^3	1	$\tilde{W}^1, \tilde{W}^2, \tilde{W}^3$	1/2
Gluons, Gluinos	g	1	$\tilde{g}$	1/2
Higgs, Higgsinos	$H_u^0, H_u^+, H_d^0, H_d^-$	0	$\tilde{H}_u^0,\ \tilde{H}_u^+,\ \tilde{H}_d^0,\ \tilde{H}_d^-$	1/2

The Lagrangian density of the MSSM is constructed in analogy to the SM Lagrangian (2.29). It contains kinetic terms for all fields as well as gauge and Yukawa

[7] Since the superpartners of left- and right-handed Standard Model fermions may mix to lighter and heavier mass eigenstates, it is sometimes said that two superpartners are introduced for each SM fermion. However, since this mixing is neither an intrinsic feature of Supersymmetry nor necessary for Supersymmetry to be a viable extension of the SM, this usage of "particle" does not seem to be appropriate, especially since the Standard Model fermions themselves are commonly divided into left-handed and right-handed particles.

[8] In order to avoid possible ambiguities, off-shell squarks and sleptons are not represented symbolically, i.e. $\tilde{t}^*$ denotes the antitop squark, but not an off-shell top squark.

interaction terms. Details about the construction of the MSSM Lagrangian can be found for example in [12]. Possible supersymmetric and gauge invariant interaction vertices basically arise from Standard Model vertices by replacing any two particles by their superpartners. In analogy to the SM, electroweak symmetry breaking in the MSSM is realized by the Higgs mechanism. As in the SM, three degrees of freedom are absorbed by performing a gauge transformation that gives rise to mass terms for the W and Z bosons. Since the two Higgs-doublets in the MSSM have eight degrees of freedom in total, five physical Higgs-boson fields remain. These are the electrically neutral fields h^0, A^0, H^0, and the electrically charged fields H^+ and H^-.

If Supersymmetry was *exact*, superpartners would only differ in spin. However, in order to realize electroweak symmetry breaking, Supersymmetry must be broken. Furthermore, no superparnter of any SM particle has been observed yet, which strongly suggests that sparticles are considerably heavier than their SM superpartners. In order for quadratic divergences to the squared Higgs-boson mass to cancel, Supersymmetry breaking must be "soft", meaning the SUSY-breaking Lagrangian may not contain dimensionless coupling and mass parameters. The most general soft SUSY-breaking Lagrangian of the MSSM requires to introduce 105 parameters in addition to the 19 parameters of the SM [45]. Fortunately, many of these additional parameters imply flavor-mixing or CP-violating processes of that type that are strongly constrained by experimental limits [12]. Therefore, squark- and slepton-mass-matrices are usually assumed to be proportional to the 3×3 unit matrix in family space. Making further the assumption that the trilinear interaction of scalars does conserve the squark or slepton flavor and is proportional to the Yukawa coupling constant of the involved slepton or squark flavor, only 14 additional parameters remain. These are the three bino, wino, and gluino mass parameters M_1, M_2, and M_3, five squark- and slepton-mass parameters m_Q, m_L, $m_{\bar{u}}$, $m_{\bar{d}}$, and $m_{\bar{e}}$, three trilinear scalar interaction parameters A_{u0}, A_{d0}, and A_{e0}, and three parameters in the Higgs sector [12]. Among the latter are the mass parameters m_{H_u} and m_{H_d} for the Higgs doublets that couples to up-type particles and down-type particles, respectively.

An important feature of the MSSM is that the sparticle gauge eigenstates listed in Table 2.2 are not necessarily the mass eigenstates of the theory. Left- and right-handed squarks and sleptons can mix to lighter (denoted by the index "1") and heavier (denoted by the index "2") mass eigenstates. Importantly for this thesis: While the mass eigenstates of the first- and second-generation squarks are typically nearly degenerated, the mass splittings between the lighter and heavier third-generation squarks can be large. Based on the above-mentioned assumptions, the squared-mass matrix for the top squarks in the gauge-eigenstate basis $(\tilde{t}_L\, \tilde{t}_R)$ becomes

$$\boldsymbol{m}^{\mathbf{2}}_{\tilde{\boldsymbol{t}}} \equiv \begin{pmatrix} m_Q^2 + m_t^2 + \Delta_{\tilde{u}_L} & m_t(a_t^* - \mu \cot\beta) \\ m_t(a_t - \mu^* \cot\beta) & m_{\bar{u}}^2 + m_t^2 + \Delta_{\tilde{u}_R} \end{pmatrix} . \tag{2.38}$$

Here, m_Q denotes the universal mass parameter for left-handed squark doublets, $m_{\bar{u}}$ the universal mass parameter for right-handed up-type squark singlets, $\tan\beta$ the ratio of the Higgs-doublets' vacuum expectation values, and μ the Higgsino-mass parameter. In the MSSM the latter is the only additional parameter that does not break Supersymmetry. The terms $\Delta_{\tilde{u}_L}$ and $\Delta_{\tilde{u}_R}$ can be expressed in terms of the weak mixing angle, the Z-boson mass, and β. However, these terms are small in comparison to m_t^2. The coupling parameter a_t is defined as $A_{u0}\gamma_t$, where A_{u0} is the trilinear scalar interaction parameter for up-type squarks and γ_t the top quark Yukawa coupling constant. In order to derive the top-squark mass eigenstates and the corresponding mass eigenvalues from (2.38), $\boldsymbol{m_{\tilde{t}}^2}$ must be diagonalized. Due to the large top quark Yukawa coupling constant, the off-diagonal entries will typically induce a large mixing, which may result in a significant mass splitting between the lighter and the heavier top squark. The squared-mass matrices for sleptons, first- and second generation squarks, and sbottom squarks are defined in analogy to (2.38). Thus, also left- and right-handed bottom squarks and tau sleptons mix to some extent. Since the Higgs coupling constants of squarks and sleptons of the first and second generations are small, their left- and right-handed states do almost not mix. Furthermore, their mass eigenstates are typically degenerated.

Since they carry the same gauge quantum numbers and spin, the electrically neutral wino, the bino, and the electrically neutral higgsinos may superimpose to four different mass eigenstates $\tilde{\chi}_1^0$, $\tilde{\chi}_2^0$, $\tilde{\chi}_3^0$, and $\tilde{\chi}_4^0$ (ordered by increasing mass), which are named *neutralinos*. Similarly, the electrically charged winos and higgsinos can mix to the mass eigenstates $\tilde{\chi}_1^\pm$ and $\tilde{\chi}_2^\pm$ ($m_{\tilde{\chi}_1^\pm} \leq m_{\tilde{\chi}_2^\pm}$), which are referred to as *charginos*. The gluino cannot mix with any other particle of the MSSM.

2.2.1.1. Hierarchy Problem

Contributions from fermion and gauge-boson loops to the squared Higgs-boson mass diverge quadratically with the cut-off scale Λ_{UV}. As addressed in Section 2.1.5, in the Standard Model the cancellation of these divergences requires an enormous amount of fine-tuning. In supersymmetric models, this problem can be naturally resolved. If SUSY-breaking is soft, the quadratic divergences automatically cancel at all orders of the perturbation series. Consider for example the loop of a Standard Model fermion, as illustrated in Fig. 2.6(a). Its contribution to the squared Higgs-boson mass is

$$\Delta m_H^2 = \frac{y_f^2}{8\pi^2}\left(-\Lambda_{\mathrm{UV}}^2 + \mathcal{O}\left(\ln\left(\Lambda_{\mathrm{UV}}/m_f\right)\right) + ...\right). \tag{2.39}$$

Here y_f denotes the fermion's Yukawa coupling constant, and m_f its mass. The term that is quadratic in Λ_{UV} is canceled by a term that arises from loops of the fermion's scalar superpartner, as exemplified in Fig. 2.6(b). Each of the contributions from the left- and the right-handed superpartner amount to

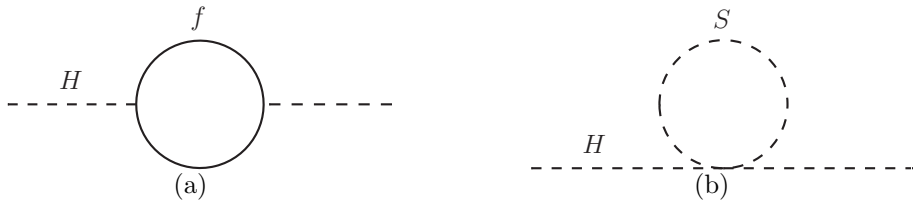

Figure 2.6.: Contributions from fermion- and scalar-loops to the squared Higgs-boson mass.

$$\Delta m_H^2 = \frac{\gamma_f^2}{16\pi^2}\left(\Lambda_{\mathrm{UV}}^2 - \mathcal{O}\left(\ln\left(\Lambda_{\mathrm{UV}}/m_S\right)\right) + ...\right). \tag{2.40}$$

Similarly, the quadratic divergences that arise from gauge-boson and gaugino loops as well as Higgs-boson and higgsino loops cancel out. However, since Supersymmetry is broken, the logarithmically divergent terms remain. Here, the largest contributions arise from loops of the left- and the right handed top squark and the left-handed bottom squark. Additional radiative corrections arise from two-loop diagrams with an intermediate gluino. The total corrections to the squared mass parameter for the up-type Higgs doublet, which couples to the top squark, then reads

$$\Delta m_{H_u}^2 \approx -\mu^2 - \frac{3}{8\pi^2}(m_Q^2 + m_{\bar{u}}^2 + |A_t|^2)\ln\left(\frac{\Lambda}{\mathrm{TeV}}\right) - \frac{2}{\pi^3}\gamma_t^2\alpha_s|M_3|^2\ln^2\left(\frac{\Lambda}{\mathrm{TeV}}\right), \tag{2.41}$$

where Λ denotes the scale at which Supersymmetry-breaking effects occur [46]. In order for Supersymmetry to be a natural solution of the hierarchy problem, each term $\delta m_{H_u}^2$ on the right side of Eq. (2.41) should be less than or of the order of $m_{H_u}^2$. Otherwise, the different contributions needed to be fine-tuned to cancel each other. As a measure of the amount of fine-tuning one can define

$$\Delta \equiv \frac{2\delta m_{H_u}^2}{m_h^2}. \tag{2.42}$$

In order for Δ to be less than 20%, the masses of the left- and right-handed top squarks and the left-handed bottom squark should be below 500 to 700 TeV, the mass of the gluino should be below 900 GeV to 1.5 TeV, and two higgsinos should be lighter than 200 to 350 GeV [5].

2.2.1.2. R-Parity Conservation

In contrast to the Standard Model, Supersymmetry allows for gauge-invariant and renormalizable terms in the Lagrangian that violate the conservation of the lepton

number L and the baryon number B. However, by now such processes have not been observed yet. The strongest limit on the violation of L and B conservation arise from lower bounds on the proton lifetime. As exemplified in Fig. 2.7, the proton decay would violate the conservation of both L and B by 1.

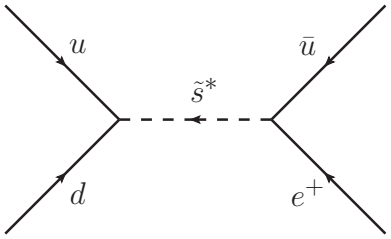

Figure 2.7.: Lepton and baryon number conservation violating process that contributes to the proton decay.

Such processes would result in an extremely short proton lifetime, which motivates the introduction of a new multiplicative quantum number, R *parity*, which is defined as

$$P_R = (-1)^{3\,(B\,-\,L)+2\,S}\,, \tag{2.43}$$

where S denotes the particle's spin. While Standard Model particles have even R parity ($P_R = +1$), sparticles obtain odd R parity ($P_R = -1$).

Assuming R parity to be conserved, processes like the one illustrated in Fig. 2.7 are not allowed. Furthermore, R-parity conservation requires sparticles to be produced in pairs and their decay chains to terminate with the lightest supersymmetric particle (LSP). In many scenarios the LSP is the lightest neutralino ($\tilde{\chi}_1^0$), which is a viable dark-matter candidate. Throughout this thesis, R parity is assumed to be conserved and $\tilde{\chi}_1^0$ to be the LSP.

2.2.1.3. Unification of Gauge Couplings

As a consequence of the renormalization, the gauge-coupling constants are running (cf. Section 2.1.4). While the coupling constant of $\mathrm{U(1)_Y}$ increases as the energy scale Q gets larger, the strong coupling constant decreases with Q. In the Standard Model, this does also apply for the coupling constant of $\mathrm{SU(2)_L}$. However, as can be seen in Fig. 2.8, in the SM, the gauge coupling constants (represented by the dashed lines) do not coincide at any energy scale. In the MSSM, additional contributions from sparticle loops alter the running of the coupling constants. As can be seen in Fig. 2.8, for sparticle masses in the range between 100 GeV and 10 TeV, the coupling constants coincide at a *unification scale* of about 10^{16} GeV. In this sense, Supersymmetry allows for the unification of gauge couplings.

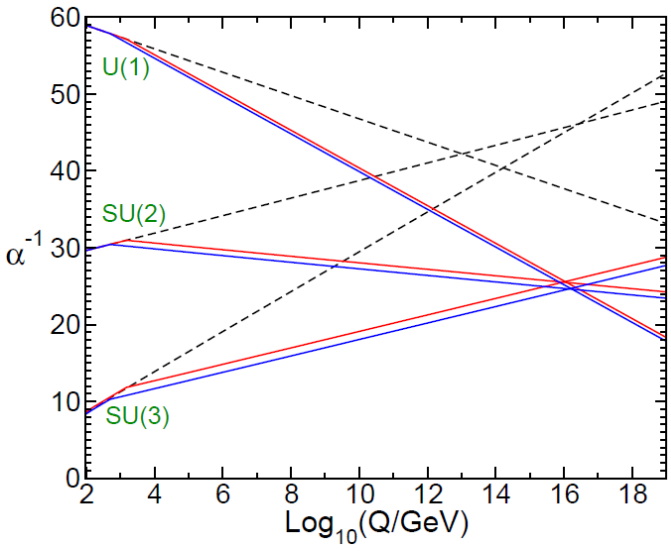

Figure 2.8.: Evolution of the inverse gauge coupling constants as a function of Q in the Standard Model (represented by the dashed lines) and the MSSM (indicated by the solid lines).

2.2.2. Constrained Minimal Supersymmetric Standard Model

In analogy to the electroweak symmetry, Supersymmetry is spontaneously broken. While the Lagrangian density is invariant under Supersymmetry transformations, its vacuum state is not. However, since Supersymmetry cannot be broken by any particle of the MSSM, commonly a *hidden sector*, where the actual SUSY breaking takes place, is introduced.

In *gravity-mediated models* the breaking is mediated through gravitational-strength interactions. In the minimal case of the *Constrained Minimal Supersymmetric Standard Model* (CMSSM) all terms in the soft SUSY-breaking Lagrangian are determined by four parameters [12]. These are the parameters for scalar and gaugino masses m_0 and $m_{1/2}$ at the unification scale $M_{\mathrm{GUT}} \approx 2 \cdot 10^{16}$ GeV, the universal trilinear scalar interaction parameter A_0, and a parameter in the Higgs sector. The fourteen free parameters in the soft SUSY-breaking Lagrangian discussed in Section 2.2.1 become

$$m_Q^2 = m_{\bar{u}}^2 = m_{\bar{d}}^2 = m_L^2 = m_{\bar{e}}^2 = m_{H_u}^2 = m_{H_d}^2 = m_0^2, \tag{2.44}$$

$$M_1 = M_2 = M_3 = m_{1/2}, \tag{2.45}$$

$$A_{0u} = A_{0d} = A_{0e} = A_0. \tag{2.46}$$

As free parameter in the Higgs sector $\tan\beta$ can be chosen. In the CMSSM, the sign of μ constitutes a fifth free parameter.

2.2.3. Phenomenology of Light Top and Bottom Squarks

Experimental limits on flavor-changing neutral currents and CP violation strongly constrain the soft SUSY-breaking Lagrangian of the MSSM [12]. Fixing certain parameters in the Lagrangian, such limits can be interpreted as constraints on other parameters. For example, assuming the gluino mass to be less than about 1 TeV and a certain mixing between down and strange squarks, limits on the amount of K^0-$\bar{K}^0$ mixing can be interpreted as lower bounds on the masses of the involved squarks. Since such bounds are more stringent for the squarks of the first and second generations ($\tilde{q}$), the latter are often preferred to be heavy, see e.g. [47, 48]. In order for Supersymmetry to be the natural solution of the hierarchy problem, the left- and the right-handed top squark and the left-handed bottom squark, in contrast, must be relatively light. The mixing of left- and right-handed squarks may then result in one top-squark mass eigenstate that is significantly lighter than the squarks of the first and second generations. Also, one bottom-squark mass eigenstate may be considerably lighter than the latter. Consequently, third-generation squarks may be copiously produced at the LHC.

Based on the assumption that $m_{\tilde{t}_1} < m_{\tilde{b}_1} < m_{\tilde{q}}$, the production and possible two-body decays of light third-generation squarks are discussed in the following. Within this discussion, it is assumed that all processes that involve flavor transitions between the first two generations and the third generation of quarks and squarks are strongly suppressed. Since light top and bottom squarks may originate from the decay of gluinos that are produced in association with first- and second-generation squarks, possible decays of the latter are addressed as well. Signatures of Supersymmetry with light third-generation squarks at *particle level*, i.e. before the interaction of final-state particles with the detector, are then deduced by "sticking together" relevant production processes and decay modes.

2.2.3.1. Production of Light Top and Bottom Squarks

Much in analogy to the production of bottom and top quarks in the Standard Model, the main processes of direct top- and bottom-squark production are the pair production induced by gluon exchange in the s-channel, squark exchange in the t-channel, and squark exchange in the u-channel (cf. Appendix A, Fig. A.1). Since $\tilde{t}\tilde{t}^*$ and $\tilde{b}\tilde{b}^*$ production induced by gluino exchange in the t-channel (cf. Fig. A.2) requires the initial state to contain a $t\bar{t}$ and a $b\bar{b}$ pair, respectively, it is strongly suppressed by the PDFs (cf. Section 2.1.3). Similarly, the pair production of same-sign third-generation squarks induced by gluino exchange in the t- and the u-channel (cf. Fig. A.3) is suppressed by the PDFs. For similar masses, the cross section of direct pair production of third-generation squarks is therefore small compared to the cross section of direct pair production of first- and second-generation squarks. In Fig. 2.9, the NLO cross sections for sparticle production as a function of their

average mass calculated with PROSPINO2.1 [54] are shown. As can be seen, over the whole range of considered sparticle masses, the cross section for $\tilde{q}\tilde{q}^*$ production (represented by the lower green line) is more than one order of magnitude larger than the cross section for $\tilde{t}_1\tilde{t}_1^*$ production (represented by the dark blue line). The cross section for $\tilde{q}\tilde{q}$ production (represented by the upper green line) is even larger than the cross section for $\tilde{q}\tilde{q}^*$ production. Certainly, when comparing these cross sections it has to be taken into account that only one third-generation squark mass eigenstate out of four is considered. For degenerate squark masses ($\tilde{t}_1$ will be purely composed by $\tilde{t}_L$ then), $\tilde{t}_R\tilde{t}_R^*$, $\tilde{b}_L\tilde{b}_L^*$, and $\tilde{b}_R\tilde{b}_R^*$ production will similarly contribute to the cross section for direct pair production of third-generation squarks.

Further contributions to the direct production of third-generation squarks may originate from the production of single top squarks in association with a bottom squark (s-channel), a squark of the first or second generation (t-channel), and a chargino. However, like the contribution from single-top-quark production to the Standard Model background, the contribution from single-top-squark production to a potential signal is small in the search presented in this thesis. Therefore, it is not further considered.

Besides the direct production, top and bottom squarks may be produced from the gluino decays $\tilde{g} \to t\tilde{t}^*$ and $\tilde{g} \to b\tilde{b}^*$. The main processes of gluino production are the squark-associated production ($\tilde{q}\tilde{g}$) and the pair production ($\tilde{g}\tilde{g}$), whose cross sections are represented by the upper and the lower red line, respectively. Further contributions to the gluino-induced production may originate from the production of $\tilde{q}\tilde{q}$ and $\tilde{q}\tilde{q}^*$ pairs with the subsequent decay of a squark into a quark and a gluino.

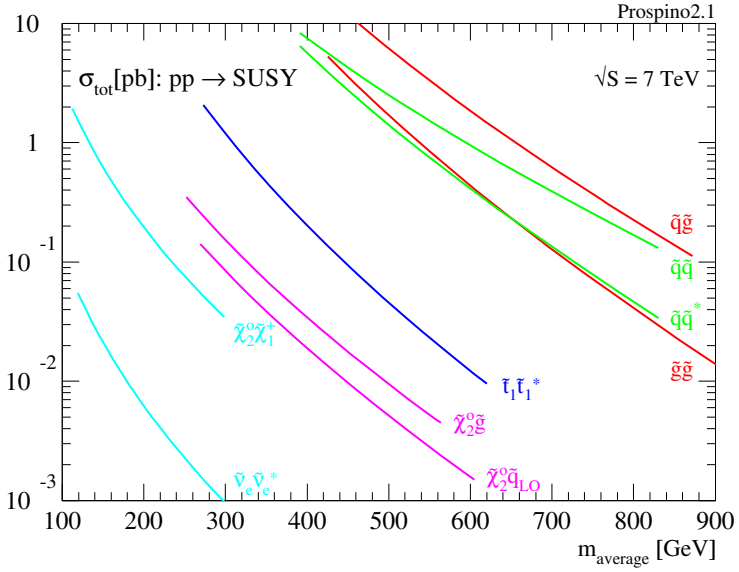

Figure 2.9.: Cross sections for $\tilde{q}\tilde{q}$, $\tilde{q}\tilde{q}^*$, $\tilde{q}\tilde{g}$, $\tilde{g}\tilde{g}$ [49], $\tilde{t}_1\tilde{t}_1^*$ [50], $\tilde{\chi}_2^0\tilde{q}$, $\tilde{\chi}_2^0\tilde{g}$ [51, 52], $\tilde{\chi}_2^0\tilde{\chi}_1^+$, and $\tilde{\nu}_e\tilde{\nu}_e^*$ [53] production in proton-proton collisions at $\sqrt{s} = 7$ TeV.

2.2.3.2. Decay of Light Top and Bottom Squarks

Assuming $m_{\tilde{t}_1} < m_{\tilde{b}_1} < m_{\tilde{q}}$, the only possible two-body decays of the lighter top squark that are not flavor-suppressed are the decay into a top quark and a neutralino, as shown in Fig. 2.10(a), the decay into a bottom quark and a chargino, which is illustrated in Figs. 2.10(b) - (d), and, if $m_{\tilde{t}_1} > m_t + m_{\tilde{g}}$, the decay into a top quark and a gluino. As can be seen in Fig. 2.9, if the gluino is lighter than the lighter top squark, the cross section for $\tilde{t}_1\tilde{t}_1^*$ production is more than one order of magnitude smaller than the cross section for $\tilde{g}\tilde{g}$ production and about two orders of magnitude smaller than the one for $\tilde{q}\tilde{g}$ production. The dominant sources of top and bottom quark production are then the gluino three-body decays $\tilde{g} \to t\bar{t}\tilde{\chi}^0$, $\tilde{g} \to b\bar{b}\tilde{\chi}^0$, and $\tilde{g} \to t\bar{b}\tilde{\chi}^{\mp}$. The discussion of top and bottom squark decays is therefore restricted to the cases $m_{\tilde{t}} < m_t + m_{\tilde{g}}$ and $m_{\tilde{b}} < m_b + m_{\tilde{g}}$.

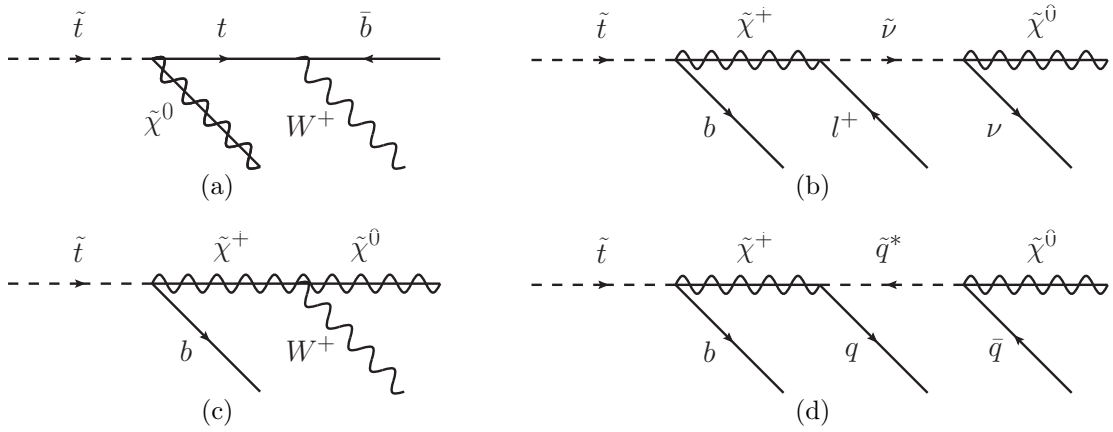

Figure 2.10.: Decays of the lighter top squark into a top quark and a neutralino (a) and a bottom quark and a chargino (b, c, d). For $m_{\tilde{t}_1} < m_{\tilde{b}_1} < m_{\tilde{q}}$ and $m_{\tilde{t}_1} < m_t + m_{\tilde{g}}$ these are the only possible two-body decays that are not flavor-suppressed.

The top quark almost exclusively decays into a bottom quark and a W^+ boson (cf. Section 2.1.1). The W^+ boson subsequently decays either hadronically into a pair of an up-type quark and a down-type antiquark of the first or second generation, or leptonically into a charged antilepton and a neutrino. The chargino decay either results in a state that contains a neutralino and a W^+ boson (cf. Fig. 2.10(c)), or a neutralino and a W-like final state. Within this thesis, "W-like final state" refers to states that comprise a charged antilepton and a neutrino (cf. Fig. 2.10(b)), or a pair of an up-type quark and a down-type antiquark of the first or second generation (cf. Fig. 2.10(d)). While no assumption about the slepton masses is made, the first- and second-generation squarks are assumed to be heavier than the lighter top squark. In the considered decay cascades, the chargino decay $\tilde{\chi}^+ \to q\tilde{q}^* \to q\bar{q}\tilde{\chi}^0$ therefore

requires the intermediate antisquark to be produced off-shell. Hence, this decay only becomes relevant if all chargino two-body decays are kinematically forbidden.[9]

Both two-body decays of the lighter top squark discussed above will result in states that comprise a bottom quark, a W boson/W-like final state, and an LSP. If both decays are kinematically allowed, the branching ratios depend on the masses of the involved particles and the composition of neutralinos and charginos. If both are kinematically forbidden, the three-body decay $\tilde{t}_1 \to bW^+\tilde{\chi}_1^0$ becomes important. In scenarios where even this decay is kinematically forbidden, possible flavor-suppressed decays and the four-body decay $\tilde{t}_1 \to bl^+\nu\tilde{\chi}_1^0$ become relevant. However, such scenarios are beyond the scope of this thesis (see also Section 6).

Possible two-body decays of the lighter bottom squark arise from the processes discussed above by replacing particles with top flavor by antiparticles with bottom flavor and vice versa. Assuming $m_{\tilde{b}_1} > m_{\tilde{t}_1} + m_W$, the decay $\tilde{b}_1 \to \tilde{t}_1 + W^-$ arises as third possibility. Except for the decay $\tilde{b}_1 \to b\tilde{\chi}^0$, all possible not-flavor suppressed two-body decays of the lighter bottom squark will result in states with a bottom quark, two W bosons/W-like final states, and an LSP. Since $\tilde{t}_1$ is assumed to be lighter than $\tilde{b}_1$, it can be expected that at least one of the decays $\tilde{b}_1 \to t\tilde{\chi}_1^-$ and $\tilde{b}_1 \to \tilde{t}_1 + W^-$ is kinematically allowed.

The discussion of possible two-body decays of the lighter top and the lighter bottom squark above is not exhaustive, insofar as the considered processes may include additional decay steps. Among these, the intermediate decays $\chi_2^\pm \to \tilde{\chi}_1^\pm X^0$ and the terminating decays $\tilde{\chi^0}_{2,3,4} \to \tilde{\chi}_1^0 X^0$ with $X^0 \equiv Z, h^0$ are relevant. Due to their large Higgs coupling constants, top and bottom squarks strongly couple to the higgsinos. Depending on the composition of neutralinos and charginos and the mixing of left- and right-handed top and bottom squarks (cf. Section 2.2.1), the lighter top and the lighter bottom squark may decay with a large branching ratio into the heavier neutralino and chargino states, though the decay into the lighter states is kinematically preferred. Depending on the mass differences between the heavier and the lighter chargino and neutralino states, the Z boson and the lightest neutral Higgs boson will be produced on- or off-shell, resulting in a pair of potentially soft quarks or leptons.

The possible decays of the heavier top and bottom squarks are basically the same as those of the lighter ones. The main difference is that the former decays may include further initial decay steps, such as $\tilde{t}_2 \to X^0\tilde{t}_1$ and $\tilde{b}_2 \to X^0\tilde{b}_1$. However, since the heavier mass eigenstates will be less frequently produced, their decays are less relevant with regard to the formulation of expected signatures.

[9] Due to the large top-quark mass, the chargino three-body decay $\tilde{\chi}^+ \to t\bar{b}\tilde{\chi}^0$ is always suppressed. If $m_{\tilde{\chi}^\pm} > m_W + m_{\tilde{\chi}^0}$, the chargino will predominantly decay into a W boson and a neutralino. If $m_{\tilde{\chi}^\pm} < m_W + m_{\tilde{\chi}^0}$, the three-body decay $\tilde{\chi}^+ \to t\bar{b}\tilde{\chi}^0$ is kinematically forbidden, because $m_{\tilde{\chi}^\pm} < m_t + m_b + m_{\tilde{\chi}^0}$.

2.2.3.3. Decay of First and Second Generation Squarks

Assuming the masses of first- and second-generation squarks to be nearly degenerated, the decays $\tilde{q} \to \tilde{q}^* W^+$ and $\tilde{q} \to \tilde{q} X^0$ are kinematically forbidden. If $m_{\tilde{q}} < m_{\tilde{g}}$, the only possible two-body decays that are not flavor-suppressed are the decay into a quark of the first or second generation and a neutralino, as shown in Fig. 2.11(a), and the decay into a quark and a chargino, as illustrated in Fig. 2.11(b). If $m_{\tilde{q}} > m_{\tilde{g}}$, the squark may also decay into a quark and a gluino, as shown in Fig. 2.11(c).

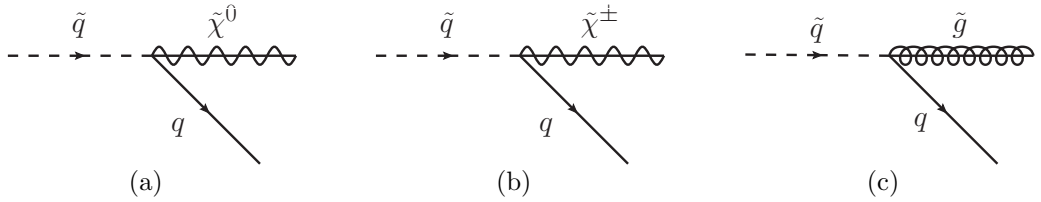

Figure 2.11.: Possible not flavor-suppressed two-body decays of first and second generation squarks in scenarios where their masses are nearly degenerated. The decay into a gluino and a quark (c) requires $m_{\tilde{q}} > m_{\tilde{g}}$.

2.2.3.4. Signatures of Light Top and Bottom Squarks

In the following, signatures of direct pair production and gluino-induced production of light third-generation squarks are discussed. Since possible additional initial, intermediate, and terminating decay steps are not explicitly considered, the discussed signatures can be regarded as minimal. Pairs of additional quarks and leptons can always be produced from on and off-shell decays of Z and lightest neutral Higgs bosons. As discussed in the beginning of Section 2.2.3.1, the discussion of signatures of direct pair production is restricted to the cases $m_{\tilde{t}} < m_t + m_{\tilde{g}}$ and $m_{\tilde{b}} < m_b + m_{\tilde{g}}$.

Signatures of Direct Top-Squark Pair Production Direct $\tilde{t}\tilde{t}^*$ production will result in states that comprise two bottom quarks, two W boson/W-like final states and two LSPs. Two examples for the decay of a $\tilde{t}\tilde{t}^*$ pair are shown in Fig. 2.12. Depending on the decays of the W bosons and the composition of the W-like final states, direct $\tilde{t}\tilde{t}^*$ production will result in an all-hadronic final state (two b-quark jets and four light-quark jets), a single-lepton final state (two b-quark jets, two light-quark jets, and one charged lepton), or a dileptonic final state (two b-quark jets and two charged leptons). Within this thesis "light-quark jet" refers to jets that originate from quarks of the first and second generations. Within the considered decay cascades, charged leptons are produced along with neutrinos in W-boson and two- or three-body chargino decays. In contrast to leptons that are produced within jets, these leptons can be assumed to be well isolated from other activity.

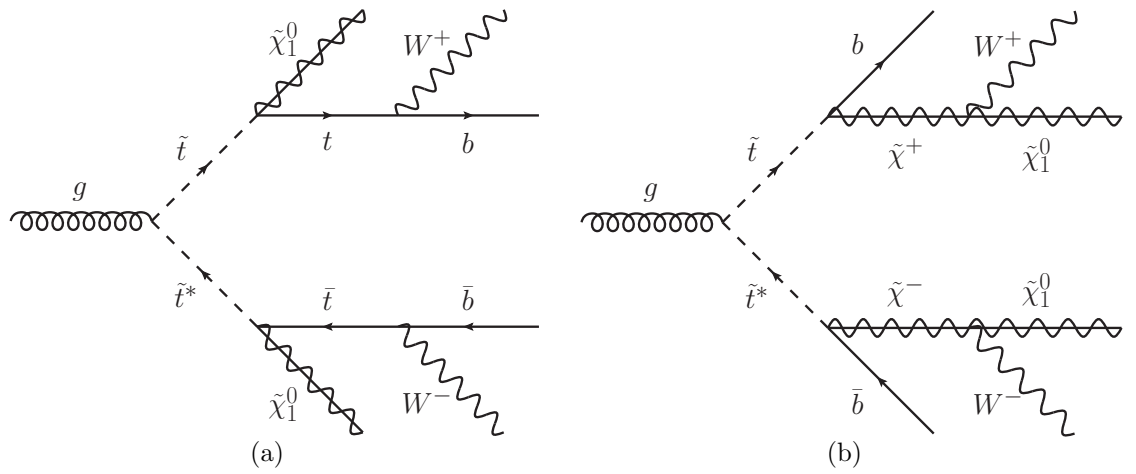

Figure 2.12.: Examples for the decay of a $\tilde{t}\tilde{t}^*$ pair. The top squarks either decay into a top quark and a neutralino (a) or a bottom quark and a chargino (b).

Since the LSPs are massive and produced from the decays of heavy and potentially high-energetic sparticles, they are expected to carry away a large amount of momentum. Like the neutrinos produced along with the isolated leptons, the LSPs escape detection, resulting in a significant imbalance of the visible transverse momentum.

Signatures of Direct Bottom-Squark Pair Production Direct $\tilde{b}\tilde{b}^*$ production gives rise to a larger number of possible final states than direct $\tilde{t}\tilde{t}^*$ production. These final states can be classified by the number of W bosons/W-like final states. If both bottom squarks decay into a bottom quark and an LSP, final states will be characterized by two high-energetic bottom-quark jets and a significant imbalance of the visible transverse momentum. However, assuming the branching ratio for the decay $\tilde{b} \to b\tilde{\chi}^0$ to be small (< 0.25) as in the CMSSM benchmark scenarios considered later in this thesis (cf. Section 4.3.1), the contribution from the process $\tilde{b}\tilde{b}^* \to b\bar{b}\tilde{\chi}^0\tilde{\chi}^0$ ($< 6.25\%$) can be ignored. In less than about 40% of all $\tilde{b}\tilde{b}^*$ events one bottom squark will then decay into a bottom quark and an LSP, while the decay of the other will result in a state that contains two W bosons/W-like final states in addition, as illustrated in Fig. 2.13(a). These events will have a similar signature as expected from direct $\tilde{t}\tilde{t}^*$ production. The main difference will result from the different event topology. Since the bottom quark and the LSP produced from the decay $\tilde{b} \to b\tilde{\chi}^0$ need to rebalance all other activity, one bottom-quark jet might be highly boosted. Also, the imbalance of transverse momentum might be more significant. In more than about 55% of all events, both bottom-squark decays result in states that comprise a bottom quark, two W bosons/W-like final states, and an LSP, as shown in Fig. 2.13(b).

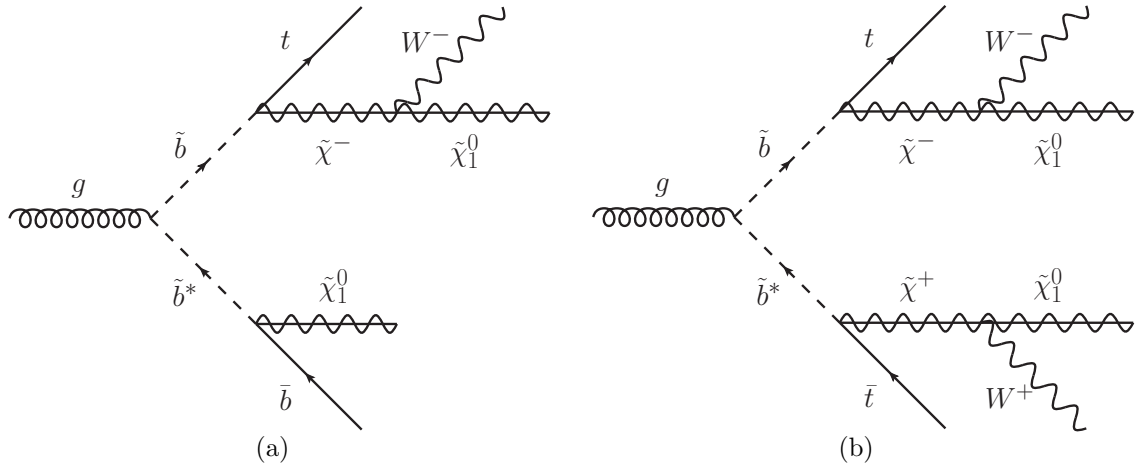

Figure 2.13.: Examples for the decay of a $\tilde{b}\tilde{b}^*$ pair. Assuming the branching ratio for the decay $\tilde{b} \to b\tilde{\chi}^0$ to be small (< 0.25), the $\tilde{b}\tilde{b}^*$ pair will decay in less than about 40% as illustrated in (a) and in more than about 55% as exemplified in (b).

Besides the common characteristics of direct top- and bottom-squark pair production, final states will be characterized by a large multiplicity of light-quark jets and isolated leptons.

Signatures of Gluino-Induced Production Since the strong interaction conserves the quark flavor, top and bottom squarks from gluino decays are always produced in association with a top and a bottom quark, respectively. Except for the decay $\tilde{g} \to b\tilde{b}^* \to b\bar{b}\tilde{\chi}^0$, the gluino decay into third-generation squarks therefore always results in states with two bottom quarks, two W bosons/W-like final states, and two LSPs. The branching fractions for the decays $\tilde{g} \to b\tilde{b}^*$ and $\tilde{g} \to t\tilde{t}^*$ strongly depend on the hierarchy of gluino and squark masses, which motivates the distinction of the following three cases.

- If $m_{\tilde{t}_1} + m_t < m_{\tilde{g}} < m_{\tilde{q}}$ and $m_{\tilde{b}_1} + m_b < m_{\tilde{g}} < m_{\tilde{q}}$, the gluino exclusively decays into third-generation squarks. If the mass differences between the gluino and the lighter top and bottom squarks are not too large, the decays $\tilde{g} \to t\tilde{t}_1^*$ and $\tilde{g} \to b\tilde{b}_1^*$ will be the dominant source of third-generation squark production. Assuming the same branching ratio for the decay $\tilde{b} \to b\tilde{\chi}^0$ as above (< 0.25), the contribution from the process $\tilde{g}\tilde{g} \to b\bar{b}b\bar{b}\tilde{\chi}^0\tilde{\chi}^0$ to the production of third-generation squarks induced by $\tilde{g}\tilde{g}$ production is smaller than 6.25% times the squared branching ratio for the decay $\tilde{g} \to b\tilde{b}_1^*$. Hence, it can be neglected. Gluino-pair production will then result in states with four bottom quarks, two or four W boson/W-like final states, and two LSPs. If the gluino decays with

the same frequencies into $t\tilde{t}_1^*$ and $b\tilde{b}_1^*$ pairs, $\tilde{g}\tilde{g}$ pair production will even result in more than about 85% in a four-top-like final state, as exemplified in Fig. 2.14. Within this thesis, "top-like final state" refers to states that comprise a bottom quark and a W boson/W-like final state. Besides a significant imbalance of the visible transverse momentum, final states will be characterized by a large multiplicity of b-quark jets, light-quark jets, and isolated leptons. The squark-associated gluino production can be expected to result in states with at least two bottom quarks, two W bosons/W-like states, two LSPs, and one potentially high-energetic quark from the decay $\tilde{q} \to q\tilde{\chi}_1^0$, as illustrated in Fig. 2.15. As squarks of the first and second generations can also decay into a gluino and a quark, $\tilde{q}\tilde{g}$ production may even result in final state with more isolated leptons and light-quark jets than $\tilde{g}\tilde{g}$ production.

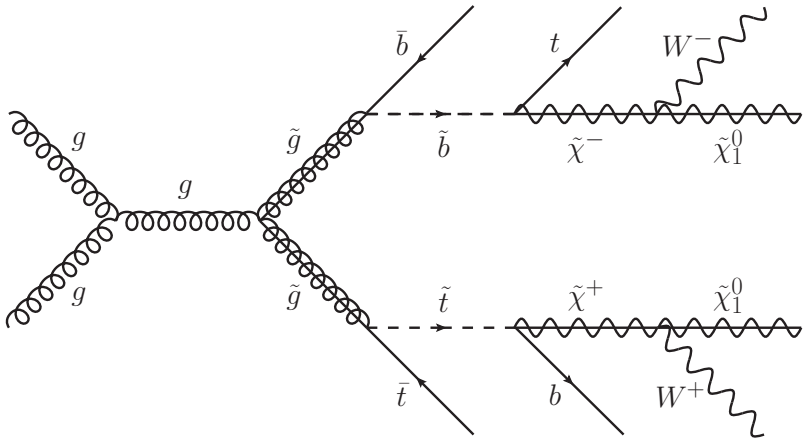

Figure 2.14.: Example for the production and decay of a gluino pair. For $m_{\tilde{t}_1} + m_t < m_{\tilde{g}} < m_{\tilde{q}}$ and $m_{\tilde{b}_1} + m_b < m_{\tilde{g}} < m_{\tilde{q}}$ gluino pair production is likely to result in states with four top quarks/top-like final states and two LSPs.

- If $m_{\tilde{g}} > m_{\tilde{q}}$, the gluino may decay into squark-antiquark pairs of all flavors. The branching ratio for the decay into third-generation squarks is reduced accordingly. In addition, the squark-induced gluino production is kinematically forbidden. Hence, the cross section for the gluino-induced production of third-generation squarks is considerably smaller. Gluino-pair production and squark-associated production will give rise to a variety of final states. Assuming one decay chain to contain a gluino that decays into a $t\tilde{t}^*$ or $b\tilde{b}^*$ pair and the other decay chain not to contain any third-generation squarks, the gluino-induced production can be expected to result in a similar final state as the direct $\tilde{t}\tilde{t}^*$ production, accompanied by at least one or two potentially high-energetic light-quark jets.

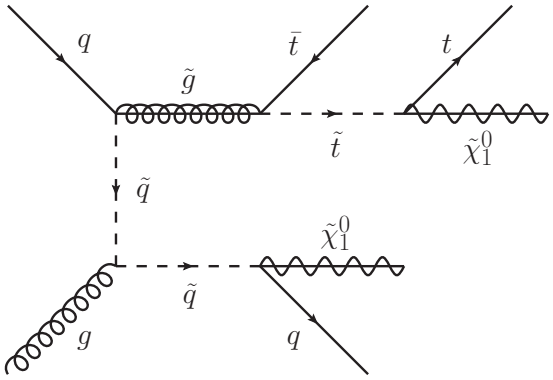

Figure 2.15.: Example for the squark-associated production and decay of a gluino. For $m_{\tilde{t}_1} + m_t < m_{\tilde{g}} < m_{\tilde{q}}$ and $m_{\tilde{b}_1} + m_b < m_{\tilde{g}} < m_{\tilde{q}}$ the squark-associated production is likely to result in states with at least two top quarks/top-like final states, two LSPs, and one potentially high-energetic quark of the first or second generation.

- If $m_{\tilde{g}} < m_{\tilde{t}} + m_t$ and $m_{\tilde{g}} < m_{\tilde{b}} + m_b$, the only possible gluino decay is the three-body decay into a quark, an antiquark, and a neutralino or chargino, e.g. $\tilde{g} \to t\bar{t}\tilde{\chi}^0$. If the first and second generation squarks are not decoupled, the gluino three-body decay into third-generation quarks will only slightly be preferred, if at all. Final states will be similarly composed as in the case $m_{\tilde{g}} > m_{\tilde{q}}$. The kinematics, however, will be different.

2.2.4. Simplified Models

Reflecting the large number of free parameters in the soft SUSY-breaking Lagrangian of the MSSM, the obtained results can be interpreted in a variety of supersymmetric models. However, even under the simplifying assumptions of only fourteen free parameters in the SUSY-breaking Lagrangian and light top and bottom squarks, as discussed in Sections 2.2.1 and 2.2.3, it is practically impossible to scan the whole parameter space. Besides a few benchmark models, such as the CMSSM described in Section 2.2.2 and the *Gauge-Mediated Supersymmetry-Breaking* (GMSB) model, simplified models [55, 56] are therefore commonly used for the interpretation of results at the ATLAS and CMS experiments. While complete models like the CMSSM and the GMSB model are characterized by different processes of sparticle production and decay, simplified models just cover a particular process, e.g. only the pair production of top squarks with the subsequent decay of each top squark into a top quark and the LSP (as illustrated above in Fig. 2.12(a)). The basic idea behind simplified models is that any complete scenario can be decomposed in simplified model scenarios. Hence, exclusion limits set among the parameters of simplified models

might be combined to obtain limits on complete models. An implementation of such an approach can be found for example in [57]. However, it should be noted that in general the possibility of propagating limits strongly depends on the way the Standard Model background is predicted. As will be discussed later in Section 7, in many searches the background in a potentially signal-enhanced region of the phase space is predicted from *control regions* or *control samples* that are assumed to be signal depleted. While this assumption might be well motivated for a specific simplified model, it might not hold for a realistic scenario, where contributions to the control regions may arise from additional processes of sparticle production and decay.

In this thesis, the results are interpreted in the context of the CMSSM and a simplified model that contains the pair production of gluinos each of which subsequently decays into a $t\bar{t}$ pair and an LSP, as illustrated in Fig. 2.16. The model has no intermediate mass state. Hence, the free parameters of this model are the gluino and the LSP mass.

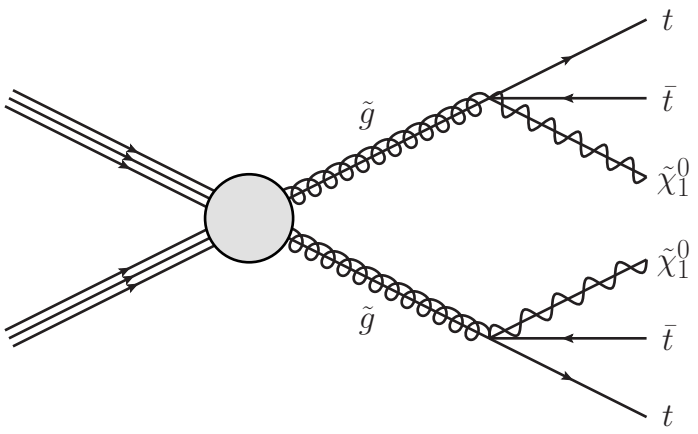

Figure 2.16.: Four-top quark simplified model.

In addition, two simplified models that contain the direct pair production of third generation squarks are examined. One of these covers the pair production of top squarks with the subsequent decay of each top squark in a top quark and an LSP, as illustrated in Fig. 2.12(a). Here, the free parameters are the top squark and the LSP mass. The other one contains the pair production of bottom squarks each of which decays into a top quark and a chargino. The charginos subsequently decay into a W boson an the LSP, as shown in Fig. 2.13(b). The free parameters of this model are the bottom squark and the LSP mass. The chargino mass is fixed to be halfway between the bottom squark and the LSP mass.

2.3. Other Extensions of the Standard Model

Shortcomings of the Standard Model (cf. Section 2.1.5) have inspired for a variety of models for new physics. In the following, a few extensions of the Standard Model that may involve similar signatures as Supersymmetry are outlined.

2.3.1. Extra Dimensions

Theories with extra spatial dimensions constitute extensions of the four-dimensional Minkowski-space. A general introduction to theories with extra dimensions is given in [58] and [59].

In *Kaluza-Klein scenarios* [60,61], compact finite extra dimensions are introduced. In the simplest case of one extra dimension with compactification radius R, a set of coordinates is given by (x^μ, z), where z is the coordinate along the extra dimension running from 0 to $2\,\pi R$. The points $z = 0$ and $z = 2\,\pi R$ are identified, leading to the picture of a "curled up" extra dimension. To illustrate the propagation of particles in this (4+1)-dimensional space-time, a free particle with Spin $S = 0$ is considered. Such a particle can be described by solutions of the five-dimensional Klein-Gordon-equation

$$(\Box_{(5)} + m^2)\,\Phi_{(5)} = 0\,, \tag{2.47}$$

where m denotes the particle's mass and $\Box_{(5)}$ the five-dimensional d'Alembert operator $\Box - (\frac{\partial}{\partial z})^2$. A complete set of solutions of Eq. (2.47) is given by the functions $\Phi_{(5)} = e^{ip_\mu x^\mu} e^{inz/R}$ with $n \in \mathbb{Z}$. Substituting the term $(\frac{\partial}{\partial z})^2\,\Phi_{(5)}$ in Eq. (2.47) by $(n/R)^2\,\Phi_{(5)}$ yields the four-dimensional Klein-Gordon equation with an additional mass term,

$$(\Box + m^2 + (n/R)^2)\,\Phi = 0\,. \tag{2.48}$$

Hence, from the (3+1)-dimensional point of view, this particle appears as resonance with a mass of $m^2_{(4)} = m^2 + (n/R)^2$. Assuming all fields to propagate in the extra dimension, excited states of the Standard Model fermions and gauge bosons will show up as resonances with masses of $m^2_{(4)} = m^2 + (n/R)^2$ as well [62]. A particle that propagates in the extra dimension (*Kaluza-Klein particle* or *Kaluza-Klein resonance*) carries a quantized momentum of $p_z = n/R$, $n \in \mathbb{Z}$. In analogy to R-parity conservation in supersymmetric models, the conservation of momentum therefore requires Kaluza-Klein resonances to be produced in pairs and their decay chains to terminate with the lightest Kaluza-Klein particle (LKP), e.g. the first excited state of the photon, leading to similar signatures as Supersymmetry. Like the LSP, the LKP is a natural dark matter candidate. It is straightforward to extent this minimal model of *universal extra dimensions* (UED) to more than one extra dimension. To explain why no Kaluza-Klein resonance has been observed yet, the compactification radii in models with UED need to be small ($R \lessapprox 10^{-17}\,\mathrm{cm}$).

In *ADD models* [63], named after N. Arkani-Hamed, S. Dimopoulos, and G.R. Dvali, in contrast, large extra dimensions are introduced. To explain why these extra dimensions have not been observed yet, all Standard Model particles are assumed to be trapped to the (3+1)-dimensional space-time. Only gravitons may freely propagate in the extra dimensions. This may explain the weakness of gravity relative to the other known interactions. For example, introducing d compact extra dimensions with the radius R, the $(4+d)$-dimensional Planck scale $\Lambda_{\mathrm{Pl}_{4+d}}$ becomes

$$\Lambda_{\mathrm{Pl}_{4+d}} \sim R^{-\left(1+\frac{d}{2}\right)} \Lambda_{\mathrm{Pl}}^{1+\frac{2}{d}} . \tag{2.49}$$

Hence, the fundamental Planck scale could be comparable to the electroweak scale. Assuming the latter to be the only fundamental short distance scale in nature, the hierarchy problem addressed in Section 2.1.5 is trivially resolved: The introduced cut-off scale is the electroweak scale, such that the the large corrections to the bare Higgs-boson mass are not required. Since extra dimensions involve deviations from the law of gravity at distances $r < R$ [58,59], measurements of the gravitational interaction at short lengths may constrain the number of extra dimensions. Assuming the fundamental Planck scale and the electroweak scale to be of the same size, models with $d = 1$ extra dimension can indeed be excluded because they would involve a deviation from the law of gravity at distances $r \leq 10^{13}\,\mathrm{cm}$. The case of $d \geq 2$ extra dimensions corresponds to a radius of $R \leq 0.1\,\mathrm{mm}$, which motivates to search for deviations from the law of gravity in the sub-millimeter range. Besides the detection of black holes [64], evidences for large extra dimensions at the LHC may stem from an enhanced production of final states with a mono-jet and a significant amount of missing transverse energy, resulting from a real graviton that escapes detection as well as a deviation of the measured Drell-Yan cross section from the predicted one due to contributions from virtual graviton exchange.

Signatures of *warped extra dimensions* introduced in *Randall-Sundrum models* [65, 66] may result from the observation of heavy resonances. In Randall-Sundrum models, excited states of the Standard Model gauge bosons may directly decay into ordinary particles because no symmetry protects the lightest Kaluza-Klein particle from decay. At the LHC, one emphasis is the search for $t\bar{t}$ resonances, see e.g. [67–72]. These might e.g. result from the decay of the first excited state of the gluon. In models with R-parity conserving Supersymmetry, dijet resonances may only result from the decay of neutral Higgs bosons and scalar gluon superpartners, as introduced in the Minimal R symmetric Supersymmetric Standard Model [73]. However, for $\tan\beta > 5$ the decay of H^0 and A^0 into pairs of up-type quarks is heavily suppressed.

2.3.2. Grand Unified Theories

While Supersymmetry constitutes an extension of the Standard Model by symmetries that can be regarded as *external*[10], the SM can also be extended by additional gauge symmetries, which constitute *internal* symmetries. Examples are Grand Unified Theories (GUTs), were the Standard Model gauge group is embedded in some higher gauge group G, e.g. SO(10), SU(5), or E(6). Above a unification scale, all gauge fields are assumed to couple with the same strength to elementary particles. At lower energies, G breaks according to some pattern of symmetry breaking to subgroups [9, 74]. For example, SO(10) breaks to SU(5) and an additional U(1), SU(5) then breaks to the SM gauge group $\mathrm{SU(3)_C} \times \mathrm{SU(2)_L} \times \mathrm{U(1)_Y}$. Indications for an additional U(1) symmetry at the LHC may originate from the observation of a neutral heavy resonance. In contrast to the KK-resonance of a gauge boson, this resonance would correspond to a new fundamental interaction. So-called *leptoquarks* are predicted in models with an SU(5) or E(6) symmetry. Leptoquarks carry an electric charge of $\pm 4/3$ or $\pm 1/3$ and may directly decay into a lepton and a quark, e.g. a tau and a top quark. At the LHC, they will be produced in pairs. Thus, an excess of events with two bottom-quark jets and a large multiplicity of light-quark jets and isolated leptons may hint at their existence.

2.3.3. Fourth Generation of Quarks

Besides the assumption of new gauge interactions, the Standard Model may be extended by introducing a fourth generation of quarks [75]. While an additional generation of chiral quarks is strongly disfavored by the Higgs-search results [76], heavy vector-like top (T) and bottom (B) quark partners are predicted in different viable extensions of the SM. Assuming that these mainly decay into quarks of the third generation and massive electroweak gauge or Higgs bosons, e.g. $T \to tZ$, $T \to tH$, and $B \to tW^-$, the production of $T\bar{T}$ and $B\bar{B}$ pairs is likely to result in final states with two bottom-quark jets and a large multiplicity of light-quark jets and isolated leptons.

[10] According to the Super-Poincaré algebra (cf. Section 2.2), the consecutive application of two SUSY transformations leads to a translation in space-time. In a sense, the generators of SUSY transformations can therefore be regarded as something like the square roots of the momentum operator.

3. Experimental Setup

Searches for physics beyond the Standard Model might roughly be divided into two categories: *direct* searches, which aim to identify signatures from on-shell produced new-physics particles, and *indirect* searches, which focus on signatures that result from the exchange of virtual particles. In this thesis, a direct search for Supersymmetry is performed. An important experimental technique for such searches is the controlled acceleration and collision of particles at collider experiments. The world's most powerful particle accelerator and collider to date is the Large Hadron Collider, which is described in Section 3.1. Possible signatures of new physics can be detected by four large experiments, which are installed around the interaction points. Among these is the CMS experiment, which is described in Section 3.2.

3.1. The Large Hadron Collider

The LHC [77] is a 26.7 km long, ring-shaped hadron accelerator and collider operated by the *European Organization for Nuclear Research* (CERN[1]). It is placed near Geneva and built in the former tunnel of the *Large Electron-Positron Collider* (LEP) between 70 and 140 m below the surface of France and Switzerland.

After having passed a chain of pre-accelerators, protons (or lead ions) with an energy of 450 GeV (177 GeV) are injected in the LHC, where they circulate in two counter-rotating beams that consist of up to 2808 (592) bunches with nominally $1.15 \cdot 10^{11}$ protons ($7 \cdot 10^7$ lead ions) each. Superconducting dipole magnets that provide a magnetic field of up to 8.3 T keep the bunches in their orbits. Within about 20 minutes, the protons (lead ions) can be accelerated by radio-frequency cavities to energies of up two 7 TeV (2.76 TeV) per nucleon. Finally, the beams are brought to collision at interaction points, around which four large experiments are installed. These are the multipurpose experiments ATLAS [78] and CMS [79], which are designed for a variety of physics analyses and searches, the LHCb experiment [80], which is dedicated to the analysis of CP violation and the indirect search for new physics in b-hadron decays, and the ALICE experiment [81], which is specialized on the study of quark-gluon plasma produced in heavy-ion collisions. Due to the circular beam structure, the bunches can be used for repeated bunch crossings. Depending on the number of protons (heavy ions) within a bunch, one *run* can last for up to 30 hours. Afterwards, the beams need to be dumped and injected again.

[1] Abbreviation from the former name *Conseil Européen pour la Recherche Nucléaire*.

The rate for the production of a particular final state f from proton-proton collisions is given by the product of the *hadronic cross-section* and the *instantaneous luminosity* $\mathcal{L}$. The former is obtained by convoluting the *partonic cross section* with the parton distribution functions, which will be discussed later in Section 4.1. The instantaneous luminosity is defined as

$$\mathcal{L} = f \frac{N_B \, n_p^2}{4\pi \, \sigma_x \, \sigma_y} F \,, \tag{3.1}$$

where f denotes the revolution frequency, N_B the number of proton bunches, n_p the number of protons per bunch, σ_x the beam size in horizontal direction, and σ_y the beam size in vertical direction [20]. The factor F accounts for the reduction of the effective beam size due to the beam crossing angle at the interaction point. The total number of events of a certain type is given by the product of the hadronic cross-section and the *integrated luminosity* $L = \int \mathcal{L} \, dt$.

First proton-proton collisions with stable beams were achieved at a center-of-mass energy of $\sqrt{s} = 450$ GeV in November 2009. From March 2010 on, the LHC operated at a center-of-mass energy of $\sqrt{s} = 7$ TeV for proton-proton collisions, delivering a total integrated luminosity of $47.0\,\mathrm{pb}^{-1}$ in 2010 and $6.1\,\mathrm{fb}^{-1}$ in 2011, out of which $43.2\,\mathrm{pb}^{-1}$ and $5.6\,\mathrm{fb}^{-1}$, respectively, were recorded by the CMS experiment. As can be seen in Fig. 3.1, the instantaneous luminosity during 2011 increased by more than one oder of magnitude. With $1.5 \cdot 10^{11}$ protons per bunch, which is larger than the design value, and 1,380 bunches per beam a maximal luminosity of $4 \cdot 10^{33}\,\mathrm{cm}^{-2}\mathrm{s}^{-1}$ was obtained in 2011. In 2012, the LHC operated at a center-of-mass energy of $\sqrt{s} = 8$ TeV, delivering an integrated luminosity of $23.3\,\mathrm{fb}^{-1}$, out of which $21.8\,\mathrm{fb}^{-1}$ were collected by the CMS experiment [82].

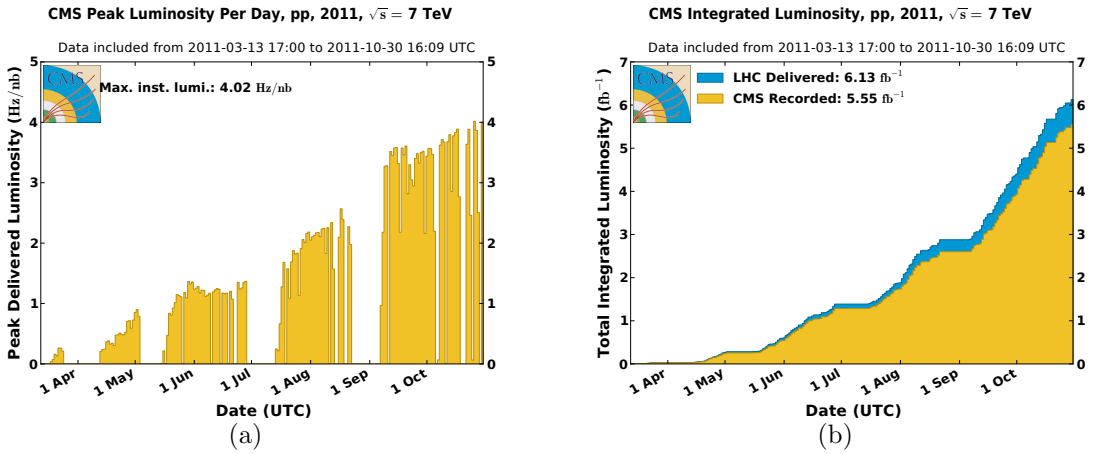

(a) (b)

Figure 3.1.: Evolution of the instantaneous (a) and the integrated luminosity (b) delivered by the LHC and recorded by the CMS experiment in 2011. Figures taken from [82].

3.2. The CMS Experiment

The CMS experiment is one of two multipurpose experiments at the LHC located in a cavern about 100 m below the surface of France. It is designed for a broad program of physics studies, including the searches for the Higgs boson and physics beyond the Standard Model. As illustrated in Fig. 3.2, the CMS detector exhibits the typical onion-like structure of most particle detectors. A tracking system in the center is surrounded by calorimeters and a muon system. In order to identify charged particles and to measure their momenta, a superconducting solenoid provides a uniform magnetic field with a flux density of 3.8 T parallel to the beam line.

After introducing the CMS coordinate system, in Sections 3.2.1 to 3.2.4 those subsystems of the CMS detector that are relevant within this thesis are described. In Section 3.2.5 the trigger and data acquisition system is addressed, followed by a brief description of the CMS computing model and the analysis tools used within this thesis in Section 3.2.6.

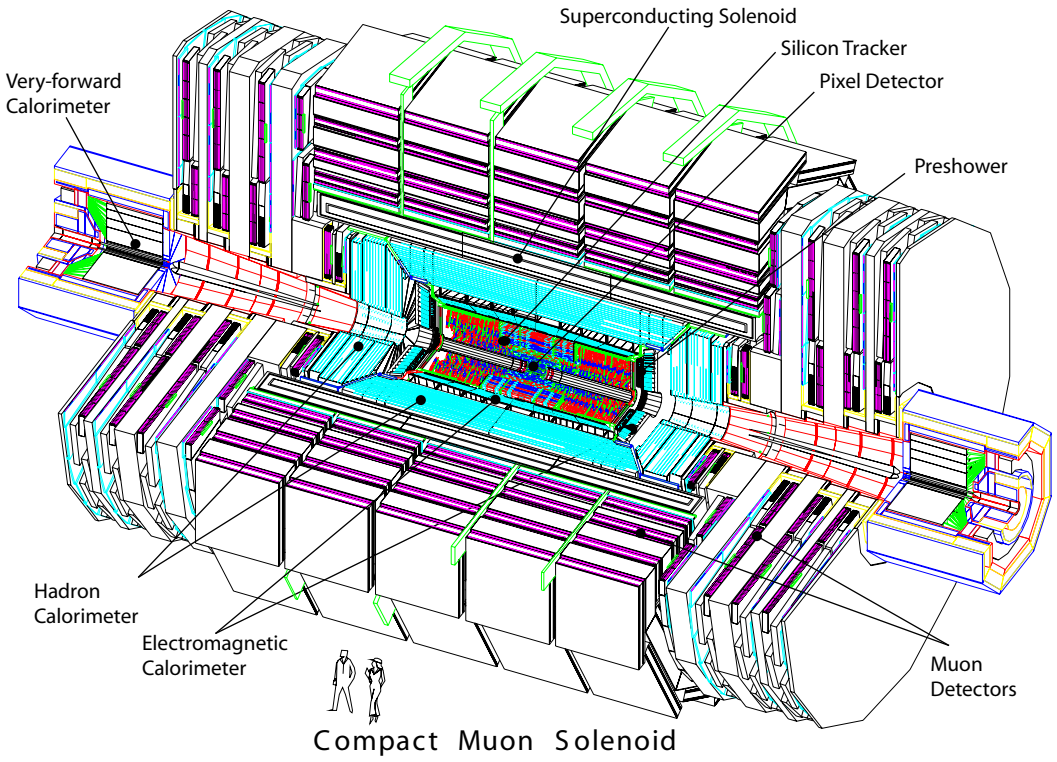

Figure 3.2.: The CMS detector. Taken from [83].

Coordinate System

The coordinate system used in CMS is right-handed and has its origin in the center of the detector at the nominal interaction point. The x axis points to the center of the LHC ring, the y axis points vertically upwards, and the z axis points along the beam pipe. Given the symmetry of the detector, it is often useful to use spherical coordinates instead of cartesian ones: the azimuthal angle ϕ is measured from the x axis in the x-y plane ($0 \leq \phi \leq 2\pi$) and the polar angle θ is measured from the z axis. The distance from the beam pipe is named r. Instead of the polar angle θ, the pseudorapidity $\eta \equiv -\ln\tan(\theta/2)$ is often used.

3.2.1. Tracking System

The innermost part of the CMS detector is the tracking system, which has a geometrical coverage up to $|\eta| < 2.5$. In order to reconstruct the trajectories of charged particles that are produced in the proton-proton collisions, their positions are measured at several locations. Since the particle flux decreases with $1/r^2$, the highest precision is needed in the region close to the beam pipe. Therefore, the beam pipe is surrounded by three *barrel* layers of silicon pixel sensors at radii $r = 4.4$ cm, $r = 7.3$ cm, and $r = 10.2$ cm, as illustrated in Fig. 3.3. At each side of the barrel layers, two *endcap* discs of pixel sensors are located.

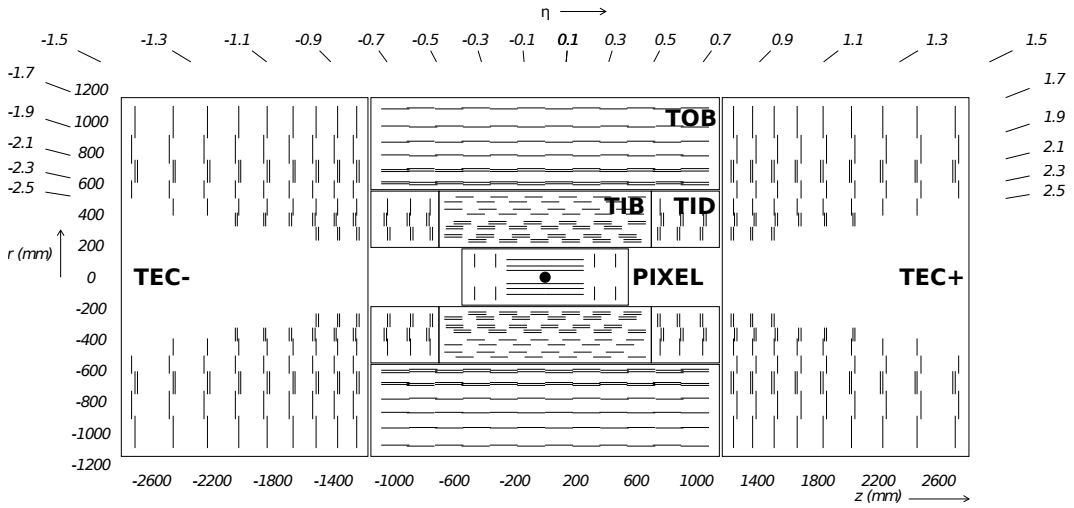

Figure 3.3.: Layout of the CMS tracking system in r-z view. The black lines mark the different tracker layers as described in the text. Figure taken from [84].

With a hit-position efficiency well above 99%, typically three hits for $|\eta| < 2.2$ and two hits for $2.2 < |\eta| < 2.5$ are detected. In total, the pixel detector consists of 1,400 modules with about 66 million silicon pixels. With a pixel size of $100 \times 150\,\mu\text{m}^2$ a hit resolution of $10 - 20\,\mu\text{m}$ is obtained. For $r \gtrapprox 20$ cm the particle flux allows to use silicon microstrip detectors instead of pixel sensors. The strip tracker consists of 15 thousand strips with about 10 million readout channels. The strips are arranged in an inner and outer system, each of which again consists of several layers. The strip size varies from a minimal size of 10 cm $\times$ 80 μm $\times$ 320 μm in the region with 20 cm $< r <$ 55 cm, which defines the tracker inner barrel (TIB), and a maximal size of 25 cm $\times$ 185 μm $\times$ 500 μm in the region with 55 cm $< r <$ 100 cm, which defines the tracker outer barrel (TOB). The inner strip tracker is complemented by three tracker inner discs (TID) at each side of the barrel layers, while the tracker endcaps (TEC) are composed by nine discs each. The resolution of hit-positions in the strip tracker varies from 23 to 52 μm in the r-ϕ plane and 230 to 530 μm in z direction.

For pions with 0.5 GeV $< p_{\text{T}} <$ 500 GeV, a total track-reconstruction efficiency of 80 to 90% is obtained. For muons with 0.5 GeV $< p_{\text{T}} <$ 500 GeV the track-reconstruction efficiency is larger than 99% [85]. The good track resolution enables a precise reconstruction of primary vertices and, by this, to distinguish between particles that are produced in the hard scattering process and those that originate from pile-up interactions. Importantly for this thesis, the tracker resolution also allows for the identification of B-hadrons, which arise from initially produced bottom quarks and decay apart from the primary vertex. The good hit-position resolution enables a track-p_{T} resolution at the percent level for tracks up to 100 GeV [79].

3.2.2. Electromagnetic Calorimeter

The tracking system is surrounded by the electromagnetic calorimeter (ECAL), which is designed to measure the energy and position of mainly electrons and photons, but also charged hadrons. It consists of scintillating lead tungstate ($PbWO_4$) crystals, which act as both the absorber material and as scintillators. The crystals have a radiation length of $X_0 = 0.89$ cm and emit 80% of the light radiated within a time slot of 25 ns. The layout of the ECAL is sketched in Fig. 3.4.

The ECAL barrel (EB) has an inner radius of about 1.3 m and covers a region up to $|\eta| < 1.479$. It consists of 61,200 crystals with a front face of $22 \times 22\,\text{mm}^2$ and a length of 23 cm, corresponding to 25.8 radiation lengths. Avalanche photodiodes are exploited to detect the scintillation light.

At each side of the barrel, the ECAL endcaps (EE) extent the geometrical coverage to $|\eta| = 3.0$. The ECAL endcaps consist of 7,300 crystals with a front face of $28.6 \times 22\,\text{mm}^2$. Their length of 22 cm equals 24.9 radiation lengths. The scintillation light is detected by vacuum photodiodes.

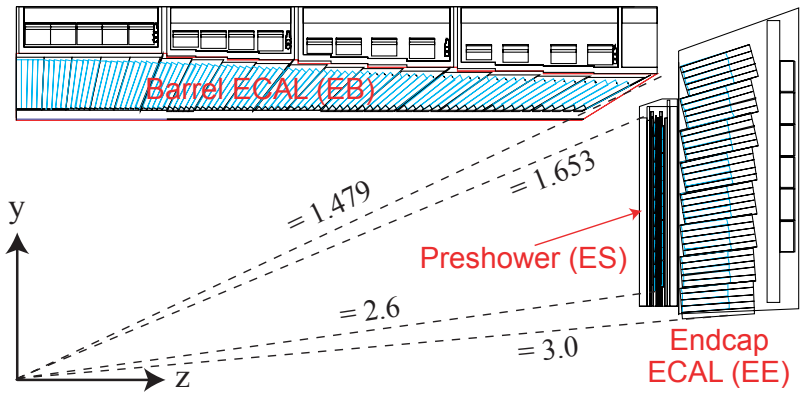

Figure 3.4.: Layout of the CMS electromagnetic calorimeter. Taken from [83].

In front of each endcap a sampling calorimeter that covers a region of $1.653 < |\eta| < 2.6$ is installed. This *preshower detector* consists of one layer of lead as absorber and two layers of silicon strip sensors as active material, which corresponds to three interaction lengths. With its high resolution, the preshower detector improves the identification of neutral pions that decay into two photons.

The relative energy resolution for electrons is parametrized by the standard formula for the calorimeter-based resolution,

$$\frac{\sigma(E)}{E} = \sqrt{\left(\frac{N}{E}\right)^2 + \left(\frac{S}{\sqrt{E}}\right)^2 + C^2}\,, \tag{3.2}$$

where the energy E and N are given in GeV. The first term represents stochastic effects due to fluctuations in the lateral shower, the second term arises from instrumental noise, and the constant term represents intercalibration errors. In test beam measurements, N, S, and C were determined to amount 0.036, 0.124, and 0.0026, respectively [83].

3.2.3. Hadronic Calorimeter

The electromagnetic calorimeter is surrounded by the hadronic calorimeter (HCAL), which is a sampling calorimeter intended to measure the energy and position of hadrons. As main absorber material, brass has been chosen, because it has a relative short hadronic interaction length ($X_0 = 16.4\,\text{cm}$), which allows to keep the detector compact. Between the absorber layers plastic scintillator tiles are installed. The hadronic calorimeter is subdivided into four subsystems, which are the hadronic barrel (HB), the hadronic endcap (HE), the hadronic outer barrel (HO), and the hadronic forward (HF) calorimeter.

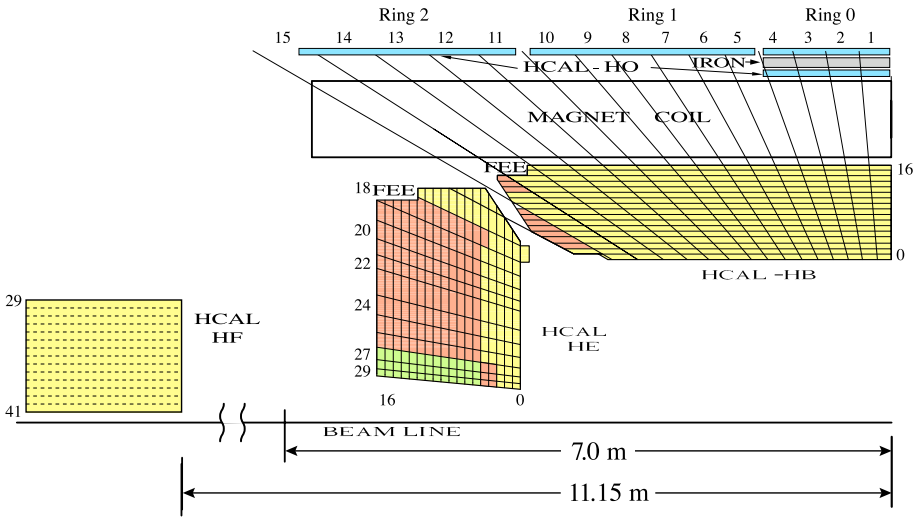

Figure 3.5.: Tower structure of the CMS hadronic calorimeter. Taken from [83].

The HB is placed between the ECAL barrel and the solenoid and covers a range up to $|\eta| = 1.3$. It consists of 16 absorber layers, as illustrated in Fig. 3.5. This corresponds to a depth of 5.8 interaction lengths at $|\eta| = 0$, increasing to 10.6 interaction lengths at $|\eta| = 1.3$. The absorber layers are interspersed with plastic scintillator tiles, where all tiles lying upon another in η-ϕ are read out as a single channel via wavelength-shifting fibre cables that are connected to hybrid photodetectors. Each of these *towers* matches with 5×5 crystals of the ECAL.

The hadronic endcap calorimeter is similarly segmented and read out as the HB calorimeter and extents the geometrical coverage of the HCAL to $|\eta| = 3$.

The hadronic outer calorimeter is situated outside the solenoid. Its main purpose is to compensate the lack of material in the HB, in particular in the very central region. However, so far the HO has not been used during the reconstruction of physics objects.

The hadronic forward calorimeter is located at $|z| = 11.2\,\mathrm{m}$ and covers the region $3.0 < |\eta| < 5.0$. Since the HF absorbs the largest part of the particle flux, radiation-hard quartz fibres are chosen as active material. Together with absorber layers of steel, they are arranged in towers in η-ϕ.

The energy resolution combined for the ECAL and HCAL has been tested using pions with $30\ \mathrm{GeV} < p_\mathrm{T} < 300\ \mathrm{GeV}$ [83]. It can be parametrized as

$$\frac{\sigma(E)}{E} = \sqrt{\left(\frac{1.2}{\sqrt{E}}\right)^2 + 0.069^2}\,, \tag{3.3}$$

where the energy E is given in GeV.

3.2.4. Muon System

Since muons are typically minimal ionizing, they traverse the tracking system and the calorimeters without a significant loss of energy. Therefore, a dedicated system of muon detectors outside the solenoid is required. The CMS muon system covers a region up to $|\eta| = 2.4$ and consists of three types of detectors, as illustrated in Fig. 3.6. In the barrel region ($|\eta| < 1.2$) four layers of *drift tubes* (DT) are installed. These provide a spatial resolution of about 100 μm in r direction. The endcap discs ranging from $|\eta| = 0.9$ to $|\eta| = 2.4$ are equipped with *cathode strip chambers* (CSC), which enable measurements with high time and good spatial resolution even though the particle flux is high. The obtained spatial resolution in r and z direction is about 200 μm. In the region of $|\eta| < 1.6$ *resistive plate chambers* (RPC) are placed in both the barrel and the endcap region. These are used for triggering and timing.

Since muon tracks are less curved in the endcap region, the momentum resolution strongly depends on the pseudorapidity. The relative p_T resolution for muons with a p_T between 20 and 100 GeV obtained by the muon system alone is about 10% for $|\eta| < 0.2$ and 10 to 20% for $1.8 < |\eta| < 2.0$ [86]. By combining information from the tracking system and the muon chambers, a relative p_T resolution in the order of a few percent is obtained (see Section 5.2).

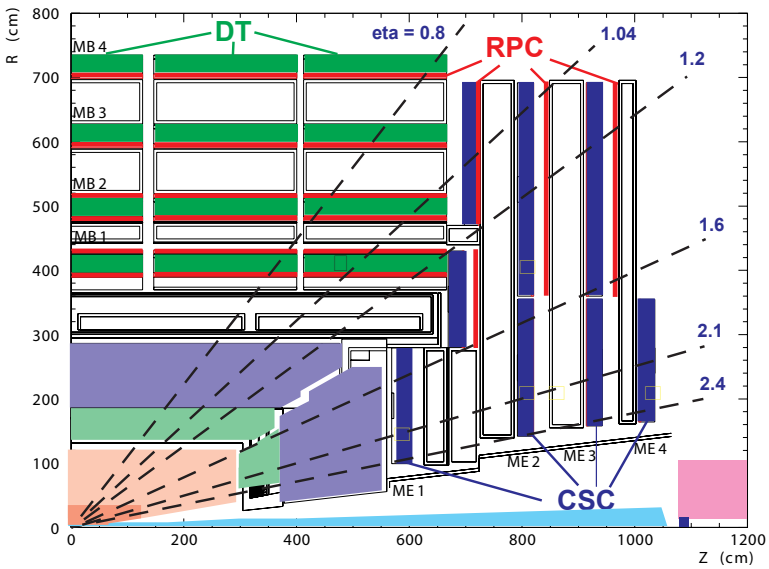

Figure 3.6.: Layout of one quarter of the CMS muon system in r-z view. Taken from [83].

3.2.5. Trigger and Data Acquisition

The bunch-crossing rate of 20 kHz in 2011 (nominally 40 kHz) exceeds the data-acquisition rate of about 200 Hz by far. In order to reduce the rate accordingly, a fast and efficient online selection of events is required. This is achieved by a two-step *trigger system*.

In the first step, the hardware-based *level-1 trigger* (L1T) filters events to a rate of about 10-100 kHz. During a time slot of 3.2 μs the data is temporarily stored in pipelines. Based on information from the calorimeters and the muon system with a reduced granularity, a minimal event reconstruction is performed. Since the track reconstruction is too time-consuming, information from the tracker is not used at this stage.

In the second step, the L1T-selected data is processed by the *high-level trigger* (HLT). Within a time slot of 50 ns, events are reconstructed based on information from all subdetectors. Since the HLT is software-based, more sophisticated reconstruction algorithms can be applied at this stage. Remarkably, already at this level a simplified version of the CMS particle-flow algorithm described later in Section 5 is used.

In order to quickly identify possible detector components that do not work properly, about 10% of all events are processed by the Data Quality Monitoring (DQM) system. Based on the distributions of dedicated quantities, the performance of all subsystems, including the trigger system, is certified on a run-by-run basis online.

3.2.6. Computing Model and Analysis Tools

With a data size of 1 MB per event, approximately 200 MB of data per second were recorded during proton-proton collisions at the CMS experiment in 2011. In order to store and process the huge amount of accumulated data, dedicated storage and computing resources are required. Since the requirements would be difficult to fulfill at one place, storage and computing resources are distributed in a tiered structure among all collaborating institutes [87]. By this, also a fast and reliable data transfer becomes important.

At the *Tier-0* center at CERN, the *raw data* obtained from the data-acquisition system is repacked into *primary datasets* based on trigger information. For example, all events that pass a single-muon trigger are repacked into the single-muon dataset. In 2011 about 10 different types of primary dataset were extracted from the raw data. The repacked data is archived to tape and a first offline reconstruction is performed. The output of this reconstruction is stored in the *reconstructed data* (RECO) and the *analysis object data* (AOD) format. Since the AOD format only comprises information about reconstructed objects, much less space is allocated per event. To a lesser extent this does also apply for the RECO format. In order to certify the performance of the detector and the reconstruction algorithms offline,

dedicated DQM datasets are produced at Tier-0. During analyses only those runs where all subsystems were fully functional are considered. Hence, the data analyzed correspond to lower integrated luminosities than the recorded ones.

Both the raw and the reconstructed data are distributed among seven *Tier-1* centers via the LHC computing Grid [88]. The Tier-1 centers provide secure copies of the raw data and simulated events as well as computing resources for a second reconstruction of the data. The latter is done after the determination of the final calibration and alignment constants.

Finally, the reconstructed data is distributed among approximately 50 *Tier-2* centers, one of which is located at DESY in Hamburg. The Tier-2 centers provide computing resources for analyses and for the production of simulated events. These resources can be accessed via the LHC Grid.

The analyses presented in this thesis are performed on the local batch system of the German *National Analysis Facility* (NAF). In order to reduce the time of one analysis turn-around, AOD files with a smaller event size are produced from the centrally produced ones. This is done by dropping those collections of physical objects that are not used in the analyses from the event content. The analyses are implemented in the CMS software framework (CMSSW). As main tools for the object and the event selection, producer and filter modules of the CMS *Physcis Analysis Toolkit* (PAT) [89] and privately written producer and filter modules are used.

4. Event Simulation

Searches for new physics aim to identify deviations from Standard Model predictions. Since the latter cannot be derived analytically, two different types of techniques are usually exploited. The first type aims for a complete simulation of physical processes ranging from the single proton-proton collision to the read-out of the detector response. Reflecting the probabilistic nature of particle physics, the involved steps are successively simulated based on *Monte Carlo methods*: Pseudo-random numbers are generated according to probability functions derived from physics models. However, as cross sections can only be calculated up to certain orders of coupling constants (cf. Section 2.1.4), the predictions obtained from the event simulation already involve uncertainties on the level of the hard scattering process. Furthermore, the computation of gluon emission and splitting as well as hadronization in the non-perturbative regime lacks an accurate description of QCD from first principles. Finally, the prediction of the detector response suffers from the complexity of the detector and the non-trivial description of low-energetic nuclear and molecular interactions. In particular when considering hadronic final states, the resulting uncertainties may be large, which motivates the second type of techniques. Broadly speaking, the distribution of Standard Model events in a potentially signal-enhanced region of the phace space (*signal region*) is predicted from signal depleted control samples or control regions obtained from data. Such *data-driven methods* have the advantage that theoretical and experimental uncertainties may cancel to a large extent. However, as long as not evident from first principles, these methods, in turn, need to be validated in simulated events. In order to interpret results within specific models of physics beyond the Standard Model, the usage of simulated events is, in the end, unavoidable.

In Section 4.1, the event-simulation chain is outlined, followed by a brief description of the event generator programs used in this thesis in Section 4.2. Details about the simulated signal and background events are discussed in Section 4.3. While all 7 TeV samples are centrally provided by the CMS collaboration, the production of 14 TeV samples is performed within this thesis using the local computing resources.

4.1. Event Generation

The generation of simulated events basically comprises the following steps: the calculation of the hard scattering process, the simulation of *initial and final state radiation*, *the underlying event*, the fragmentation of quarks and gluons into hadrons, their decays into stable particles, additional inelastic proton-proton interactions (*pile-up*

interactions or *pile-up*), and the interaction of stable particles with the detector. Except for the latter two, these steps are illustrated in Fig. 4.1 by the example of $t\bar{t}+H$ production and decay. Based on the *factorization theorem* [90,91], these steps are simulated independently by means of perturbation theory at high energies and empirical approaches at low energies, as discussed in the following.

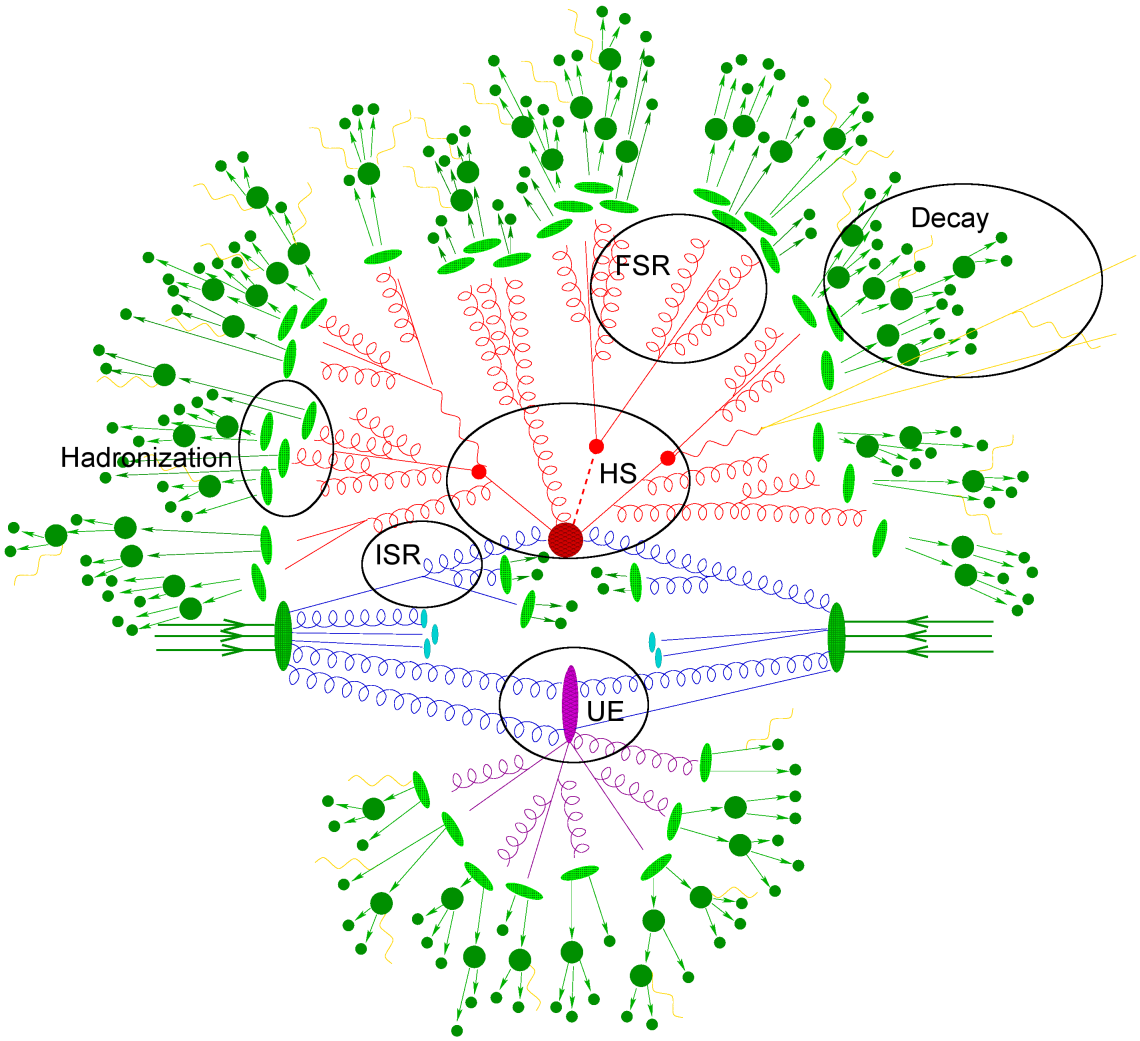

Figure 4.1.: Illustration of $t\bar{t}+H$ production and decay. The open ellipses indicate the different steps that are distinguished during the event generation: the hard scattering process (HS), initial (ISR) and final (FSR) state radiation, hadronization, decay, and the underlying event (UE). Not illustrated are pile-up interactions and the interaction of particles with the detector. Figure (modified) taken from [92].

4.1.1. Hard Scattering Process

The initial state comprises two partons i and j from the colliding protons p_1 and p_2. The probabilities of finding these partons with momentum fractions x_1 and x_2 of the total proton momentum are given by the parton distribution functions $f_i(x_1, \mu_f^2)$ and $f_j(x_2, \mu_f^2)$, respectively, where μ_f denotes the *factorization scale*. In analogy to the renormalization scale (cf. Section 2.1.4), the factorization scale is introduced to absorb divergences from soft and collinear gluon emission. The distribution of initial states can be expressed in terms of *parton-parton luminosities*

$$L_{ij}(s, \hat{s}, \mu_f^2) = \frac{1}{s} \int_{\hat{s}}^{s} \frac{ds'}{s'} f_i\left(\frac{s'}{s}, \mu_f^2\right) f_j\left(\frac{\hat{s}}{s'}, \mu_f^2\right) \tag{4.1}$$

with $\sqrt{s}$ the proton-proton and $\sqrt{\hat{s}}$ the partonic center-of-mass energy. The cross section $\sigma_{p_1 p_2 \to f}$ for the production of a particular final state f from proton-proton collisions is obtained by convoluting the parton-parton luminosities with the *partonic cross section* $\hat{\sigma}_{ij \to f}$,

$$\sigma_{p_1 p_2 \to f} = \sum_{i,j=q,\bar{q},g} \int_0^s d\hat{s}\, L_{ij}(s, \hat{s}, \mu_f^2) \times \hat{\sigma}_{ij \to f}\,. \tag{4.2}$$

The partonic cross section is calculated by means of perturbation theory, as outlined in Section 2.1.3. It should be noted that the parton-parton luminosities cannot be interpreted as probabilities of finding particular initial states. Due to the convolution in equation (4.2), the frequency of finding a particular initial state depends on the partonic cross sections as well. Therefore, the cross section for the hard scattering process does not factorize like the cross section for the production of a particle and its decay when the Narrow Width Approximation (NWA) is applicable.[1] Substituting $L_{ij}(s, \hat{s}, \mu_f^2)$ in the convolution integral (4.2) by its definition (4.1) and $\hat{s}$ by $x_1 x_2 s$ yields the following expression for the cross section of the hard scattering process:

$$\sigma_{p_1 p_2 \to f} = \sum_{i,j=q,\bar{q},g} \int_0^1 dx_1 \int_0^1 dx_2\, f_i(x_1, \mu_f^2)\, f_j(x_2, \mu_f^2) \times \hat{\sigma}_{ij \to f}\,. \tag{4.3}$$

This has to be evaluated using pseudo-random numbers.

[1] While the branching ratios of a particle decay always sum up to one, the partonic cross sections $\hat{\sigma}_{ij \to f}$ do not sum up to the same number for different parton-parton Luminosities L_{ij}.

4.1.2. Initial and Final State Radiation

Since they are colored, the initial and final state partons of the hard scattering process can radiate gluons. These gluons can, in turn, further emit gluons or split into $q\bar{q}$ pairs and so forth, resulting in a *parton shower*, as illustrated in Fig. 4.1 by the red lines. At leading order, three possible QCD *splittings* exist, which are $g \to gg$, $g \to q\bar{q}$, and $q \to qg$. Since α_s increases with decreasing Q (cf. Section 2.1.4), these splittings are mostly soft, e.g. $E_g \to 0$. In addition, they are mostly collinear, e.g. $\theta_{qg} \to 0$. Since the calculation of multiparton radiation at matrix-element level is very time-consuming and leads to divergences in the case of soft and collinear splittings, it is typically restricted to a few hard well-separated partons, depending on the generator program. Instead, the parton shower (in the following "parton shower" shall not cover splittings included in the matrix-element calculation) is simulated by effective parametrizations via Dokshitzer-Gribov-Lipatov-Altarelli-Parisi (DGLAP) splitting functions [93–95] and Sudakov Form Factors [96]. The former represent the possible QCD splittings of a parton produced at an energy scale Q_{max}. The latter describe the probability of not having a splitting between Q_{max} and a lower energy scale Q. The parton shower is evolved from high energies down to a cut-off scale $Q_{\mathrm{cut}} \sim 1$ GeV, below which hadronisation models are needed to describe QCD.

4.1.3. Matrix Element-Parton Shower Matching

If the matrix-element calculation includes the radiation of additional hard partons, simulated events with equivalent phase-space configurations may be double-counted. For example, the generation of an event where the production of a $t\bar{t}$ pair in association with n additional hard partons is calculated at matrix-element level may result in the same configuration as the generation of an event where the matrix element only covers the production of a $t\bar{t}$ pair in association with $n-1$ additional hard partons, but a further hard parton arises from the parton shower. In order to avoid such double-counting and to merge samples with different multiplicities of additional partons from the matrix element, the latter type of events is rejected by a *matching algorithm*. Relevant within this thesis is the MLM matching algorithm [97]. In the first step, the parton shower is evolved, and jets are clustered from partons. In the second step, the additional partons from the matrix-element calculation are matched to jets with a p_{T} above a certain *matching scale*, where the jets coming from the $t\bar{t}$ decay are neglected. If each additional parton is matched to such a jet the event is kept, else rejected. Among the matched events, only those where the number of additional partons equals the number of jets with a p_{T} above the matching scale are kept. Consider, for example, the production of a $t\bar{t}$ pair in association with three hard partons. If all three additional partons can be matched to a jet with a p_{T} above the matching scale and the number of such jets is three, the event is kept. By this, exclusive $t\bar{t}+n$-Jets samples are produced, where $n = 1, 2, ..., N$ denotes the number

of additional partons from the matrix element. For the case $n = N$ also those events are kept where the number of jets is larger than the number of additional partons, provided that all non-matched jets are softer than each of the matched jets. By this an inclusive $t\bar{t} + N$-Jets sample is produced and all multiplicities of additional jets are taken into account without double-counting.

4.1.4. Underlying Event

Besides the initial partons of the hard scattering process, further partons of the colliding protons may interact. Depending on the event generator, the modeling of these *multiple parton interactions* (MPI) is either interleaved with the simulation of initial state radiation or performed afterwards. For a given center-of-mass energy $\sqrt{s}$, the MPI activity is expected to increase with the energy scale Q of the hard scattering process, corresponding to a smaller impact parameter between the colliding protons, on average. In addition, the hadronization of the proton remnants gives rise to further, mostly soft final-state particles. In contrast to MPI, these particles are mostly produced along the beam direction and carry small transverse momenta. Hence, they hardly affect the transverse observables in physics analyses. The processes associated with MPI and the hadronization of the proton remnants are collectively referred to as "underlying event".

4.1.5. Hadronization and Decay

The event generators used within this thesis exploit two types of hadronization models, which are *string fragmentation* and *cluster fragmentation* models. Both describe the formation of hadrons from quarks and their decays into particles that are considered stable, i.e. do not decay before detection. These are typically charged pions, protons, neutrons, strange-flavored hadrons, electrons, muons, neutrinos, and photons.

String fragmentation models are based on the assumption that the potential between two partons linearly increases with the distance r, leading to field strings between them. At a certain distance, the production of a new quark-antiquark pair is energetically favored, resulting in two separate strings. These break further until each string corresponds to an on-shell hadron.

In cluster fragmentation models all gluons that remain after the parton shower are first split into quark-antiquark pairs. Then, quarks that are close to each other in phase-space are grouped to colorless *clusters*. In Fig 4.1 these are represented by the light green ellipses. After potential splittings of heavy clusters into lighter ones, the remaining clusters decay independently of each other isotropically in their rest frames into pairs of hadrons.

4.1.6. Pile-Up

Within a bunch crossing, further protons may interact with each other. These pile-up interactions give rise to additional, mostly soft final-state particles. For a given instantaneous luminosity $\mathcal{L}$ the number of inelastic proton-proton interactions n in a bunch crossing can be described by the Poisson distribution

$$P(n) = \frac{(\mathcal{L} \cdot \sigma)^n}{n!} e^{-\mathcal{L} \cdot \sigma}, \tag{4.4}$$

where σ denotes the total inelastic proton-proton cross section. Pile-up is simulated by generating so-called *minimum-bias* events. These are events that are recorded using triggers with minimum requirements. Each proton-proton interaction that passes the simulation steps described above is interleaved with a number of simulated minimum-bias events. Reflecting the increasing instantaneous luminosity in 2011 this number is described by the sum of individual Poisson distributions.

4.1.7. Detector Simulation

The last step of the event generation constitutes the detector simulation, which comprises the simulation of the detector geometry, the magnetic field, the interaction of final-state particles with the detector material, both dead and active, and the electronic read-out chain. A full simulation is provided by the GEANT4 software package [98]. Since the full simulation is comparatively time-consuming, a fast simulation [99] is applied in the case that many simulated events are needed. The fast simulation is based on a simplified detector geometry. The detector simulation provides simulated events in the same format as the CMS data-acquisition system (cf. Section 3.2.5), such that simulated events and data can directly be compared with each other.

4.2. Event Generators

In the following a brief description of the event generator programs used within this thesis is given. These programs comprise *multi-purpose event generators*, which are capable to perform all steps of the event simulation described in Section 4.1, *matrix-element generators*, which calculate and evaluate matrix elements, and more specialized generator programs.

Pythia

PYTHIA is a multi-purpose event generator, which is commonly used in high-energy physics. It is capable to simulate all Standard Model processes as well as physics beyond the SM processes. The hard scattering is calculated at leading order. Since

the matrix-element calculation does not include the radiation of additional hard partons, initial and final state radiation is completely covered by the parton shower. Pythia exploits a string fragmentation model for the hadronization. Within this thesis, Pythia 6.4.24 [100] with tune Z2 [101] for the underlying event is used. This tune exploits the CTEQ6L1 PDFs [102] provided by the CTEQ collaboration. For the simulation of τ decays, Pythia is interfaced to Tauola 27.121.5 [103], which is a software package dedicated for this purpose. Tauola takes spin information as well as QED corrections into account.

Herwig++

Herwig++ is a multi-purpose event generator that can simulate most Standard Model processes and different physics beyond the SM processes. It calculates the hard scattering process at leading order. In contrast to Pythia, Herwig++ exploits a cluster fragmentation model. Within this thesis Herwig++ 2.3 [104] with the MRST PDFs [105] is used.

MadGraph

MadGraph is a matrix-element generator that is specialized on proton-proton and proton-antiproton collisions. It calculates $2 \to n$ processes at leading order, where the number of final state objects n can in principle be arbitrary large. Hence, the matrix-element calculation may include the radiation of additional hard partons. Since this provides a better description of the jet multiplicity in data, MadGraph is usually preferred to Pythia and Herwig++ for the simulation of events at matrix-element level. However, since the number of possible diagrams and the complexity of calculations rapidly increases with the number of final-state particles, the event simulation with MadGraph is comparatively time-consuming and typically restricted to final states with eight or less particles. For the simulation of parton showers, the underlying event, and fragmentation processes MadGraph has to be interfaced to other generator programs. In order to avoid double-counting of equivalent phase-space configurations, the MLM matching algorithm described above is exploited. In this thesis MadGraph 5.1.1 [106], which exploits the CTEQ6L1 PDFs, is used.

Powheg

Powheg (POsitive Weight Hardest Emission Generator) is a matrix-element generator optimized for heavy-quark production in proton-proton and proton-antiproton collisions. The matrix-element calculation is done at next-to-leading order. Hence, the simulation with Powheg includes the production of up to one additional hard partons at matrix-element level. In this thesis, Powheg 301 [107–109] with the CTEQ6M PDFs [102] is used.

4.3. Simulated Event Samples

In order to design searches for Supersymmetry and measurements of sparticle properties, characteristic *benchmark scenarios* that represent different regions of the parameter space of interest are defined. While typically only a few benchmark scenarios are examined, the interpretation of results in the context of a specific supersymmetric model requires a systematic scan of the parameter space. In Section 4.3.1, the simulated signal-benchmark samples and model scans used in the search at $\sqrt{s} = 7$ TeV are described. In order to derive a prediction of the Standard Model background in the considered signal regions, all relevant background processes are simulated, which is discussed in Section 4.3.2. The SUSY benchmark samples used in the study at a center-of-mass energy of $\sqrt{s} = 14$ TeV are described later in Section 10.

4.3.1. Simulated Signal Samples

In the search for Supersymmetry in final states with a single isolated lepton, b-quark jets and missing transverse energy, the CMSSM low mass scenarios LM8 and LM6 (cf. Appendix B.1) are chosen as signal benchmarks. Though in both scenarios the lighter top and the lighter bottom squark are lighter than the first and second generation squarks, the scenarios represent different regions of the CMSSM parameter space.

In scenario LM8, the gluino ($m_{\tilde{g}} = 738$ GeV) is heavier than the lighter top squark ($m_{\tilde{t}_1} = 544$ GeV) and the lighter bottom squark ($m_{\tilde{b}_1} = 710$ GeV), but lighter than the first and second generation squarks, whose masses are around 800 GeV. Consequently, gluino-pair production ($\tilde{g}\tilde{g}$) and the squark-associated gluino production ($\tilde{q}\tilde{g}$) result in states with many b-quarks, as can be seen in Fig. 4.2(a). Since squarks of the first and second generation can decay into a quark and a gluino, $\tilde{q}\tilde{q}^*$ and $\tilde{q}\tilde{q}$ production may result in similar states (see also Section 2.2.3.4). This is also true for the neutralino- and the chargino-associated squark production, which contribute to the processes labeled as "other". The direct production of $\tilde{t}\tilde{t}^*$ and $\tilde{b}\tilde{b}^*$ pairs is of minor relevance in scenario LM8.

In scenario LM6, the gluino ($m_{\tilde{g}} = 932$ GeV) is heavier than the lighter top ($m_{\tilde{t}_1} = 647$ GeV) and the lighter bottom squark ($m_{\tilde{b}_1} = 785$ GeV) and also heavier than the first and second generation squarks, whose masses are around 830 GeV. Hence, $\tilde{g}\tilde{g}$ and $\tilde{q}\tilde{g}$ production results in states with lower b-quark multiplicities as in scenario LM8, which can be seen in Fig. 4.2(b). Since squarks of the first and second generation cannot decay into a quark and a gluino, $\tilde{q}\tilde{q}^*$ and $\tilde{q}\tilde{q}$ production do only result in b-quark states in the rare cases where additionally produced Z or neutral Higgs bosons decay into a pair of third generation quarks. Though still suppressed with regard to other processes that involve the production of b-quarks, direct $\tilde{t}\tilde{t}^*$ and $\tilde{b}\tilde{b}^*$ production is of larger relevance than in scenario LM8.

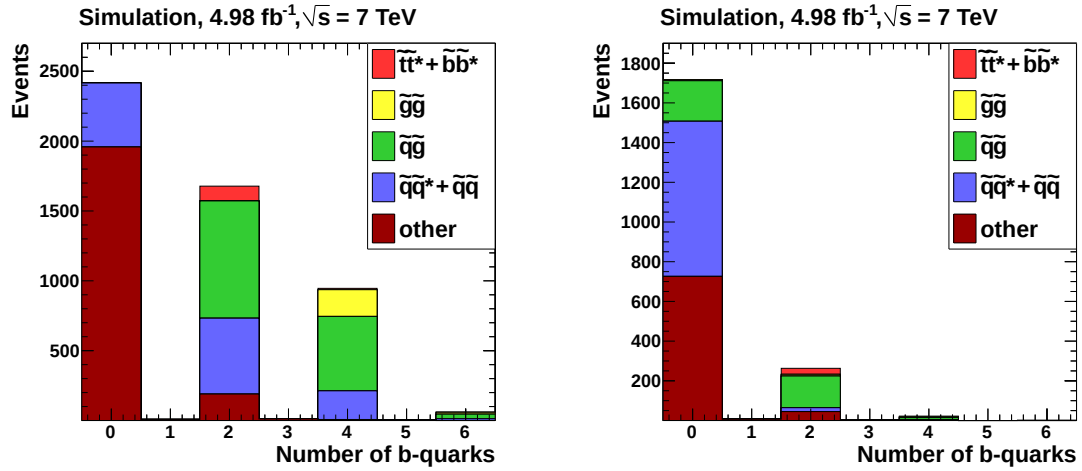

(a) LM8 (b) LM6

Figure 4.2.: Number of b-quarks at generator-level for different processes of sparticle production in the CMSSM low mass scenarios LM8 (a) and LM6 (b).

Almost not visible in Figs. 4.2(a) and (b), very few events come along with an odd b-quark multiplicity (one or three). These are the events where a single top or bottom squark is produced (see also Section 2.2.3.1).

Results of the search at $\sqrt{s} = 7$ TeV are interpreted in the CMSSM. For fixed parameters A_0, $\tan\beta$, and $\mathrm{sign}\,\mu$, a scan in the m_0 - $m_{1/2}$ plane is performed by varying m_0 and $m_{1/2}$ in steps of a size of 20 GeV. For each point, 10,000 events are generated. In addition, the results are interpreted in the context of the simplified model described in Section 2.2.4. It contains the pair production of gluinos, which subsequently decay with branching fraction $\mathcal{B}(\tilde{g} \to t\bar{t}\chi_1^0) = 1$. A scan in the $m_{\tilde{g}}$ - $m_{\chi_1^0}$ plane is performed by varying $m_{\tilde{g}}$ and $m_{\chi_1^0}$ in steps of 25 GeV. Here, 50,000 events are generated for each point.

All mass spectra and branching fractions are computed at the electroweak scale using the renormalization equations as implemented in SoftSUSY [110]. The production and decay of sparticles in the LM8 and the LM6 scenario are simulated using Pythia only. The particle-level events are then passed to Geant for the CMS full detector simulation. The events in the CMSSM and simplified model scans are generated using Pythia and the CMS fast detector simulation. Simulated CMSSM samples, numbers of generated events and assumed cross sections are listed in Table 4.1. Next-to-leading-order and Next-to-leading-logarithm K factors [49,111–114] are applied to all contributing subprocesses.

Table 4.1.: Simulated 7 TeV CMSSM samples, numbers of generated events, and assumed cross sections. For the scan, m_0 and $m_{1/2}$ are varied in steps with a size of 20 GeV. For each point 10,000 events are generated.

Sample	$\mathbf{m_0}$ **[GeV]**	$\mathbf{m_{1/2}}$ **[GeV]**	$\mathbf{A_0}$	$\tan\beta$	sign μ	**No. events**	**Cross-sec. [pb]**
LM8	500	300	-300	10	+	421,190	1.029 (NLO)
LM6	85	400	0	10	+	427,625	0.404 (NLO)
Scan	20 - 2000	20 - 760	0	10	+	66,564,000	

4.3.2. Simulated Background Samples

The following Standard Model processes are relevant within this thesis:

- $\boldsymbol{t\bar{t}}$ **+ Jets:** Production of top anti-top quark pairs in association with hard jets. At leading order, the production is induced by gluon exchange in the s-channel and quark exchange in the t- and the u-channel (see Appendix A for Feynman diagrams). As decays in light flavor quarks are strongly suppressed by the CKM matrix (cf. Section 2.1.1), both top quarks can be expected to decay into a W boson and a bottom quark. Decays of $t\bar{t}$ pairs are classified in *fullhadronic* decays, where both W bosons decay hadronically, *semileptonic* decays, where one W boson decays hadronically and the other leptonically, and *dileptonic* decays, where both W bosons decay leptonically. The branching ratios for the fullhadronic and the semileptonic $t\bar{t}$ decay roughly amount 4/9 each, the branching ratio for the dileptonic $t\bar{t}$ decay is about 1/9.

- $\boldsymbol{W}$ **+ Jets:** Production of leptonically decaying W bosons from fusion of an up-type quark and a down-type antiquark (and the charge conjugated processes) in association with hard jets. Since the proton valence quarks consist of two up quarks and one down quark, more positively than negatively charged W bosons are produced in proton-proton collisions. Bottom quarks may originate from gluon splittings. The production of hadronically decaying W bosons in association with hard jets is not relevant, because its cross section is many orders of magnitude smaller than that for QCD multijet production.

- **Single Top:** Production of single top quarks in association with an antibottom quark (s-channel), a negatively charged quark of the first or second generation (t-channel), or a W boson (and the charge conjugated processes). The former processes are often refereed to as "s-channel single top" and "t-channel single top", which is misleading, insofar as the W-boson-associated production occurs in both channels as well.

- **$Z/\gamma^* + \mathbf{Jets}$:** Production of lepton-antilepton pairs from Drell-Yan processes in association with hard jets. In leptonic searches, only the decay into pairs of charged leptons is relevant, whereas in all-hadronic searches, also the decay into neutrino-antineutrino pairs is of interest. Hence, the $Z/\gamma^* + \text{Jets}$ sample used in the search at $\sqrt{s} = 7$ TeV only comprises the decay into pairs of charged leptons, whereas the sample used in the study at $\sqrt{s} = 14$ TeV also includes the invisible Z decays. Bottom quarks may originate from gluon splittings. The production of hadronically decaying Z bosons and photons in association with hard jets is not relevant, because its cross section is many orders of magnitude smaller than that of QCD multijet production.

- **QCD:** Multijet production from strong interaction processes. Charged leptons may stem from light-meson in-flight decays, semileptonic three-body decays of heavy-flavor quarks ($b \to q\, l\, \bar{\nu}_l$, $c \to q'\, \bar{l}\, \nu_l$), and photon conversions ($\gamma \to l^+ l^-$). Missing transverse energy exclusively results from jet energy mismeasurements, which are mainly due to instrumental effects and neutrinos produced along with a charged lepton in decays of heavy-flavor quarks.

The production and decay of $t\bar{t}$ pairs and electroweak vector bosons is simulated using MadGraph interfaced to Pythia. The simulation of $t\bar{t}$ pair production at center-of-mass energies of $\sqrt{s} = 7$ TeV and $\sqrt{s} = 14$ TeV and the simulation of electroweak processes at $\sqrt{s} = 14$ TeV includes the production of up to three additional hard partons at matrix-element level. For a center-of-mass energy of $\sqrt{s} = 7$ TeV, the simulation of electroweak processes includes the production of up to four additional hard partons at matrix-element level. The factorization and renormalization scales are set to

$$Q^2 = m_{\mathrm{X}}^2 + \sum_i p_{T,i}^2 \,, \tag{4.5}$$

where m_{X} denotes the mass of the top quark, the W boson, and the Z boson, respectively. The sum runs over the transverse momenta of all additional hard partons from the matrix element. The matching scale is set to 40 GeV for the simulation of $t\bar{t} + \text{Jets}$ production and 20 GeV for the production of electroweak vector bosons in association with hard jets. For the simulation at $\sqrt{s} = 14$ TeV, the choice of the matching scale is checked by varying this scale up and down by a factor of 2 and 0.5, respectively. Reflecting the thight phase space cuts at matrix-element level, the distributions of control variables are found not to depend on the matching scale.

The production and decay of single top quarks at $\sqrt{s} = 7$ TeV is simulated using Powheg interfaced to Pythia. For $\sqrt{s} = 14$ TeV the hard scattering process is simulated using MadGraph instead of Powheg. This is done because MadGraph allows the simulation of events with a certain $H_{\mathrm{T}}^{\mathrm{parton}}$, defined as the scalar sum of the transverse momenta of all quarks and gluons at matrix-element level, and a certain $\not{E}_{\mathrm{T}}^{\mathrm{parton}}$, which is defined as the absolute value of the vectorial sum of

the neutrinos' transverse momenta at matrix-element level. In order to avoid an overlap with the simulation of $t\bar{t}+\text{Jets}$ events, the simulation of single-top-quark production in association with a quark of the first or second generation (t-channel) at $\sqrt{s} = 14$ TeV is restricted to the case of maximally one additional hard parton at matrix-element level. For the same reason, the simulation of single-top-quark production in association with a W boson ($t + W$) does not include the production of any additional hard parton at matrix-element level.

QCD multijet production is simulated using PYTHIA only. In order to increase the number of simulated events in the phase space of interest, events are generated assuming a cross section that is flat with respect to the momentum transfer $\hat{p}_T$ of the hard scattering process. During the analysis, QCD multijet events are therefore reweighted by the inverse "flattening factor" $(\hat{p}_T/15)^{-4.5}$.

For a center-of-mass energy of $\sqrt{s} = 7$ TeV the event generation includes the simulation of pile-up as described in Section 4.1. Since the pile-up interaction multiplicity distribution (pile-up distribution) of simulated events differs from that estimated for data, simulated events are reweighted such that the distributions of simulated events and data match. This is done separately for each simulated event sample. In order to cross check this weighting procedure, the pile-up distributions of simulated events and data are compared with each other in Appendix B.2.

For the production of simulated 7 TeV samples, all particle-level events are passed to GEANT for the full detector simulation. All 14 TeV samples are produced using the fast detector simulation.

7 TeV Background Samples

In Table 4.2 the simulated event samples used in the search at $\sqrt{s} = 7$ TeV, the numbers of generated events, the assumed cross sections [115], and the event weights that result for an integrated luminosity of $\mathcal{L} = 4.980\,\text{fb}^{-1}$ are listed. The suffix "+ Jets" in the naming shall indicate those samples, where the matrix-element calculation includes the radiation of additional hard partons. For the study of theoretical uncertainties $t\bar{t}+\text{Jets}$ samples with systematic variations of the factorization, renormalization, and matching scales are produced. The factorization and renormalization scales are simultaneously varied up ("Q^2 scale up") and down ("Q^2 scale down") by a factor of 2 and 0.5, respectively. The matching scale is set to 60 GeV ("matching scale up") and 30 GeV ("matching scale down"). Variations of the factorization and renormalization scales in principle affect the total cross section. However, since the uncertainties resulting from the assumed cross sections are studied separately, all simulated $t\bar{t}+\text{Jets}$ events are normalized using the same cross section.

Table 4.2.: Simulated 7 TeV background samples, numbers of generated events, assumed cross sections, and event weights for an integrated luminosity of $\mathcal{L} = 4.980\,\text{fb}^{-1}$. All samples are centrally provided by the CMS collaboration.

Sample	**No. events**	**Cross-sec. [pb]**	**weight**
$t\bar{t}$+Jets	59,517,528	157.5 (NLO)	0.013
$t\bar{t}$+Jets Q^2 scale up	3,696,269	157.5 (NLO) [d]	0.21
$t\bar{t}$+Jets Q^2 scale down	4,004,587	157.5 (NLO) [d]	0.20
$t\bar{t}$+Jets matching scale up	4,029,823	157.5 (NLO)	0.20
$t\bar{t}$+Jets matching scale down	1,545,688	157.5 (NLO)	0.51
Single top + $\bar{b}$ (s-channel)	259,971	3.19 (NNLO)	0.061
Single top + q (t-channel)	3,900,171	41.92 (NNLO)	0.054
Single top + W	814,390	7.87 (NNLO)	0.048
Single anti-top + b (s-channel)	137,980	1.44 (NNLO)	0.052
Single anti-top + q (t-channel)	1,944,826	22.65 (NNLO)	0.058
Single anti-top + W	809,984	7.87 (NNLO)	0.048
$W(\to l\bar{\nu}) + \text{Jets}$ [a]	8,702,716	34.8 (LO)	0.020
$W(\to l\bar{\nu}) + \text{Jets}$ [b]	5,327,746	48.49 (LO)	0.045
$Z/\gamma^*(\to l\bar{l}) + \text{Jets}$ [c]	36,058,014	3,048 (NNLO)	0.42
QCD	10,715,600	22.13×10^9 (LO)	$\hat{p}_T$ dependent

[a] $250\ \text{GeV} < H_\text{T}^\text{parton} < 300\ \text{GeV}$
[b] $H_\text{T}^\text{parton} > 300\ \text{GeV}$
[c] $m_{l\bar{l}}^\text{parton} > 50\ \text{GeV}$
[d] Set to central value, see text

14 TeV Background Samples

The simulated background samples used in the study at $\sqrt{s} = 14$ TeV, the numbers of generated events, the assumed cross sections, as obtained from the simulation with MADGRAPH interfaced to PYTHIA, and the event weights that result for an integrated luminosity of $\mathcal{L} = 300\,\text{fb}^{-1}$ are listed in Table 4.3. Since they are not relevant for the study at 14 TeV, the production of fullhadronically decaying $t\bar{t}$ pairs and single top quarks in association with a bottom squark (s-channel) are not simulated. As all simulated 14 TeV samples are produced within this thesis using the local computing resources, the event generation is strongly limited by the available CPU time and storage space. The generation of events with MADGRAPH is therefore restricted to events with H_T^parton and $\not{E}_\text{T}^\text{parton}$ above certain thresholds, which

are nonetheless well below the selection requirements on the level of reconstructed objects. Since missing transverse energy in QCD multijet events exclusively results from jet energy mismeasurements, no $\not{E}_{\mathrm{T}}$ requirement can be applied during the event generation in this case. However, with respect to the available CPU time this does not pose a large problem. As PYTHIA only calculates $2 \to 2$ processes at leading order, the simulation of QCD multijet events is much faster than the simulation of e.g. $t\bar{t}+$ Jets events with MADGRAPH interfaced to PYTHIA. In order to save storage space, a loose preselection on the level of reconstructed objects is applied in the case of QCD events.

Table 4.3.: Simulated 14 TeV background samples, numbers of generated events, assumed cross sections, and event weights for an integrated luminosity of $\mathcal{L} = 300\,\mathrm{fb}^{-1}$. All samples are produced within this thesis.

Sample	**No. events**	**Cross-sec. [pb]**	**weight**
Semileptonic $t\bar{t}$+Jets [a]	312,311	2.68 (LO)	2.58
Dileptonic $t\bar{t}$+Jets [a]	137,495	0.42 (LO)	0.91
Single top $+ q$ (t-channel) [a]	42,574	0.035 (LO)	0.25
Single top + W [a]	89,989	0.0058 (LO)	0.019
Single anti-top $+ q$ (t-channel) [a]	19,894	0.012 (LO)	0.18
Single anti-top + W [a]	89,995	0.0058 (LO)	0.019
W$(\to l\bar{\nu})$+Jets [a,b]	483,151	3.65 (LO)	2.27
$Z/\gamma^*(\to l\bar{l})$+Jets [c]	201,867	1.36 (LO)	2.02
$Z/\gamma^*(\to \nu\bar{\nu})$+Jets [a]	71,779	0.53 (LO)	2.19
QCD	140,350,000	10.62×10^{10} (LO)	$\hat{p}_T$ dependent

[a] $H_{\mathrm{T}}^{\mathrm{parton}} > 700$ GeV and $\not{E}_{\mathrm{T}}^{\mathrm{parton}} > 100$ GeV

[b] The event weight slightly depends on the subprocess

[c] $H_{\mathrm{T}}^{\mathrm{parton}} > 700$ GeV and $m_{l\bar{l}}^{\mathrm{parton}} > 50$ GeV

5. Object Reconstruction

After different steps of reprocessing, as partly described in Section 3.2.6, the data recorded at the CMS experiment become available for analyses. In order to predict the Standard Model background in potentially signal-enhanced regions of the phase space and to interpret the obtained results, signal and background processes are simulated, as described in Section 4. The output of the detector simulation is stored in the same format as the data, such that simulated events and data can directly be compared with each other. The analysis starts with the reconstruction of physics objects. Typical signatures of the particles relevant within the object reconstruction are illustrated in Fig. 5.1.

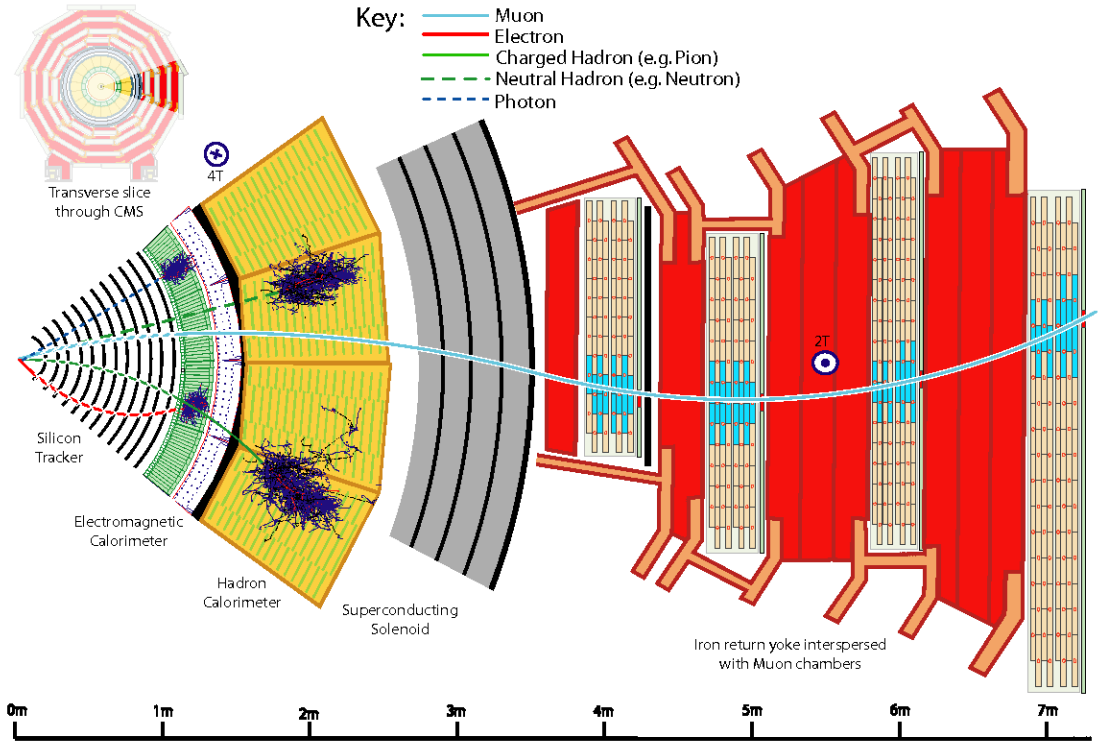

Figure 5.1.: Transverse slice through the CMS detector. The colored lines represent the typical signatures of different particles.

At first, the positions of all proton-proton interactions (*primary vertices*) are reconstructed from charged-particle tracks, as outlined in Section 5.1. Then, muons and electrons are reconstructed, which is described in Sections 5.2 and 5.3. Since taus decay before detection, they are difficult to identify. Hadronically decaying taus ($\tau \to \bar{q}q'\nu_\tau$) produce jets, which can only to a limited extent be distinguished from quark and gluon jets. In this thesis, tau jets are not discriminated from light quark and gluon jets. Leptonically decaying taus (e.g. $\tau \to \mu\bar{\nu}_\mu\nu_\tau$) can hardly be discriminated from directly produced muons and electrons. Thus, hadronically decaying taus might pass the jet selection criteria, while leptonically decaying taus are likely to pass the muon or electron selection criteria. For the reconstruction of jets and the calculation of the missing transverse energy, the four-momenta of all final-state particles are reconstructed using the CMS particle-flow approach, which is introduced in Section 5.4. The reconstruction of jets and the identification of bottom-quark jets (b-jets) are described in Sections 5.5 and 5.6 (while the calculation of event quantities, such as $\not{E}_\mathrm{T}$, is addressed later in Section 6).

5.1. Primary Vertex Reconstruction

Primary vertices are reconstructed from tracks that fulfill certain quality criteria on the number of associated hits in the inner tracking system, the normalized χ^2 of the trajectory fit and the impact parameter with respect to the nominal beam spot [116]. Based on the z position of the closest approach to the beam axis, selected tracks are grouped to primary-vertex candidates, where each vertex candidate is required to be separated by at least 1 cm from the next closest vertex candidate. Then, vertex candidates that contain more than two tracks are used as input to an adaptive vertex fitter [117]: Each track is weighted by its distance to the primary vertex. From the weighted tracks, the position of the primary vertex is recalculated. This procedure is iterated until the final vertex coordinates are found. As estimate for the number of tracks compatible with the position of the primary vertex, the number of degrees of freedom is defined as

$$N_\mathrm{dof} = 2 \cdot \sum_{i=1}^{n_\mathrm{tracks}} w_i - 3 \tag{5.1}$$

where w_i denotes the final track weights. For each primary vertex, the squared transverse momenta of the associated tracks are summed up. The primary vertex with the largest sum is associated to the hard scattering process. All other primary vertices are considered as originating from pile-up interactions. The spatial resolution of primary vertices with more than 30 tracks has been measured to be between 20 and 25 μm [116].

5.2. Muon Reconstruction

Muons can easily be identified because they are typically the only particles that traverse the muon chambers. Since they are electrically charged, they leave a track in the inner tracking system as well. In order to reconstruct muons, at first, tracks in the muon chambers (*standalone-muon tracks*) and the inner tracking system (*tracker tracks*) are reconstructed independently from one another, as described in [83]. Then, a combined track (*global track*) from hits of both the standalone-muon and the tracker track is reconstructed using a Kalman-filter technique [118]. The relative p_{T} resolution of such a *global muon* ranges from 1 to 2% for muons with a p_{T} between 20 and 100 GeV and $|\eta| < 2.0$. At high p_{T}, the muon system significantly contributes with its large lever arm, keeping the resolution below 10% [119].

Muon Selection Criteria

Selected muons are required to have a transverse momentum of $p_{\mathrm{T}} > 20$ GeV and a pseudorapidity of $|\eta| < 2.1$. The p_{T} requirement is motivated by the assumption that muons produced within sparticle decay cascades originate from the decays of on-shell W-bosons or two- or three-body decays of potentially heavy charginos (cf. Section 2.2.3.4). Hence, they are expected to carry a considerable amount of transverse momentum. In the cases of third-generation squarks with masses in the order of the top-quark mass and "compressed" sparticle mass spectra, a lower p_{T} requirement would be desirable. From an experimental point of view, some restriction on the p_{T} requirement arises from the trigger thresholds. The data analyzed in this thesis has been recorded using triggers that require the presence of a muon or electron with a p_{T} larger than 15 GeV (cf. Section 6.1). The selection of events where the muon that leads in p_{T} (leading muon) has an offline reconstructed p_{T} below 15 GeV would therefore strongly suffer from the trigger inefficiency in this region. Hence, it is convenient (though not necessary), to require the minimal p_{T} of the leading muon to be somewhat above the trigger threshold.

The η requirement is mainly driven by the geometrical coverage of the subdetectors and the larger energy scale at which sparticles will be produced. The larger the partonic center-of-mass energy is, the more likely the initial partons are to carry similar momentum fractions. Hence, sparticles will be produced more centrally than their Standard Model superpartners on average (see e.g. [120]). This does also apply for their decay products.

Muons produced in the decay of electroweak gauge and Higgs bosons and their superpartners can be assumed to be well isolated from other activity in the detector. In order to distinguish such *prompt* muons from those that are produced within jets, an isolation criterion is applied. Within an *isolation cone* of radius $\Delta R \equiv \sqrt{(\Delta\eta)^2 + (\Delta\phi)^2} = 0.3$ centered around the muon direction at the primary vertex, the transverse energy in the calorimeters and the transverse momenta of all tracks,

as measured in the silicon tracker, are summed up. To exclude contributions from the muon itself, the energy deposits within smaller *veto cones* centered around the muon direction in the calorimeters are subtracted. The radii of these veto cones amount $\Delta R = 0.07$ in the electromagnetic and $\Delta R = 0.1$ in the hadronic calorimeter. Isolation and veto cones are sketched in Fig 5.2.

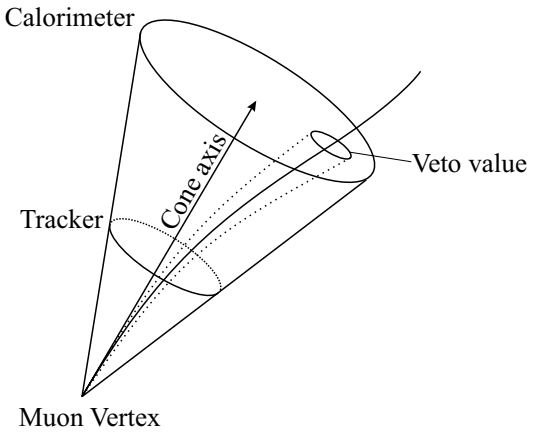

Figure 5.2.: Muon isolation and veto cones. Figure taken from [83].

The relative isolation I_{rel} is then defined as this sum divided by the muon p_{T},

$$I_{\text{rel}} = \frac{\sum\limits_{\Delta R<0.3} (E_{\text{T}}^{\text{ecal}} + E_{\text{T}}^{\text{hcal}} + p_{\text{T}}^{\text{tracker}})}{p_{\text{T}}^{\mu}} . \tag{5.2}$$

Selected muons are required to have a relative isolation smaller than 0.1. In addition, they have to fulfill several identification-quality criteria [119, 121].

The muon selection efficiency is determined using a *tag-and-probe* technique on the Z peak [122]. A sample of events containing two oppositely charged muons with an invariant mass compatible with the Z-boson mass is selected. Requiring one muon (the "tag muon") to pass the selection criteria outlined above, the efficiency of any selection criterion that does not enter the definition of the other muon (the "probe muon") can be determined by measuring the fraction of muons that pass the selection criterion in question. The overall muon selection efficiency is measured to be 0.91 for the first data taking period in 2011 (run period A) and 0.88 for the second period (run period B) [123] and well described by the event simulation. Therefore a scale factor of one is applied to the muon selection efficiency. The uncertainty on this factor amounts to 1% for run period A and 2.5% for run period B. The probability of misidentifying a particle as muon (muon misidentification rate) is found to be in the order of one permil [119].

Muon Veto Criteria

The search presented in this thesis is performed in the exclusive one-lepton channel. Events with a second lepton passing looser criteria are rejected. For this purpose muon *veto criteria* are defined. These consist of the requirements of $p_{\mathrm{T}} > 15$ GeV, $|\eta| < 2.5$, $I_{\mathrm{rel}} < 0.15$, and looser identification-quality criteria [119, 121].

5.3. Electron Reconstruction

In contrast to muons, electrons that enter the ECAL produce electromagnetic showers and get stopped. From the associated energy deposits in the ECAL cells an energy cluster can be reconstructed. Since electrons are charged, this cluster is related to a track in the silicon tracker. However, due to the large amount of material in the tracker the emission of bremsstrahlung photons is frequent, resulting in additional energy clusters in the ECAL. Together with the *seed cluster* associated with the primary electron these are grouped into a *supercluster* [83, 124]. Electron tracks are built by matching superclusters to pairs or triplets of hits in the pixel tracker. Based on a dedicated model of energy loss via bremsstrahlung, trajectories are then fitted with a Gaussian Sum Filter [125].

Electron Selection Criteria

In analogy to selected muons, selected electrons are required to have a transverse momentum of $p_{\mathrm{T}} > 20$ GeV and a supercluster with a pseudorapidity of $|\eta| < 2.5$, where electrons with a supercluster in the barrel-endcap transition region ($1.4442 < |\eta| < 1.566$) are excluded. The isolation variable I_{rel} is similarly defined as in the muon case. However, the requirement on I_{rel} depends on the electron pseudorapidity. In the barrel region, selected electrons must satisfy $I_{\mathrm{rel}} < 0.07$, in the endcap region they must fulfill the requirement $I_{\mathrm{rel}} < 0.06$. In addition, selected electrons have to fulfill a set of quality and photon-conversion rejection criteria [126].

The overall electron selection efficiency, which factorizes into the tracking and the identification efficiency, is measured using the tag-and-probe method described in Section 5.2. The electron tracking efficiency amounts 96% at an offline reconstructed p_{T} of 20 GeV and increases with the p_{T}. The identification efficiency, including the isolation requirement, increases with the electron p_{T} as well and saturates at about 87% in the central region and 83% in the forward region, respectively. The overall electron selection efficiency is measured to be 0.73 and well described by the event simulation. A scale factor of one is applied to the electron selection efficiency. The uncertainty on this factor amounts to 1.5%. The electron misidentification rate is found to be in the order of one percent [124].

Electron Veto Criteria

The electron veto criteria consist of the requirements of $p_{\mathrm{T}} > 15$ GeV, $|\eta| < 2.5$ (excluding the barrel-endcap transition region), $I_{\mathrm{rel}} < 0.15$ in the barrel and $I_{\mathrm{rel}} < 0.1$ in the endcap region, and a set of looser quality and photon-conversion rejection criteria [126].

5.4. Particle-Flow Approach

In order to reconstruct all final-state particles in an event, the CMS particle-flow approach [127] is used. First, charged-particle tracks in the silicon tracker and the muon chambers are reconstructed. Then, energy deposits in the calorimeter cells are grouped to clusters. In general, final-state particles can produce several of such elementary signatures. In order to fully reconstruct all particles without double-counting signatures, charged tracks and energy clusters are linked to blocks. For example, tracks are extrapolated to the calorimeters and matched to energy clusters, if their positions agree. Potential Bremsstrahlung photons are added to tracks by extrapolating tangents to the track to the ECAL and matching these to energy clusters. Finally, particles are reconstructed from these blocks by applying dedicated identification criteria.

5.5. Jet Reconstruction

Due to confinement in the strong interaction (cf. Section 2.1.3), gluons and quarks produced in the hard scattering process show up as jets at particle-level. In order to reconstruct properties of the underlying partons, final-state particles, as reconstructed by the particle-flow algorithm, are grouped to jets by some algorithm. In this thesis, jets are reconstructed from particle-flow candidates using the anti-k_{T} algorithm [128] with a distance parameter of $R = 0.5$. For all objects i and all pairs of objects i and j the weighted distances

$$d_i = k_{\mathrm{T}_i}^{-2}\,, \tag{5.3}$$

$$d_{ij} = \min\left(\frac{1}{k_{\mathrm{T}_i}^2}, \frac{1}{k_{\mathrm{T}_j}^2}\right)\frac{\Delta R_{ij}}{R} \tag{5.4}$$

are calculated. Here, $\Delta R_{ij} = (y_i - y_j)^2 + (\phi_i - \phi_j)^2$ denotes the distance between i and j in rapidity-azimuth space and k_{T_i} the transverse momentum of i. Among all distances d_i and d_{ij}, the smallest is determined. If this is the distance d_{ij} between two objects i and j, these objects are combined to a pseudo-jet, which is added to the list of input objects, while the objects i and j are removed. If a distance of type d_i has

the smallest value, the corresponding object is considered a jet and removed from the list of input objects. This procedure is repeated until all objects are clustered into jets. The anti-k_T algorithm is infrared and collinear safe, i.e. the clustering is insensitive to the emission of soft particles and collinear splittings. From a theoretical point of view this is important, since soft and collinear QCD splittings cannot be calculated by means of perturbation theory. From an experimental point of view, it has the advantage that the result is largely independent of the reconstruction of soft particles and the spatial detector resolution. In contrast to other infrared and collinear safe algorithms, the anti-k_T algorithm provides regular boundaries and a shape very similar to a simple cone of size R.

Jet Energy Corrections

In general, the energy of a reconstructed jet does not equal the energy of the underlying particle-level jet. To correct for this, the CMS collaboration provides dedicated calibration factors, which are sequentially applied on the four-momenta of reconstructed jets in data and simulated events [129]. These calibration factors correct for the η and p_T dependencies of the jet energy response as well as energy contributions from pile-up interactions. The remaining differences between data and simulated events are accounted for by applying scale factors to the measured four-momenta. These range from 1 to 1.02 [129].

Jet Energy Resolution

The relative energy resolution of jets that are reconstructed from calorimeter energy deposits only (*calorimeter jets*) can be parametrized by formula (3.2) and is in most relevant p_T regions dominated by a term that is proportional to $\sqrt{E}$. The jet energy resolution of particle-flow jets, in contrast, can be expected to also depend on the track-p_T resolution of charged hadrons, which is proportional to p_T, as well as artefacts of the particle-flow algorithm, in particular an imperfect track-cluster matching. Empirically, it is found that the energy resolution of particle-flow jets can be described by a variation of the standard formula for the calorimeter-based resolution,

$$\frac{\sigma(p_\mathrm{T})}{p_\mathrm{T}} = \sqrt{\mathrm{sgn}(N) \cdot \left(\frac{N}{p_\mathrm{T}}\right)^2 + S^2 \cdot p_\mathrm{T}^{M-1} + C^2}\,, \tag{5.5}$$

where N, S, M, and C are free parameters. Compared to Eq. (3.2), a negative sign of the first term is allowed, and an additional parameter M is introduced in the second term. Hence, these terms cannot directly be interpreted as noise and stochastic terms anymore. The energy resolution of jets in data is found to be worse than the resolution in simulated events [129]. To correct for this, reconstructed jets

in simulated events are matched to particle-level jets by a standard ΔR criterion. The four-momenta of reconstructed jets are then scaled by the factor

$$c = 1 + SF \cdot \frac{p_{\mathrm{T}}^{\mathrm{reco}} - p_{\mathrm{T}}^{\mathrm{particle}}}{p_{\mathrm{T}}^{\mathrm{reco}}}\,, \tag{5.6}$$

where SF denotes an η-dependent scale factor and $p_{\mathrm{T}}^{\mathrm{reco}}$ and $p_{\mathrm{T}}^{\mathrm{particle}}$ represent the transverse momenta of the reconstructed jet and the matched particle-level jet, respectively. By this, the jet energy resolution in simulated events gets artificially worsened. The scale factor SF ranges from 1.05 for $0.0 < |\eta| < 0.5$ to 1.29 for $|\eta| > 2.3$.

Jet Selection Criteria

Selected jets are required to have a transverse momentum of $p_{\mathrm{T}} > 40$ GeV and a pseudorapidity of $|\eta| < 2.4$. The p_{T} requirement is designed such that jets from pile-up interactions are strongly suppressed, while jets that arise from the hard scattering process are mostly selected. The η requirement is mainly driven by the geometrical coverage of the tracking system and the more central production of particles produced within the cascade of sparticle decays. In addition, selected jets have to fulfill different quality criteria [130], which are designed to reject jets that arise from noise and spurious energy deposits. To avoid ambiguities, selected jets are required to be spatially separated from selected muons and electrons by $\Delta R > 0.3$.

5.6. B-Jet Identification

While muons, electrons, and hadronically decaying taus can easily be distinguished at detector-level, the identification of jet flavors is more difficult because the signatures of jets are very similar. Indeed, jets originating from up, down, and strange quarks cannot be distinguished from each other. To some extent, the former can be discriminated from gluon jets using variables that are sensitive to the jet shape and the jet substructure, see e.g. [131]. Since jets produced within the cascades of sparticle decays mostly originate from quarks, such a distinction might improve the reach of many searches for Supersymmetry at the LHC as well as measurements of sparticle properties after a possible discovery of SUSY. However, by now *gluon tagging* suffers from a comparatively low efficiency [132] and has not yet been established in searches for new physics at the CMS experiment.

Instead, bottom-quark jets can be relatively well distinguished from other-flavor jets. Since the bottom-quark decay into a virtual W boson and an up or charm quark is strongly suppressed by the CKM matrix (cf. Section 2.1.1), bound states including b-quarks are long-lived in comparison to other hadrons that decay before detection. With a typical lifetime of $\tau_B \approx 1.6\,\mathrm{ps}$ [20] B-hadrons travel a significant

distance ($c\tau_B \approx 500\,\mu$m) before decay, leading to a *secondary vertex* that is spatially well separated from the primary vertex. To a lesser extent this does also apply for D-mesons, which arise from the hadronisation of c-quarks. Based on properties that are associated with such a vertex or related to the semileptonic three-body decay of bottom quarks, the CMS collaboration has developed a variety of algorithms to identify b-jets [133]. In this thesis, the impact parameter significance is used to discriminate between tracks that originate from secondary vertices and tracks that originate from the primary vertex (prompt tracks). The impact parameter of a track is defined as its distance to the primary vertex at the point of closest approach, as illustrated in Fig. 5.3.

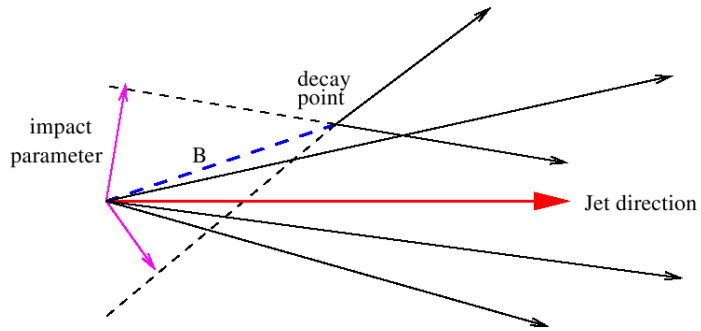

Figure 5.3.: Illustration of the track impact parameter. The dashed blue line marks the flight distance of the B-meson. The extrapolations of the tracks that originate from its decay are indicated by the dashed black lines.

It is calculated in three dimensions and signed according to the scalar product of the vector pointing from the primary vertex to the point of closest approach (represented by the magenta arrows in Fig. 5.3) with the jet direction (represented by the red arrow). Tracks originating from the decay of particles traveling along the jet axis tend to have positive impact parameter values, while the impact parameters of prompt tracks can have positive and negative signs. Since the resolution of the impact parameter strongly depends on the transverse momentum and the pseudorapidity of the track, the impact parameter significance, defined as the ratio of the impact parameter value and its uncertainty, is used as discriminating variable instead of the impact parameter itself. To identify b-jets, tracks in a jet are sorted by decreasing values of the impact parameter significance. To reject fake and badly reconstructed tracks, only those tracks that pass dedicated quality criteria [133] are considered. Since the probability of having several tracks with high positive values is low for u-, d-, and s-jets, the impact parameter significance of the n-th ranked tracked can be used as *b-discriminator*. CMS has measured the performance of two such *track counting algorithms*, which use the impact parameter significance of the second and third ranked track as discriminator. While the former algorithm

is designed for an efficient selection of b-jets, the latter is rather suited for a pure selection. In this thesis the algorithm that uses the impact parameter significance of the the second ranked track is used. The corresponding b-discriminator distribution of selected jets in simulated $t\bar{t}$ events that can be matched to a b-quark, c-quark, or any other particle is shown in Fig. 5.4. Selected jets are identified as b-jet if they have a b-discriminator larger than 3.3. As can be seen, the largest contribution to the fraction of jets that are misidentified as b-jet originates from c-jets.

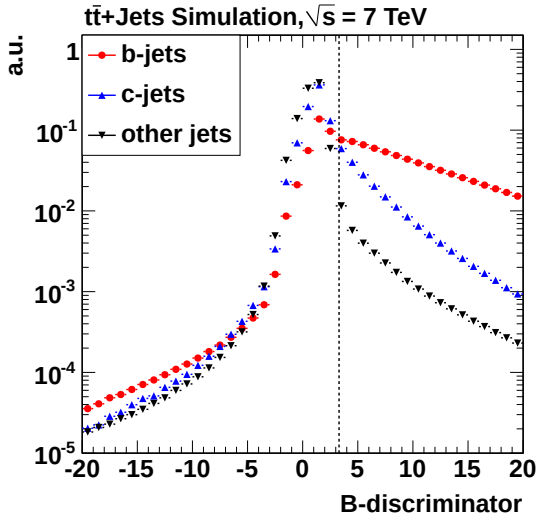

Figure 5.4.: B-discriminator of selected jets in simulated $t\bar{t}$+Jets events that can be matched to a b-quark, c-quark, or any other particle. All distributions are normalized to unit area. Selected jets are identified as b-jet if they have a b-discriminator larger than 3.3, which is marked by the vertical dashed black line.

The b-jet selection efficiency (b-tag efficiency) is found to be smaller in data than in simulated events, while the efficiency of misidentifying other jets as b-jet (udsg-mistag rate) is determined to be somewhat larger in data [133]. In order to correct for the resulting differences between data and simulated events, the CMS collaboration provides scale factors [133, 134], which are applied on the b-tag efficiency and the udsg-mistag rate in simulated events, as described later in Section 6.4. So far, the CMS collaboration has not measured the c-mistag rate. Therefore, the b-tag efficiency scale factor is applied on the c-mistag rate [134].

6. Event Selection

The possibility of light top and bottom squarks motivates to search for Supersymmetry in final states with isolated leptons, bottom-quark jets, and missing transverse energy at the LHC. As discussed in Section 2.2.3, assuming $m_{\tilde{t}_1} < m_{\tilde{b}_1} < m_{\tilde{g}}$ and R parity to be conserved, the production of third-generation squarks can be expected to result in states with at least two bottom quarks, two W bosons/W-like final states, and two stable LSPs. Again, "W-like final state" refers to states that either comprise a charged lepton and an antineutrino, or a pair of an up-type quark and a down-type antiquark of the first or second generation. Within the considered decay cascades of top and bottom squarks, such states are either produced from the chargino two-body decays $\tilde{\chi}^+ \to l^+\tilde{\nu}$ and $\tilde{\chi}^+ \to \nu\tilde{l}^*$ with the subsequent decays $\tilde{\nu} \to \nu\tilde{\chi}^0$ and $\tilde{l}^* \to l^+\tilde{\chi}^0$, respectively, or the chargino three-body decays $\tilde{\chi}^+ \to \nu l^+\tilde{\chi}^0$ and $\tilde{\chi}^+ \to q\bar{q}'\tilde{\chi}^0$. For similar masses of sleptons and first and second generation squarks ($m_{\tilde{l}} \approx m_{\tilde{q}}$), the branching ratio for the hadronic (leptonic) chargino three-body decay will be close to that for the hadronic (leptonic) W-boson decay. A pair of W bosons/W-like final states then can be expected to result with the same probability ($\approx 44\%$) in a "fullhadronic composition" ($q\bar{q}q\bar{q}$) as in a "single-lepton composition" ($l\bar{\nu}q\bar{q}$). However, while the squarks of the first and second generation are assumed to be heavier than the lighter top and bottom squarks, no assumption about the slepton masses is made. Within the considered decay cascades of top and bottom squarks, the chargino two-body decays $\tilde{\chi}^+ \to l^+\tilde{\nu}$ and $\tilde{\chi}^+ \to \nu\tilde{l}^*$ might therefore be kinematically allowed, leading to a preference of single-lepton compositions over fullhadronic ones.

As discussed in Section 2.2.3.4, the direct pair production of bottom squarks and the gluino-induced production of third-generation squarks may also result in states including four W bosons/W-like final states. Up to a possible shift of branching ratios due to leptonic chargino two-body decays, such states will result with a probability of approximately 20% in a fullhadronic composition and with a probability of about 40% in a single-lepton composition. In approximately 30% of all four-W events exactly two leptons will be produced, in about 10% exactly three leptons.

Since for both considered multiplicities of W bosons/W-like final states the single-lepton composition has the largest branching ratio ($\geqq 0.4$), a search in final states with a single lepton is performed. Associated therewith, at least two light-quark jets from a hadronically decaying W boson/hadronically composed W-like final state can be assumed to be produced in addition.

Though motivated by the possibility of light top and bottom squarks, the search presented in this thesis is not particularly designed for third-generation squarks

whose masses are in the order of the top quark mass. Such "very light" top and bottom squarks might require a precise measurement of the $t\bar{t}$ production cross section or dedicated searches.[1] In this search, the gluino and all squarks are assumed to be heavier than the top quark. Therefore, the production of top and bottom squarks is expected to result in states with a larger hadronic activity than the production of Standard Model particles. As measure for the hadronic activity the scalar sum of the transverse momenta of all selected jets, H_{T}, is used. Associated with the larger mass scale at which sparticles will be produced, in most supersymmetric scenarios also a larger amount of missing transverse energy is expected. The latter is quantified by $\not\!\!E_{\mathrm{T}}$, defined as the magnitude of the negative vectorial sum of the transverse momenta of all final-state particles, as reconstructed by the particle-flow algorithm (cf. Section 5.4). Since $\not\!\!E_{\mathrm{T}}$ is not adjusted for jet energy scale corrections by default (so-called *type-1* corrections [136] are not applied), an additional uncertainty on $\not\!\!E_{\mathrm{T}}$ is introduced, as discussed later in Section 8.3.2.

The search presented in the following is based on the full set of data recorded at the CMS experiment during proton-proton collisions at a center-of-mass energy of $\sqrt{s} = 7$ TeV in 2011. With all subdetectors fully functional, an integrated luminosity of $\mathcal{L} = 4.98\,\mathrm{fb}^{-1}$ has been recorded. Events have been collected using triggers that require the presence of a lepton, a large hadronic activity, and missing transverse energy, as outlined in Section 6.1. In order to match subsets of data that have been recorded using triggers with different thresholds and to compare these with simulated events, requirements on the offline reconstructed lepton, H_{T}, and $\not\!\!E_{\mathrm{T}}$ that are somewhat above the maximal trigger thresholds are applied. (The sensitivity of H_{T} and $\not\!\!E_{\mathrm{T}}$ will be fully exploited within the data-driven background prediction presented later in Section 7.) Together with a primary-vertex requirement and the rejection of events with instrumental noise, this basically constitutes the event preselection, which is described in Section 6.2. Reflecting the minimal signature expected from top and bottom squark production resumed above, events are required to contain at least four jets, as described in Section 6.3. Since top and bottom squark production are expected to result in states with either two or four bottom quarks, the search is done in two different bins of the b-jet multiplicity, which is discussed in Section 6.4. Finally, event yields and variables that are sensitive to a possible deviation from the SM prediction are presented in Section 6.5.

[1] For $m_{\tilde{t}_1} = m_t$, the cross section for $\tilde{t}_1\tilde{t}_1$ production in proton-proton collisions at $\sqrt{s} = 7$ TeV roughly amounts one fifth of the cross section for $t\bar{t}$ production [135]. If their decay products are not too soft, the pair production of very light top squarks might therefore result in a significant deviation of the measured $t\bar{t}$-production cross section from the prediction. However, if all not flavor-suppressed two- and three-body decays of the lighter top squark are kinematically forbidden, the only possible decays are flavor-suppressed decays, such as $\tilde{t}_1 \to c\tilde{\chi}_1^0$, and the four-body decays $\tilde{t}_1 \to bl^+\bar{\nu}\tilde{\chi}_1^0$ and $\tilde{t}_1 \to bq\bar{q}'\tilde{\chi}_1^0$. Since these decays can be very slow, the lighter top squark might be long-lived, which might require dedicated searches.

6.1. Trigger Selection

Events have been recorded using lepton-hadron *cross triggers* that require the presence of a muon or electron with a transverse momentum $p_{\mathrm{T}}^{\mathrm{trigger}}$ above a certain threshold in association with a large hadronic activity. The latter is quantified by $H_{\mathrm{T}}^{\mathrm{trigger}}$, which is defined as the value of H_{T} calculated at trigger level. As measure for the missing transverse energy, a requirement on $\not{H}_{\mathrm{T}}^{\mathrm{trigger}}$, defined as the magnitude of the negative vectorial sum of the transverse momenta of all jets at trigger level, has been added in the second part of 2011. Both variables are calculated from jets with $p_{\mathrm{T}} > 40$ GeV and $|\eta| < 3$ that have been clustered using the anit-k_T algorithm with a distance parameter of 0.5. However, while $H_{\mathrm{T}}^{\mathrm{trigger}}$ is computed from calorimeter jets, the calculation of $\not{H}_{\mathrm{T}}^{\mathrm{trigger}}$ exploits a simplified implementation of the particle-flow algorithm. In order not to exceed the maximal rate of data acquisition and processing of about 200 Hz in 2011, trigger thresholds were adapted to the instantaneous luminosity, which increased by more than two orders of magnitude. In the muon channel the requirement on the lepton p_{T} was raised from 8 GeV to 15 GeV, in the electron channel from 10 GeV to 15 GeV. The thresholds on $H_{\mathrm{T}}^{\mathrm{trigger}}$ were increased from 200 GeV to 300 GeV in the muon channel and from 200 GeV to 250 GeV in the electron channel. The requirement on $\not{H}_{\mathrm{T}}^{\mathrm{trigger}}$ was introduced with a threshold of 20 GeV and raised to a threshold of 40 GeV towards the end of 2011. The trigger thresholds that were in place during the different run periods defined in terms of CMS-run numbers are summarized in Table 6.1.

Table 6.1.: Trigger thresholds of the lepton-hadron cross triggers for the different run periods in 2011. All values are given in GeV.

Run numbers	Muon-hadron trigger			Electron-hadron trigger		
	$p_{\mathrm{T}}^{\mathrm{trigger}}$	$H_{\mathrm{T}}^{\mathrm{trigger}}$	$\not{H}_{\mathrm{T}}^{\mathrm{trigger}}$	$p_{\mathrm{T}}^{\mathrm{trigger}}$	$H_{\mathrm{T}}^{\mathrm{trigger}}$	$\not{H}_{\mathrm{T}}^{\mathrm{trigger}}$
160404 - 163869	> 8	> 200	-	> 10	> 200	-
163870 - 166861	> 15	> 200	-	> 15	> 200	-
166862 - 172802	> 15	> 250	> 20	> 15	> 250	-
172803 - 178078	> 15	> 250	> 40	> 15	> 250	> 25
180253 - 180252	> 15	> 300	> 40	> 15	> 250	> 40

Since the reconstruction of physics objects at trigger level is based on simplified algorithms and a reduced granularity, the efficiencies of the offline and the online event selection differ from each other. This difference is typically expressed in terms of *trigger turn-on curves*, which represent the efficiencies of triggering events as functions of the relevant offline selection criteria. Reflecting the increasing thresholds

listed in Table 6.1, the turn-on curves for the cross triggers used within this analysis can be expected to strongly differ from each other. To match different subsets of data, it is therefore desirable to apply offline selection criteria such that the selected events are triggered with the same efficiency by all triggers. Furthermore, in order to compare data with simulated events, where no trigger selection is applied,[2] possible inefficiencies need to be corrected for by applying scale factors. Hence, the efficiencies of the lepton-hadron cross triggers need to be measured, which is done separately as a function of the lepton, the H_{T}, and the $\not\!\!E_{\mathrm{T}}$ selection [123].

Lepton-Trigger Efficiency

The trigger efficiencies as a function of the lepton selection are determined using the tag-and-probe technique described in Section 5.2. Events are selected if they pass the cross trigger in question and contain two oppositely charged leptons of the same flavor, one of which (the "tag lepton") can be matched to a "trigger lepton". Here, "trigger lepton" refers to an HLT object that passes the lepton part of the cross trigger. In addition, the tag lepton is required to pass the trigger requirements at the level of offline reconstructed objects as well. The other lepton (the "probe lepton") then can be tagged as muon or electron by requiring the invariant dilepton mass to be compatible with the Z-boson mass. The trigger efficiency as a function of the lepton selection, e.g. the lepton p_{T}, can be probed by counting the number of events where the probe lepton can be matched to a trigger lepton as well. The efficiencies for triggering muons and electrons that pass the selection criteria applied in this analysis (cf. Sections 5.2 and 5.3) amount to 0.97 ± 0.02 in both lepton channels.

Hadron-Trigger Efficiency

The trigger efficiencies as functions of the H_{T} and the $\not\!\!E_{\mathrm{T}}$ selection are measured in data that have been recorded using single-lepton triggers. The latter are chosen such that the thresholds are at least as tight as those of the lepton part of the cross triggers. Events that contain exactly one selected muon or electron are selected. In order to match the lepton selection described later in Section 6.2.2, events with a second muon or electron fulfilling the looser veto criteria defined in Sections 5.2 and 5.3 are rejected. The efficiency for triggering events with a certain H_{T} and $\not\!\!E_{\mathrm{T}}$ then can simply be obtained by counting the events where in addition to the single-lepton trigger also the cross trigger in question triggered. The efficiencies are determined to be larger than 99% for $H_{\mathrm{T}} > 375$ GeV and $\not\!\!E_{\mathrm{T}} > 100$ GeV.

[2] Despite the fact that only a few triggers have been included during the event simulation, possible scale factors needed to be measured anyhow. It is therefore more comfortable not to apply any trigger selection on simulated events at all.

6.2. Preselection

The aim of the event preselection is to obtain a clean and homogeneous data sample that can be compared to simulated events. The preselection comprises a primary-vertex requirement, the rejection of events from beam-background processes and events that are affected by instrumental noise or reconstruction algorithm failures, the H_{T} selection, and the $\not\!\!E_{\mathrm{T}}$ selection. After shortly describing these steps in Sections 6.2.1, 6.2.2, and 6.2.3, a few control distributions of the preselected data and simulated events are discussed in Section 6.2.4.

6.2.1. Primary Vertex Selection and Event Cleaning

Primary vertices are reconstructed as described in Section 5.1. In order to ensure the presence of a proton-proton collision, events are required to contain at least one primary vertex that has been reconstructed from more than four tracks and is located within 24 cm in z and 2 cm in xy direction from the nominal interaction point. To reject events that originate from beam-background processes, e.g. from interactions of protons with residual gas molecules upstream the beam pipe, the fraction of high-quality tracks in events with at least ten charged-particle tracks is required to be greater than 25%. To identify events from beam-background processes with a muon, a dedicated filter that utilizes the CSC subdetector is used.

A small fraction of events ($< 0.1\%$) is affected by instrumental noise, which may give rise to artificial missing transverse energy. To reject these events, three standard *noise filters* are employed. In some events instrumental noise in the Hybrid Photo Detectors and their readout boxes cause anomalous signals in the hadronic calorimeter. Based on timing and pulse-shape information, these events are identified and vetoed. About 1% of the electromagnetic calorimeter crystals are noisy and therefore not read out. Since the energy deposited in these crystals cannot be taken into account during the reconstruction of physics objects, the affected events need to be rejected. For this purpose two noise filters are exploited. One of these removes events where the trigger primitive E_{T} at the noisy cell exceeds a certain threshold. The other one rejects events based on the amount of energy deposited in the crystals surrounding the noisy cell.

Finally, in a few events the tracking algorithm fails because of too many seed clusters. In order to reject such events, the scalar sum of the p_{T} of the tracks associated with the primary vertex is required to be greater than 10% of the scalar sum of the p_{T} of all jets within the tracker acceptance.

All noise filters are applied on simulated events as well, even though they partly do not affect these.

6.2.2. Lepton Selection

Events are required to contain exactly one muon or electron that passes the selection criteria described in Sections 5.2 and 5.3, respectively. Besides an isolation criterion these basically consist of a requirement on the transverse momentum of $p_{\mathrm{T}} > 20$ GeV and requirements on the pseudorapidity of $|\eta| < 2.1$ in the muon channel and $|\eta| < 2.5$ in the electron channel. Since no trigger selection is applied on simulated events, the latter are scaled down by the lepton trigger efficiency of 0.97. Events with a second muon or electron that fulfill the looser veto criteria are rejected. Besides the possibility to combine results obtained in different exclusive lepton channels, the motivation for this is to obtain a homogeneous background, which facilitates the background prediction from data.

6.2.3. H_{T} and $\not{E}_{\mathrm{T}}$ Selection

In order to select events where the trigger efficiency as a function of H_{T} reaches its maximum ($> 99\%$), H_{T} is required to be larger than 375 GeV. For a requirement on the offline reconstructed missing transverse energy of $\not{E}_{\mathrm{T}} > 100$ GeV, the $\not{H}_{\mathrm{T}}$ parts of the cross triggers would be similarly efficient. However, for the data-driven background prediction presented later, a control sample of events with 60 GeV $< \not{E}_{\mathrm{T}} < 160$ GeV is used. Therefore, a looser requirement of $\not{E}_{\mathrm{T}} > 60$ GeV is applied. While the cross trigger with $\not{H}_{\mathrm{T}}^{\mathrm{trigger}} > 20$ GeV is maximal efficient for this requirement, the cross trigger with $\not{H}_{\mathrm{T}}^{\mathrm{trigger}} > 40$ GeV has an efficiency of about 80% at an offline reconstructed $\not{E}_{\mathrm{T}}$ of 60 GeV. To correct for the resulting discrepancies between different subsets of data on the one hand and data and simulated events on the other, selected data events are weighted by the inverse trigger efficiency as a function of $\not{E}_{\mathrm{T}}$. Due to this weighting the numbers of selected events are not necessarily whole numbers.

It should be mentioned that such an event weighting could not be avoided by using different triggers without loosing statistics. As alternative to the triggers used in this search, isolated-lepton triggers or cross triggers that require the presence of an isolated lepton and three central jets with $p_{\mathrm{T}} > 30$ GeV and $|\eta| < 2.6$ could be used. However, the maximum thresholds of the isolated-lepton triggers on the lepton p_{T} amount to 24 GeV in the muon channel and 32 GeV in the electron channel. The maximum thresholds of the lepton-jets cross trigger on the lepton p_{T} are 17 GeV in the muon channel and 25 GeV in the electron channel. Furthermore, the isolation criteria at trigger level might necessitate tighter requirements on the isolation of the offline reconstructed leptons. In total, either a tighter lepton selection or a weighting procedure similar to that performed in this analysis needed to be applied.

6.2.4. Control Plots

In the following, a few control distributions of the preselected data and simulated events are discussed. Data are always represented by black dots with error bars indicating the statistical uncertainty. The contributions of the different SM processes expected from the event simulation are represented by colored areas and summed up. The distributions of signal events in the LM8 and the LM6 benchmark scenario are marked by a solid blue and a dashed black line, respectively. If not stated differently, all scale factors discussed in Sections 6.2.2 and 6.2.3 are applied and simulated events are weighted according to the assumed cross sections, an integrated luminosity of $\mathcal{L} = 4.98\,\mathrm{fb}^{-1}$, and the expected number of pile-up interactions in data (cf. Section 4.3.2).

6.2.4.1. Trigger Efficiency Weighting

The trigger efficiency weighting is cross checked by comparing how well the $\not\!\!E_\mathrm{T}$ distribution of selected events is reproduced by the event simulation during the different run periods. Due to the changing run conditions subsets of data cannot be compared directly. In Fig. 6.1, the $\not\!\!E_\mathrm{T}$ distribution in the range between 60 GeV and 100 GeV is shown for run period A, where no requirement on $\not\!\!H_\mathrm{T}^\mathrm{trigger}$ was in place, and run period B, where the requirement on $\not\!\!H_\mathrm{T}^\mathrm{trigger}$ was introduced.

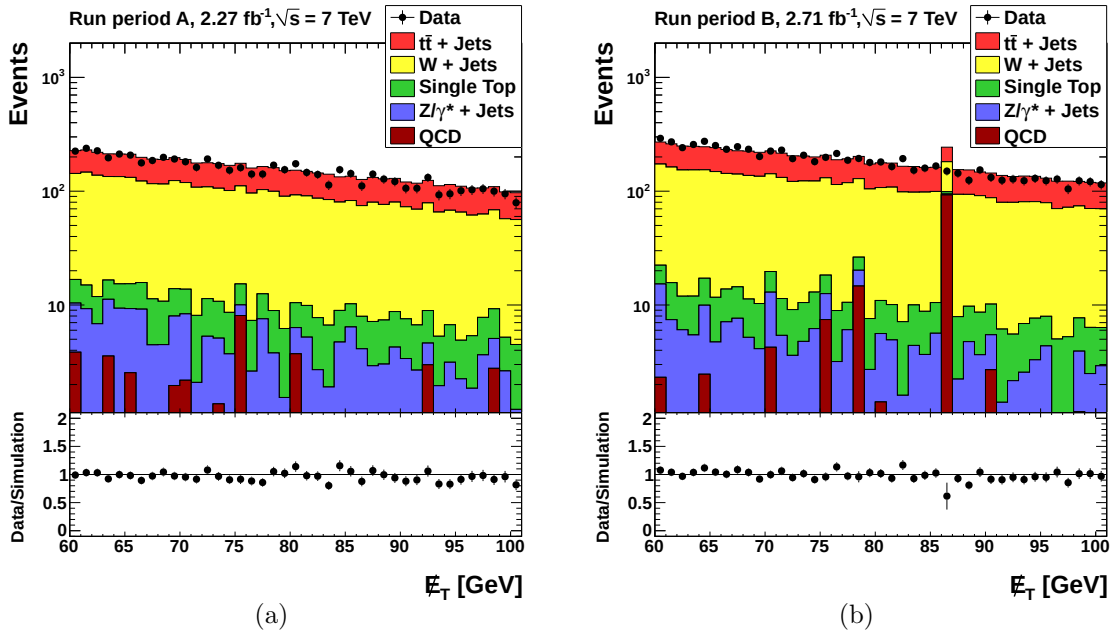

(a) (b)

Figure 6.1.: $\not\!\!E_\mathrm{T}$ after the preselection during run period A (a) and run period B (b). The results are combined for the muon and the electron channel.

Simulated events are weighted to the integrated luminosities of $\mathcal{L}_{\mathrm{A}} = 2.27\,\mathrm{fb}^{-1}$ and $\mathcal{L}_{\mathrm{B}} = 2.71\,\mathrm{fb}^{-1}$ that have been recorded during run period A and B, respectively. To account for the increasing instantaneous luminosity in 2011, the pile-up reweighting of simulated events is done separately for the different run periods. In Fig. 6.1(a) simulated events are weighted according to the number of pile-up interactions estimated for run period A. In Fig. 6.1(b) the pile-up weighting of simulated events is based on the number of pile-up interactions estimated for run period B.As can be seen in Fig. 6.1, in the range between 60 GeV and 100 GeV the two $\not\!\!E_{\mathrm{T}}$ distributions are similarly well described by simulated events.[3] The data-to-simulation ratio amounts to $r_A = 0.97 \pm 0.01$ for run period A and $r_B = 0.99 \pm 0.01$ for run period B. To account for possible further run conditions that differently affect the $\not\!\!E_{\mathrm{T}}$ distributions of the preselected data, the overall data-to-simulation ratio for run period B is normalized such that in the region with $\not\!\!E_{\mathrm{T}} > 100$ GeV the data-to-simulation ratios for the two run periods equal each other. In this region the preselected data are almost not affected by the trigger weighting because the $\not\!\!H_{\mathrm{T}}$ parts of all cross triggers are nearly fully efficient ($> 99\%$). In the region of 60 GeV $< \not\!\!E_{\mathrm{T}} <$ 100 GeV the data-to-simulation ratio for run period B then amounts $r'_B = 0.96 \pm 0.02$. This value is very well compatible with that for run period A.

6.2.4.2. Leptonic Variables

The transverse momentum and the pseudorapidity of the selected lepton in the muon channel are shown in Fig. 6.2. At this stage of the event selection, the largest contributions to the Standard Model background in this channel originate from W+Jets events (58%) and $t\bar{t}$ + Jets events (37%). Notably, only four QCD events (which correspond to one weighted entry) pass the preselection in the muon channel. This is mainly due to the isolation requirement. In QCD multijet events, muons are produced within jets, e.g. from semileptonic three-body decays of heavy-flavor quarks ($b \to q\,\mu\,\bar{\nu}_\mu$, $c \to q'\,\bar{\mu}\,\nu_\mu$) and light-meson decays in flight. Hence, they are accompanied by a comparatively large hadronic activity and do mostly not pass the isolation criterion. By requiring one selected muon, the background from simulated QCD multijet events (with $\hat{p}_T > 15$ GeV) is reduced by almost five orders of magnitude. The remaining events are mostly rejected by the requirement of $\not\!\!E_{\mathrm{T}} > 60$ GeV. Since missing transverse energy in QCD events only results from jet energy mismeasurement, QCD events mainly populate regions of low $\not\!\!E_{\mathrm{T}}$.

[3] The "spike" in the distribution of simulated QCD events in the bin 86 GeV $< \not\!\!E_{\mathrm{T}} <$ 87 GeV for run period B (cf. Fig. 6.1(b)) corresponds to one non-weighted entry with a large weight. The latter results from the $\hat{p}_T$ - dependent cross section weighting of simulated QCD events, as described in Section 4.3.2. Additionally, this entry is associated with a large number of pile-up interactions. Since events with many pile-up interactions are very rare in run period A, this entry obtains a small weight when weighting according to the number of pile-up interactions estimated for run period A. Therefore, it is not visible in Fig. 6.1(a).

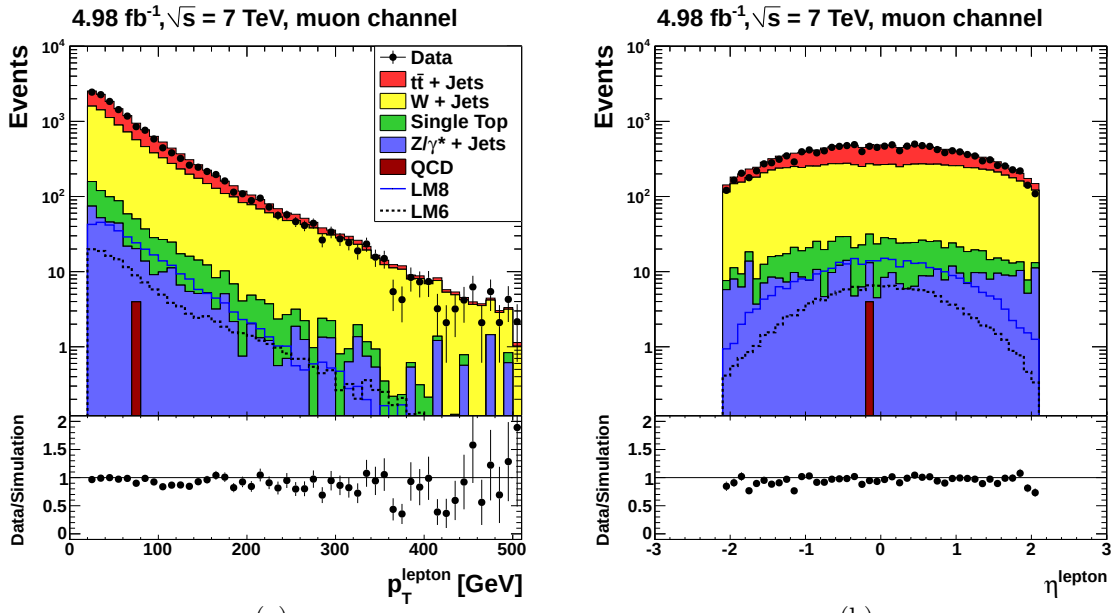

(a) (b)

Figure 6.2.: Transverse momentum (a) and pseudorapidity (b) of the selected lepton in the muon channel after the event preselection.

To a large extent this does also apply for $Z/\gamma^* + \text{Jets}$ events. Except for $Z \to \tau\bar{\tau}$ decays where at least one τ decays leptonically, $\not{E}_\text{T}$ only results from jet energy mismeasurement.[4] By additionally vetoing events with a second muon or electron that fulfills the looser veto criteria, the background from $Z/\gamma^* + \text{Jets}$ events is already strongly suppressed by the event preselection.

In Figs. 6.3, p_T and η of the selected lepton in the electron channel are shown. Since electrons with a supercluster in the transition region between the barrel and the endcaps of the ECAL ($1.4442 < |\eta| < 1.566$) are rejected, the η distribution shows a dip at these values. The SM background in this channel is similarly composed as in the muon channel. The largest contributions originate from W+Jets events (57%) and $t\bar{t} + \text{Jets}$ events (36%). The main difference is that much more QCD events (208) pass the preselection in the electron channel. This is mainly because charged hadrons are more likely to be misidentified as electron than as muon.

[4] The decays $Z \to \nu\bar{\nu}$ are not considered in this search because their contribution to the simulated SM background is negligible. As in QCD multijet events, charged leptons are produced within jets and do mostly not pass the isolation criterion. However, the cross section for the production of neutrino-antineutrino pairs from Drell-Yan processes in association with hard jets is many orders of magnitude smaller than that for QCD multijet production. Within the search presented here, "$Z/\gamma^* + \text{Jets}$" only refers to events where the Z/γ^* decays into pairs of charged leptons.

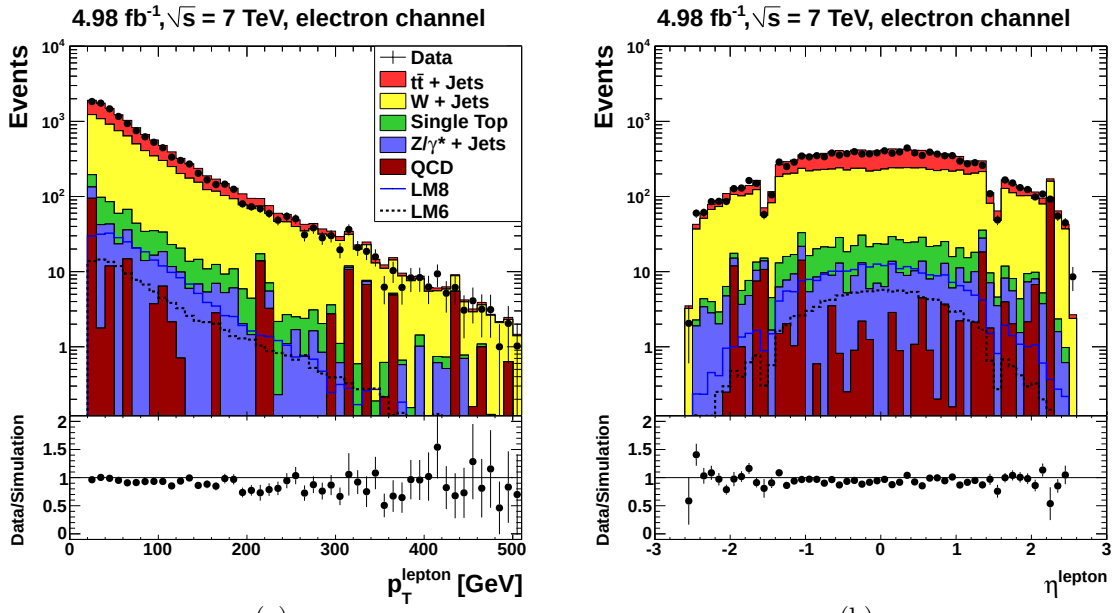

(a) (b)

Figure 6.3.: Transverse momentum (a) and pseudorapidity (b) of the selected lepton in the electron channel after the event preselection.

In general, the lepton-p_{T} and η distributions are well described by simulated events. The ratio of data to simulated events amounts 0.95 in the muon channel and 0.94 in the electron channel. The "spikes" in the distribution of QCD events result from the partly large weights. Comparing the distributions of signal events with each other, it is found that leptons in the LM6 scenario tend to be produced with a higher transverse momentum than leptons in the LM8 scenario. This can be interpreted as an effect of the leptonic chargino decays $\chi^+_{1,2} \to l^+\tilde{\nu}$ and $\chi^+_{1,2} \to \nu\tilde{l}^*$ with the subsequent decays $\tilde{\nu} \to \nu\chi^0_1$ and $\tilde{l}^* \to l^+\chi^0_1$. In scenario LM6, these decays are kinematically allowed. Therefore, charged leptons may be directly produced from the decay of a heavy and potentially high-energetic sparticle into a lighter one. In scenario LM8, the sleptons are heavier than all neutralinos and charginos. Except for the very rare processes of direct slepton production, isolated leptons are therefore always produced from the decay of a massive electroweak gauge or Higgs boson. Since events with a second lepton are vetoed, these will be mostly W bosons. Hence, leptons produced in scenario LM8 can be expected to be less boosted on average. However, even with respect to benchmark scenario LM6, a tighter requirement on the lepton p_{T} would only allow for a slight increase of the signal-to-background ratio. Within this analysis, leptonic variables are therefore not further investigated. Unless stated differently, the results presented in the following are combined for the muon and the electron channel.

6.2.4.3. Hadronic Variables

In Fig. 6.4, H_{T} and the multiplicity of selected jets are shown.

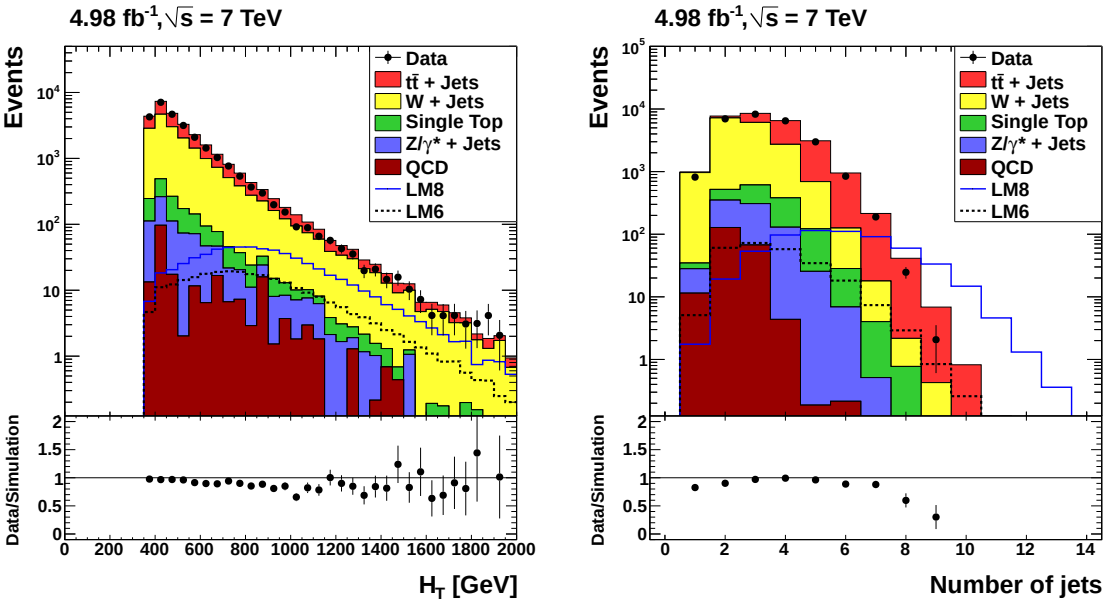

(a) (b)

Figure 6.4.: H_{T} (a) and the number of selected jets (b) after the event preselection. The results are combined for the muon and the electron channel.

Except for the little slope in the data-to-simulation ratio, the H_{T} distribution is well reproduced by the event simulation. This is basically also true for the jet multiplicity distribution. In the range between two and seven jets the data are well described by simulated events. At larger jet multiplicities the ratio drops down, which might be due to a non-perfect simulation of the parton-shower. For $n_{\mathrm{Jets}} \geqq 8$ by far the largest contribution to the simulated Standard Model background originates from semileptonic $t\bar{t}+$ Jets events (88%). The generation of these includes the simulation of two b-quarks, two quarks of the first or second generations, and up to three additional partons at matrix-element level (cf. Section 4.3.2). Hence, the generation of events with eight and nine jets necessarily requires at least one jet and two jets, respectively, to be described by the parton shower, which is rather suited to describe the emission of quarks and gluons at low energies.[5]

[5] A similar drop-off is also observed in other analyses that are based on the same datasets and simulated event samples. For example, in a measurement of differential $t\bar{t}$ pair production cross sections in the semileptonic decay channel [137], the data-to-simulation ratio similarly drops off at $n_{\mathrm{Jets}} = 8$. In a measurement of differential cross sections in the dileptonic channel [138] the ratio drops off at $n_{\mathrm{Jets}} = 6$. This corresponds to events where four jets, at least one of which is described by the parton shower, are produced in addition to the dileptonically decaying $t\bar{t}$ pair.

Reflecting the larger energy scale at which sparticles in the LM8 and the LM6 scenario are produced, their decays result in final states with a larger hadronic activity than the production of Standard Model particles. While the H_{T} distribution of background events is steadily falling off,[6] the distributions of signal events show a "mass turn-on": At low values of H_{T} the distributions are slightly increasing, reaching their maxima at $H_{\mathrm{T}} \approx 700$ GeV. At large values of H_{T} they show a similar exponential decay as the distribution of Standard Model events.

A particular jet multiplicity, in contrast, first of all characterizes a certain event topology. As can be seen in Fig. 6.4(a), the production of $t\bar{t}$ pairs results in final states with similar jet multiplicities as the production of sparticles in scenario LM6, though the latter are produced at much higher energies. In scenario LM8, the production of sparticles results in final states with significantly larger jet multiplicities, even though the gluino and all squarks are lighter than in scenario LM6. This is due to the different mass hierarchies. In scenario LM8 ($m_{\tilde{t}_1}, m_{\tilde{b}_1} < m_{\tilde{g}} < m_{\tilde{q}}$), the gluino may only decay into $t\tilde{t}^*$ and $b\tilde{b}^*$ pairs. As discussed in Section 2.2.3.4, in most cases the gluino decay will therefore result in states that comprise a $t\bar{t}$ - like final state and an LSP. Associated therewith, also the cross sections for gluino-pair production and the squark-associated gluino production are large (the gluino may also be produced from the decay $\tilde{q} \to \tilde{g}q$). The production of sparticles in scenario LM6 ($m_{\tilde{t}_1}, m_{\tilde{b}_1} < m_{\tilde{q}} < m_{\tilde{g}}$), in contrast, is dominated by the direct production of squark-squark and squark-antisquark pairs of all flavors, resulting in final states with similar lepton and jet multiplicities as the production of Standard Model particles. In addition, the gluino may decay in squark-antiquark pairs of all flavors.

6.2.4.4. Missing Transverse Energy

In analogy to $\not{H}_{\mathrm{T}}^{\mathrm{trigger}}$, $\not{H}_{\mathrm{T}}$ is defined as the magnitude of the negative vectorial sum of the transverse momenta of all selected jets. In Fig. 6.5, $\not{H}_{\mathrm{T}}$ and $\not{E}_{\mathrm{T}}$ are shown. The shapes of the distributions are partly not well modeled. In particular in the $\not{E}_{\mathrm{T}}$ distribution, a trend of the simulation overshooting the data is present. The bump in the $\not{H}_{\mathrm{T}}$ distribution around 400 GeV reflects the H_{T} requirement of $H_{\mathrm{T}} > 375$ GeV and mainly originates from events with exactly one selected jet. In these events, $\not{H}_{\mathrm{T}}$ necessarily equals H_{T} and is therefore always larger than 375 GeV. A small contribution also originates from events with exactly two jets. Since $\not{E}_{\mathrm{T}}$ is calculated from all final-state particles, it is a more accurate estimate for the missing transverse energy than $\not{H}_{\mathrm{T}}$. The bump at 400 GeV is therefore only slightly visible in the $\not{E}_{\mathrm{T}}$ distribution. Partly associated therewith, $\not{H}_{\mathrm{T}}$ is less sensitive to a possible deviation from the Standard Model prediction than $\not{E}_{\mathrm{T}}$. In SM events with a large missing transverse energy, $\not{E}_{\mathrm{T}}$ mainly results from the p_{T} of a neutrino that is produced along with a charged lepton in the decay of a boosted W-boson.

[6] The increase at 400 GeV is purely due to the binning.

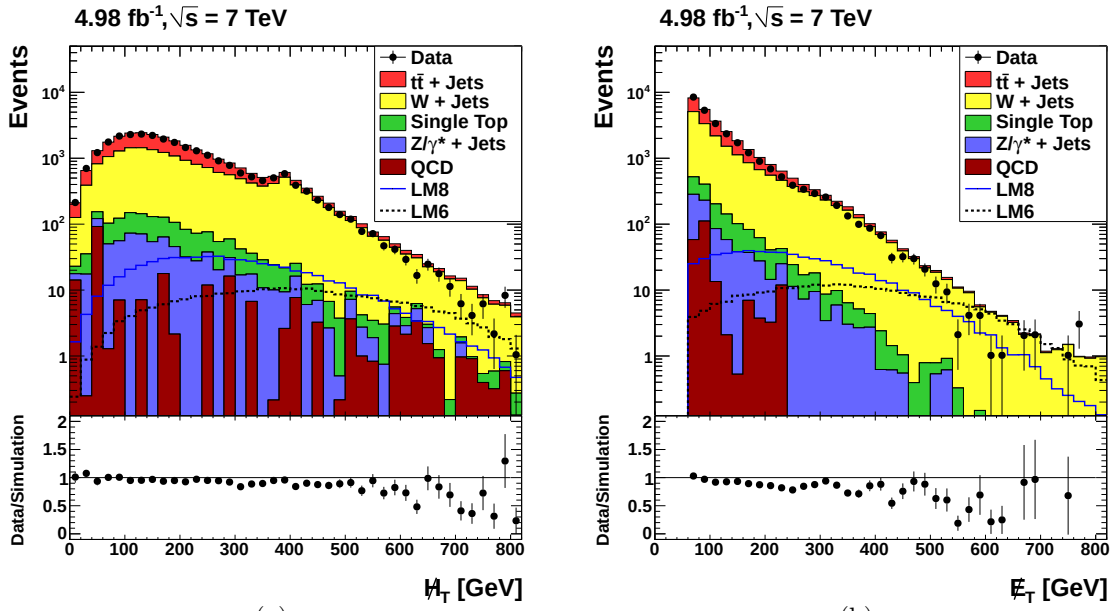

(a) (b)

Figure 6.5.: $\not{H}_T$ (a) and $\not{E}_T$ (b) after the event preselection. The results are combined for the muon and the electron channel.

In this case, the W-boson decay products will be emitted by likely angles resulting in a large hadronic activity in the opposite hemisphere and final states with $\not{H}_T > \not{E}_T$. In signal events, in contrast, the missing transverse energy mainly originates from two stable LSPs. A potential boost of the leptonically decaying W boson/leptonically composed W-like final state will therefore not cause the hadronic activity to take place in a preferred direction with respect to the direction of $\not{E}_T$. In Standard Model events with a little missing transverse energy, $\not{H}_T$ tends to be larger than $\not{E}_T$. This can be understood when considering the difference between $\not{H}_T$ and $\not{E}_T$ as a resolution effect. Since the missing transverse energy quantified by $\not{H}_T$ is reconstructed with a worse resolution than the missing transverse energy quantified by $\not{E}_T$, $\not{H}_T$ can be regarded as "fluctuating" around $\not{E}_T$. Since $\not{H}_T$ is by definition always positive, these fluctuations tend to be positive. Especially in the case of QCD multijet events this effect is well visible in Fig. 6.5. As can be seen, the $\not{E}_T$ and $\not{H}_T$ distributions of signal events are basically similar, while the$\not{H}_T$ distributions of SM events are broadened with respect to the $\not{E}_T$ distributions. In this search, $\not{E}_T$ is therefore used instead of $\not{H}_T$.

In scenario LM6, the decay of sparticles results in states with a larger missing transverse energy than in scenario LM8. Besides the larger masses of the squarks and the gluino in scenario LM6, this is mainly due to the above-mentioned difference in event topologies. Since the decay of sparticles in scenario LM6 results in less final

state objects, the two LSPs will, on average, carry larger transverse momenta.

In general, in order to distinguish between kinematic effects and effects that result from different event topologies, it is instructive to bin the analysis in the energy scale of the hard process. Up to differences in the boost along the beamline resulting from different initial states, $M_{\text{eff}} \equiv p_{\text{T}}^{\text{lepton}} + \not{E}_{\text{T}} + H_{\text{T}}$, might be used for this purpose.

6.3. Jet Selection

Events are required to contain at least four jets that pass the selection criteria defined in Section 5.5. These basically consist of the requirements of $p_{\text{T}} > 40$ GeV and $|\eta| < 2.4$. In the following, the event selection requirement of at least four jets is referred to as "jet selection". The η distribution of selected jets after the jet selection is shown in Fig. 6.6.

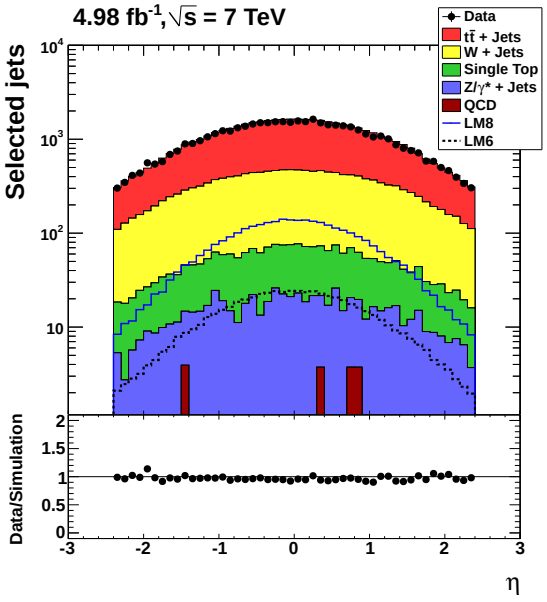

Figure 6.6.: Pseudorapidity of selected jets after the jet selection.

As can be seen, the data are well described by simulated events. Like the selected lepton in the muon and the electron channel (cf. Figs. 6.2(b) and 6.3(b)), jets in the LM8 and the LM6 scenario are produced more centrally.

The p_{T} of the four leading jets after the jet selection is shown in Fig. 6.7. Except for the little slope in the data-to-simulation ratio, which already shows up in the H_{T} distribution after the event preselection (cf. Fig. 6.4(a)), the leading and second leading jet p_{T} are well described by simulated events. The third and fourth leading jet p_{T} are not well reproduced by the event simulation.

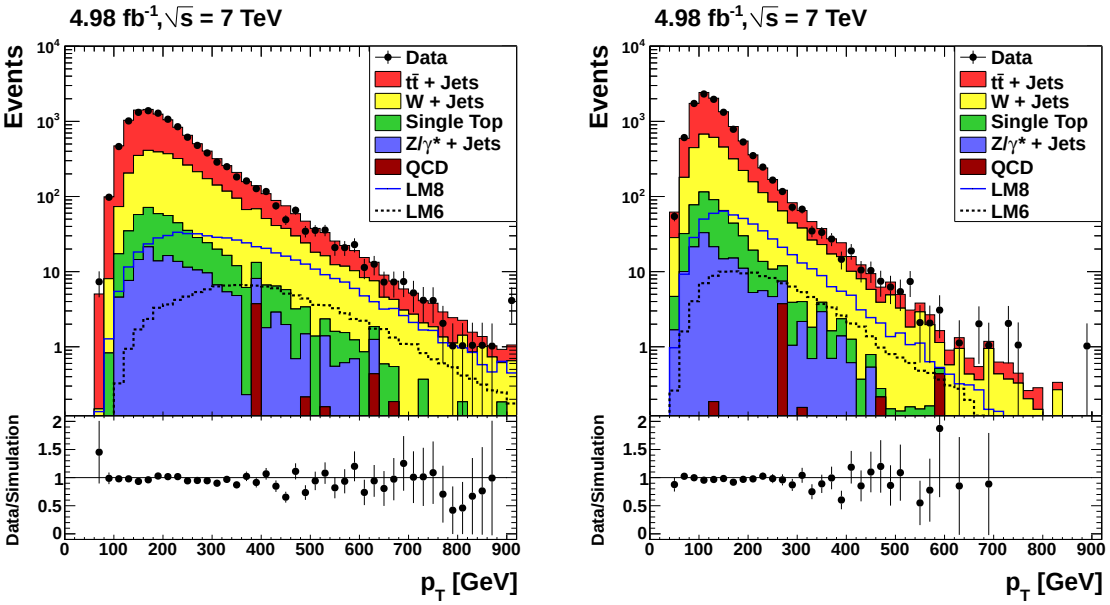

(a) leading jet (b) 2nd leading jet

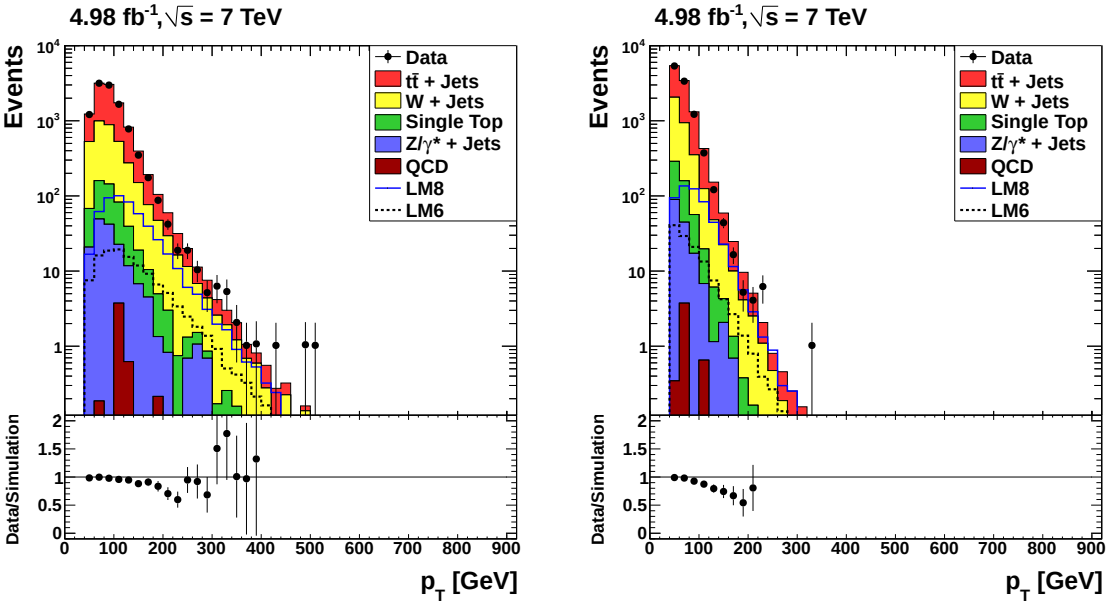

(c) 3rd leading jet (d) 4th leading jet

Figure 6.7.: P_T of the leading (a), second leading (b), third leading (c), and fourth leading (d) selected jet after the jet selection.

This can be explained by the uncertainties on the jet energy scale and the jet energy resolution and the probably non-perfect modeling of the parton shower addressed above in Section 6.2.4.

6.4. B-Jet Selection

B-jets are selected using the track counting algorithm described in Section 5.6. The b-discriminator is defined as the impact parameter significance of the 2nd high-quality track, where tracks are ordered by decreasing impact parameter significance. Selected jets are identified as b-jet if they have a b-discriminator larger than 3.3. In Fig. 6.8, the b-discriminator of selected jets and the b-jet multiplicity of events after the jet selection are shown.

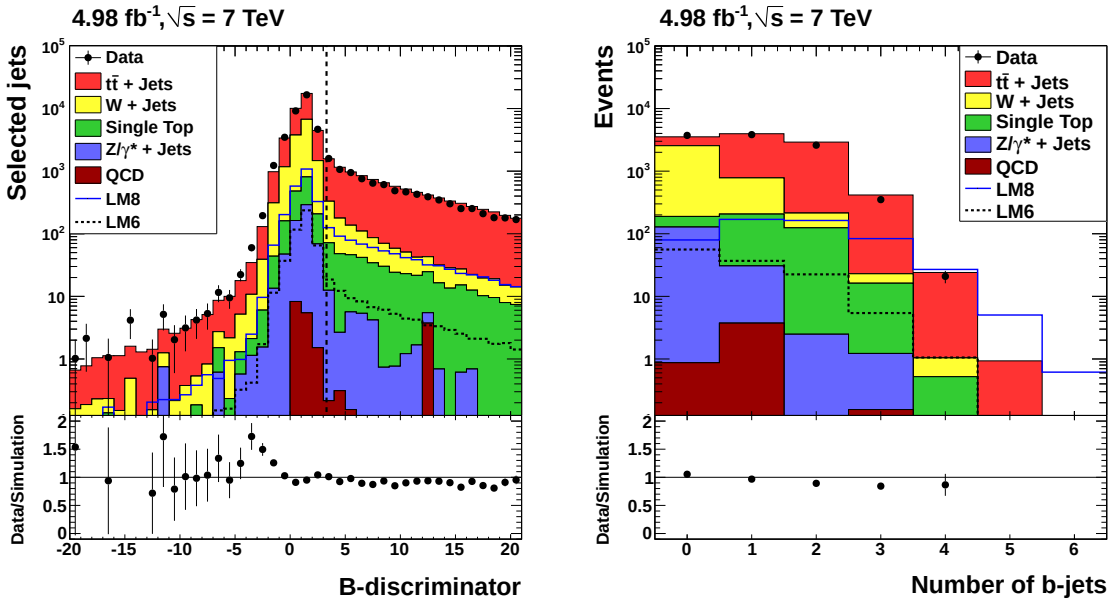

(a) (b)

Figure 6.8.: B-discriminator of selected jets (a) and b-jet multiplicity (b) after the jet selection. The vertical dashed black line marks the requirement on the b-discriminator of $b_{\text{disc}} > 3.3$.

The b-jet selection efficiency (b-tag efficiency) is found to be smaller in data than in simulated events [133]. The efficiency of misidentifying other jets as b-jet (udsg-mistag rate), on the other hand, is determined to be somewhat larger in data. Associated therewith, the b-discriminator distribution of selected jets is not perfectly described by the event simulation. Due to the steep increase of the distribution, large discrepancies arise in the range between -5 and 0, as can be seen in Fig. 6.8(a). However, as long as no requirement on the b-discriminator in this range is applied, this is not worrying. The b-jet multiplicity distribution of data is well reproduced by simulated events.

B-Tag Efficiency Weighting

In order to correct for different b-tag efficiencies and mistag rates in data and simulated events, the CMS collaboration has determined data-to-simulation scale factors as a function of the jet transverse momentum, the jet pseudorapidity and the jet flavor [133, 134]. Since these scale factors have to be applied on the level of selected jets in simulated events, in a first step, the b-tag efficiency and the mistag rates in simulated events are determined. For this purpose, jets that pass the jet selection criteria are matched to particles on generator level. This is done using the standard jet-parton matching of the CMS PAT. The matched jets are divided into three categories: jets that are matched to a bottom quark, jets that are matched to a charm quark, and jets that are matched to any other particle (mostly up, down, and strange quarks and gluons). For each of these categories, the tagging efficiency is obtained by dividing the number of jets that pass the b-discriminator requirement of $b_{\mathrm{disc}} > 3.3$ by the number of all jets within this category. For example, the b-tag efficiency in simulated events is obtained by dividing the number of all jets that are matched to a bottom quark on generator level and pass the b-discriminator requirement by all jets that are matched to a bottom quark. The efficiencies are determined in bins of p_{T} and η, as illustrated in Fig 6.9, which shows the b-tag efficiency in simulated $t\bar{t}+\mathrm{Jets}$ events.

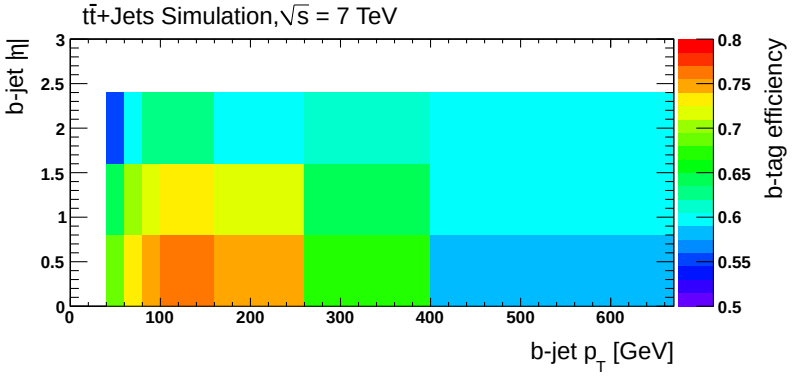

Figure 6.9.: B-tag efficiency in simulated $t\bar{t}+\mathrm{Jets}$ events after the jet selection.

Since they depend on the event selection, the efficiencies are determined separately for the muon and the electron channel from simulated events that pass the jet selection. To account for different event topologies, this is done separately for the different Standard Model processes. The b-tag efficiency, the c-mistag rate, and the udsg-mistag rate in simulated $t\bar{t}+\mathrm{Jets}$ events, $W+\mathrm{Jets}$ events, and single top events as a function of p_{T} are shown in Fig. 6.10.

In the second step, a p_{T}-, η-, and flavor-dependent tagging efficiency ϵ_j is assigned to each jet j. Again, this is done separately for the muon and the electron channel and separately for the different Standard Model processes.

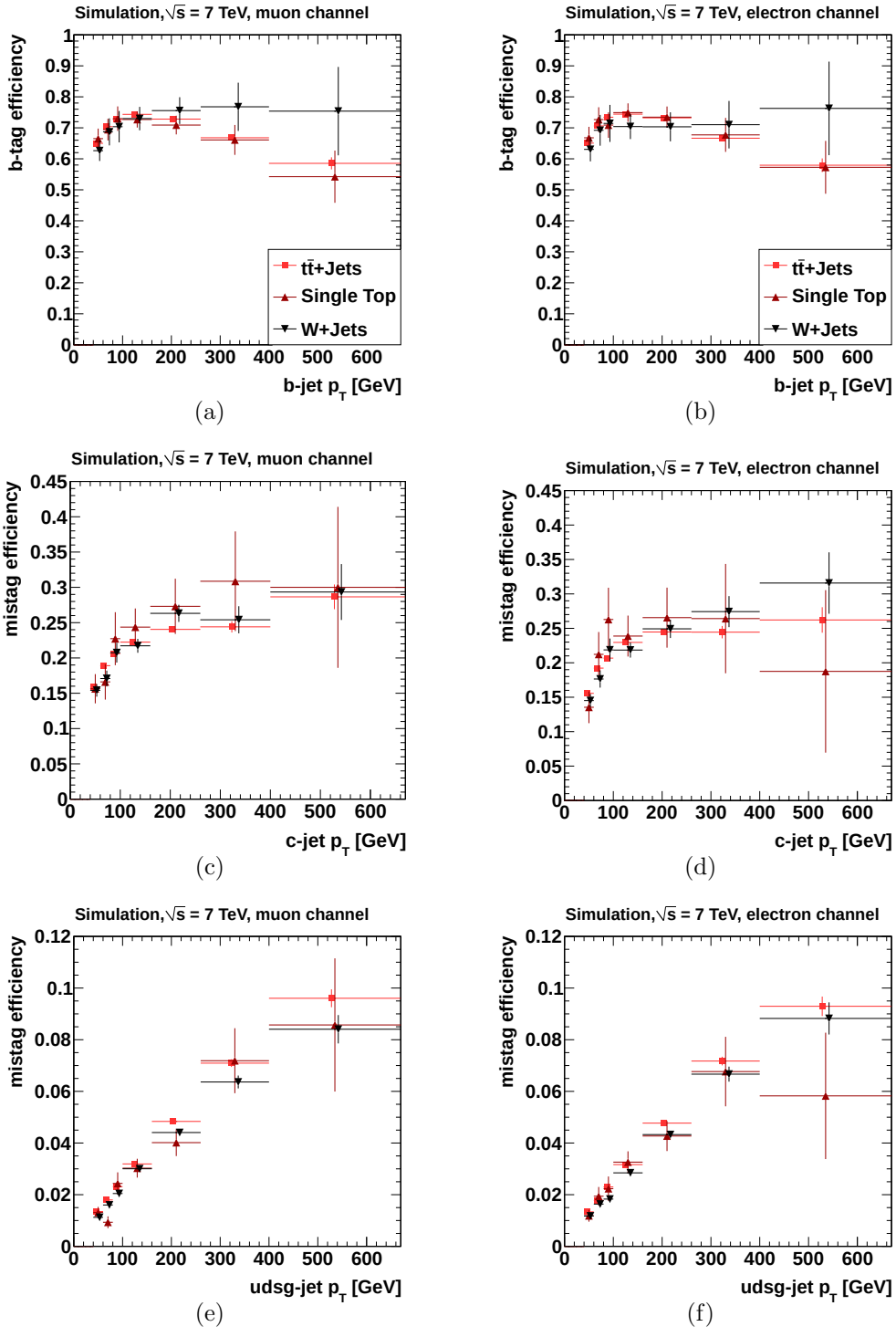

Figure 6.10.: B-tag efficiency (top), c-mistag rate (middle), and udsg-mistag rate (bottom) in simulated events after the jet selection in the muon channel (left) and in the electron channel (right). For better visibility, the markers are slightly shifted from one another in x direction.

The tagging efficiencies are multiplied by the measured scale factors SF_j. Since the c-mistag rate has not been measured yet, the c-mistag rate is scaled by the b-tag efficiency scale factors [134]. For each event the probabilities that exactly zero, exactly one, exactly two, and three ore more jets are identified as b-jet are calculated. These probabilities are given by the following expression, where n denotes the number of selected jets in the event:

$$P(n_{\text{b-tags}}|n) = \begin{cases} \prod_{j=1}^{n}(1-\epsilon_j\,SF_j) & \text{for } n_{\text{b-jets}} = 0 \\ \sum_{j=1}^{n}\epsilon_j\,SF_j\prod_{k\neq j}^{n}(1-\epsilon_k\,SF_k) & \text{for } n_{\text{b-jets}} = 1 \\ \sum_{j=1}^{n-1}\sum_{k>j}^{n}\epsilon_j\,SF_j\epsilon_k\,SF_k\prod_{l\neq j,k}^{n}(1-\epsilon_l\,SF_l) & \text{for } n_{\text{b-jets}} = 2 \\ 1-P(0|n)-P(1|n)-P(2|n) & \text{for } n_{\text{b-jets}} \geqq 3 \end{cases} \tag{6.1}$$

Scale factors on the selection efficiency of simulated events are then applied in terms of probability weights. Instead of requiring simulated events to contain a certain number of b-tagged jets, simulated events are weighted by the corresponding probability. In contrast to other possible implementations of the scale factors, this weighting procedure has the advantage that no simulated event is rejected. Hence, the statistical uncertainty on the number of events predicted by the event simulation is lower as in the case where cuts on the b-jet multiplicity are applied. The weighting procedure is checked by comparing the b-jet multiplicity distribution of simulated events that pass the jet selection with the distribution of their probability weights. For this purpose, all scale factors are set to one and no cross section and pile-up weighting is applied. In Fig. 6.11, this comparison is illustrated for simulated $t\bar{t}+\text{Jets}$ events. As can be seen, in both the muon and the electron channel the b-jet multiplicity distribution of events is very well reproduced by the weighting technique. This does also apply for simulated W+Jets events (cf. Appendix C.2, Figs. C.4(a), C.4(b)). In general, for samples with large statistics this is expected to be the case. For samples with low statistics discrepancies may arise from the fact that the distributions are predicted based on different numbers of simulated events. For this reason, the b-jet multiplicity distribution of simulated single top events and the distribution of their probability weights slightly differ from each other (cf. Figs. C.4(c), C.4(d)). Due to the small number of non-weighted simulated $Z/\gamma^*+\text{Jets}$ and QCD events that pass the jet selection, proper tagging efficiencies cannot be determined in this case. These events are weighted based on the efficiencies obtained from simulated W+Jets events (cf. Figs. C.5), which involve a similar topology as $Z/\gamma^*+\text{Jets}$ events. All simulated signal events are weighted based on the tagging efficiencies obtained from simulated $t\bar{t}+\text{Jets}$ events. By this, the b-jet multiplicity distributions of events in the LM6 and the LM8 benchmark scenario are well reproduced (cf. Fig. C.6).

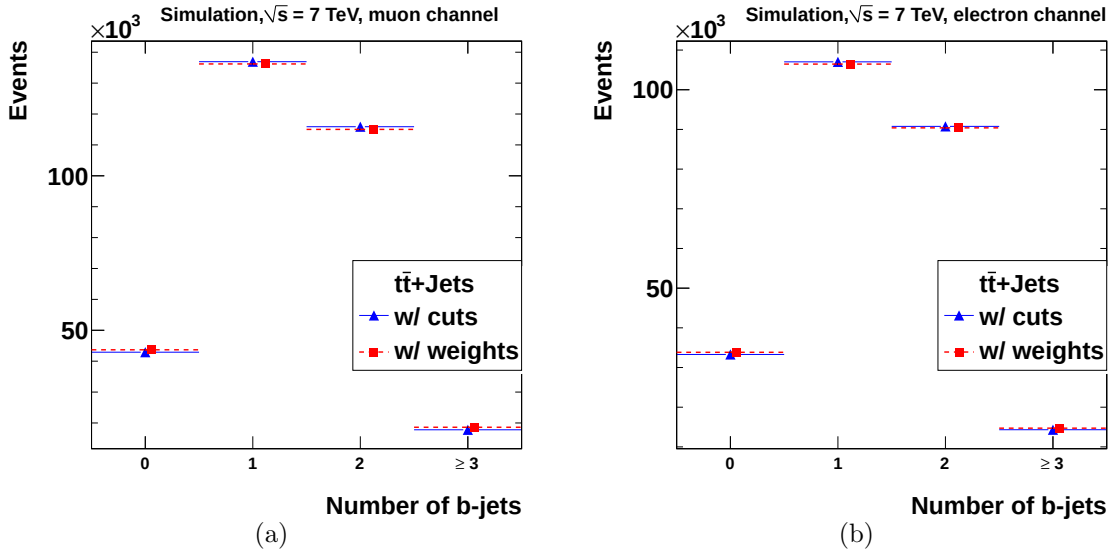

Figure 6.11.: Number of b-jets in simulated $t\bar{t}$ events that pass the jet selection in the muon (a) and the electron channel (b). The distributions obtained when applying weights are represented by the red markers, those obtained when applying cuts are indicated by the blue markers. For better visibility, the markers are slightly shifted from one another in x direction. All scale factors are set to one and no cross section and pile-up weighting is applied.

In Fig. 6.12, the b-jet multiplicity distributions of simulated Standard Model events (a), probability weights (b), and data events after the jet selection are shown. In the case of probability weights, b-tag efficiency and mistag-rate scale factors are applied. In the following, the application of b-tag requirements on simulated events always implies the usage of these weights. As can be seen, the data are slightly better described when applying the scale factors. Since the probability weights sum up to one for each event, the overall data-to-simulation ratio of 0.97 stays the same.

B-Jet Selection

While the direct pair production of top squarks is expected to result in states with two b-quarks, the direct pair production of bottom squarks and the gluino-induced production of third-generation squarks may also result in state that include four bottom quarks (cf. 2.2.3.4). Consequently, the search is done in two different bins of the b-jet multiplicity. However, since the b-tag efficiency ranges from about 60% to 80%, the multiplicity of b-jets is lower than that of b-quarks. The search is therefore done in the inclusive 1-b-tag channel and the inclusive 3-b-tag channel, where events are required to contain at least one b-jet and at least three b-jets, respectively.

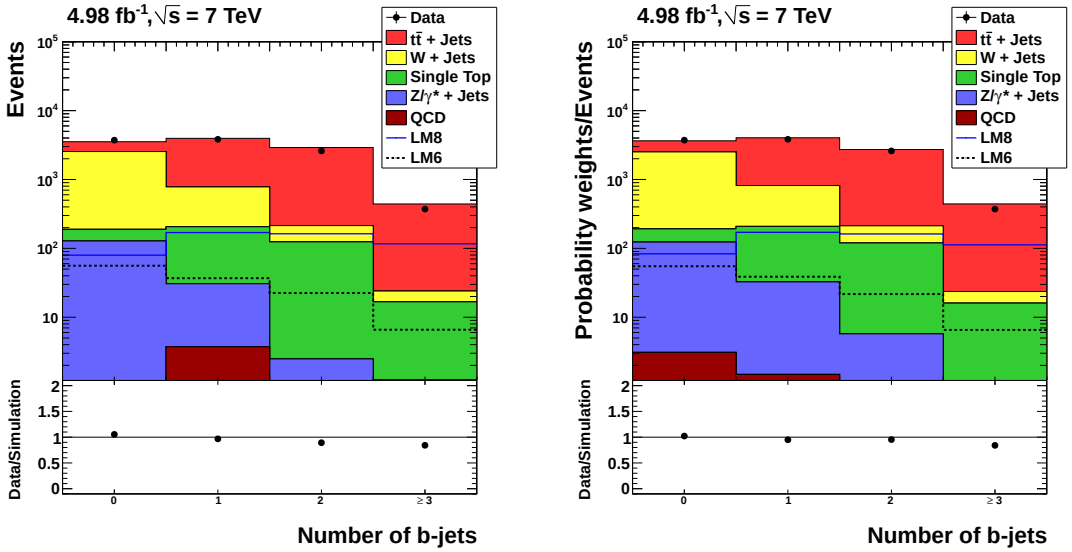

(a) (b)

Figure 6.12.: B-jet multiplicity distributions of simulated events (a), probability weights (b), and data after the jet selection. In the case of probability weights, b-tag efficiency and mistag-rate scale factors are applied.

6.5. Selected Events

In Table 6.2 the numbers of selected data and simulated Standard Model events and the corresponding data-to-simulation ratios after the successively applied event selection steps are shown. Results in the inclusive 2-b-tag channel are shown for comparison as well. Unless stated differently, the uncertainties given in this section are only statistical. As can be seen, the number of selected data events is always lower than the number of simulated events.

Table 6.2.: Numbers of data and simulated Standard Model events after the successively applied event selection steps. Uncertainties are only statistical.

Selection	Data	All SM	Data/All SM
preselection	26571 ± 167	28071 ± 105	0.95 ± 0.01
jet selection	10525 ± 105	10845 ± 22	0.97 ± 0.01
$\geqq 1$ b-tag	6800 ± 84	7200 ± 12	0.94 ± 0.02
$\geqq 2$ b-tags	2970 ± 56	3166 ± 6	0.94 ± 0.02
$\geqq 3$ b-tags	372 ± 20	442 ± 1	0.84 ± 0.06

However, except for the inclusive 3-b-tag channel, all data-to-simulation ratios are compatible with each other within the statistical uncertainties and close to a value of one. Only in the inclusive 3-b-tag channel the number of simulated events significantly differs from the number of data events. Comparing the data-to-simulation ratios for the individual lepton channels with each other (cf. Appendix C.3, Tables C.1 and C.2) it is found that the discrepancy in the 3-b-tag channel is more present in the electron channel. After the event selection with the requirement of at least three b-jets the data-to-simulation ratio amounts to 0.87 ± 0.06 in the muon channel and 0.81 ± 0.07 in the electron channel.

In Table 6.3, the numbers of simulated Standard Model events are given separately for the individual processes. As discussed in Section 6.2.4, the background from QCD multijet events is already significantly suppressed by the event preselection. Also the background from $Z/\gamma^* + \text{Jets}$ events is strongly reduced at this stage. The largest contributions to the Standard Model background after the preselection originate from W+Jets events (57%) and $t\bar{t} + \text{Jets}$ events (36%). By selecting events with at least four jets, the background from W+Jets events and the remaining background from $Z/\gamma^* + \text{Jets}$ events are reduced by factors of about five and four, respectively. Since the decay of a $t\bar{t}$ pair in the semileptonic decay channel already implies the production of at least four hard quarks, the background from $t\bar{t} + \text{Jets}$ events is only slightly affected by the jet selection. The background from single top events, where at least two hard quarks can be expected to be produced, is reduced by a factor of 2.3. By requiring at least one b-tagged jet, all backgrounds that do not include a top quark are reduced by a factor of about four. The largest contributions to the Standard Model background in the 1-b-tag channel originate from $t\bar{t} + \text{Jets}$ events (85%) and W+Jets events (10%). In the 3-b-tag channel the contribution from $t\bar{t} + \text{Jets}$ events even amounts to 95%. Among the simulated $t\bar{t} + \text{Jets}$ events by far the largest contribution comes from events that contain a semileptonically decaying $t\bar{t}$ pair with a muon or electron in the final state (cf. Appendix C.3, Table C.3).

Table 6.3.: Numbers of simulated Standard Model events for the individual processes after the successively applied event selection steps. Only statistical uncertainties are shown.

Selection	$t\bar{t}$+Jets	Single Top	W+Jets	$Z/\gamma^* + \text{Jets}$	QCD
preselection	10234	853	16135	637	211
jet selection	7280	374	3028	157	4.8
$\geqq 1$ b-tags	6147	305	709	37	1.7
$\geqq 2$ b-tags	2930	129	100	6.1	0.2
$\geqq 3$ b-tags	418	16	7.6	0.5	< 0.1

Further contributions originate from semileptonic $t\bar{t}$ decays with a leptonically decaying τ and dileptonic $t\bar{t}$ decays where one lepton does not pass the muon and electron veto criteria. The largest contribution to the background from single top events originates from the production in association with a W boson (cf. Appendix C.3, Table C.5). The contributions from $Z/\gamma^* + \text{Jets}$ production, QCD multijet production, $t\bar{t}$ pair production in the fullhadronic decay channel, and single top $+ b$ production (s-channel) together amount 0.7% in the inclusive 1-b-tag channel and 0.2% in the inclusive 3-b-tag channel. These processes are therefore not explicitly considered in the following.

In Table 6.4 the numbers of simulated signal events in the SUSY benchmark scenarios LM8 and LM6 and the resulting signal-to-background ratios are shown. Within the given precision of three digits after the decimal point the statistical uncertainties on the ratios are mostly zero and therefore not given. After the preselection the signal-to-background ratio in scenario LM8 is 2.3 times larger than the ratio in scenario LM6, which roughly reflects the different cross sections for sparticle production (cf. Section 4.3.2). By the successively applied selection requirements on the jet multiplicity and the b-jet multiplicity the signal-to-background ratio in scenario LM8 continually increases, while the ratio in scenario LM6 roughly stays the same. This is mainly due to the different mass hierarchies. As addressed above in Section 6.2.4, the decay of sparticles in scenario LM6 ($m_{\tilde{t}}, m_{\tilde{b}} < m_{\tilde{q}} < m_{\tilde{g}}$) on average results in states with lower jet and b-jet multiplicities as in scenario LM8 ($m_{\tilde{t}}, m_{\tilde{b}} < m_{\tilde{g}} < m_{\tilde{q}}$). Some effect, which is however beyond the scope of this thesis, might also result from the performance of the jet algorithm. Jets that originate from the decay of a high-energetic W boson or top quark may overlap and be clustered as one jet by the anti-k_T algorithm. If such effects do contribute, they will be more present in scenario LM6, where W bosons and top quarks can be expected to be produced with larger momenta than in scenario LM8.

Table 6.4.: Numbers of simulated signal events in the SUSY benchmark scenarios LM8 and LM6 and the resulting signal-to-background ratios.

Selection	LM8	LM6	LM8/All SM	LM6/All SM
preselection	603	260	0.021	0.009
jet selection	529	122	0.049	0.011
$\geqq 1$ b-tags	445	67	0.062	0.009
$\geqq 2$ b-tags	274	28	0.087	0.009
$\geqq 3$ b-tags	112	6.5	0.254	0.015

With respect to the total inelastic cross section of $\sigma = 73.5 \pm 1.6\,\text{mb}$ [139], the SM background is reduced by a factor of approximately $5 \cdot 10^{10}$ with the event

selection in the inclusive 1-b-tag channel and a factor of about $8 \cdot 10^{11}$ with the event selection in the inclusive 3-b-tag channel. Based on this a possible deviation from the Standard Model prediction that originates from Supersymmetry with light top and bottom squarks can be searched for. In the following the distributions of variables that are sensitive to such a deviation are presented. This is always done for the inclusive 1-b-tag channel and the inclusive 3-b-tag channel. The distributions for the inclusive 0-b-tag channel and the inclusive 2-b-tag channel are shown for comparison in Appendix C.1.

Hadronic Variables

In Figs. 6.13 and 6.14, the H_{T} and the jet multiplicity distributions are shown. In the 1-b-tag channel the selected data are basically similarly well described as after the event preselection (cf. Section 6.2.4, Fig. 6.4): While the data-to-simulation ratio shows a slope for H_{T}, it drops off for the jet multiplicity at $n_{\mathrm{Jets}} = 8$. The data-to-simulation ratio for the jet multiplicity in the 3-b-tag channel shows an overall offset with respect to the ratio in the 1-b-tag channel. This suggests that the observed lower data-to-simulation ratio at $n_{\text{b-jets}} = 3$ (cf. Table 6.2) is not associated with the modeling of the jet multiplicity.

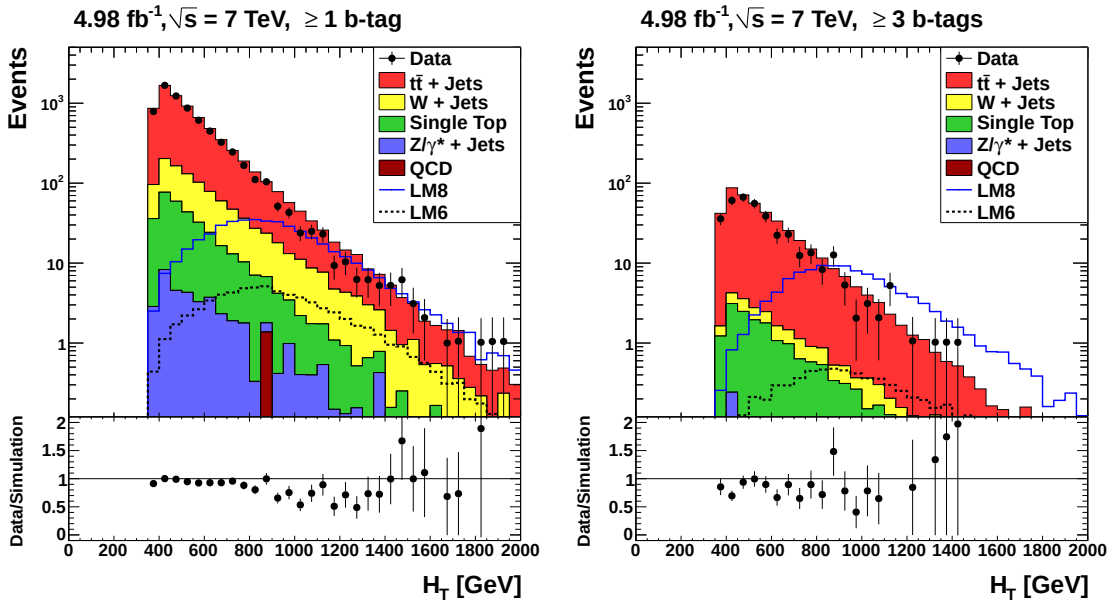

(a) (b)

Figure 6.13.: H_{T} after the event selection with the requirement of at least one b-jet (a) and at least three b-jets (b).

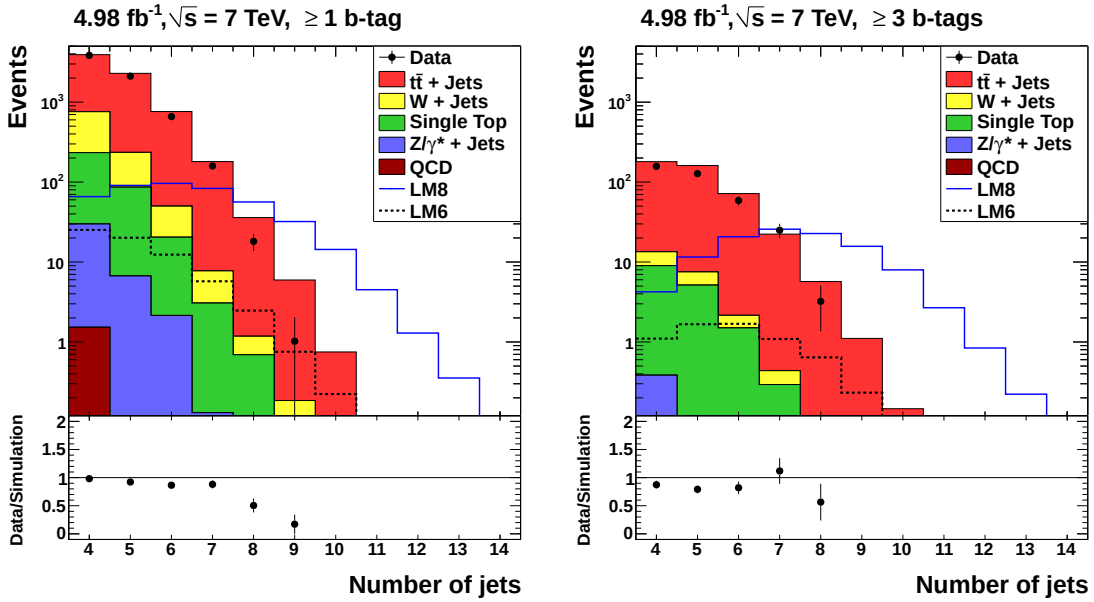

(a) (b)

Figure 6.14.: Number of selected jets after the event selection with the requirement of at least one b-jet (a) and at least three b-jets (b).

$\not\!\!E_T$ and Y_{MET}

In Fig. 6.13 the missing transverse energy after the event selection in the inclusive 1-b-tag channel and the inclusive 3-b-tag channel is shown. In both b-tag channels a clear trend of the simulation overshooting the data is present. The sensitivity of $\not\!\!E_T$ to a possible signal from Supersymmetry is - first of all - associated with two assumptions, both of which are well motivated, though not intrinsic features of Supersymmetry: the assumption of R parity conservation and the assumption of sparticles being heavier than their SM superpartners. Assuming R parity to be conserved, two lightest supersymmetric particles escape detection. Assuming sparticles to be produced at larger energy scales, their decay products (including the two stable LSPs and potentially produced neutrinos) are likely to carry larger transverse momenta.[7] However, as discussed in Section 6.2.4, the amount of missing transverse energy also depends on the mass hierarchy of sparticles. Depending on the specific scenario by which Supersymmetry is broken, the amount of $\not\!\!E_T$ relative to the energy scale at which sparticles are produced will be smaller or larger. A variable that relates the amount of missing transverse energy to the energy scale is $Y_{MET} \equiv \not\!\!E_T/\sqrt{H_T}$. The distribution of this variable is shown in Fig. 6.16.

[7] For this reason the decay of sparticles can - first of all - also be expected to result in states with a larger hadronic activity than the decay of SM particles.

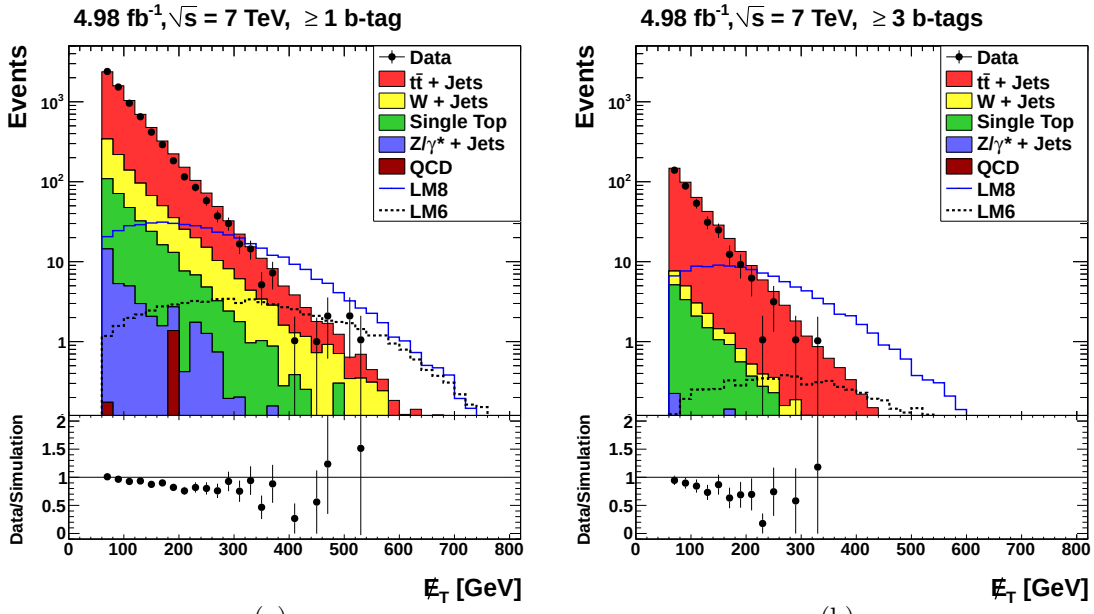

(a) (b)

Figure 6.15.: $\not\!\!E_{\mathrm{T}}$ after the event selection with the requirement of at least one b-jet (a) and at least three b-jets (b).

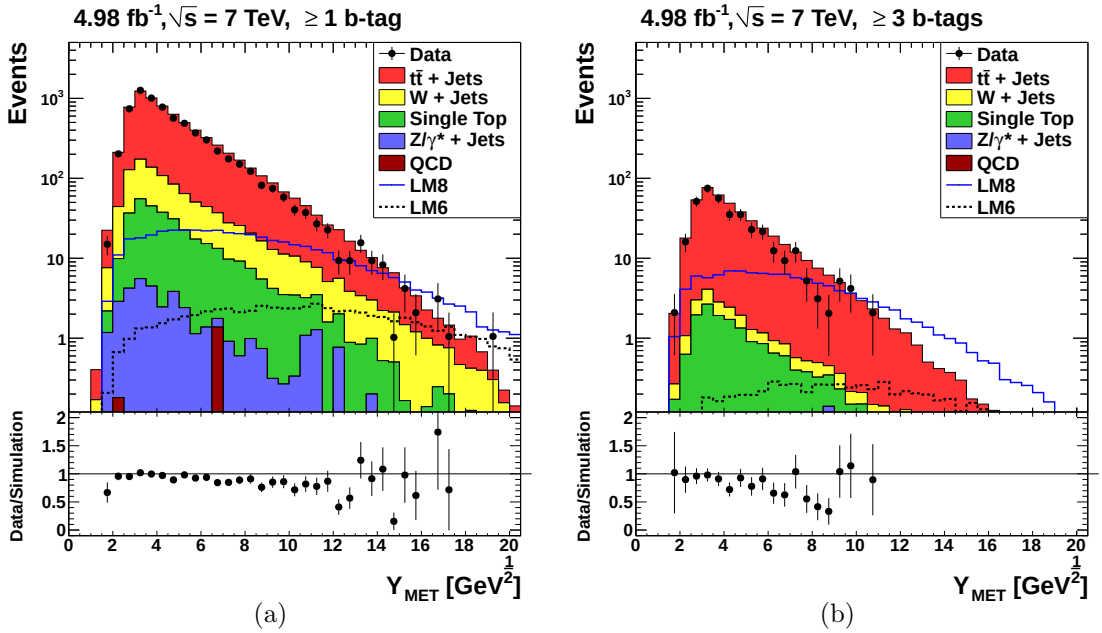

(a) (b)

Figure 6.16.: Y_{MET} after the event selection with the requirement of at least one b-jet (a) and at least three b-jets (b).

In general, Y_{MET} yields additional sensitivity to supersymmetric scenarios that are associated with comparatively short decay cascades and/or large mass differences between the initially produced sparticles and the LSP.

Transverse W-Boson Mass

In Fig. 6.17 the transverse W-boson mass

$$m_T \equiv \sqrt{p_{\mathrm{T}}^{\mathrm{lepton}} \not{E}_{\mathrm{T}} \left(1 - \cos\phi\right)},$$

where ϕ denotes the angle between the lepton p_{T} vector and the $\not{E}_{\mathrm{T}}$ vector, is shown. Within the statistical uncertainties the distribution of data is well described by simulated events in both b-tag channels. The sensitivity of m_T to a possible signal from R-parity conserving Supersymmetry originates from the correlation between the charged lepton and the antineutrino that are produced in a leptonic W-boson decay. The invariant mass calculated from their transverse momentum vectors is always smaller than or equal to the W-boson mass. At generator level the corresponding distribution therefore shows a kinematic edge at the W mass. In single-lepton searches the missing transverse energy in background events mainly originates from a neutrino that is produced along with the single lepton in a leptonic W-boson decay.

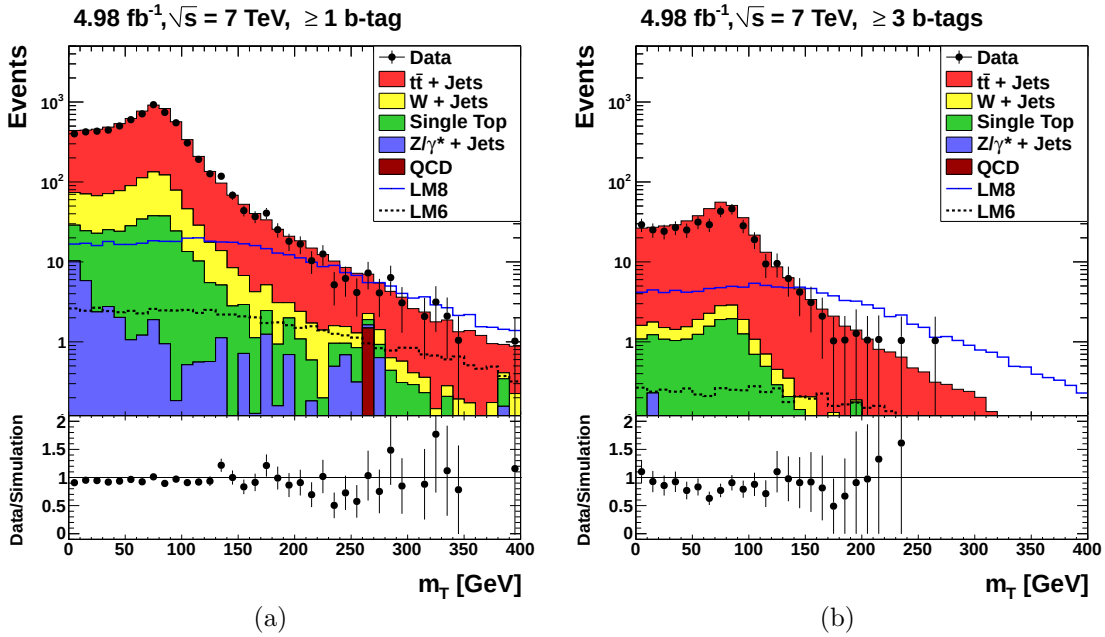

(a) (b)

Figure 6.17.: Transverse W-boson mass after the event selection with the requirement of at least one b-jet (a) and at least three b-jets (b).

At the level of reconstructed objects, the m_T distribution of background events therefore shows a similar decrease at $m_T = m_W$. As can be seen in Fig. 6.17, this edge is smeared, which has mainly two reasons: First, due to the limited energy resolution of the detector the missing transverse energy is only a rough measure for the neutrino transverse momentum. Secondly, some events that contain two leptonically decaying W bosons pass the event selection. These are mostly dileptonic $t\bar{t}+$ Jets events where one lepton does not fulfill the muon and electron veto criteria. In these events $\not\!\!E_{\mathrm{T}}$ does not reflect the momentum of the neutrino that is produced along with the single lepton.

In signal events almost no correlation between the single lepton and $\not\!\!E_{\mathrm{T}}$ is present, because the missing transverse energy mainly results from the two stable LSPs. As can be seen in Fig. 6.17, in the range between 0 GeV and 150 GeV the m_T distributions of signal events are almost flat. At $m_T = 150$ GeV, the distributions start to slightly decrease. Consequently the signal-to-background ratio can be increased by a requirement on the transverse W-boson mass. By an additional requirement on $m_T > 120$ GeV the signal-to-background ratios in the considered b-tag channels can be increased by a factor of about six in scenario LM8 and a factor of about seven in scenario LM6 (cf. Appendix C.3, Table C.5). However, within this search a signal region defined by the requirements of a large H_{T} and a large Y_{MET} is exploited. As discussed later in Section 7, in order to predict the background in this region from data, it is essential to have enough events in control regions at low H_{T} and Y_{MET}. By requiring m_T to be larger than 120 GeV, the total number of selected events (cf. Table C.6) is by far too low.

7. Background Prediction From Data

By selecting events with a single isolated lepton, four jets, $H_{\mathrm{T}} > 375\,\mathrm{GeV}$, and $\not\!\!E_{\mathrm{T}} > 60\,\mathrm{GeV}$, the Standard Model background is reduced by a factor of approximately $5 \cdot 10^{10}$ in the inclusive 1-b-tag channel and a factor of about $9 \cdot 10^{11}$ in the inclusive 3-b-tag channel. Based on this, a possible deviation from the Standard Model prediction that originates from Supersymmetry with light top and bottom squarks can be searched for. Variables that are sensitive to such a deviation have been presented in Section 6.5. In general, the sensitivity of such variables is associated with two distinct aspects: the different energy scales at which the Standard Model particles and their superpartners are produced, and the different event topologies, which mainly result from different mass hierarchies and the assumption of R-parity conservation. Somewhat surprisingly, the only intrinsic difference between the Standard Model particles and their superpartners, the difference in spin, does not seem to yield any remarkable sensitivity at this stage of searches.[1]

In order to identify a possible signal, a precise prediction of the Standard Model background is desirable. As discussed in Section 6, especially in those regions of the phase space where the addressed variables are most sensitive, a reliable prediction from simulated events is subtle. Additionally, the measurement is strongly affected by experimental uncertainties in these regions. Most searches therefore aim to predict the distribution of Standard Model events from background dominated control regions or control samples that are obtained from data. This is often done by inverting an event selection criterion that is assumed not to affect the kinematics or topology of background events much. In some searches a control sample is obtained by combining observables of different events in order to break a correlation that is assumed to be present in signal events, but absent in background events. Usually, the assumptions such a data-driven method is based on are justified by studies in simulated events. At first glance, it might therefore seem that the precision of the Standard Model prediction or the measurement cannot be improved. However, a key point here is that these methods do not need to be fully data-driven in the sense that they are evident from first principles. It is sufficient to show that theoretical and experimental systematic uncertainties cancel to a certain extent. Applying a data-driven method, one might conclude: "We still do not know, if the simulated events predict the background correctly, but we can show that our method (to this or that extent) is robust against a possible mismodeling and mismeasurements."

[1] Variables that are sensitive to the spin of sparticles will rather become important within the effort of model discrimination after a possible discovery of new physics.

Within the search presented in this thesis, a factorization method with H_{T} and $Y_{\mathrm{MET}} \equiv \not{E}_{\mathrm{T}}/\sqrt{H_{\mathrm{T}}}$ is applied. In simulated Standard Model events, these variables are found to be largely uncorrelated. This suggests to predict the Standard Model background in a potentially signal-enhanced region at large H_{T} and Y_{MET} from three background dominated control regions defined by low values of H_{T} and/or Y_{MET}. The advantage of such a method is that both the theoretical and the experimental systematic uncertainties may cancel to a large extent. In Section 7.1, the factorization method is described, control and signal regions are defined, and the distributions of signal and background events in these regions are discussed. The factorization method with H_{T} and Y_{MET} is often motivated by the assumption that $\sqrt{H_{\mathrm{T}}}$ is proportional to the missing transverse energy from jet energy mismeasurements. It is argued that such a correlation can be expected because the energy resolution of the calorimeter is dominated by a term that is proportional to $\sqrt{E}$ (cf. Section 3.2). However, already in all-hadronic searches it is not clear why such a correlation between H_{T} and $\not{E}_{\mathrm{T}}$ should be expected.[2] In single-lepton searches, in addition, at least some amount of missing transverse energy will result from the transverse momentum of a neutrino that is produced along with a charged lepton in a W-boson decay. In order to understand, why H_{T} and Y_{MET} appear uncorrelated to a large extent, the dependence of $\not{E}_{\mathrm{T}}$ on H_{T} is studied in simulated events. In Section 7.2 this is done in detail for events that contain a semileptonically decaying $t\bar{t}$ pair with a muon or electron in the final state. These events constitute the largest background after the event selection with at least one b-jet (68%) and at least three b-jets (77%). Based on this, the background from other relevant Standard Model processes is addressed in Section 7.3.

It should be noted that the studies presented in this chapter do not aim for a perfect decorrelation of H_{T} and $\not{E}_{\mathrm{T}}$. On their own, they also cannot justify the assumption that a certain correlation between H_{T} and Y_{MET} is present in data. The purpose of this chapter is to illustrate the method, to understand why a certain correlation is present in simulated events, and to hint at the relevant uncertainties by this. Confidence in the applicability of the method is obtained from the cancellation of theoretical and experimental uncertainties, as discussed later in Section 8. To some extent also the exclusive 0-b-tag channel can be exploited to cross check the correlation between H_{T} and Y_{MET} in data.

[2] In general, the triangular inequality $\sqrt{H_{\mathrm{T}}} \leqq \sum_j \sqrt{p_{T_j}}$, where j runs over all selected jets, holds. Except for events that only contain one selected jet and QCD dijet events, a given H_{T} can be composed of jet transverse momenta in different ways, each of which is associated with a different amount of jet energy mismeasurement as quantified by the expression on the right side of the inequality. Hence, the correlation between H_{T} and the missing transverse energy from jet energy mismeasurements can be expected to depend on the event topology. In addition, by clustering jets from particle-flow candidates, the jet energy resolution also depends on the track-p_{T} resolution of charged hadrons, which is proportional to p_T (see also Section 5.5).

7.1. Factorization Method with H_{T} and Y_{MET}

In simulated Standard Model events H_{T} and $Y_{\mathrm{MET}} \equiv \not{E}_{\mathrm{T}}/\sqrt{H_{\mathrm{T}}}$ are found to be largely uncorrelated. To illustrate this, in Fig. 7.1 the H_{T} distributions of events that pass the event selection in the 1-b-tag channel and the 3-b-tag channel, respectively, are shown in exclusive bins of Y_{MET}.

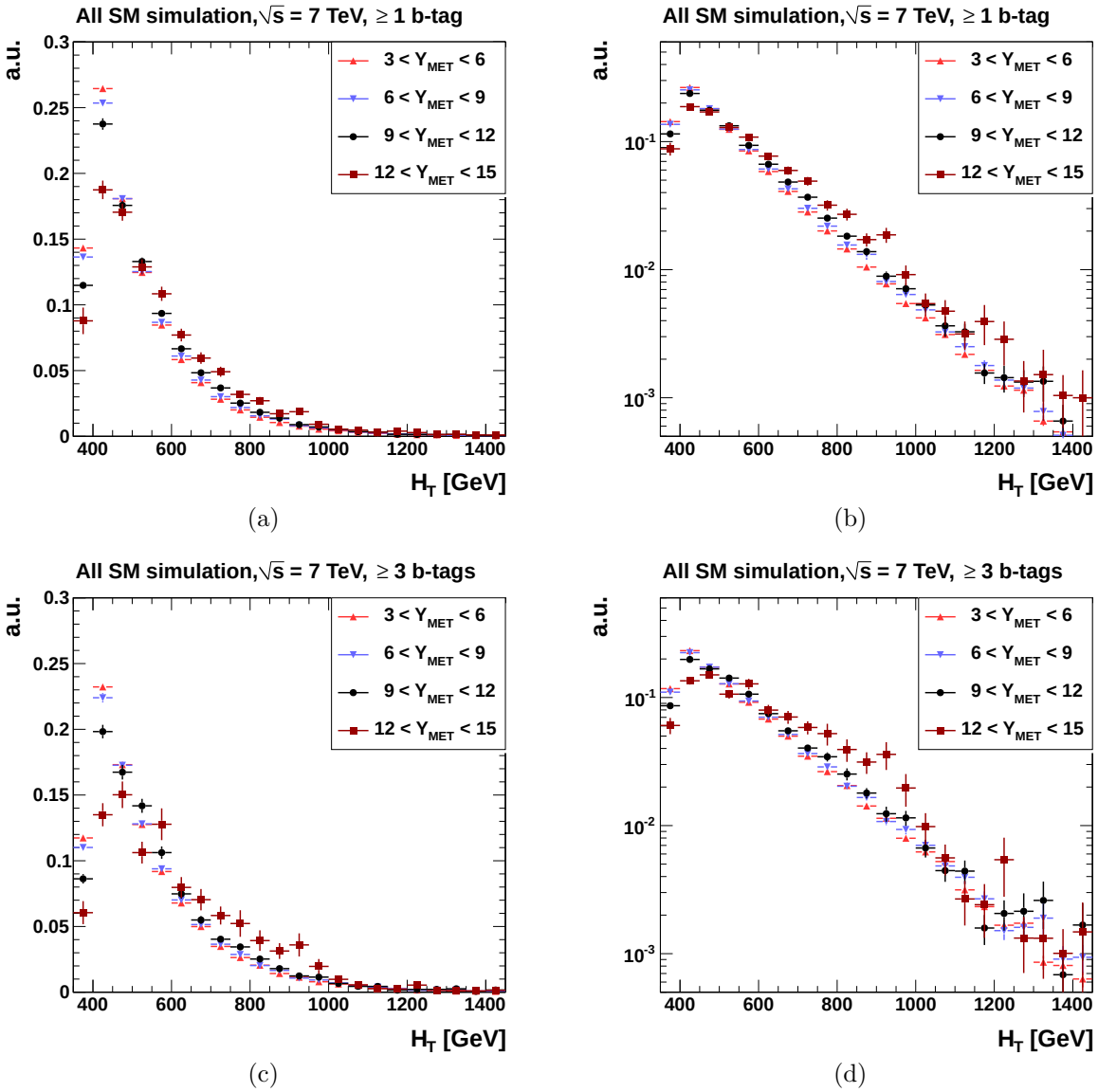

Figure 7.1.: H_{T} of simulated Standard Model events after the event selection with the requirement of at least one b-jet (top) and at least three b-jets (bottom) in exclusive bins of Y_{MET}. All distributions are normalized to unit area in the region of $H_{\mathrm{T}} > 375$ GeV. The histograms are shown once on a linear scale (left) and once on a logarithmic scale (right).

In order to compare their shapes, the distributions are normalized to unit area in the region of $H_{\mathrm{T}} > 375$ GeV. For better visibility, the histograms are shown once on a linear scale and once on a logarithmic scale. As can be seen in Fig. 7.1, in both b-tag channels the exponential behavior of the H_{T} distribution is basically independent of the Y_{MET} requirement. Only in the first bins of H_{T}, the distributions significantly differ from each other. Here, the entries that correspond to lower Y_{MET} requirements clearly lie above those that comprise events with larger Y_{MET}. Since these differences affect the normalization at larger values of H_{T} it seems that the overall steepness of the exponential decay slightly decreases with Y_{MET}. However, when normalizing the distributions to the same area in the region of $H_{\mathrm{T}} > 500$ GeV, it becomes visible that in this region the distributions that correspond to Y_{MET} requirements between 3 $\mathrm{GeV}^{\frac{1}{2}}$ and 12 $\mathrm{GeV}^{\frac{1}{2}}$ show the same exponential decrease (cf. Appendix D.1, Figs. D.3(a) and D.3(b)). Normalizing the distributions in the region of $H_{\mathrm{T}} > 600$ GeV, in the 1-b-tag channel all distributions show the same decrease in this region (cf. Fig. D.3(c)). At further increased H_{T} this seems to apply for the 3-btag channel as well (cf. Fig. D.3(f)). Due to the limited number of simulated events one cannot be sure in this case. The differences at low values of H_{T} mainly result from requiring events to contain a minimal number of selected jets. Since the latter is correlated with the number of b-tagged jets, these differences are more present in the 3-b-tag channel, as will be discussed in detail in Section 7.2.

Within the chosen binning (21 bins in H_{T}, four bins in Y_{MET}) and axis ranges (375 GeV $< H_{\mathrm{T}} <$ 1400 GeV, 3 $\mathrm{GeV}^{\frac{1}{2}} < Y_{\mathrm{MET}} <$ 15 $\mathrm{GeV}^{\frac{1}{2}}$), the distributions in Figs. 7.1(b) and 7.1(d) contain all information about the correlation. Within a given Y_{MET} bin the correlation between H_{T} and Y_{MET} could in principle be different. However, if this was the case, all differences from the correlation found in the distributions shown in Fig. 7.1 would have to cancel each other. For example, if the H_{T} distribution of events with 6 $\mathrm{GeV}^{\frac{1}{2}} < Y_{\mathrm{MET}} <$ 7.5 $\mathrm{GeV}^{\frac{1}{2}}$ showed a steeper decrease than the H_{T} distribution of events with 6 $\mathrm{GeV}^{\frac{1}{2}} < Y_{\mathrm{MET}} <$ 9 $\mathrm{GeV}^{\frac{1}{2}}$, these discrepancies needed to be canceled by the contribution from events with 7.5 $\mathrm{GeV}^{\frac{1}{2}} < Y_{\mathrm{MET}} <$ 9 $\mathrm{GeV}^{\frac{1}{2}}$. The distribution of the latter needed to be much flatter than the one of events with 6 $\mathrm{GeV}^{\frac{1}{2}} < Y_{\mathrm{MET}} <$ 7.5 $\mathrm{GeV}^{\frac{1}{2}}$. Though in principle possible, there is no physical reason to expect such a discontinuity. Nevertheless, in order to get confidence about this, but also to further illustrate the correlation, Y_{MET} is shown in exclusive bins of H_{T} in Fig. 7.2. Here, all distributions are normalized to unit area in the range of $Y_{\mathrm{MET}} > 3$ $\mathrm{GeV}^{\frac{1}{2}}$. The above-mentioned differences at low values of H_{T} show up as discrepancies between the Y_{MET} distribution of events with 375 GeV $< H_{\mathrm{T}} <$ 650 GeV and the other distributions. As can be seen in Figs. 7.2(a) and 7.2(c), in the first three bins of Y_{MET} this distribution lies above the other distributions. At large Y_{MET} the distribution of events with 375 GeV $< H_{\mathrm{T}} <$ 650 GeV shows a more steeper decrease than the other distributions.

Apart from this, no significant difference is visible. In the following, the illustration chosen in Fig. 7.1 is preferred to the one exploited in Fig. 7.2.

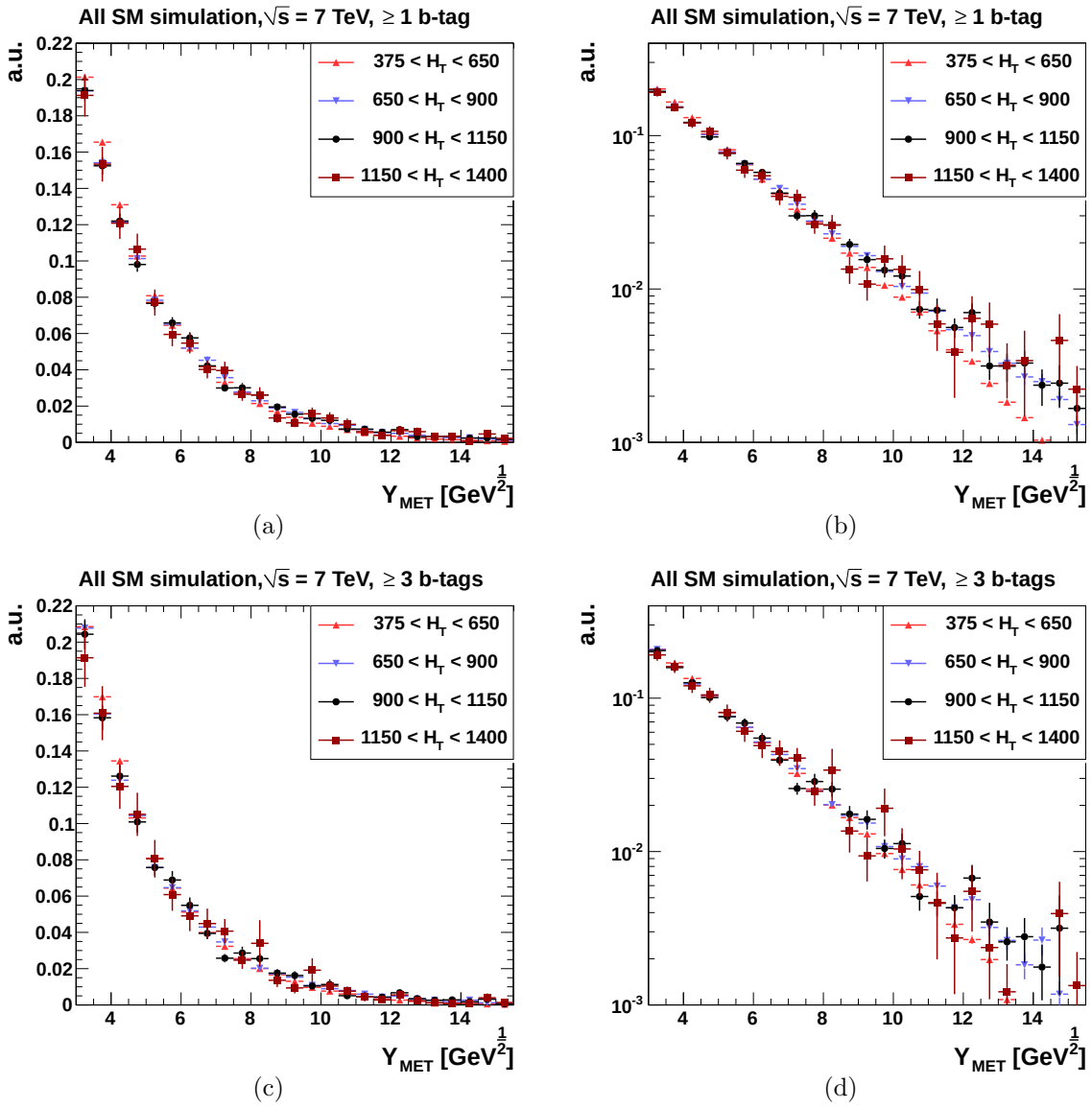

Figure 7.2.: Y_{MET} of simulated Standard Model events after the event selection with the requirement of at least one b-jet (top) and at least three b-jets (bottom) in exclusive bins of H_{T}. All distributions are normalized to unit area in the region of $Y_{\mathrm{MET}} > 3$ GeV$^{\frac{1}{2}}$. The histograms are shown once on a linear scale (left) and once on a logarithmic scale (right).

7.1.1. Factorization Ansatz

As discussed in Section 6.5, both variables H_{T} and Y_{MET} discriminate between the Standard Model background and a potential signal from Supersymmetry with light top and bottom squarks. Mainly due to the larger energy scale, at which sparticles are produced, their decays can be expected to result in states with a larger hadronic activity. Reflecting the different event topologies of signal and background events, which result from different mass hierarchies and the assumption of R-parity conservation, signal events are likely to come along with a more significant amount of missing transverse energy. The fact that H_{T} and Y_{MET} are found to be largely uncorrelated then suggests to predict the background in a potentially signal-enhanced region at large H_{T} and Y_{MET} from control regions with low H_{T} and/or low Y_{MET}. Assuming that the probability distribution of selecting an event with a certain H_{T} and Y_{MET} approximately factorizes in the individual one-dimensional distributions, the ratio of events with low Y_{MET} and events with large Y_{MET} will nearly be independent of H_{T}. (Vice versa, the ratio of events with low H_{T} and events with large H_{T} will nearly be independent of Y_{MET}.) This motivates to define a signal region D, and three background dominated control regions A, B, and C, such that

$$\frac{n_{\mathrm{A}}}{n_{\mathrm{C}}} = \kappa \, \frac{n_{\mathrm{B}}}{n_{\mathrm{D}}} \,, \tag{7.1}$$

where n_{A}, n_{B}, n_{C}, and n_{D} represent the numbers of background events in the regions A, B, C, and D, and κ denotes a factor that accounts for the small correlation between H_{T} and Y_{MET}. If H_{T} and Y_{MET} were perfectly uncorrelated, κ would be one. Within this search, the value of κ is taken taken from simulated events. The uncertainty on the correlation is evaluated as a deviation from that value, which is discussed in Section 8. The factorization ansatz (7.1) allows to predict the number of background events n_{D} in region D from the control regions as

$$n_{\mathrm{D}} = \kappa \, n_{\mathrm{B}} \, \frac{n_{\mathrm{C}}}{n_{\mathrm{A}}} \,. \tag{7.2}$$

The contamination of the control regions A, B, and C by signal events is accounted for when interpreting the obtained results, which is discussed later in Section 9.

7.1.2. Signal and Control Regions

The choice of control and signal regions is optimized balancing two opposing requirements: a small background contribution to the signal region, but nonetheless enough background events in the control regions such that the statistical uncertainties on the background prediction are small. In order to account for the different numbers of selected events in the 1-b-tag channel and the 3-b-tag channel, signal and control regions are optimized individually for each channel. The definitions of the different regions are given in Table 7.1.

Table 7.1.: Definition of control and signal regions A, B, C, and D exploited in the inclusive 1-b-tag channel and the inclusive 3-b-tag channel.

Region	$\geqq 1$ b-tag		$\geqq 3$ b-tags	
	H_{T} [GeV]	Y_{MET} $\left[\mathrm{GeV}^{\frac{1}{2}}\right]$	H_{T} [GeV]	Y_{MET} $\left[\mathrm{GeV}^{\frac{1}{2}}\right]$
A	$375 - 800$	$3.25 - 5.5$	$375 - 600$	$3.25 - 6.5$
B	> 800		> 600	
C	$375 - 800$	> 5.5	$375 - 600$	> 6.5
D	> 800		> 600	

As discussed in Section 6.1, for a requirement on the offline reconstructed missing transverse energy of $\not\!\!E_{\mathrm{T}} > 100$ GeV, the $\not\!\!H_{\mathrm{T}}$ parts of all cross triggers are maximal efficient ($> 99\%$). However, as can be seen in Fig. 7.3, by this requirement (represented by the upper gray lines), many background events in the control regions would be rejected. Therefore, only a requirement of $\not\!\!E_{\mathrm{T}} > 60$ GeV (represented by the lower gray lines) is applied. The discrepancies that result from the trigger inefficiency in the region of 60 GeV $< \not\!\!E_{\mathrm{T}} <$ 100 GeV are corrected for by weighting selected events accordingly (cf. Section 6.2.3). In both b-tag channels the simulated Standard Model events are mainly located in the control regions.

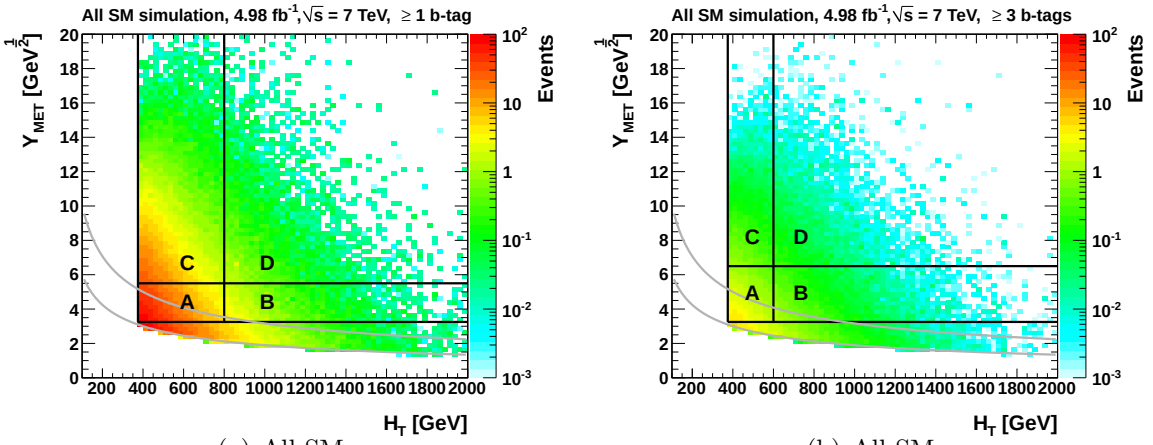

(a) All SM (b) All SM

Figure 7.3.: Distribution of simulated Standard Model events in the H_{T} - Y_{MET} plane after the event selection in the inclusive 1-b-tag channel (a) and the inclusive 3-b-tag channel (b).

In contrast to this, events in the benchmark scenarios LM8 and LM6 are present in all regions, as can be seen in Fig. 7.4. Comparing the distributions of events in the different benchmark scenarios with each other it is found that events in scenario LM6 come along with a larger Y_{MET} than events in scenario LM8 on average, which is due to the different event topologies (cf. Section 6.2.4). Comparing the distributions of signal events in the the different b-tag channels with each other it turns out that events in the inclusive 3-b-tag channel are located at larger values of H_{T} than events in the inclusive 1-b-tag channel. This results from the fact that in the inclusive 3-b-tag channel preferably events with many jets are selected.

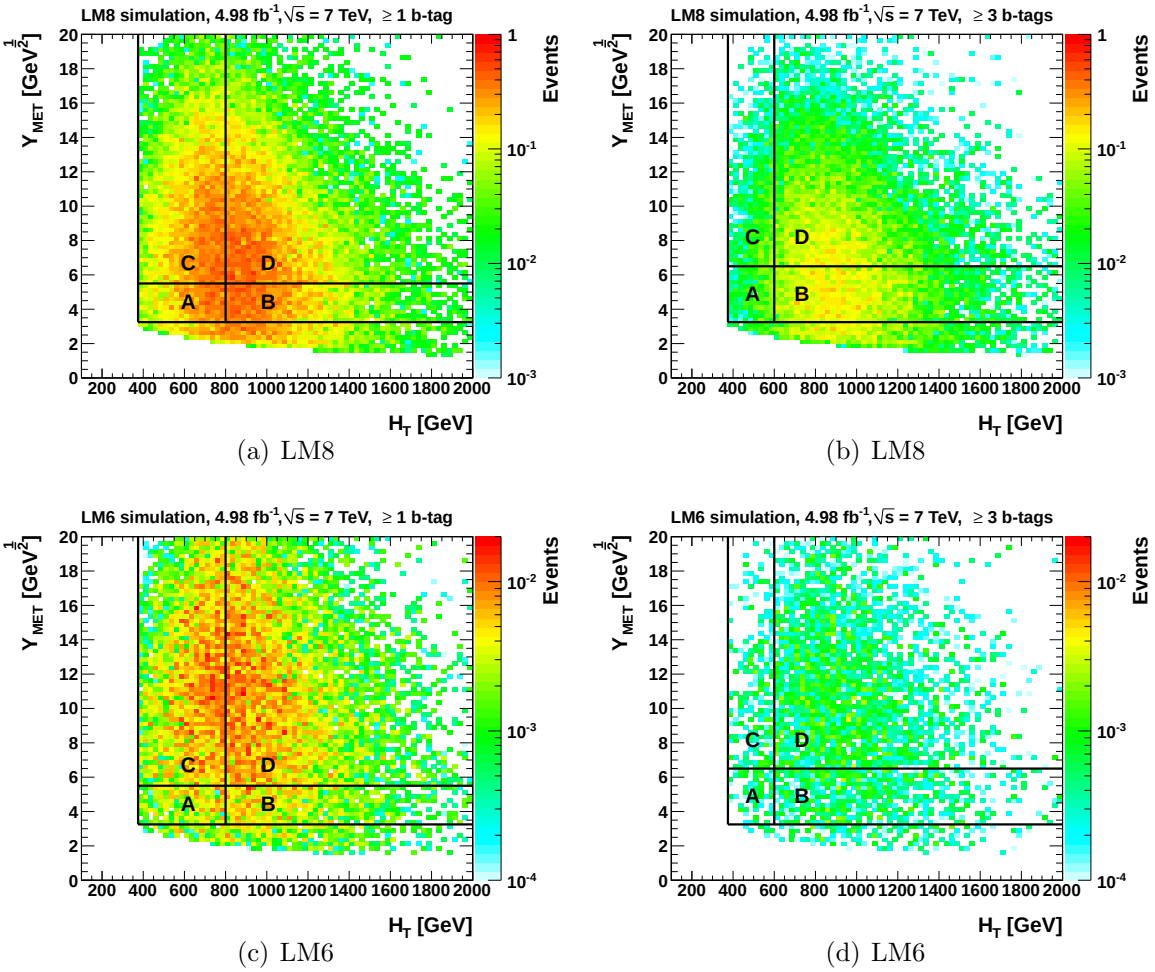

(a) LM8 (b) LM8

(c) LM6 (d) LM6

Figure 7.4.: Distribution of simulated signal events in the benchmark scenario LM8 (top) and LM6 (bottom) in the H_{T} - Y_{MET} plane after the event selection in the inclusive 1-b-tag channel (left) and the inclusive 3-b-tag channel (right). Note the different z-axis ranges.

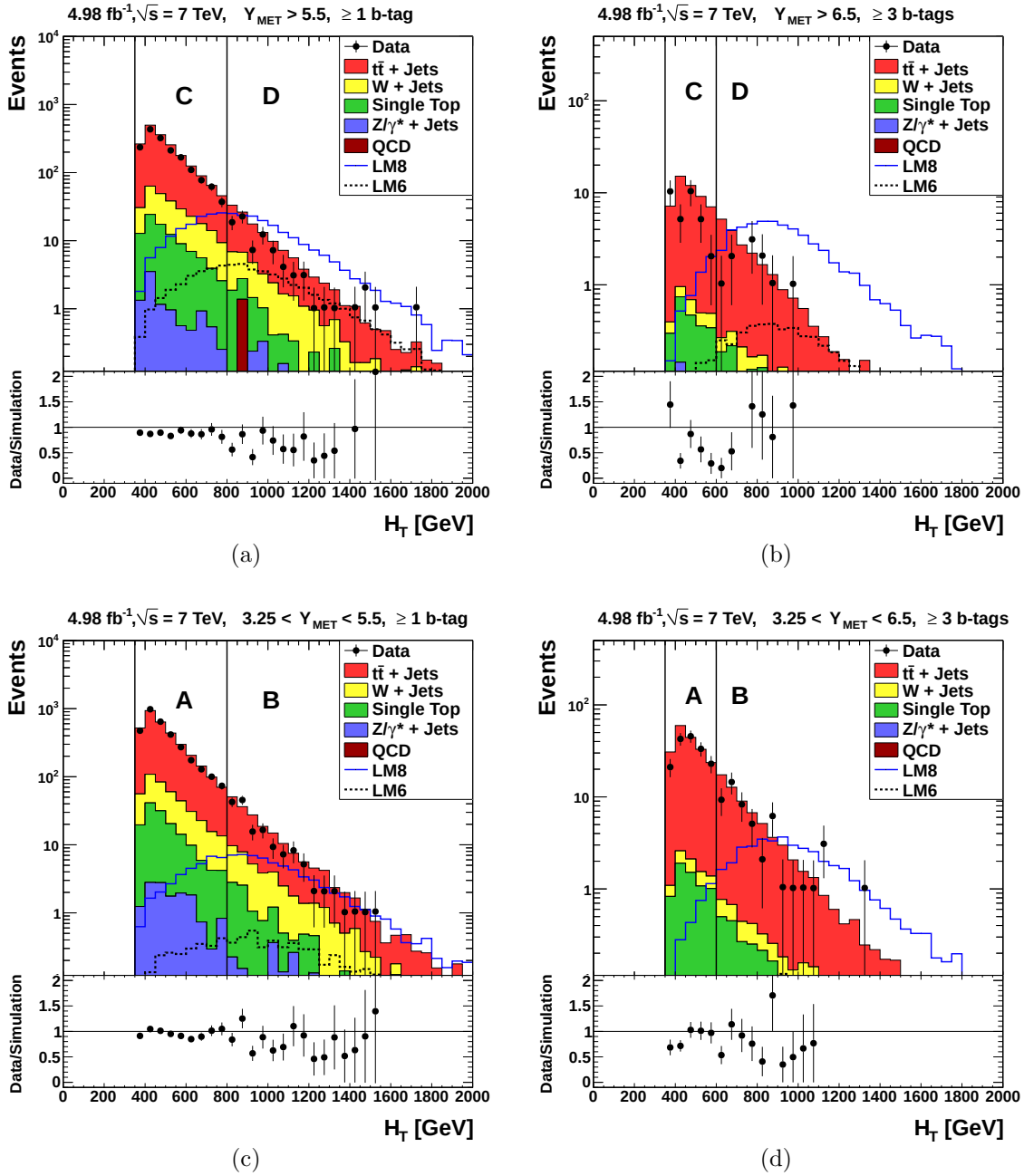

Figure 7.5.: H_T of selected events after the event selection in the inclusive 1-b-tag channel (left) and the inclusive 3-b-tag channel (right) in the different control and signal regions, as indicated by the vertical black lines.

In Fig. 7.5 the one-dimensional H_T distributions of data and simulated events in the different control and signal regions are shown. The corresponding Y_{MET} dis-

tributions are shown in Appendix D.1, Fig. D.2. As can be seen, the number of events predicted by the Standard Model simulation systematically lies above the data, which further motivates the application of a data-driven background method.

Before discussing it in more detail, a second way to illustrate the correlation between H_{T} and Y_{MET} is introduced. The two-dimensional distributions in Fig. 7.3 essentially contain the same information as the distributions in Fig. 7.1, but with a larger granularity. However, practically it is not feasible to draw a conclusion about the correlation from Fig. 7.3. A possibility to illustrate the correlation between H_{T} and Y_{MET} in the two-dimensional plane is to normalize the distribution in bins of Y_{MET} along the H_{T} axis. The two-dimensional plane is scanned along the Y_{MET} axis and for each bin in Y_{MET} the H_{T} distribution is normalized to unit area in the region of $H_{\mathrm{T}} > 375$ GeV. In Fig. 7.6 the resulting two-dimensional distributions after the event selection in the inclusive 1-btag channel and the inclusive 3-b-tag channel are shown. Vice versa, the H_{T} - Y_{MET} plane can be scanned along the H_{T} - axis and for each bin in H_{T} the Y_{MET} distribution can be normalized in the region of $Y_{\mathrm{MET}} > 3$ GeV$^{\frac{1}{2}}$ (which is shown for completeness in Appendix D.1, Fig. D.1). The main advantage besides the finer binning is that this illustration more easily allows to deduce a conclusion about the κ - factor. The main disadvantage is that statistical errors cannot be represented in the two-dimensional histogram. Depending on the purpose, therefore either the illustration chosen in Fig 7.1 or the one introduced here is used in the following.

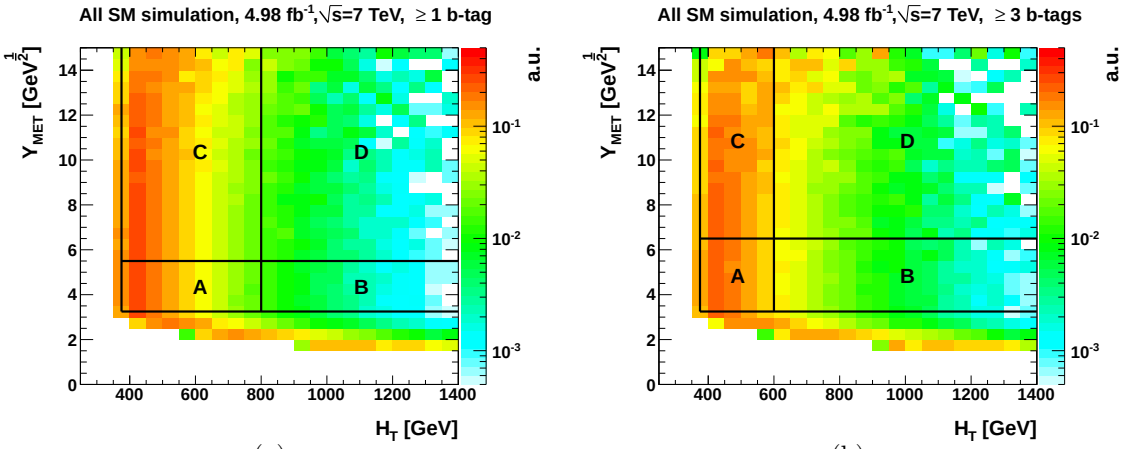

Figure 7.6.: Distribution of simulated Standard Model events in the H_{T} - Y_{MET} plane after the event selection in the inclusive 1-b-tag channel (left) and the inclusive 3-b-tag channel (right). For each bin in Y_{MET} the distribution is normalized to unit area in the region of $H_{\mathrm{T}} > 375$ GeV.

7.2. Background from Semileptonic $t\bar{t}$ Decays with a Muon or Electron in the Final State

The fact that H_{T} and $Y_{\mathrm{MET}} \equiv \not{E}_{\mathrm{T}}/\sqrt{H_{\mathrm{T}}}$ are found to be largely uncorrelated suggests that the expectation value $\langle \not{E}_{\mathrm{T}} \rangle$ of the missing transverse energy is roughly proportional to the square root of H_{T}:

$$\langle \not{E}_{\mathrm{T}} \rangle \sim \sqrt{H_{\mathrm{T}}}\,. \tag{7.3}$$

Furthermore, it can be assumed that the width of the $\not{E}_{\mathrm{T}}$ distribution, as e.g. quantified by the root mean square[3] $\not{E}_{\mathrm{T}}^{\mathrm{rms}}$, is approximately proportional to $\sqrt{H_{\mathrm{T}}}$:

$$\not{E}_{\mathrm{T}}^{\mathrm{rms}} \sim \sqrt{H_{\mathrm{T}}}\,. \tag{7.4}$$

In order to understand, why H_{T} and Y_{MET} appear largely uncorrelated, the functional correlation between $\not{E}_{\mathrm{T}}$ and H_{T} is studied in simulated events. The focus of these studies is on events that contain a semileptonically decaying $t\bar{t}$ pair with a muon or electron in the final state because these events constitute the largest background after the event selection in the inclusive 1-b-tag channel (68%) and the inclusive 3-b-tag channel (77%). All results presented in this chapter are based on a sample of simulated events that contain such a $t\bar{t}$ pair at generator level. If not stated differently, only events with $H_{\mathrm{T}} > 375$ GeV and $Y_{\mathrm{MET}} > 3.25\ \mathrm{GeV}^{\frac{1}{2}}$ are considered.

In semileptonic $t\bar{t}$ events, $\not{E}_{\mathrm{T}}$ originates from two sources: a neutrino that is produced along with the single isolated lepton in a W-boson decay, and energy mismeasurements, which mainly concerns jets. Since the momenta of muons and electrons can be reconstructed with a good resolution (cf. Sections 5.2 and 5.3), the contribution from lepton energy mismeasurements is small, but nevertheless accounted for in the following. In order to check if one of the two sources of $\not{E}_{\mathrm{T}}$ is dominant, the distributions of simulated events in the $\not{E}_{\mathrm{T}}^{\mathrm{fake}}$-$p_{\mathrm{T}}^{\nu}$ plane are shown in Fig. 7.7. Here $\not{E}_{\mathrm{T}}^{\mathrm{fake}}$ is defined as $|\vec{\not{E}}_{\mathrm{T}} - \vec{p_{\mathrm{T}}^{\nu}}|$ with $\vec{p_{\mathrm{T}}^{\nu}}$ the momentum vector of the neutrino at generator level. The black lines mark the expectation values of $\not{E}_{\mathrm{T}}^{\mathrm{fake}}$ as a function of p_{T}^{ν}. As can be seen, in both b-tag channels the missing transverse energy mainly results from the neutrino momentum. Only for $p_{\mathrm{T}}^{\nu} < 40$ GeV, $\not{E}_{\mathrm{T}}^{\mathrm{fake}}$ is larger than p_{T}^{ν} on average. This has two reasons: First, $\not{E}_{\mathrm{T}}^{\mathrm{fake}}$ is positive by definition. Therefore its expectation value is also always positive. Before applying any event selection requirement the average $\not{E}_{\mathrm{T}}^{\mathrm{fake}}$ roughly amounts 25 GeV for a neutrino momentum smaller than 20 GeV. Secondly, by the requirement of $\not{E}_{\mathrm{T}} > 60$ GeV, events with a

[3] The root mean square (rms) of a set of n values $\{x_1, x_2, ..., x_n\}$ is defined as $x^{\mathrm{rms}} \equiv \sqrt{\frac{1}{n}(x_1^2 + x_2^2) + ... + x_n^2}$.

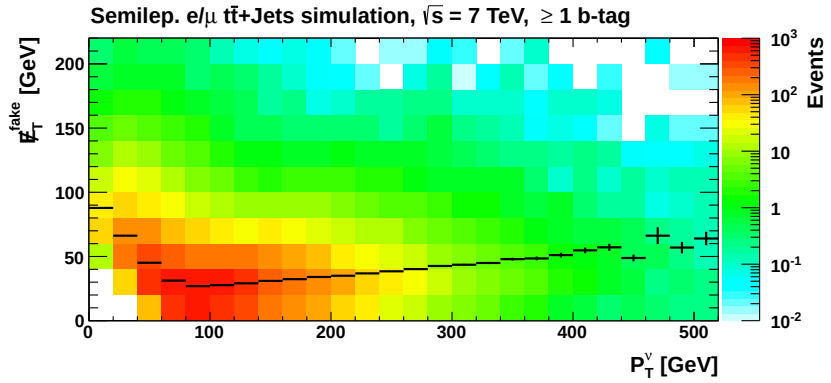

(a)

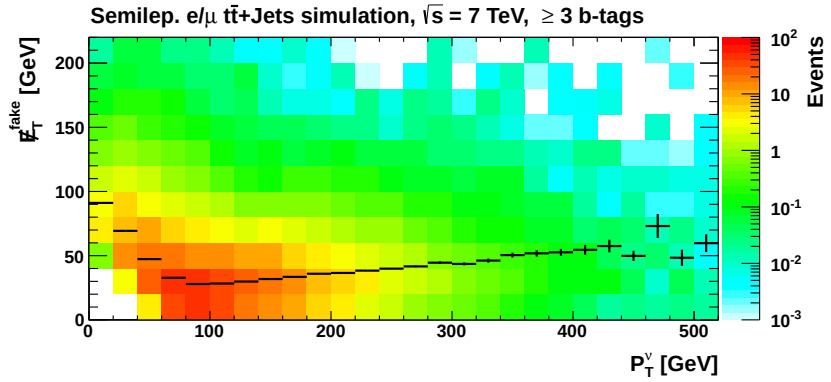

(b)

Figure 7.7.: Distribution of simulated $t\bar{t}$ events in the $\not\!\!E_{\mathrm{T}}^{\mathrm{fake}}$ - p_{T}^{ν} plane after the event selection in the inclusive 1-b-tag channel (a) and the inclusive 3-b-tag channel (b) with the additional requirement of $Y_{\mathrm{MET}} > 3.25$ GeV$^{\frac{1}{2}}$. A preselection on events that contain a semileptonically decaying $t\bar{t}$ pair with a muon or electron at generator level is applied. The black lines mark the expectation values of $\not\!\!E_{\mathrm{T}}^{\mathrm{fake}}$ as a function of p_{T}^{ν}. Note the different z-axis ranges.

low p_{T}^{ν} are only selected if they come along with a comparatively large $\not\!\!E_{\mathrm{T}}^{\mathrm{fake}}$.

In order to study the correlation between H_{T} and Y_{MET} separately for the two sources of missing transverse energy, $\not\!\!E_{\mathrm{T}}$ is split into a component that results from the neutrino and a component that is associated with energy mismeasurements:

$$\not\!\!E_{\mathrm{T}} = p_{\mathrm{T}}^{\nu} + (\not\!\!E_{\mathrm{T}} - p_{\mathrm{T}}^{\nu}). \tag{7.5}$$

It should be noted that $(\not\!\!E_{\mathrm{T}} - p_{\mathrm{T}}^{\nu})$ does not directly reflect the missing transverse energy from energy mismeasurements. It describes the difference between the magnitude of the observed missing transverse energy and the magnitude of the "real"

missing transverse energy given by the the neutrino p_T. Since $\not{E}_{\mathrm{T}}^{\mathrm{fake}}$ is defined as the magnitude of a vectorial quantity, it is always larger than $(\not{E}_{\mathrm{T}} - p_{\mathrm{T}}^{\nu})$.

Each component in (7.5) is assumed to approximately fulfill the functional correlations given in equations (7.3) and (7.4). This assumption is not stringent since different effects may cancel out each other. However, they constitute a natural starting point to study the correlation. In Fig. 7.8, p_{T}^{ν} and $(\not{E}_{\mathrm{T}} - p_{\mathrm{T}}^{\nu})$ of simulated events that pass the event selection in the inclusive 1-b-tag channel are shown in exclusive bins of H_{T}. In order to compare their shapes, the distributions are normalized to unit area. As can be seen, both distributions get broadened with increasing H_{T}. Associated therewith, also their mean values gets shifted towards larger values with increasing H_{T}. This does apply for the inclusive 3-b-tag channel as well (cf. Appendix D.2, Fig D.4). These effects are investigated in more detail separately for the neutrino momentum in Section 7.2.1 and $(\not{E}_{\mathrm{T}} - p_{\mathrm{T}}^{\nu})$ in Section 7.2.2 examining the inclusive 1-b-tag channel. All results presented in these Sections are shown for the inclusive 3-b-tag channel in Appendix D.2. In Sections 7.2.3 and 7.2.4, the influence of the event selection on the correlation between H_{T} and Y_{MET} is addressed, and the dependence of the correlation factor κ on the definition of the control and signal regions is checked.

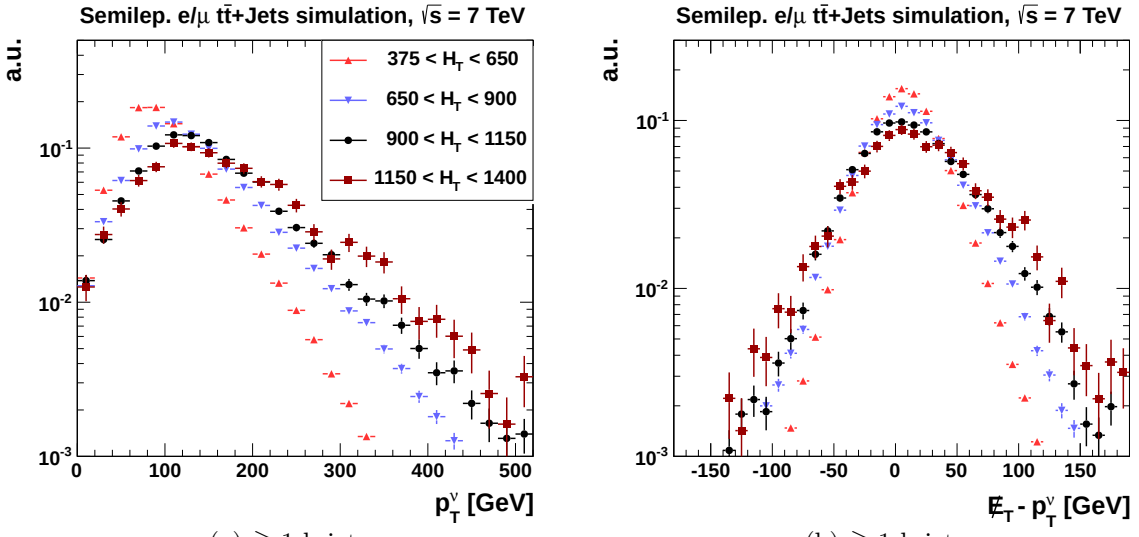

(a) $\geqq 1$ b-jet (b) $\geqq 1$ b-jet

Figure 7.8.: p_{T}^{ν} (left) and $\not{E}_T - p_T^{\nu}$ (right) of simulated events after the event selection in the inclusive 1-b-tag channel with the additional requirement of $Y_{\mathrm{MET}} > 3.25\ \mathrm{GeV}^{\frac{1}{2}}$ in exclusive bins of H_{T}. A preselection on events that contain a semileptonically decaying $t\bar{t}$ pair with a muon or electron at generator level is applied. All distributions are normalized to unit area.

7.2.1. Correlation between H_{T} and p_{T}^{ν}

In Fig. 7.9, the distribution of simulated events in the H_{T} - p_{T}^{ν} plane is shown. The black markers represent the mean p_{T}^{ν} as a function of H_{T}, which is fitted in the range between 350 GeV and 1400 GeV with the function

$$\langle p_{\mathrm{T}}^{\nu} \rangle = a \cdot {H_{\mathrm{T}}}^{b} \,, \tag{7.6}$$

where a and b denote real numbers with a positive and $0 < b < 1$. This ansatz is motivated by the following assumption: Both $\langle p_{\mathrm{T}}^{\nu} \rangle$ and $\langle H_{\mathrm{T}} \rangle$ increase with the energy scale Q of the hard scattering process. Since H_{T} reflects the sum of the transverse momenta of at least four quarks, its expectation value is assumed to increase faster with Q than $\langle p_{\mathrm{T}}^{\nu} \rangle$.[4] The mean neutrino p_T as a function of H_{T} is therefore expected to increase with a power of H_{T} that is between zero and one. Applying a least square fit, the following values for the parameters a and b are obtained: $a = 3.37$, $b = 0.56$. In Fig. 7.9 the fitted function is represented by the yellow line.

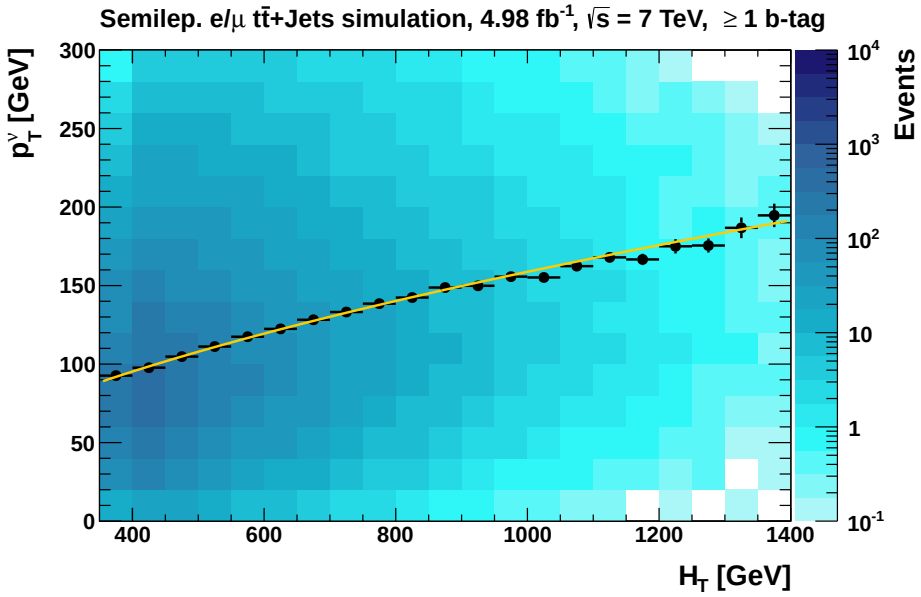

Figure 7.9.: Distribution of simulated $t\bar{t}$+Jets events in the p_{T}^{ν} - H_{T} plane after the event selection in the inclusive 1-b-tag channel with the additional requirement of $Y_{\mathrm{MET}} > 3.25\ \mathrm{GeV}^{\frac{1}{2}}$. A preselection on events that contain a semileptonically decaying $t\bar{t}$ pair with a muon or electron at generator level is applied. The black markers represent the mean p_{T}^{ν} as a function of H_{T}. The yellow line represents the best fit.

[4] Taking only the four quarks from the semileptonic $t\bar{t}$ decay into account it is found that before any selection requirement $\langle H_{\mathrm{T}}^{\mathrm{parton}} \rangle$ roughly increases four times faster with Q than $\langle p_{\mathrm{T}}^{\nu} \rangle$.

In order to check how the quality of the fit varies with parameter b, the fit is repeated with fixed parameters $b = 0.46$ and $b = 0.66$. As can be seen in Fig. 7.10, the fitted functions do not describe the mean p_{T}^{ν} as a function of H_{T} well. Also shown in Fig. 7.10 is the fit with a fixed parameter of $b = 0.5$, which lies somewhat below the best fit. This already hints at one reason for which Y_{MET} and H_{T} do not appear perfectly uncorrelated in simulated events.

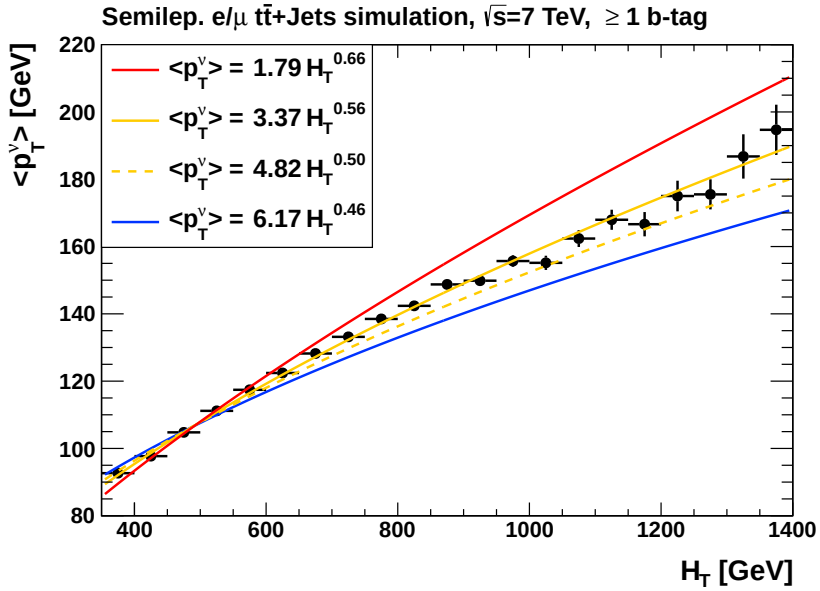

Figure 7.10.: Mean p_{T}^{ν} as a function of H_{T} in simulated $t\bar{t}$+Jets events after the event selection in the inclusive 1-b-tag channel with the additional requirement of $Y_{\mathrm{MET}} > 3.25\ \mathrm{GeV}^{\frac{1}{2}}$. A preselection on events that contain a semileptonically decaying $t\bar{t}$ pair with a muon or electron at generator level is applied. The best fit with floating exponent is marked by the yellow line. The solid red, the solid blue, and the dashed yellow line represent fits with fixed exponent.

Motivated by the fact that $\langle p_{\mathrm{T}}^{\nu} \rangle$ is non-zero for $H_{\mathrm{T}} = 0$, one might extend ansatz (7.6) by a constant term. Before applying any selection requirement, this "offset" roughly amounts 50 GeV. Of course, after requiring H_{T} to be larger than 375 GeV, such a term has no physical meaning anymore. Nevertheless, this ansatz might allow for a more accurate description of the functional correlation between $\langle p_{\mathrm{T}}^{\nu} \rangle$ and H_{T}. Applying a least square fit, the following parametrization is obtained: $\langle p_{\mathrm{T}}^{\nu} \rangle = -8.14\ \mathrm{GeV} + 4.57 \cdot H_{\mathrm{T}}^{0.52}$. As measure for the quality of the fit, the χ^2 divided by the number of degrees of freedom is calculated. Comparing the obtained values (4.37 for the fit with two free parameters and 4.56 for the fit with three free parameters) with each other, it is found that both fits describe the correlation similarly well. Therefore, the ansatz with two fit parameters is used in the following.

The width of the p_{T}^{ν} distribution as a function of H_{T}, as quantified by the root mean square $(p_{\mathrm{T}}^{\nu})_{\mathrm{rms}}$, is assumed to show a similar functional correlation as $\langle p_{\mathrm{T}}^{\nu} \rangle$. Fitting $(p_{\mathrm{T}}^{\nu})_{\mathrm{rms}}$ with the function (7.6), the following values for the parameters a and b are obtained: $a = 0.73$ and $b = 0.69$. In order to check if $(p_{\mathrm{T}}^{\nu})_{\mathrm{rms}}$ as a function of H_{T} can be similarly well described by functions with a different exponent, the fit is repeated with fixed parameters $b = 0.50$, $b = 0.59$, and $b = 0.79$. As can be seen in Fig. 7.11, these values for the exponent of H_{T} do not allow for a good description of the correlation between $(p_{\mathrm{T}}^{\nu})_{\mathrm{rms}}$ and H_{T}.

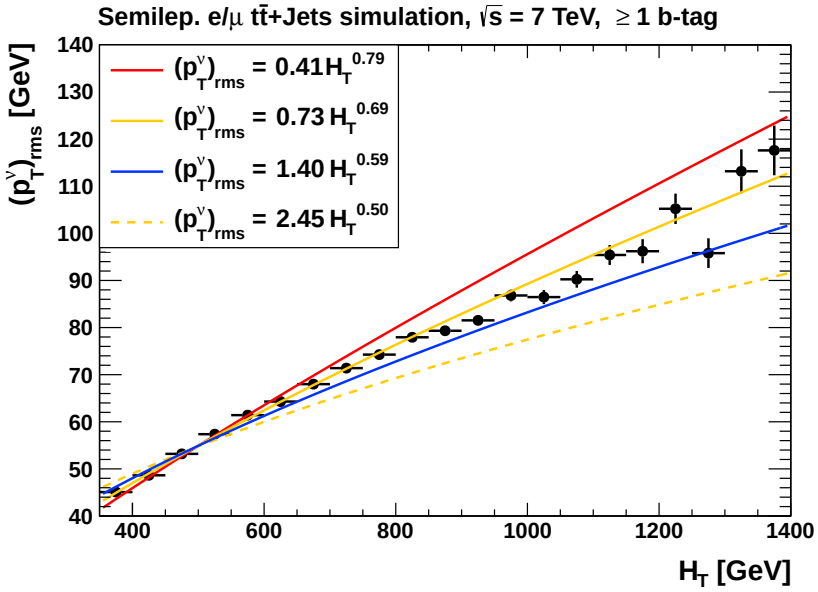

Figure 7.11.: Root mean square of p_{T}^{ν} as a function of H_{T} in simulated $t\bar{t}$+Jets events after the event selection in the inclusive 1-b-tag channel with the additional requirement of $Y_{\mathrm{MET}} > 3.25\ \mathrm{GeV}^{\frac{1}{2}}$. A preselection on events that contain a semileptonically decaying $t\bar{t}$ pair with a muon or electron at generator level is applied. The best fit with floating exponent is marked by the yellow line. The solid red, the solid blue, and the dashed yellow line represent fits with fixed exponent.

In order to draw a conclusion about the correlation between Y_{MET} and H_{T}, in Fig. 7.12, the distribution of simulated events in the plane that is spanned by $p_{\mathrm{T}}^{\nu}/\sqrt{H_{\mathrm{T}}}$ and H_{T} is shown. The black markers represent the mean value of $p_{\mathrm{T}}^{\nu}/\sqrt{H_{\mathrm{T}}}$, which is fitted by the function (7.6). The function by which $\langle p_{\mathrm{T}}^{\nu}/\sqrt{H_{\mathrm{T}}} \rangle$ can be fitted best is marked by the yellow line. Reflecting the fact that the correlation between $\langle p_{\mathrm{T}}^{\nu} \rangle$ and H_{T} can be described best by the function $\langle p_{\mathrm{T}}^{\nu} \rangle = 3.37 \cdot H_{\mathrm{T}}^{0.56}$, $\langle p_{\mathrm{T}}^{\nu}/\sqrt{H_{\mathrm{T}}} \rangle$ slightly increases with H_{T}. Associated therewith, the ratio of events with large Y_{MET} and events with low Y_{MET} slightly grows, leading to a shift of the correlation factor κ towards values larger than one.

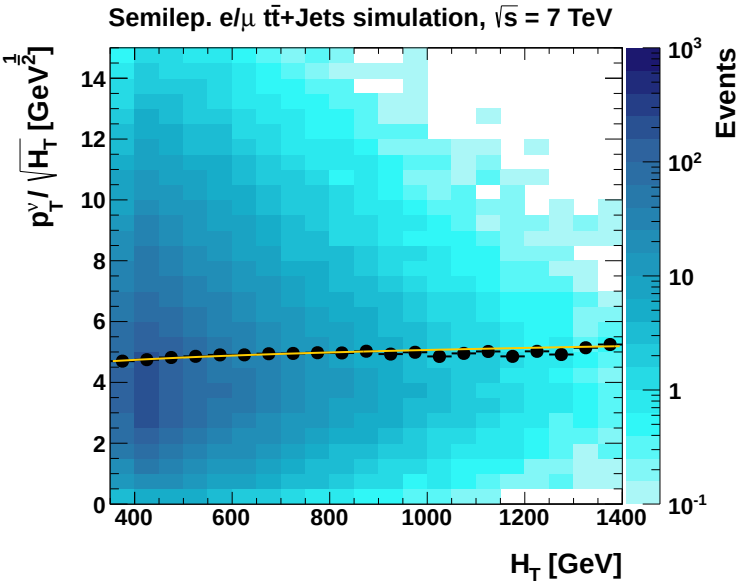

Figure 7.12.: Distribution of simulated $t\bar{t}$+Jets events in the $p_\mathrm{T}^\nu/\sqrt{H_\mathrm{T}}$ - H_T plane after the event selection in the inclusive 1-b-tag channel with the additional requirement of $Y_\mathrm{MET} > 3.25$ GeV$^{\frac{1}{2}}$. A preselection on events that contain a semileptonically decaying $t\bar{t}$ pair with a muon or electron at generator level is applied. The black markers represent the mean $p_\mathrm{T}^\nu/\sqrt{H_\mathrm{T}}$ as a function of H_T. The yellow line represents the best fit.

The width of $p_\mathrm{T}^\nu/\sqrt{H_\mathrm{T}}$ gets slightly broadened with increasing H_T (which will be shown later in Section 7.2.3). The resulting effect on κ depends on the Y_MET requirement, by which regions C and D are separated from regions A and B. If this Y_MET requirement is below $\langle p_\mathrm{T}^\nu/\sqrt{H_\mathrm{T}}\rangle$, the broadening will result in a decrease of the ratio of events with large Y_MET over events with low Y_MET. Vice versa, a Y_MET requirement above $\langle p_\mathrm{T}^\nu/\sqrt{H_\mathrm{T}}\rangle$ will lead to an increase of the ratio. The fitted mean value of $p_\mathrm{T}^\nu/\sqrt{H_\mathrm{T}}$ ranges from 4.79 at $H_\mathrm{T} = 400$ GeV to 5.20 at $H_\mathrm{T} = 1400$ GeV. Since this value is close to the requirement of $Y_\mathrm{MET} > 5.5$, by which the regions A and B are separated from the regions C and D, the broadening of $p_\mathrm{T}^\nu/\sqrt{H_\mathrm{T}}$ does only slightly effect the value of κ in this channel.

In Fig. 7.13, the distribution of simulated events in the $p_\mathrm{T}^\nu/\sqrt{H_\mathrm{T}}$ - H_T is normalized in bins of $p_\mathrm{T}^\nu/\sqrt{H_\mathrm{T}}$ along the H_T axis and in bins of H_T along the $p_\mathrm{T}^\nu/\sqrt{H_\mathrm{T}}$ axis, respectively. As can be seen, the functional correlation between p_T^ν and H_T corresponds to a slight "shift" of events from region B or C to region D, depending on the normalization. Taking only the contribution from the neutrino p_T to the missing transverse energy into account, $\kappa \equiv n_\mathrm{A}\, n_\mathrm{D}/(n_\mathrm{B}\, n_\mathrm{C})$ amounts to 1.14 ± 0.04.

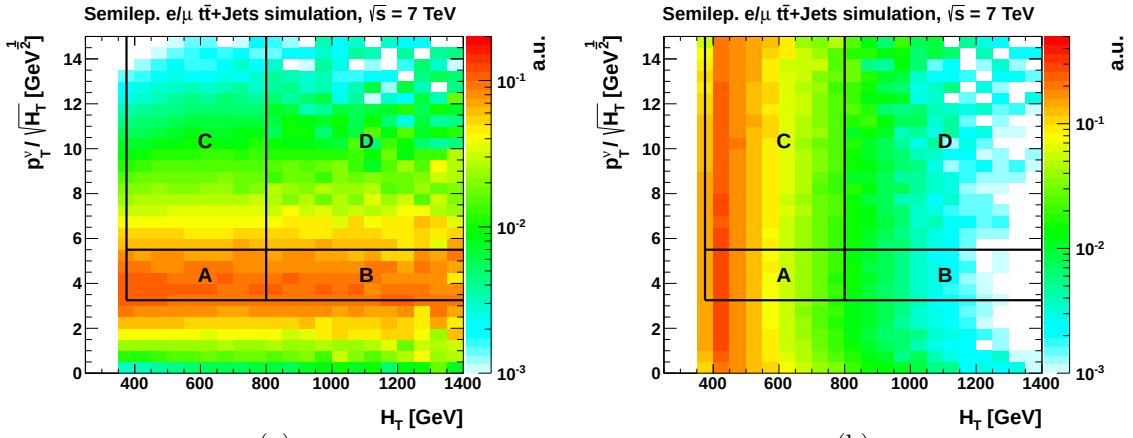

(a) (b)

Figure 7.13.: Distribution of simulated events in the $p_{\mathrm{T}}^{\nu}/\sqrt{H_{\mathrm{T}}}$ - H_{T} plane after the event selection in the inclusive 1-b-tag channel with the additional requirement of $Y_{\mathrm{MET}} > 3.25\ \mathrm{GeV}^{\frac{1}{2}}$. A preselection on events that contain a semileptonically decaying $t\bar{t}$ pair with a muon or electron at generator level is applied. In Fig. (a), for each bin in H_{T} the distribution is normalized to unit area in the region of $p_{\mathrm{T}}^{\nu}/\sqrt{H_{\mathrm{T}}} > 0\ \mathrm{GeV}^{\frac{1}{2}}$. In Fig. (b), for each bin in $p_{\mathrm{T}}^{\nu}/\sqrt{H_{\mathrm{T}}}$ the distribution is normalized to unit area in the region $H_{\mathrm{T}} > 375$ GeV.

7.2.2. Correlation between H_{T} and $\not{E}_{\mathrm{T}} - p_{\mathrm{T}}^{\nu}$

In Fig. 7.14 the distribution of simulated events in the H_{T} - $(\not{E}_{\mathrm{T}} - p_{\mathrm{T}}^{\nu})$ plane is shown. The black markers represent the mean $(\not{E}_{\mathrm{T}} - p_{\mathrm{T}}^{\nu})$ as a function of H_{T}. This mean value is not zero, which has the following reason: In events with $\not{E}_{\mathrm{T}}^{\mathrm{fake}} < p_{\mathrm{T}}^{\nu}$, $\not{E}_{\mathrm{T}}$ is symmetrically distributed around p_{T}^{ν}. For these events $\langle \not{E}_{\mathrm{T}} - p_{\mathrm{T}}^{\nu} \rangle$ is zero. In events with $\not{E}_{\mathrm{T}}^{\mathrm{fake}} > p_{\mathrm{T}}^{\nu}$ the missing transverse energy tends to be larger than p_{T}^{ν}. In these events $\langle \not{E}_{\mathrm{T}} - p_{\mathrm{T}}^{\nu} \rangle$ is positive. However, since the contribution from $\langle \not{E}_{\mathrm{T}} - p_{\mathrm{T}}^{\nu} \rangle$ to $\not{E}_{\mathrm{T}}$ is small, it can be neglected in the following. In analogy to the case discussed in Section 7.2.1, the width of the $(\not{E}_{\mathrm{T}} - p_{\mathrm{T}}^{\nu})$ distribution as a function of H_{T}, as quantified by the root mean square $(\not{E}_{\mathrm{T}} - p_{\mathrm{T}}^{\nu})_{\mathrm{rms}}$, is fitted with the function

$$(\not{E}_{\mathrm{T}} - p_{\mathrm{T}}^{\nu})_{\mathrm{rms}} = a \cdot {H_{\mathrm{T}}}^{b}\,, \tag{7.7}$$

where $a > 0$ and $0 < b < 1$ denote real numbers. The best fit yields a value for parameter b of 0.61. In order to check how the quality of the fit varies with parameter b, the fit is repeated with fixed parameters $b = 0.51$ and $b = 0.71$. As can be seen in Fig. 7.15, these values for the exponent of H_{T} do not allow for a good description of the correlation between $(\not{E}_{\mathrm{T}} - p_{\mathrm{T}}^{\nu})_{\mathrm{rms}}$ and H_{T}.

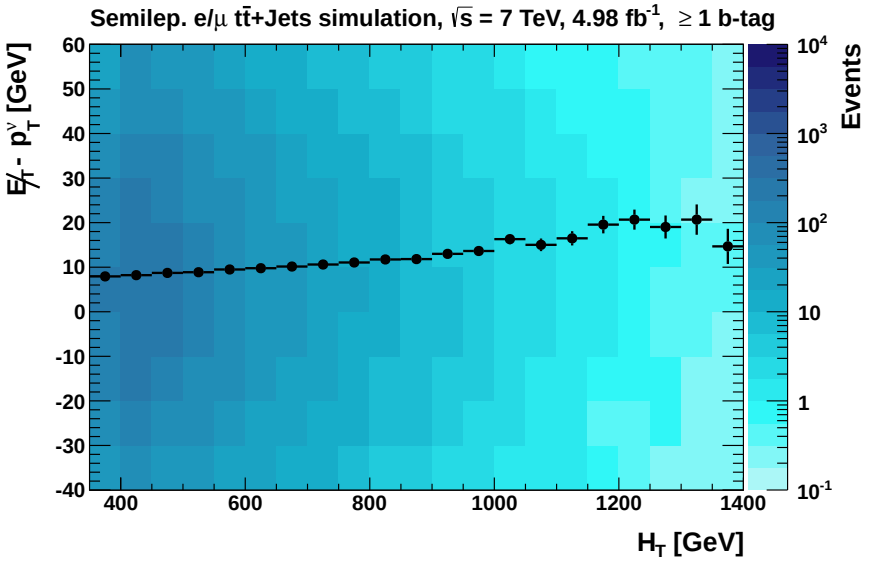

Figure 7.14.: Distribution of simulated $t\bar{t}$+Jets events in the H_{T} - $(\not{E}_{\mathrm{T}} - p^{\nu}_{\mathrm{T}})$ plane after the event selection in the inclusive 1-b-tag channel with the additional requirement of $Y_{\mathrm{MET}} > 3.25\ \mathrm{GeV}^{\frac{1}{2}}$. A preselection on events that contain a semileptonically decaying $t\bar{t}$ pair with a muon or electron at generator level is applied. The black markers represent the mean $(\not{E}_{\mathrm{T}} - p^{\nu}_{\mathrm{T}})$ as a function of H_{T}.

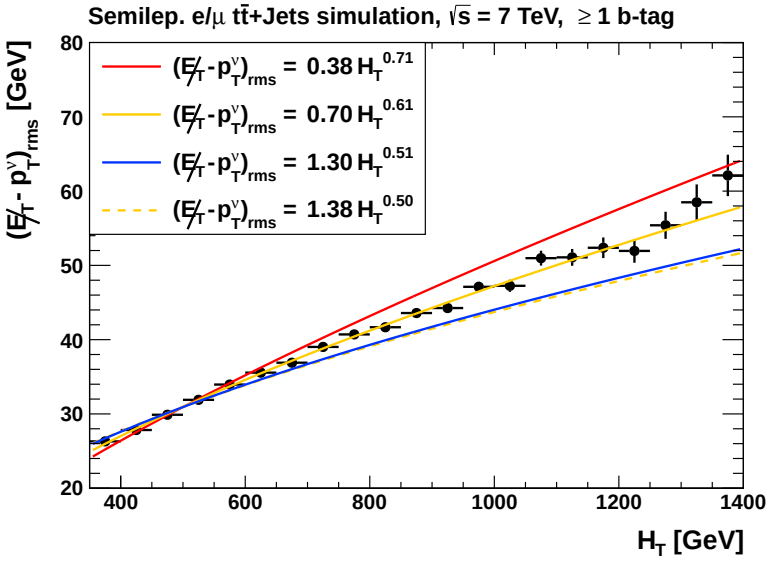

Figure 7.15.: Root mean square of $(\not{E}_{\mathrm{T}} - p^{\nu}_{\mathrm{T}})$ as a function of H_{T} in simulated $t\bar{t}$+Jets events after the event selection in the inclusive 1-b-tag channel with the additional requirement of $Y_{\mathrm{MET}} > 3.25\ \mathrm{GeV}^{\frac{1}{2}}$. The best fit with floating exponent is marked by the yellow line. The solid red, the solid blue, and the dashed yellow line represent fits with fixed exponent.

In Fig. 7.16, the distribution of simulated events in the $(\not\!\!E_{\mathrm{T}} - p_{\mathrm{T}}^{\nu})/\sqrt{H_{\mathrm{T}}}$ - H_{T} plane is normalized in bins of $(\not\!\!E_{\mathrm{T}} - p_{\mathrm{T}}^{\nu})/\sqrt{H_{\mathrm{T}}}$ along the H_{T} axis and in bins of H_{T} along the $(\not\!\!E_{\mathrm{T}} - p_{\mathrm{T}}^{\nu})/\sqrt{H_{\mathrm{T}}}$ axis, respectively. Associated with the fact that $(\not\!\!E_{\mathrm{T}} - p_{\mathrm{T}}^{\nu})_{\mathrm{rms}}$ as a function of H_{T} is proportional to $H_{\mathrm{T}}^{0.6}$, the distribution of $(\not\!\!E_{\mathrm{T}} - p_{\mathrm{T}}^{\nu})/\sqrt{H_{\mathrm{T}}}$ gets slightly broadened with H_{T}. Taking both the contribution from the neutrino p_{T} and the contribution from energy mismeasurements to the missing transverse energy into account, $\kappa \equiv n_{\mathrm{A}}\, n_{\mathrm{D}}/(n_{\mathrm{B}}\, n_{\mathrm{C}})$ amounts to 1.14 ± 0.04 as well.

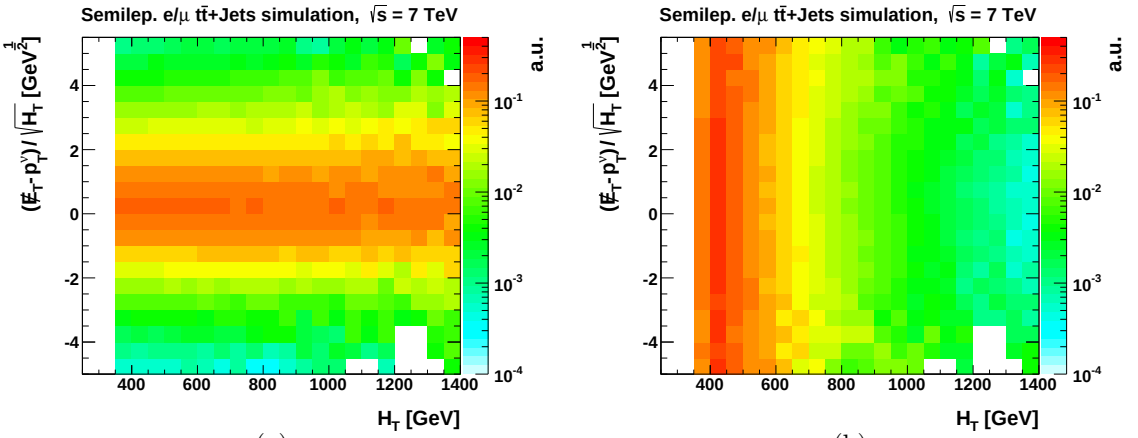

(a) (b)

Figure 7.16.: Distribution of simulated events in the $(\not\!\!E_{\mathrm{T}} - p_{\mathrm{T}}^{\nu})/\sqrt{H_{\mathrm{T}}}$ - H_{T} plane after the event selection in the inclusive 1-b-tag channel with the additional requirement of $Y_{\mathrm{MET}} > 3.25\ \mathrm{GeV}^{\frac{1}{2}}$. A preselection on events that contain a semileptonically decaying $t\bar{t}$ pair with a muon or electron at generator level is applied. In Fig. (a), for each bin in H_{T} the distribution is normalized to unit area in the whole region of $(\not\!\!E_{\mathrm{T}} - p_{\mathrm{T}}^{\nu})/\sqrt{H_{\mathrm{T}}}$. In Fig. (b), for each bin in $(\not\!\!E_{\mathrm{T}} - p_{\mathrm{T}}^{\nu})/\sqrt{H_{\mathrm{T}}}$ the distribution is normalized to unit area in the region $H_{\mathrm{T}} > 375$ GeV.

Conclusions

In semileptonic $t\bar{t}$ events with a muon or electron in the final state, $\not\!\!E_{\mathrm{T}}$ mainly results from a neutrino that is produced along with the single isolated lepton in a W-boson decay. In the inclusive 1-b-tag channel, the mean neutrino p_{T} can be described best by the function $\langle p_{\mathrm{T}}^{\nu} \rangle = 3.37 \cdot H_{\mathrm{T}}^{0.56}$. Associated therewith, $\langle p_{\mathrm{T}}^{\nu}/\sqrt{H_{\mathrm{T}}} \rangle$ slightly increases with H_{T}, leading to a shift of the correlation factor κ towards values larger than one. The width of $p_{\mathrm{T}}^{\nu}/\sqrt{H_{\mathrm{T}}}$ gets slightly broadened with increasing H_{T}. Depending on the Y_{MET} requirement by which the regions A and B are separated from the regions C and D, this results in an increase or a decrease of κ. A similar broadening effect results from jet energy mismeasurements.

7.2.3. Influence of the Event Selection

A possibility to study the correlation between H_{T} and Y_{MET} in data, is to invert an event selection criterion that is applied to reject Standard Model background events. Since the correlation in such a region might be different than in the control and signal regions that are finally exploited to predict the background, the influence of the event selection on the correlation between $\not\!\!E_{\mathrm{T}}$ and H_{T} and the correlation factor κ are investigated in this section. For this purpose, the studies presented in Sections 7.2.1 and 7.2.2 are performed for all selection steps. As in the inclusive 1-b-tag channel, p_{T}^{ν}, $(p_{\mathrm{T}}^{\nu})_{\mathrm{rms}}$, and $(\not\!\!E_{\mathrm{T}} - p_{\mathrm{T}}^{\nu})_{\mathrm{rms}}$ are fitted with the function $a \cdot H_{\mathrm{T}}^{b}$, where $a > 0$ and $0 < b < 1$ denote real numbers. The main results in terms of best fit functions are illustrated in Fig. 7.17. The corresponding values for the fit parameters and the normalized χ^2 are given in Appendix D.2, Tables D.1, D.2, and D.3. In the following, the influence of the event selection on the correlation is discussed separately for each of the successively applied event selection steps.

7.2.3.1. Preselection

Besides a primary vertex selection and the rejection of events with instrumental noise (both of which marginally affect the selection of simulated events) the event preselection is constituted by the requirements of a single isolated lepton with $p_{\mathrm{T}} > 20$ GeV, $H_{\mathrm{T}} > 375$ GeV, and $\not\!\!E_{\mathrm{T}} > 60$ GeV (cf. Section 6.2). Hence, only the lepton selection may have an influence on the correlation between H_{T} and Y_{MET} in the control and signal regions of the factorization method. Reflecting the correlation between the transverse momenta of the charged lepton and the antineutrino that are produced along with each other in a leptonic W-boson decay, the lepton p_{T} requirement can be expected to affect the p_{T}^{ν} spectrum. If the charged lepton carries a large momentum, the conservation of four-momentum requires the neutrino to carry a small momentum, and vice versa. Increasing the lepton p_{T} requirement therefore leads to a smaller neutrino p_{T} on average. As can be seen in Fig. 7.17(a), by requiring one isolated lepton with $p_{\mathrm{T}} > 20$ GeV ("preselection") the mean neutrino p_{T} slightly decreases in the first H_{T} bins. However, this effect is very small, which has the following reason. The requirements of $H_{\mathrm{T}} > 375$ GeV and $\not\!\!E_{\mathrm{T}} > 60$ GeV already apply some cut on the energy scale of the hard scattering process. Associated therewith, the W bosons produced in the top-quark decays already carry a considerable amount of momentum. Thus, also their decay products carry large momenta, even though the latter are correlated on an event-by-event basis. To put it in simple terms, in the considered phase space, most semileptonic $t\bar{t}$ events with a muon or electron in the final state already contain a lepton with $p_{\mathrm{T}} > 20$ GeV. At larger values of H_{T}, the $\langle p_{\mathrm{T}}^{\nu} \rangle$ distributions before the lepton selection ("no cuts") and after the lepton selection coincide. In this region of the phase space, the lepton p_{T} requirement has no effect anymore. In total, the lepton selection leads to a slight increase of the correlation factor κ in the order of a percent.

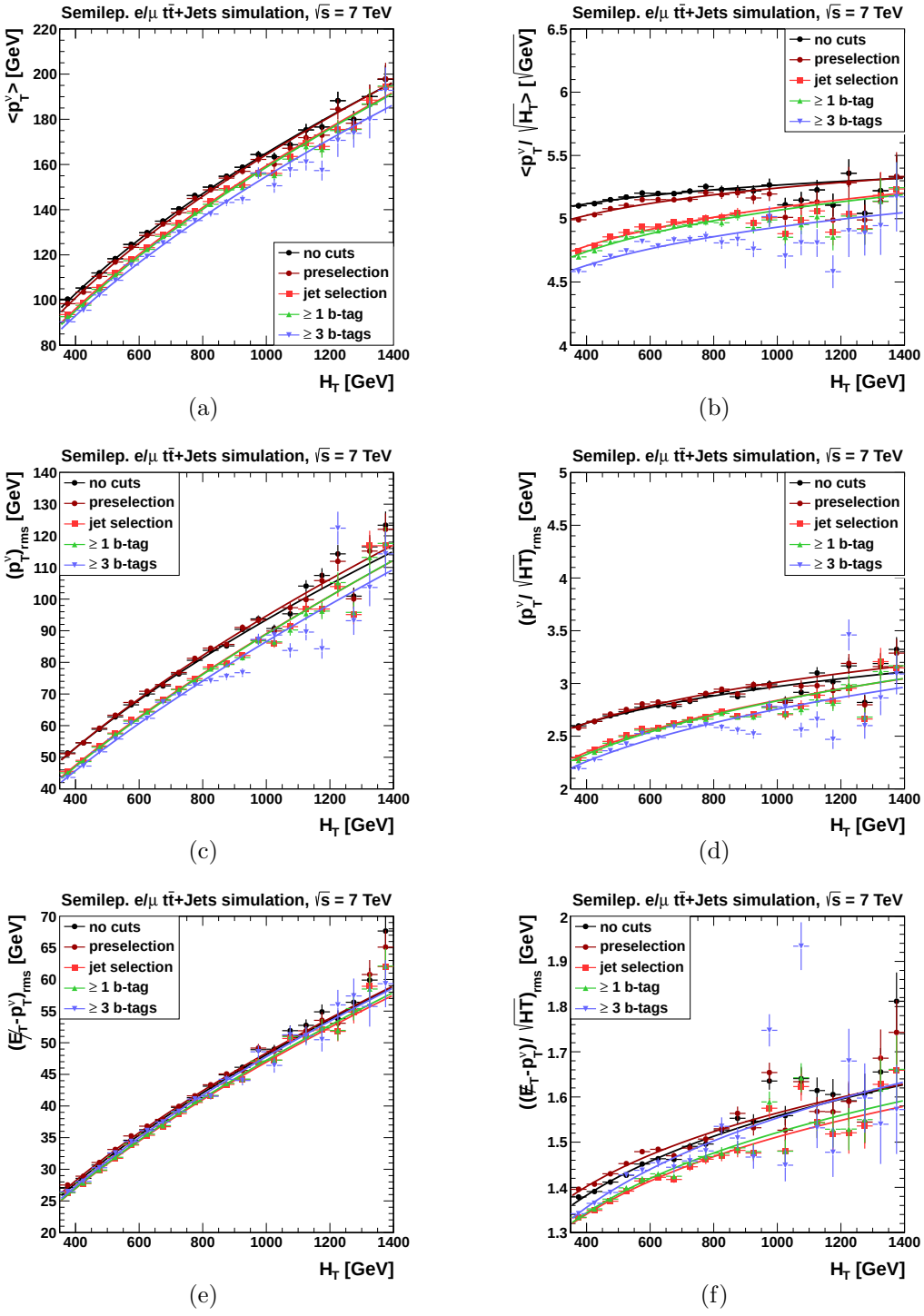

Figure 7.17.: Correlation between $\not\!\!E_{\mathrm{T}}$ and H_{T} (left) and Y_{MET} and H_{T} (right) in simulated events after the different event selection steps with the additional requirement of $Y_{\mathrm{MET}} > 3.25\ \mathrm{GeV}^{\frac{1}{2}}$. A preselection on events that contain a semileptonically decaying $t\bar{t}$ pair with a muon or electron at generator level is applied. The solid colored lines marks the best fit functions, as discussed in the text. Note the different y-axis ranges.

7.2.3.2. Jet Selection

The jet selection has a more visible effect on the correlation between H_{T} and Y_{MET} than the lepton selection. As shown in Fig. 7.18, for a given H_{T}, the shape of the $\not\!\!E_{\mathrm{T}}$ distribution depends on the number of selected jets. The larger the jet multiplicity is, the more steeper does $\not\!\!E_{\mathrm{T}}$ decrease.

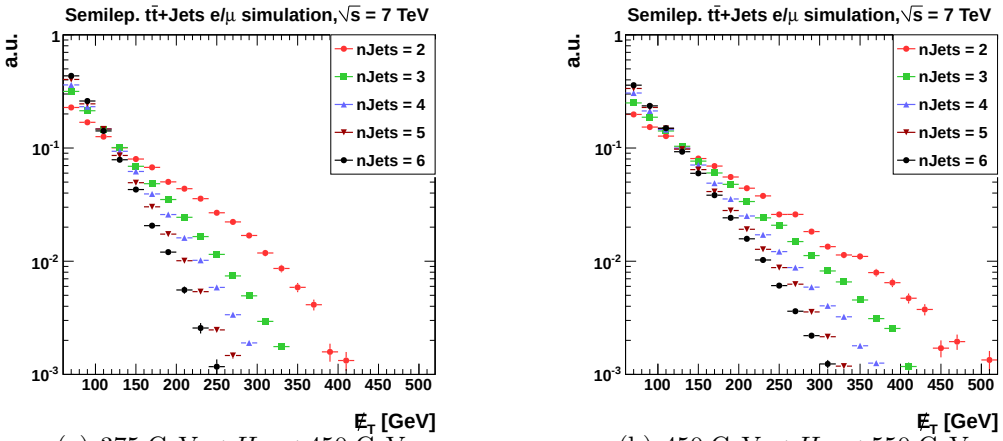

(a) 375 GeV $< H_{\mathrm{T}} <$ 450 GeV

(b) 450 GeV $< H_{\mathrm{T}} <$ 550 GeV

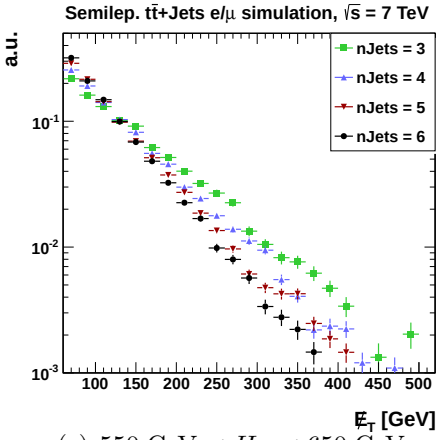

(c) 550 GeV $< H_{\mathrm{T}} <$ 650 GeV

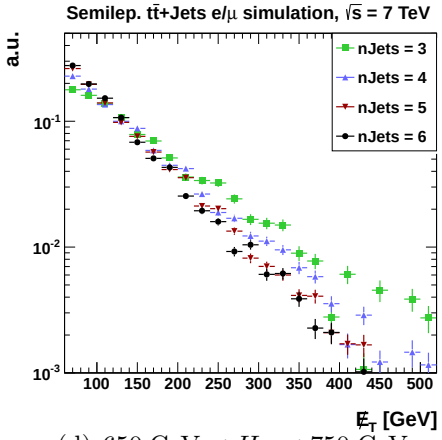

(d) 650 GeV $< H_{\mathrm{T}} <$ 750 GeV

Figure 7.18.: $\not\!\!E_{\mathrm{T}}$ after the event preselection with the additional requirement of $Y_{\mathrm{MET}} > 3.25\ \mathrm{GeV}^{\frac{1}{2}}$ in exclusive bins of H_{T} and the jet multiplicity. All distributions are normalized to unit area. A preselection on events that contain a semileptonically decaying $t\bar{t}$ pair with a muon or electron at generator level is applied. For the bins 550 GeV $< H_{\mathrm{T}} <$ 650 GeV and 650 GeV $< H_{\mathrm{T}} <$ 750 GeV the $\not\!\!E_{\mathrm{T}}$ distribution of events with exactly two jets has large statistical uncertainties and is therefore not shown.

By requiring events to contain at least four jets, preferably events with a small missing transverse are selected, which has two reasons. First, in events with many selected jets, the final state products carry smaller momenta than in events with a few selected jets. Hence, also the neutrino momentum will carry a smaller momentum on average. Secondly, the final state products will be more uniformly distributed in the transverse plane than in events with a few selected jets. Contributions to the missing transverse energy from jet energy mismeasurements are therefore more likely to cancel each other. Thus, by requiring events to contain at least four jets, preferably those events where the missing transverse energy is small with respect to H_{T} are selected. Associated therewith, the distributions of the $\not\!\!E_{\mathrm{T}}$ and Y_{MET} components as functions of H_{T} obtained after the jet selection lie below the corresponding distributions for the event preselection (see Fig. 7.17). As in the case of the lepton p_{T} requirement discussed in Section 7.2.3.1, this effect partly depends on H_{T}. At large H_{T}, most semileptonic $t\bar{t}$ events with a muon or electron in the final state already contain four selected jets, resulting in an increase of the correlation factor κ of 6 to 7% for the control and signal regions exploited in this thesis.

7.2.3.3. B-Jet Selection

The effect of the jet selection on the correlation between H_{T} and $\not\!\!E_{\mathrm{T}}$ is enhanced by the b-jet selection. The larger the jet multiplicity is, the more jets are tagged as b-jet, and vice versa (compare for example Figs. 6.14(a) and 6.14(b)). Hence, by requiring events to contain a certain number of b-jets, preferably events with many jets are selected. As discussed above in Section 7.2.3.2, in these events, $\not\!\!E_{\mathrm{T}}$ is small with respect to H_{T}, resulting in a further shift of the correlation factor κ towards larger values. For the inclusive 1-b-tag channel, this shift is small. This is because $t\bar{t}+\mathrm{Jets}$ events contain two bottom quarks at parton level, at least one of which is likely to result in a jet that is tagged as b-jet. For the inclusive 3-b-tag channel, the effect on the correlation is expected to be more prominent because at least one jet is misidentified as b-jet. Since the udsg- and c-mistag rates are small compared to the b-tag efficiency (cf. Section 6.4), events in the inclusive 3-b-tag channel contain on average more jets than events in the inclusive 1-b-tag channel. In the inclusive 3-b-tag channel, the discussed effect is therefore assumed to affect a larger H_{T} range. Only at very large H_{T}, events are likely to contain so many jets that the requirement of at least three b-tags has no influence. For this reason, the dependence of the correlation between H_{T} and Y_{MET} on the minimal H_{T} requirement addressed in the beginning of Section 7.1 is assumed to be more prominent in the inclusive-3-b-tag channel than in the inclusive 1-b-tag channel (see also Appendix D.1, Fig. D.3). However, due to the limited number of simulated events in this region of the phase space, this can hardly be probed in simulated events.

Conclusions

The main influence of the event selection on the correlation between H_{T} and $\not\!\!E_{\mathrm{T}}$ and the correlation factor κ results from the jet selection. By requiring events to contain at least four selected jets, preferably those events where $\not\!\!E_{\mathrm{T}}$ is small with respect to H_{T} are selected. At large values of H_{T}, this effect saturates, resulting in an increase of the correlation factor κ by 6 - 7% for the control and signal regions exploited in this thesis. Due to the correlation between the number of b-tags and the jet multiplicity the influence that results from the jet selection gets slightly enhanced by the requirement of at least one b-jet. The requirement of at least three b-jets can be expected to further strengthen the influence of the correlation. However, due to the limited number of simulated events in this channel, this can hardly be directly be probed. The influence on the correlation factor κ for the two sets of control and signal regions used in this search (cf. Section 7.1, Table 7.1) is summarized in Table 7.2.

Table 7.2.: Correlation factor κ obtained from simulated semileptonic $t\bar{t}$ events with a muon or electron in the final state after the successively applied event selection steps. The correlation factor is calculated from events with $H_{\mathrm{T}} > 375$ GeV and $Y_{\mathrm{MET}} > 3.25$ GeV$^{\frac{1}{2}}$ for the two sets of control and signal regions defined in Section 7.1, Table 7.1.

Selection	Signal Region	
	$H_{\mathrm{T}} > 800$ GeV $Y_{\mathrm{MET}} > 5.5$ GeV$^{\frac{1}{2}}$	$H_{\mathrm{T}} > 600$ GeV $Y_{\mathrm{MET}} > 6.5$ GeV$^{\frac{1}{2}}$
No cuts	1.05 ± 0.01	1.06 ± 0.01
Preselection	1.05 ± 0.03	1.08 ± 0.02
Jet Selection	1.12 ± 0.04	1.15 ± 0.02
$\geqq 1$ b-tag	1.14 ± 0.04	1.16 ± 0.02
$\geqq 3$ b-tags	1.11 ± 0.05	1.17 ± 0.04

Ignoring the inclusive 3-b-tag channel, where the statistical uncertainties are comparatively large, the overall increase of κ ranges from 8 to 9% for the two sets of control and signal regions exploited in this thesis. Based on the understanding of the influence of the event selection on the correlation between H_{T} and Y_{MET}, one can study the correlation between H_{T} and Y_{MET} in a further control region in data that is obtained by inverting one event selection criterion.

7.2.4. Influence of the Control and Signal Region Definition

As discussed in Sections 7.2.1 and 7.2.2, the width of $p_{\mathrm{T}}^{\nu}/\sqrt{H_{\mathrm{T}}}$ and $(\not{E}_{\mathrm{T}} - p_{\mathrm{T}}^{\nu})/\sqrt{H_{\mathrm{T}}}$ gets slightly broadened with increasing H_{T}, resulting in a dependence of the correlation factor κ on the Y_{MET} requirement by which regions A and B are separated from regions C and D. By requiring events to contain a certain number of jets, the correlation between H_{T} and Y_{MET} becomes dependent on the lower H_{T} requirement, as discussed in Section 7.2.3. In order to get a first idea of how the systematic uncertainties might affect the data-driven background prediction, the dependence of κ on the definition of the control and signal regions is studied. A global mismeasurement of H_{T}, for example, would result in an effective shift of the control and signal regions. If κ strongly depends on the definition of the regions, the systematic uncertainties can be expected to be large. Vice versa, if κ only slightly depends on the region definition, such uncertainties will largely cancel out.

In the first step, the influence of the Y_{MET} requirement by which the regions A and B are separated from regions C and D and the H_{T} requirement that separates regions A and C from regions B and D is studied. The lower requirements of $H_{\mathrm{T}} > 375$ GeV and $Y_{\mathrm{MET}} > 3.25\ \mathrm{GeV}^{\frac{1}{2}}$ are kept fix. In Fig. 7.19(a), the result of this scan is shown for semileptonic $t\bar{t}$ events with a a muon or electron in the final state that pass the event selection in the inclusive 1-b-tag channel. The black cross indicates the H_{T} and Y_{MET} criteria that separates the control and signal regions in this channel from each other. While no dependence of κ on H_{T} is observed, the correlation factor increases from $\kappa = 1.06$ at $Y_{\mathrm{MET}} = 4.5$ to $\kappa = 1.25$ at $Y_{\mathrm{MET}} = 8$. This is due to the slight broadening of $p_{\mathrm{T}}^{\nu}/\sqrt{H_{\mathrm{T}}}$ and $(\not{E}_{\mathrm{T}} - p_{\mathrm{T}}^{\nu})/\sqrt{H_{\mathrm{T}}}$ with increasing H_{T}. The larger the Y_{MET} requirement by which the regions A and B are separated from regions C and D is, the more events are effectively shifted from region B to region D.

In the second step, also the lower H_{T} and Y_{MET} requirements are varied. The lower H_{T} criterion is varied from $H_{\mathrm{T}} > 375$ GeV to $H_{\mathrm{T}} > 450$ GeV and $H_{\mathrm{T}} > 550$ GeV. The lower Y_{MET} requirement is increased from $Y_{\mathrm{MET}} > 3.25\ \mathrm{GeV}^{\frac{1}{2}}$ to $Y_{\mathrm{MET}} > 4\ \mathrm{GeV}^{\frac{1}{2}}$. In Fig. 7.19, these requirements are marked by the solid black lines. Comparing the histograms in the left column with those in the right column, it can be seen that an increase of the lower Y_{MET} requirement does not effect the dependence of κ on the definition of the control and signal regions. In contrast to this, an increase of the lower H_{T} requirement (compare the histograms in the upper, middle, and lower row of Fig. 7.19) reduces the dependence of κ on the control and signal region definition. This is due to the above-mentioned dependence of the correlation between H_{T} and Y_{MET} on the jet selection, which saturates which increasing H_{T}. The larger the H_{T} is, the smaller the dependence is. At large H_{T}, the requirement of at least four selected jets has no effect since most semileptonic $t\bar{t}$ events already contain four jets (cf. Section 7.2.3.2).

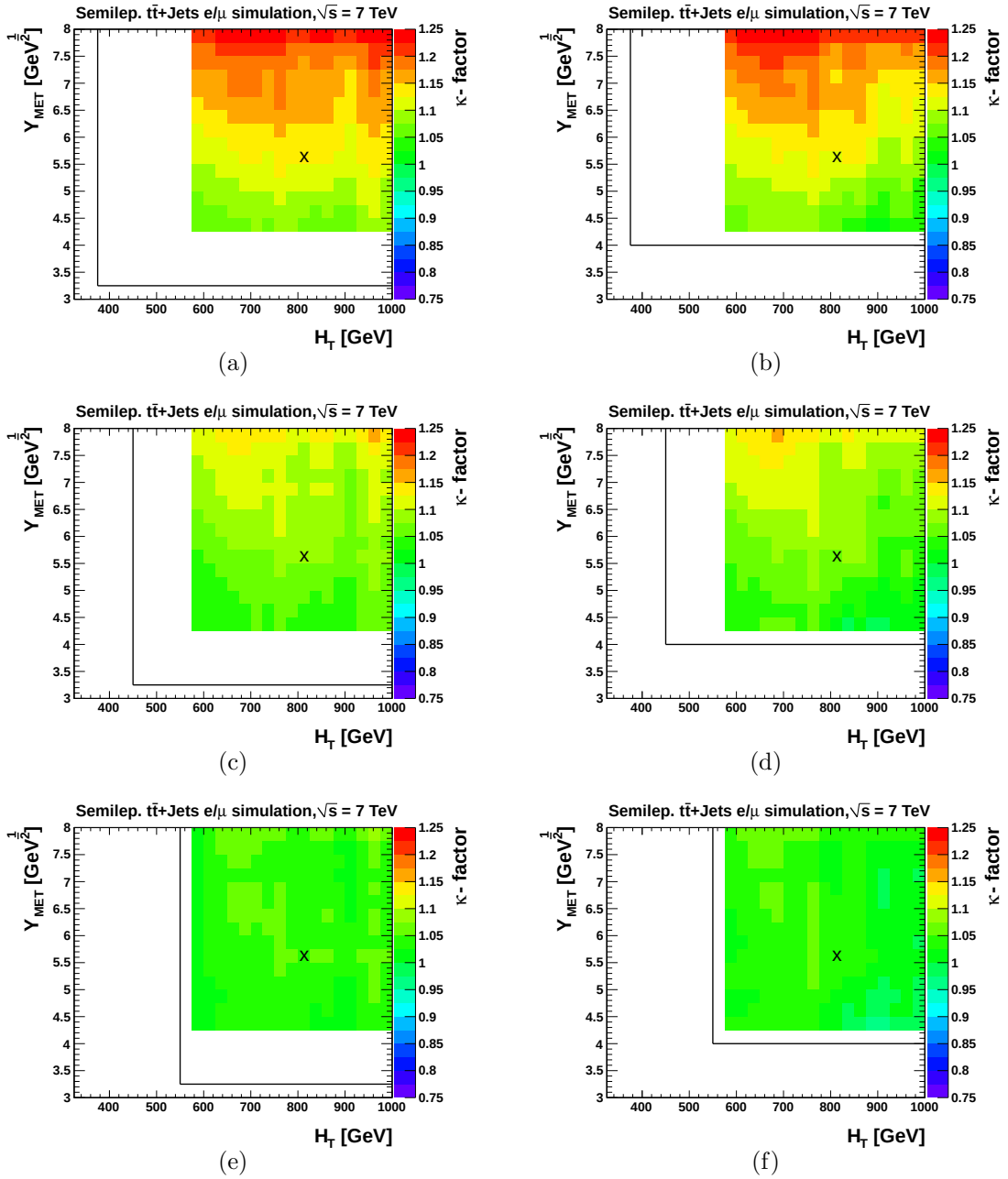

Figure 7.19.: Influence of the definition of control and signal regions on the correlation factor κ in simulated events after the event selection in the inclusive 1-b-tag channel. A preselection on events that contain a semileptonically decaying $t\bar{t}$ pair with a muon or electron at generator level is applied. The κ-scan is performed for different lower H_{T} and Y_{MET} requirements, as marked by the solid black lines. The black cross indicates the H_{T} and Y_{MET} requirements by which the control and signal regions are separated from each other in this channel.

In the last step, this study is repeated for the different event selection steps. While no dependence of κ on the definition of the control and signal regions after the lepton selection is found, the jet selection shows the same effect on the κ-scan as the additional requirement of at least one b-jet. This does also apply for the additional requirement of at least three b-jets, for which the results of the scan are shown in Appendix 7.2, Fig. D.13.

7.3. Background From Other Standard Model Processes

The largest Standard Model background after the event selection in the inclusive 1-b-tag channel and the inclusive 3-btag channel arises from semileptonic $t\bar{t}$ decays with a muon or an electron in the final state. The remaining background is mainly composed of events that contain a semileptonically decaying $t\bar{t}$ pair with a tau in the final state and events that contain a dileptonically decaying $t\bar{t}$ pair. In the inclusive 1-b-tag channel also W + Jets events contribute. The contributions of the individual processes to the simulated Standard Model background are shown in Table 7.3.

Table 7.3.: Composition of the simulated Standard Model background after the event selection in the inclusive 1-b-tag channel and the inclusive 3-b-tag channel.

Sample	$\geqq$ 1 b-tag	$\geqq$ 3 b-tags
$t\bar{t}$+Jets semilep. e/μ	67.7 %	76.5 %
$t\bar{t}$+Jets semilep. τ	7.5 %	8.4 %
$t\bar{t}$+Jets dilep.	10.2 %	9.8 %
W+Jets	9.8 %	1.7 %
Single top+W	3.1 %	2.6 %
Single top+q (t-channel)	1.0 %	0.8 %
Others	0.7 %	0.2 %

Due to the different event topologies the correlation between H_{T} and Y_{MET} might be different for the individual processes. Based on the studies performed in Section 7.2, the correlation between H_{T} and Y_{MET} in semileptonic $t\bar{t}$ events with a tau in the final state and dileptonic $t\bar{t}$ events is discussed in Sections 7.3.1 and 7.3.2. In Section 7.3.3, the correlation in W + Jets events is addressed, followed by a summary in Section 7.3.4.

7.3.1. Semileptonic $t\bar{t}$ Decays with a Tau in the Final State

The tau lepton decays with a branching fraction of 0.35 leptonically into a muon or an electron and two neutrinos ($\tau \to \mu\bar{\nu}_\mu\nu_\tau$ or $\tau \to e\bar{\nu}_e\nu_\tau$) and with a branching fraction of 0.65 hadronically ($\tau \to \bar{q}q'\nu_\tau$) [20]. While semileptonic $t\bar{t}$ events with a hadronically decaying tau mostly do not pass the lepton selection, those with a leptonically decaying tau are likely to be selected if the lepton p_T is not too soft. Since the single muon or electron is produced in the decay of a tau along with two neutrinos, it carries on average a smaller p_T than in the case where it originates from a W boson that is produced in a top-quark decay. In Fig. 7.20, the correlation factor is shown as a function of the H_T and Y_MET requirements by which the control and signal regions are separated from each other.

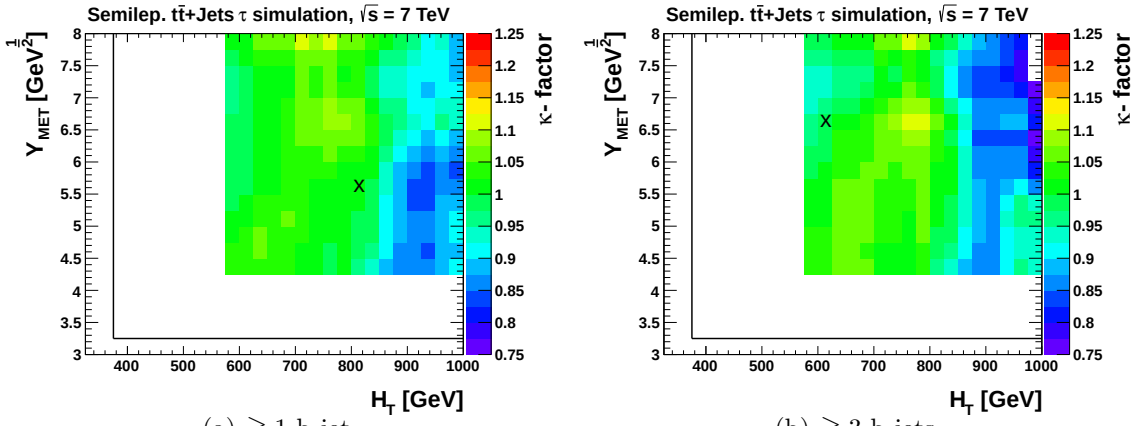

(a) $\geqq 1$ b-jet. (b) $\geqq 3$ b-jets.

Figure 7.20.: Correlation factor κ as a function of the H_T and Y_MET requirements by which the control and signal regions are separated from each other. The correlation factor is calculated from simulated events that pass the event selection in the inclusive 1-b-tag channel (left) and the inclusive 3-b-tag channel (right) for the lower requirements of $H_\mathrm{T} > 375$ GeV and $Y_\mathrm{MET} > 3.25$ GeV$^{\frac{1}{2}}$. A preselection on events that contain a semileptonically decaying $t\bar{t}$ pair with a tau at generator level is applied. The black crosses indicate the positions of the control and signal regions used in this thesis.

As can be seen, for the control and signal regions used in the inclusive 1-b-tag channel (left) and the inclusive 3-b-tag channel (right), whose positions are indicated by the black crosses, the correlation factor is roughly one and by this smaller than in semileptonic $t\bar{t}$ events with a muon or electron in the final state (cf. Section 7.2.3, Table 7.2). Also, the correlation factor is less dependent on the definition of the control and signal regions. The main difference with respect to the correlation in

semileptonic $t\bar{t}$ events with a muon or electron in the final state is found to originate from the lepton selection. While the lepton p_{T} requirement leads to a slight increase of κ for the case that the single muon or electron is directly produced in a W boson, this requirement results in a visible decrease of κ for the case that the single lepton is produced in the decay of a tau that originates from a W-boson decay.

7.3.2. Dileptonic $t\bar{t}$ Decays

In order to obtain a homogeneous background and to be able to combine results from different searches, events with a second isolated muon or electron that fulfills looser criteria are rejected (cf. Section 6.2.2). Since hadronically decaying taus are not affected by this, dileptonic $t\bar{t}$ decays where exactly one W boson decays into a hadronically decaying tau and a neutrino may pass the event selection. (Besides the jets that originate from the two bottom quarks and the hadronically decaying tau, at least one jet needed to be produced from initial and final state radiation, in order for the event to pass the jet selection.) Due to the two neutrinos that are produced along with the two leptons, dileptonic $t\bar{t}$ decays will on average result in final states with a larger missing transverse energy than semileptonic $t\bar{t}$ decays, but

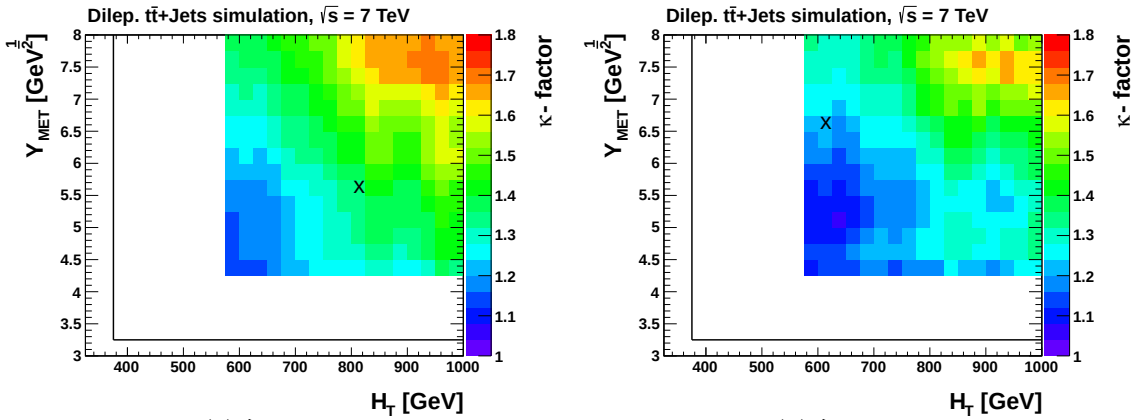

(a) $\geqq 1$ b-jet. (b) $\geqq 3$ b-jets.

Figure 7.21.: Correlation factor κ as a function of the H_{T} and Y_{MET} requirements by which the control and signal regions are separated from each other. The correlation factor is calculated from simulated events that pass the event selection in the inclusive 1-b-tag channel (left) and the inclusive 3-b-tag channel (right) for the lower requirements of $H_{\mathrm{T}} > 375$ GeV and $Y_{\mathrm{MET}} > 3.25\ \mathrm{GeV}^{\frac{1}{2}}$. A preselection on simulated events that contain a dileptonically decaying $t\bar{t}$ pair at generator level is applied. The black crosses indicate the positions of the control and signal regions used in this thesis.

a lower hadronic activity. Thus, the missing transverse energy will increase stronger with increasing H_{T} than in semileptonic $t\bar{t}$ events. As can be seen in Fig 7.21, this leads to a larger value of κ in both the inclusive 1-b-tag channel and the inclusive 3-b-tag channel and a stronger dependence of κ on the definition of the control and signal regions as in semileptonic $t\bar{t}$ events.

7.3.3. W+Jets

The main difference between $\mathrm{W}+\mathrm{Jets}$ events and semileptonic $t\bar{t}$ events with respect to the correlation between H_{T} and Y_{MET} results from the fact that the leptonically decaying W boson in the former type of event is not produced in a top quark decay. Before the jet selection, κ is smaller than one and decreases with increasing H_{T}. This suggests that the W boson in $\mathrm{W}+\mathrm{Jets}$ events carries one average a smaller p_{T} as in Semileptonic $t\bar{t}$ events with respect to H_{T}. By requiring events to contain four jets, at least one of which is b-tagged, the correlation factor κ increases. As can be seen in Fig. 7.22, after the event selection in the inclusive 1-b-tag channel κ is relatively stable against a shift of the control and signal regions. The correlation after the event selection in the inclusive 3-b-tag channel is not discussed, because the background from $\mathrm{W}+\mathrm{Jets}$ events is small in this channel (1.7%).

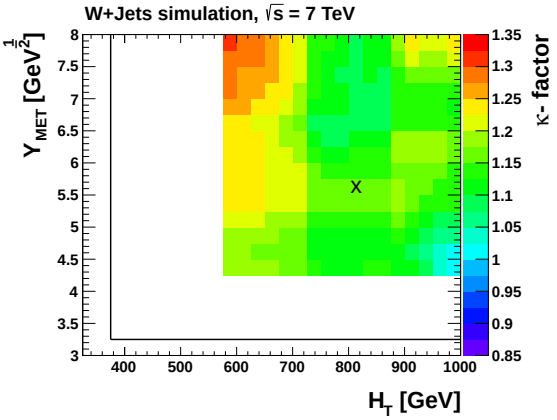

Figure 7.22.: Correlation factor κ as a function of the H_{T} and Y_{MET} requirements by which the control and signal regions are separated from each other. The correlation factor is calculated from simulated $\mathrm{W}+\mathrm{Jets}$ events that pass the event selection in the inclusive 1-b-tag channel for the lower requirements of $H_{\mathrm{T}} > 375$ GeV and $Y_{\mathrm{MET}} > 3.25$ GeV$^{\frac{1}{2}}$. The black cross indicates the position of the control and signal regions used in this channel.

7.3.4. Summary

In Table 7.4, the values of the correlation factor κ for the main Standard Model processes after the event selection in different exclusive and inclusive b-tag channels are shown. Also shown, is the correlation factor for single top events, whose contribution to the total Standard Model background amounts to 4.2% in the inclusive 1-b-tag channel and 3.6% in the inclusive 3-b-tag channel. The correlation factor is calculated from simulated events with $H_{\mathrm{T}} > 375$ GeV and $Y_{\mathrm{MET}} > 3.25$ GeV$^{\frac{1}{2}}$ for the two sets of control and signal regions defined in Section 7.1, Table 7.1. For the exclusive 1-b-tag channel and the exclusive 2-b-tag channel the same regions as for the inclusive 1-b-tag channel are used. Reflecting the small number of simulated events in the exclusive 0-b-tag channel, the same definition of control and signal regions as in the inclusive 3-b-tag channel is used. Although the inclusive 1-b-tag channel and the inclusive 3-b-tag channel are exploited for the interpretation, the number of observed and predicted events in the other b-tag channels are compared as well.

Table 7.4.: Correlation factor κ for the main Standard Model processes after the event selection in different b-tag channels. The correlation factor is calculated from simulated events with $H_{\mathrm{T}} > 375$ GeV and $Y_{\mathrm{MET}} > 3.25$ GeV$^{\frac{1}{2}}$ for the two sets of control and signal regions defined in Section 7.1, Table 7.1.

Sample	Signal Region				
	$H_{\mathrm{T}} > 800$ GeV, $Y_{\mathrm{MET}} > 5.5$ GeV$^{\frac{1}{2}}$			$H_{\mathrm{T}} > 600$ GeV, $Y_{\mathrm{MET}} > 6.5$ GeV$^{\frac{1}{2}}$	
	1 b-tag	2 b-tags	≥ 1 b-tag	0 b-tags	≥ 3 b-tags
semilep. $t\bar{t}$ e/μ	1.12 ± 0.04	1.18 ± 0.04	1.14 ± 0.04	1.11 ± 0.03	1.17 ± 0.04
semilep. $t\bar{t}$ τ	1.00 ± 0.08	1.03 ± 0.08	1.01 ± 0.07	0.97 ± 0.06	0.97 ± 0.06
dilep. $t\bar{t}$	1.34 ± 0.08	1.43 ± 0.09	1.36 ± 0.08	1.24 ± 0.06	1.24 ± 0.07
all $t\bar{t}$ + Jets	1.16 ± 0.02	1.22 ± 0.02	1.18 ± 0.01	1.14 ± 0.06	1.17 ± 0.02
all single top	1.14 ± 0.14	1.25 ± 0.16	1.18 ± 0.10	1.44 ± 0.49	1.40 ± 0.18
W + Jets	1.17 ± 0.05	1.24 ± 0.10	1.18 ± 0.04	1.25 ± 0.04	1.24 ± 0.19
all SM	1.19 ± 0.03	1.23 ± 0.02	1.20 ± 0.02	1.25 ± 0.04	1.19 ± 0.02

The overall value of the correlation factor κ is found to be consistent for all b-tag channels within the statistical uncertainties. Therefore, the value of $\kappa = 1.20 \pm 0.02$ obtained from simulated events in the inclusive 1-b-tag channel is used to describe the correlation in all channels in the following. At this point it should be noted that the overall value of κ is not simply the weighted average of the values obtained for the individual processes. For example, though the value of κ amounts to 1.18 for $t\bar{t}$ + Jets, W + Jets, and single top events in the inclusive 1-b-tag channel, the overall value obtained from simulated events is 1.20. This is because the shape of H_{T} and Y_{MET} is slightly different for the individual processes. (Even in the case that H_{T} and Y_{MET} were perfectly uncorrelated for all subprocesses, the resulting value of κ for the total Standard Model background could be different from one.)

Finally, the influence of the definition of the control and signal regions on the correlation factor κ is checked for the total Standard Model background. As can be seen in Fig 7.23, in both the inclusive 1-b-tag channel and the inclusive 3-b-tag channel, κ only slightly depends on the definition of the regions, which suggests that a global mismeasurement of H_{T} and $\not\!\!E_{\mathrm{T}}$ will not much affect the background prediction from data. The slight dependence on the Y_{MET} requirement results from the broadening of $p_{\mathrm{T}}^{\nu}/\sqrt{H_{\mathrm{T}}}$ and $(\not\!\!E_{\mathrm{T}} - p_{\mathrm{T}}^{\nu})/\sqrt{H_{\mathrm{T}}}$ with increasing H_{T}, as discussed for semileptonic $t\bar{t}$ events with a muon or electron in the final state in Section 7.2.4.

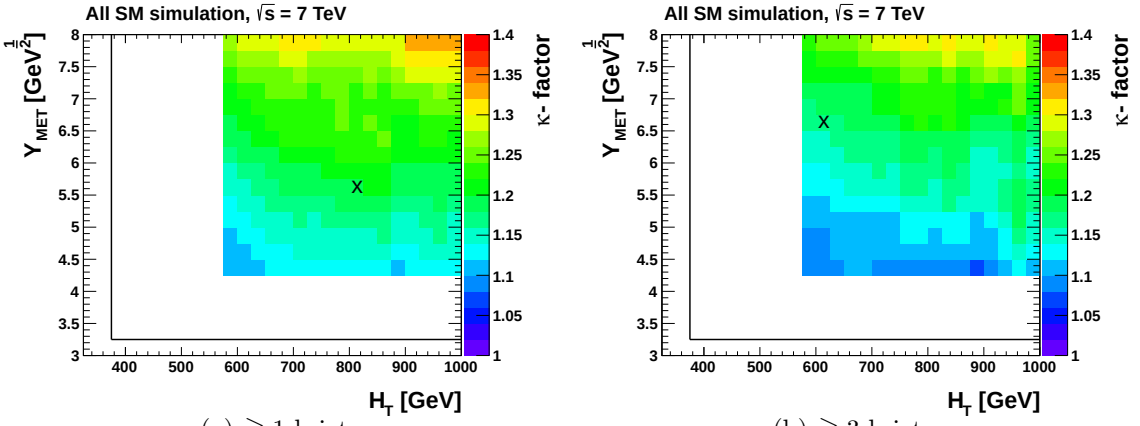

(a) $\geqq 1$ b-jet. (b) $\geqq 3$ b-jets.

Figure 7.23.: Correlation factor κ as a function of the H_{T} and Y_{MET} requirements by which the control and signal regions are separated from each other. The correlation factor is calculated from simulated events that pass the event selection in the inclusive 1-b-tag channel (left) and the inclusive 3-b-tag channel (right) for the lower requirements of $H_{\mathrm{T}} > 375$ GeV and $Y_{\mathrm{MET}} > 3.25$ GeV$^{\frac{1}{2}}$. The black crosses indicate the positions of the control and signal regions used in these channels.

8. Systematic Uncertainties

Based on the assumption that H_{T} and $Y_{\mathrm{MET}} \equiv \not{E}_{\mathrm{T}}/\sqrt{H_{\mathrm{T}}}$ are largely uncorrelated, the number of background events n_{D} in a potentially signal-enhanced region D at large H_{T} and Y_{MET} is predicted by the following factorization ansatz:

$$n_{\mathrm{D}} = \kappa \, n_{\mathrm{B}} \, \frac{n_{\mathrm{C}}}{n_{\mathrm{A}}} \, . \tag{8.1}$$

Here, n_{A}, n_{B}, and n_{C} denote the numbers of observed events in the control regions A, B, and C defined in Section 7.1.2, Table 7.1. Since a direct measurement of the correlation factor κ would be affected by a potential signal, its value of 1.20 ± 0.02 is taken from simulated events. By this, the background prediction depends on the event simulation, namely the modeling of the correlation between $\not{E}_{\mathrm{T}}$ and H_{T}. As discussed in Sections 7.2 and 7.3, in this search $\not{E}_{\mathrm{T}}$ mainly originates from the transverse momentum of a neutrino that is produced along with a charged lepton in a W-boson decay. For a given process, the neutrino momentum is expected to be modeled relatively well: The production of W bosons, both direct and in top-quark decays, is calculated at matrix-element level (cf. Section 4.3.2). Also, the branching ratios for the leptonic W-boson decay [20] and the polarization of W bosons produced in $t\bar{t}$ decays [140] are well known. The prediction of H_{T}, in contrast, depends on the simulation of parton showers and fragmentation processes, which is more subtle and requires a detailed study of theoretical uncertainties, as addressed in Section 8.1. In simulated events, this study suffers from relatively large statistical uncertainties and the unavailability of samples that are produced with different fragmentation models. Therefore, the exclusive 0-b-tag channel is exploited to cross check the prediction of κ from the event simulation in data. To a large extent, this channel can be considered as signal free, which is discussed in Section 8.2. The prediction of κ from simulated events is based on the assumption of certain object and event selection efficiencies that have been determined from data. The relevant experimental systematic uncertainties are investigated in Section 8.3. In Section 8.4, all systematic uncertainties - including the uncertainties due to the limited number of simulated events - are presented in terms of deviations from the correlation factor κ and the absolute number of background events in signal region D predicted by the event simulation. The statistical uncertainty on the numbers of observed events and the uncertainty on the predicted signal event yields are discussed in the context of the obtained results and their interpretation later in Section 9.

8.1. Theoretical Uncertainties

The theoretical uncertainties discussed in the following are related to the calculation of the hard scattering process and the simulation of initial and final state radiation, as described in Section 4.1. The uncertainty resulting from the simulation of fragmentation processes could be studied by comparing the predictions obtained from simulated event samples that are produced with the same matrix-element generator, e.g. MadGraph, but generator programs that use different hadronization models for the subsequent simulation steps, e.g. Pythia and Herwig. (In this case, also different parton shower models would be exploited.) However, mainly due to the limited computing resources such samples are not provided. Hence, this uncertainty cannot be studied directly. The non-perfect modeling of the detector response, including the simulation of the detector geometry, the magnetic field, and the interaction of final-state particles with the detector material, is implicitly accounted for by applying data-to-simulation scale factors. Since the corresponding uncertainties are dominated by the uncertainties on the measurement of object and event selection efficiencies, they are subject of Section 8.3. For a similar reason, the uncertainty that results from the modeling of pile-up interactions is discussed in Section 8.3.

8.1.1. Cross Sections

In contrast to the inclusive cross sections for $t\bar{t}+\text{Jets}$-, $W+\text{Jets}$-, and single-top-quark production, the cross sections at large H_T and Y_MET are not well known. To account for the corresponding uncertainty on the correlation between H_T and Y_MET, each of these cross sections is scaled up and down by a factor of 50%, respectively, and the uncertainty on κ is calculated. Since the correlation between H_T and Y_MET is similar for the main Standard Model processes (cf. Section 7.3), this uncertainty is small. In order to determine the effect on the absolute number of events predicted by the event simulation, the uncertainty on the cross section for $t\bar{t}+\text{Jets}$ production, which constitutes the largest background in the inclusive 1-b-tag channel (85%) and the inclusive 3-b-tag channel (95%), is calculated using MCFM 5.8 [141].

8.1.2. Factorization and Renormalization Scales

The matrix element of the hard scattering process depends on the energy scales at which the parton distribution functions and the running coupling constants are evaluated (cf. Sections 2.1.4 and 4.1). In order to determine the corresponding uncertainty on the correlation between H_T and Y_MET, the values for κ obtained from simulated $t\bar{t}+\text{Jets}$ events with systematic variations of the factorization and renormalization scales (cf. Section 4.3.2) are compared with the value derived from the $t\bar{t}+\text{Jets}$ sample without scale variations. Within the statistical uncertainties these values are compatible with each other. However, due to the small numbers of sim-

ulated events, the statistical uncertainties on the values of κ obtained from the samples with scale variations are large, which further motivates the cross check in the exclusive 0-b-tag channel. In order to determine the uncertainty on the absolute number of background events in signal region D predicted by the event simulation, the simulated $t\bar{t}+\text{Jets}$ events with scale variations are normalized using the same cross section as used for the normalization of $t\bar{t}+\text{Jets}$ events without scale variations. This is done because the uncertainty on the cross section, which partly arises from scale uncertainties, is separately accounted for (cf. Section 8.1.1). This uncertainty therefore only reflects a possible migration of events between signal region D and the control regions.

8.1.3. Matrix Element-Parton Shower Matching

Since the simulation of initial and final state radiation at matrix-element level usually provides a better description of the hard-jet multiplicity than the parton shower, all Standard Model background processes except for QCD-multijet production are simulated with MadGraph or Powheg interfaced to Pythia (cf. Section 4.3.2). In order to avoid a double-counting of simulated events with equivalent phase-space configurations, the parton shower needs to be matched to the matrix element. During the simulation of $t\bar{t}+\text{Jets}$ events with MadGraph interfaced to Pythia the MLM matching algorithm described in Section 4.1 is used for this purpose. A key parameter of this algorithm is the matching scale, i.e. the minimum p_{T} of the jets that are considered during the matching procedure. At particle level, jets with a p_{T} above the matching scale mostly originate from partons from the matrix element, while jets with a p_{T} below the matching scale are preferably described by the parton shower only. In principle, the choice of the matching scale should be arbitrary. However, as already addressed in the discussion of the jet multiplicity distribution in Sections 6.2.4 and 6.5, the parton shower does not seem to be very well suited to describe high-energetic jets. Vice versa, soft and collinear splittings cannot be calculated at matrix-element level. In order to determine the corresponding uncertainty, the predictions obtained from simulated $t\bar{t}+\text{Jets}$ events with systematic variations of the matching scale (cf. Section 4.3.2) are compared to the prediction derived from the simulated $t\bar{t}+\text{Jets}$ sample without scale variations. As in the case discussed in Section 8.1.2, the values for κ obtained from the samples with scale variations are compatible with the central value, but have large statistical uncertainties. The uncertainty on the absolute number of events in signal region D predicted by the event simulation is determined like the one resulting from factorization and renormalization scale uncertainties discussed above.

8.2. Cross Check in the 0-b-tag Channel

Since the theoretical uncertainties on the correlation factor κ cannot be studied extensively in simulated events (cf. Section 8.1), the exclusive 0-b-tag channel is exploited to cross check how well the correlation between H_{T} and Y_{MET} in data is predicted by the event simulation. Assuming the exclusive 0-b-tag channel to be signal free, the difference between the predicted and the observed values for κ can be interpreted as theoretical uncertainty on the background prediction in this channel. (The experimental uncertainties largely cancel out by the factorization ansatz, which is discussed later in Section 8.3). This uncertainty can be taken as measure for the theoretical uncertainty on κ in the inclusive 1-b-tag channel and the inclusive 3-b-tag channel. The fact that the exclusive 0-b-tag channel (30% $t\bar{t}+\,$Jets, 64% $W+\,$Jets) is differently composed than the inclusive 1-b-tag channel (85% $t\bar{t}+\,$Jets, 10% $W+\,$Jets) and the inclusive 3-b-tag channel (95% $t\bar{t}+\,$Jets, 2% $W+\,$Jets) does not poses a large problem. The corresponding uncertainty is small and mostly accounted for by varying the cross sections of the main background processes up and down (cf. Sections 8.1.1 and 8.4).

The critical point of this cross check is the assumption that the exclusive 0-b-tag channel is signal free. Assuming the production of sparticles to result in states with at least two bottom quarks, the signal contamination in this channel will be small. When interpreting results in the context of the four-top-quark simplified model, the assumption of the exclusive 0-b-tag channel being signal free is even more justified. However, in non-simplified models, e.g. the CMSSM, sparticle decays that do not result in bottom-quark states may affect the cross check in this channel. For example, in benchmark scenario LM6, the signal-to-background ratio in the exclusive 0-b-tag channel (0.012) is larger than that in the inclusive 1-b-tag channel (0.009) and only slightly smaller than the ratio in the inclusive 3-b-tag channel (0.015). It might be argued that the exclusive 0-b-tag channel can be considered as signal, because previous analyses have already excluded this part of the phase space. Based on an integrated luminosity of $\mathcal{L} = 1.1\,\mathrm{fb}^{-1}$ a search for Supersymmetry in final states with a single lepton, jets, and missing transverse energy at a center-of-mass energy of $\sqrt{s} = 7$ TeV had been performed [142]. (Meanwhile, an update of this search that is based on the full set of data recorded in 2011 is published [143].) This search uses two complementary analysis methods. One of these is the *Lepton Spectrum method* (LS method), which exploits the correlation between the charged lepton and the antineutrino produced in leptonic W-boson decays to predict the $\not\!\!E_{\mathrm{T}}$ distribution of background events from the observed lepton p_{T} spectrum.[1] Based on the event preselection and the jet selection described in Sections 6.2 and 6.3, respectively, a deviation from the Standard Model prediction in a signal region defined by $H_{\mathrm{T}} >$

[1] Up to effects resulting from a preferred polarization of the W boson in association with the different masses of the charged lepton and the antineutrino, the p_{T} distributions are the same.

500 GeV and $\not\!\!E_{\mathrm{T}} > 250$ GeV is searched for. The number of predicted background events $\hat{n}_{\mathrm{LS}} = 49.8 \pm 8.8 \pm 10.8$ in this region is found to be compatible with the number of observed events $n_{\mathrm{LS}} = 52$. (Also in the updated search no deviation from the Standard Model prediction was observed.) As can be seen in Fig. 8.1, the signal region examined by the LS method has a large overlap with the signal regions examined by the factorization method.

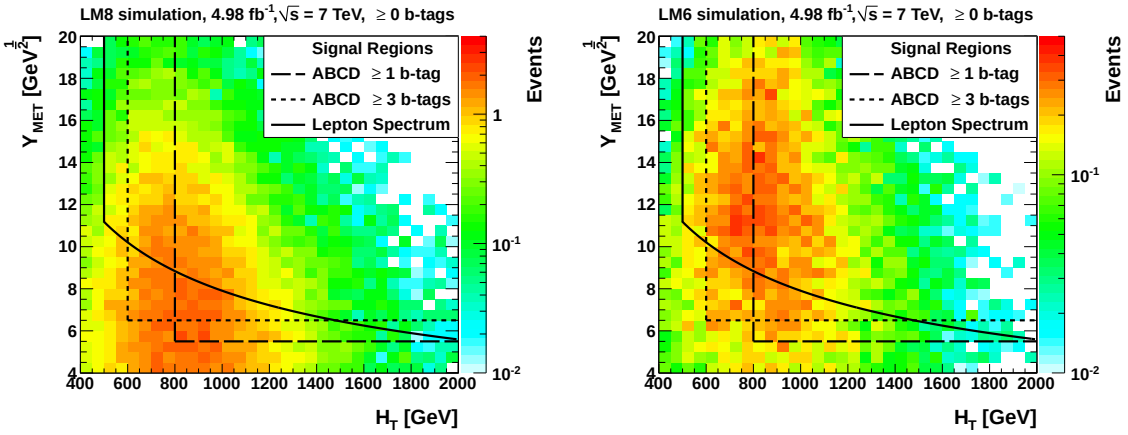

Figure 8.1.: Distribution of simulated signal events in the benchmark scenarios LM8 (left) and LM6 (right) after the event selection in the inclusive 0-b-tag channel. The black lines mark the signal regions examined by the factorization ("ABCD") and the Lepton Spectrum method.

Within the uncertainties on the number of events predicted by the LS method, the inclusive 0-b-tag channel could therefore be regarded as signal free. To a lesser extent this would also apply for the exclusive 0-b-tag channel then.

In the exclusive 0-b-tag channel a value of $\kappa = 1.19 \pm 0.13$ is observed, while a value of $\kappa = 1.25 \pm 0.04$ is extracted from the event simulation. Although these values are consistent within their statistical uncertainties, a smaller value of κ in data cannot be excluded. As measure for the uncertainty that results from this cross check the statistical uncertainties on the observed and predicted values of κ in the exclusive 0-b-tag channel are summed up in quadrature and assigned to the values of κ in the other b-tag channels.

8.3. Experimental Uncertainties

In order to account for different selection efficiencies of physics objects in data and simulated events, the CMS collaboration has determined data-to-simulation scale factors. These are applied on the level of reconstructed objects in simulated events, as described in Section 5. In addition, scale factors that account for different trigger

and lepton reconstruction efficiencies have been determined [123]. These are applied on the level of preselected events, as discussed in Section 6.2. The effects of the corresponding uncertainties are studied separately by varying up and down each scale factor by ±1 standard deviation. Finally, the uncertainties that result from the modeling of pile-up interactions and the measurement of the integrated luminosity are addressed.

8.3.1. Lepton Energy Scale

The relative uncertainty on the measured transverse momentum of the selected lepton amounts 1% for muons, 1% for electrons in the barrel region, and 2.5% for electrons in the endcap region. In order to study the corresponding uncertainty, the transverse momentum of the selected lepton is shifted up and down accordingly. The resulting imbalance on the total transverse momentum is propagated to the calculation of the missing transverse energy.

8.3.2. Jet Energy Scale

To correct for the non-perfect jet energy response, dedicated calibration factors are applied to the four-momenta of reconstructed jets in data and simulated events (cf. Section 5.5). The remaining differences between data and simulated events are accounted for by applying scale factors to the measured four-momenta (*residual corrections*). The combined uncertainty on the energy scale of jets with $|\eta| = 0.0$ ($|\eta| = 2.0$) ranges from 12% (15%) at a jet p_{T} of 10 GeV to 2.5% (3%) at a jet p_{T} of 40 GeV and 1.5% (2%) for jet p_{T} larger than 100 GeV [129]. In the forward region ($|\eta|$=4.0), the uncertainty decreases from 15% at a jet p_{T} of 10 GeV to 2.5% at a jet p_{T} of 70 GeV. From 70 GeV onwards, the uncertainty in the forward region increases again. The effect of the jet energy scale (JES) uncertainty is determined by shifting the four-momenta of reconstructed jets with $p_{\mathrm{T}} > 10$ GeV and $|\eta| < 4.7$ in simulated events up and down by the measured uncertainties. The resulting imbalance on the total transverse momentum is propagated to the calculation of $\not\!\!E_{\mathrm{T}}$. In this thesis, $\not\!\!E_{\mathrm{T}}$ is not adjusted for jet energy scale corrections by default. (So-called *type-1* and *type-2* corrections are not applied.) Following the recommendations of the CMS jet and missing transverse energy working group [144], the residual corrections are taken as measure for the corresponding uncertainty. Therefore, a total uncertainty of

$$\sigma(E_j) = \sqrt{\sigma_{\mathrm{JES}}(E_j)^2 + (E_j^{\mathrm{residual}})^2} \tag{8.2}$$

is assigned to each jet j. Here, $\sigma_{\mathrm{JES}}(E_j)$ and E_j^{residual} denote the absolute values of the jet energy scale uncertainty and the residual correction, respectively. The total

uncertainty on the missing transverse energy then reads

$$\sigma(\not{E}_{\mathrm{T}}) = \left| \vec{\not{E}}_{\mathrm{T}} - \sum_{j} \sigma(E_j)\, \vec{e}_j \right| , \tag{8.3}$$

where j runs over all reconstructed jets with $p_{\mathrm{T}} > 40$ GeV and $|\eta| < 2.4$, and $\vec{e}_j$ denotes the unit vectors along the jet axes.

8.3.3. Jet Energy Resolution

To account for different jet energy resolutions in data and simulated events, the four-momenta of reconstructed jets in simulated events are scaled by the factor

$$c = 1 + \frac{SF \cdot (p_{\mathrm{T}}^{\mathrm{reco}} - p_{\mathrm{T}}^{\mathrm{particle}})}{p_{\mathrm{T}}^{\mathrm{reco}}} , \tag{8.4}$$

where SF denotes an η-dependent scale factor provided by the CMS collaboration and $p_{\mathrm{T}}^{\mathrm{reco}}$ and $p_{\mathrm{T}}^{\mathrm{particle}}$ represent the transverse momenta of the reconstructed jets and the underlying particle-level jets, respectively. The effect of the jet energy resolution (JER) uncertainty is investigated by shifting the scale factor SF up and down by its η-dependent uncertainty. This uncertainty amounts 6% for $|\eta| < 1.7$, 8% for $1.7 < |\eta| < 2.3$, and 16% for $|\eta| > 2.3$ [129, 145]. The variation is propagated to the calculation of $\not{E}_{\mathrm{T}}$.

8.3.4. Unclustered Energy Scale

The discussion of the jet energy scale uncertainty in Section 8.3.2 is restricted to jets with $p_{\mathrm{T}} > 10$ GeV. To study the effect on $\not{E}_{\mathrm{T}}$ that arises from the uncertainty on the energy scale of the *unclustered energy*, the four-momenta of reconstructed jets with $p_{\mathrm{T}} < 10$ and $|\eta| < 4.7$ are shifted up and down by 10% and the resulting imbalance on the total transverse momentum is propagated to the calculation $\not{E}_{\mathrm{T}}$.

8.3.5. Trigger Efficiency

Since no trigger selection is applied on simulated events, the latter are scaled down by the lepton trigger efficiency of 97% (cf. Section 6.2.2). The corresponding uncertainty on the number of events in signal region D predicted by the event simulation is estimated to amount 0.2%. To account for the inefficiency of the $\not{H}_{\mathrm{T}}$ parts of the cross triggers in the region 60 GeV $< \not{E}_{\mathrm{T}} <$ 100 GeV, selected data events are weighted by the inverse trigger efficiency (cf. Section 6.2.3).

8.3.6. Lepton Reconstruction Efficiency

The lepton reconstruction efficiency is measured using the tag-and-probe technique, as described in Section 5.2. Since the efficiencies in data and simulated events are well compatible [123], a scale factor of one is applied to simulated events. The uncertainty on the scale factor varies from 1% for the muon reconstruction efficiency in run period A, 1.5% for the electron reconstruction efficiency in both run periods A and B, and 2.5% for the muon reconstruction efficiency in run period B. In total, an uncertainty of 3% is assigned to the lepton trigger and reconstruction efficiency.

8.3.7. B-Jet Identification Efficiency

In order to correct for different b-tag efficiencies and mistag rates in data and simulated events, the CMS collaboration has determined flavor-, p_{T}-, and η-dependent scale factors [133], which are applied to the tagging efficiencies of selected jets in simulated events. From these efficiencies the probabilities that a certain number of jets is tagged as b-jet are calculated on a per-event basis and applied as weights to simulated events, as described in Section 6.4. To determine the effect of the uncertainties on the b-tag efficiency and mistag rates, the scale factors are shifted up and down by the measured uncertainties and the event weights are recalculated. This is done separately for the b-tag efficiency and the udsg-mistag rate. The uncertainties on the corresponding scale factors are in the order of a few percent. So far, the CMS-collaboration has not measured the c-mistag rate. Therefore, the b-tag efficiency scale factor with twice its uncertainty is applied on the c-mistag rate. Since both scale factors are conservatively taken as correlated, they are simultaneously shifted up and down.

8.3.8. Pile-Up Simulation

Simulated events are reweighted such that the pile-up distributions of simulated events and data match (cf. Section 4.3.2). The number of pile-up interactions in data is estimated from the instantaneous luminosity and the total inelastic proton-proton cross section (cf. Section 4.1). Its uncertainty is 3.6% [146]. To account for a possible mismodeling of minimum-bias events with Pythia, an additional uncertainty of 3% is assigned to the number of pile-up interactions. Summed up in quadrature, the uncertainties amount 5% and are investigated by reweighting simulated events such that the mean number of pile-up interactions is shifted up and down accordingly.

8.3.9. Integrated Luminosity

The uncertainty of the luminosity measurement is determined to be 2.2% [147].

8.4. Summary

The systematic uncertainties that may differently effect the numbers of selected events in the control and signal regions are propagated to the correlation factor κ. Systematic uncertainties that only effect the overall normalization, such as the uncertainty on the total integrated luminosity, cancel out in the factorization method. Since the value of the correlation factor κ is found to be consistent for all b-tag channels within the statistical uncertainties, the value of $\kappa = 1.20 \pm 0.02$ obtained from simulated events in the inclusive 1-b-tag channel is used to describe the correlation in all channels. In Table 8.1, the relative systematic and statistical uncertainties on the this value are shown. The control and signal regions that correspond to the different exclusive and inclusive b-tag requirements are defined in Section 7.3.4, Table 7.4. Assuming that they are uncorrelated, all systematic uncertainties listed in Table 8.1 are added in quadrature.

Table 8.1.: Uncertainties on the correlation factor κ for different exclusive and inclusive b-tag requirements. The control and signal regions that correspond to these requirements are defined in Section 7.3.4, Table 7.4. The row labeled "0 b-tag channel" addresses the uncertainty on κ that results from the cross check in the exclusive 0-b-tag channel. The variations of the lepton energy scale, the jet energy scale, the jet energy resolution, and the unclustered energy scale are propagated to $\not\!\!E_{\mathrm{T}}$. The uncertainty on the b-tag efficiency includes the uncertainty on the c-mistag rate. All systematic uncertainties are added in quadrature.

Uncertainty	$\Delta\kappa$ 0 b-tags	$\Delta\kappa$ 1 b-tag	$\Delta\kappa$ 2 b-tags	$\Delta\kappa$ $\geqq 1$ b-tag	$\Delta\kappa$ $\geqq 3$ b-tags
Cross sections	3.4%	1.0%	2.0%	0.4%	1.4%
0 b-tag channel	10.0%	10.0%	10.0%	10.0%	10.0%
Lepton energy scale	1.2%	1.5%	1.7%	1.6%	1.2%
Jet energy scale	2.0%	2.7%	1.3%	2.0%	0.4%
Jet energy resolution	1.1%	2.1%	3.0%	2.4%	1.5%
Unclustered energy scale	0.5%	0.5%	1.1%	0.8%	0.4%
B-tag efficiency	0.1%	0.2%	0.3%	$< 0.1\%$	0.3%
udsg-mistag rate	0.1%	0.1%	0.2%	$< 0.1\%$	0.2%
Pile-up simulation	0.7%	0.6%	0.8%	0.7%	1.9%
Total systematic uncert.	10.9%	10.7%	10.9%	10.7%	10.5%
Statistical uncert. on κ	3.8%	3.7%	2.5%	2.3%	2.1%

Also shown in Table 8.1 is the statistical uncertainty on κ due to the limited number of simulated events. As can bee seen, by far the largest contribution to the total systematic uncertainty results from the cross check in the exclusive 0-b-tag channel. (Summed up in quadrature, the other systematic uncertainties only amount 3 to 4%.) The assigned uncertainty of 10% obtained from this cross check mainly results from the large statistical uncertainty on the observed value of κ in this channel. The modeling of the correlation between H_{T} and Y_{MET} could indeed be much better than this cross check suggests. Hence, the accuracy of the data-driven background prediction could benefit from a more extensive production of simulated events for the study of theoretical uncertainties. As addressed before, here, the limiting factor are the available computing resources. An accurate simulation of background processes using MadGraph or Powheg for the matrix-element calculation and the full CMS detector simulation is very time-consuming (see also Section 4.1). As can be seen in Table 8.1, the experimental systematic uncertainties largely cancel out. As an example, an upwards shift of the jet energy scale leads to a larger H_{T}. Events in the regions A and C might be shifted to the regions B and D. But, given that H_{T} and Y_{MET} are nearly uncorrelated, the prediction for the events in region D, which is proportional to the number of events in region B, increases by the same amount.

The systematic experimental uncertainties and the statistical uncertainty on the absolute number of events, in contrast, are large. As can be seen in Table 8.2, the total systematic uncertainty on the number of events in region D predicted by the event simulation amounts 24 to 30%. This nicely demonstrates the advantage of the data-driven background prediction. For example, the JES uncertainty on κ amounts 1 to 3%, while the JES uncertainty on the absolute number of events in region D predicted by the event simulation ranges from 17% to 19%. Besides the jet energy scale, the model uncertainty significantly contributes to the total systematic uncertainty on the number of events in region D. This uncertainty comprises the uncertainties on the cross section, the renormalization, factorization, and matching scales, and is evaluated in simulated $t\bar{t}+\mathrm{Jets}$ events, as described in Sections 8.1.1, 8.1.2, and 8.1.3. In the absence of samples that contain simulated $W+\mathrm{Jets}$ and single top events with scale variations, this uncertainty is also applied to the other Standard Model processes. Hence, it does not depend on the b-tag channel. In the exclusive 0-b-tag channel also the uncertainty on the jet energy resolution significantly contributes. Summed up in quadrature, the uncertainty on the b-tag efficiency, which includes the uncertainty on the c-mistag rate, and the uncertainty on the udsg-mistag rate amounts 9.8% in the inclusive 3-b-tag channel and 2 to 4% in the other b-tag channels. Conveniently, the corresponding uncertainty on κ (0.4%) almost completely cancels out. All other systematic uncertainties are in the order of a few percent.

Table 8.2.: Uncertainties on the number of Standard Model events n_D in the signal regions predicted by the event simulation for different exclusive and inclusive b-tag requirements. The signals regions that correspond to these requirements are defined in Section 7.3.4, Table 7.4. The variations on the lepton energy scale, the jet energy scale, the jet energy resolution, and the unclustered energy scale are propagated to $\not\!\!E_{\mathrm{T}}$. The uncertainty of the b-tag efficiency includes the uncertainty on the c-mistag rate. All systematic uncertainties are added in quadrature.

Uncertainty	ΔN_{D} 0 b-tags	ΔN_{D} 1 b-tag	ΔN_{D} 2 b-tags	ΔN_{D} $\geqq 1$ b-tag	ΔN_{D} $\geqq 3$ b-tags
Model uncertainty	16.0%	16.0%	16.0%	16.0%	16.0%
Lepton energy scale	0.6%	2.4%	2.1%	1.9%	2.5%
Jet energy scale	17.8%	16.7%	19.2%	17.5%	17.3%
Jet energy resolution	17.1%	4.8%	6.2%	5.3%	5.4%
Unclustered energy scale	0.1%	0.9%	1.1%	1.0%	0.5%
Lepton Trigger & ID	3.0%	3.0%	3.0%	3.0%	3.0%
B-tag efficiency	2.6%	1.2%	4.1%	1.5%	7.8%
Mistag rate	2.0%	0.8%	1.3%	1.3%	5.9%
Pile-up simulation	2.7%	2.2%	0.8%	1.6%	1.1%
Luminosity	2.2%	2.2%	2.2%	2.2%	2.2%
Total systematic uncert.	30.0%	24.2%	26.5%	24.8%	26.5%
Statistical uncertainty	11.0%	8.3%	8.6%	5.6%	3.4%

9. Results and Interpretation

After selecting events with a single isolated muon or electron, four jets, $H_{\mathrm{T}} > 375$ GeV, and $\not\!\!E_{\mathrm{T}} > 60$ GeV, the number of Standard Model background events in different signal regions is predicted from data by a factorization method with H_{T} and $Y_{\mathrm{MET}} \equiv \not\!\!E_{\mathrm{T}}/\sqrt{H_{\mathrm{T}}}$, as described in Section 7. By this, the systematic uncertainties largely cancel out, as discussed in Section 8. In this section, the obtained results are presented and interpreted. In Section 9.1, the number of observed events is compared to the number of events predicted by the factorization method. Since no significant deviation from the Standard Model prediction is observed, results are used to set limits upon the parameters of the Constrained Minimal Supersymmetric Standard Model (cf. Section 2.2.2) and the four-top quark simplified model introduced in Section 2.2.4. This is done using the CLs method with a test statistic given by a profile likelihood ratio, as described in Section 9.2. Finally, exclusion limits are presented and compared to limits obtained from other searches at the CMS experiment in Section 9.3.

9.1. Results

In Table 9.1, the number of events n_{D} observed in the different signal regions, as defined in the first column, and the number of Standard Model background events $\hat{n}_{\mathrm{D}}$ predicted from data by the factorization method, as described in Section 7.1, are shown. Since the value of the correlation factor κ is found to be consistent for all b-tag channels within the statistical uncertainties (cf. Section 7.3.4, Table 7.4), the value of $\kappa = 1.20 \pm 0.02$ obtained from simulated events in the inclusive 1-b-tag channel is used to describe the correlation in all channels. Here, the error of 0.02 is statistical only. The first uncertainties on the numbers in Table 9.1 are statistical and the second systematic. The systematic uncertainties on the number of events predicted by the factorization method equals the uncertainties of the correlation factor κ, as summarized in Section 8.4, Table 8.1. As can be seen, the number of observed events and the number of background events predicted by the data-driven method are in good agreement in all channels. No significant deviation from the Standard Model prediction is observed.

Also shown are the number of simulated SM events n_{D} in the different signal regions and the number of SM events $\hat{n}_{\mathrm{D}}$ calculated with the factorization method from simulated events. These numbers are in good agreement as well, showing the validity of the factorization ansatz for the background estimation.

Table 9.1.: Number of observed and simulated events n_{D} in the different signal regions and number of data and simulated events $\hat{n}_{\mathrm{D}}$ determined by the factorization method. The first uncertainties are statistical and the second systematic. The systematic uncertainties on $\hat{n}_{\mathrm{D}}$ in data are equal to the uncertainties on κ, as summarized in Section 8.4, Table 8.1. Published in [7].

Signal region	Sample	n_{D}	$\hat{n}_{\mathrm{D}}$
0 b-tags $H_{\mathrm{T}} > 600$ GeV $Y_{\mathrm{MET}} > 6.5\ \sqrt{\mathrm{GeV}}$	Data	155	$162 \pm 11 \pm 18$
	Σ SM	$182 \pm 22 \pm 55$	$186 \pm 19 \pm 40$
	Σ SM+LM6	$221 \pm 22 \pm 59$	$191 \pm 19 \pm 40$
	Σ SM+LM8	$218 \pm 24 \pm 61$	$194 \pm 20 \pm 41$
1 b-tag $H_{\mathrm{T}} > 800$ GeV $Y_{\mathrm{MET}} > 5.5\ \sqrt{\mathrm{GeV}}$	Data	51	$53.9 \pm 6.3 \pm 5.9$
	Σ SM	$74 \pm 5 \pm 18$	$74 \pm 4 \pm 14$
	Σ SM+LM6	$95 \pm 5 \pm 21$	$77 \pm 4 \pm 14$
	Σ SM+LM8	$132 \pm 6 \pm 29$	$90 \pm 5 \pm 16$
2 b-tags $H_{\mathrm{T}} > 800$ GeV $Y_{\mathrm{MET}} > 5.5\ \sqrt{\mathrm{GeV}}$	Data	27	$36.0 \pm 5.1 \pm 4.0$
	Σ SM	$50 \pm 3 \pm 13$	$47.5 \pm 2.1 \pm 8.1$
	Σ SM+LM6	$62 \pm 3 \pm 15$	$49.0 \pm 2.2 \pm 8.2$
	Σ SM+LM8	$103 \pm 5 \pm 24$	$62.7 \pm 2.7 \pm 9.7$
≥ 1 b-tag $H_{\mathrm{T}} > 800$ GeV $Y_{\mathrm{MET}} > 5.5\ \sqrt{\mathrm{GeV}}$	Data	84	$98 \pm 8 \pm 11$
	Σ SM	$136 \pm 6 \pm 34$	$134 \pm 5 \pm 24$
	Σ SM+LM6	$172 \pm 6 \pm 39$	$139 \pm 5 \pm 24$
	Σ SM+LM8	$280 \pm 8 \pm 63$	$177 \pm 6 \pm 28$
≥ 3 b-tags $H_{\mathrm{T}} > 600$ GeV $Y_{\mathrm{MET}} > 6.5\ \sqrt{\mathrm{GeV}}$	Data	10	$13.8 \pm 3.2 \pm 1.5$
	Σ SM	$22.6 \pm 1.1 \pm 6.0$	$21.3 \pm 0.9 \pm 4.0$
	Σ SM+LM6	$27.1 \pm 1.1 \pm 6.6$	$21.9 \pm 0.9 \pm 4.1$
	Σ SM+LM8	$66 \pm 4 \pm 15$	$34.3 \pm 1.8 \pm 4.8$

The systematic uncertainties on the number of simulated Standard Model events n_{D} are summarized in Section 8.4, Table 8.2. As already addressed in Section 8.4, a comparison of this number with the number of events $\hat{n}_{\mathrm{D}}$ predicted from data nicely demonstrates the advantage of the data-driven background estimation method. While the systematic uncertainties on the number of background events amount 24 to 30% when predicting the background from simulated events directly, they largely cancel out in the factorization method. For illustration purposes the results are graphically shown in Fig. 9.1. Here, the statistical and systematic uncertainties are summed up in quadrature. The dashes on the vertical error bars mark the contributions of the statistical uncertainties.

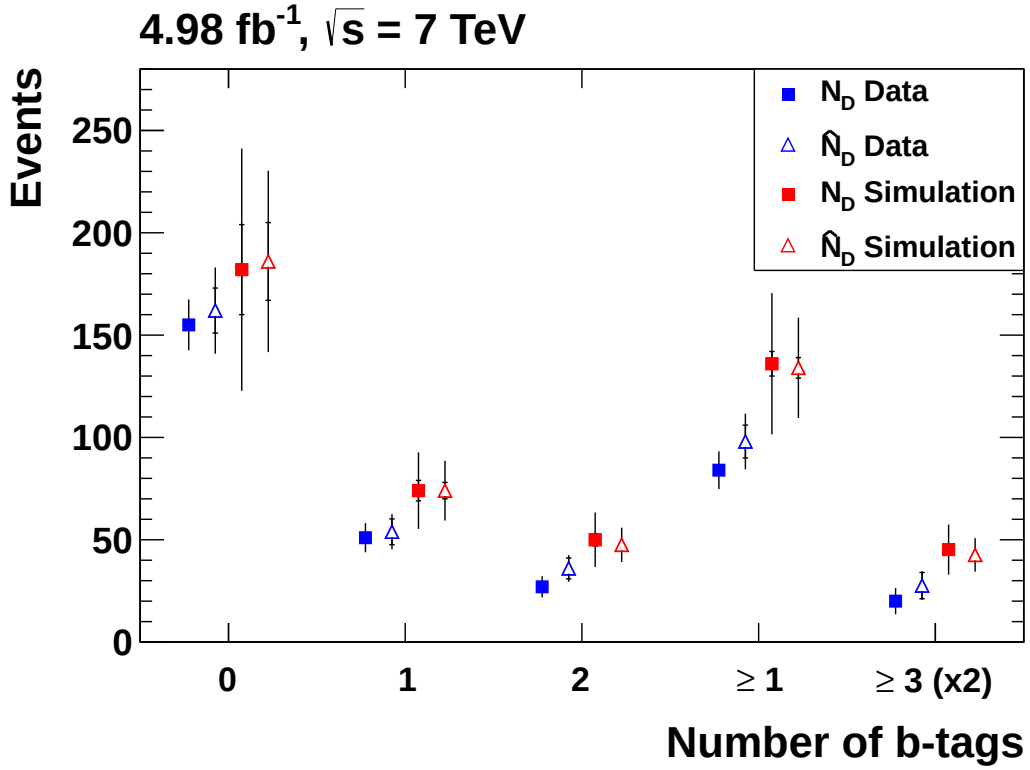

Figure 9.1.: Number of observed and simulated events n_{D} in the different signal regions and number of data and simulated events $\hat{n}_{\mathrm{D}}$ determined by the factorization method. The vertical error bars represent the statistical and systematic uncertainties summed up in quadrature. The dashes on the error bars mark the contributions of the statistical uncertainties. For better visibility, the numbers of events in the inclusive 3-b-tag channel and their uncertainties are scaled up by a factor 2.

In order to illustrate the sensitivity of the search to a deviation from the SM prediction that originates from Supersymmetry with light top and bottom squarks, the number of simulated Standard Model events with contributions of the CMSSM benchmark scenarios LM6 ("Σ SM+LM6") and LM8 ("Σ SM+LM8") added are shown. Comparing these numbers with the numbers of simulated Standard Model events without contributions from the benchmark scenarios, the search seems in particular to be sensitive to LM8-type scenarios. However, it should be noted that this, though associated with the difference in event topology, does not result from the latter. It simply reflects the larger production-cross section of third generation squarks in scenario LM8 due to the different mass hierarchy ($m_{\tilde{t}_1}, m_{\tilde{b}_1} < m_{\tilde{g}} < m_{\tilde{q}}$) and lighter squark and gluino masses (cf. Appendix B.1). If third generation squarks in scenario LM6 ($m_{\tilde{t}_1}, m_{\tilde{b}_1} < m_{\tilde{q}} < m_{\tilde{g}}$) were produced with the the same frequency

as in scenario LM8, the search would be equally sensitive to both scenarios.

Finally, also the number of background plus signal events $\hat{n}_{\mathrm{D}}$ calculated with the factorization method from simulated events are shown in Table 9.1. These numbers systematically lie below the true numbers of simulated events n_{D}, posing a severe issue that needs to be taken into account when setting exclusion limits: Since signal events may also populate the control regions (for illustration see Section 7.1.2, Fig. 7.4), the number of observed events in these regions will in general not equal the number of Standard Model events.

9.2. Likelihood Model

The expected mean number of events n_i in control or signal region i will be composed of b_i background events and s_i signal events,

$$n_i = b_i + s_i. \tag{9.1}$$

It is therefore convenient to rewrite the factorization ansatz (7.1) introduced in Section 7.1 as

$$\frac{b_{\mathrm{A}}}{b_{\mathrm{C}}} = \kappa \, \frac{b_{\mathrm{B}}}{b_{\mathrm{D}}} \, . \tag{9.2}$$

The number of signal events in region i is given by

$$s_i = s \, L \, \sigma_s \, \epsilon_i \, , \tag{9.3}$$

where L is the integrated luminosity, σ_s the cross section of sparticle production in the considered supersymmetric scenario, and ϵ_i the overall efficiency for selecting a signal event in region i. The latter includes the geometric and kinematic acceptance.[1] The parameter s is a signal strength parameter. While the selection efficiencies ϵ_i are derived from simulated events, the numbers of Standard Model background events b_i are treated as nuisance parameters.

9.2.1. Likelihood Function

Subject of the limit setting is the derivation of an upper limit s_{UL} on the signal strength parameter s. Then, an upper limit $\sigma_{s_{\mathrm{UL}}}$ on the cross section σ_s can be obtained. For this purpose a *likelihood function* is constructed. This function basically describes the probability of observing n_{A}, n_{B}, n_{C}, and n_{D} events in the control and

[1] Often, ϵ_i is referred to as "efficiency times acceptance", where "efficiency" refers to the efficiency of selecting an event that fulfills certain geometrical and kinematic acceptance criteria at parton or particle level.

signal regions A, B, C, and D given a particular supersymmetric scenario as described by the parameters σ_s and $\boldsymbol{\epsilon} \equiv (\epsilon_\mathrm{A}, \epsilon_\mathrm{B}, \epsilon_\mathrm{C}, \epsilon_\mathrm{D})^T$. The probability of observing n_D events in signal region D follows a Poisson distribution with the mean value

$$\kappa \frac{b_\mathrm{B}\, b_\mathrm{C}}{b_\mathrm{A}} + s_\mathrm{D}\,. \tag{9.4}$$

Similarly, the probabilities of observing n_A, n_B, and n_C events in the control regions A, B, and C follow Poisson distributions with the mean values $b_i + s_i$. In this way, the possible contamination of the control regions by signal events is taken into account.

In addition, two log-normal distributions $\log\mathcal{N}\big(\hat{L}, L, \sigma_L\big)$ and $\log\mathcal{N}\big(\kappa_\mathrm{sim}, \kappa, \sigma_{\kappa_\mathrm{sim}}\big)$ are introduced in the likelihood function. These model the probability distribution of the luminosity L and the correlation factor κ. Here, $\hat{L}$ denotes the measured value of the integrated luminosity, σ_L its uncertainty, κ_sim the value of kappa obtained from simulated events, and $\sigma_{\kappa_\mathrm{sim}}$ the systematic uncertainties on κ_sim.

The event selection efficiencies are modeled through a multi-dimensional Gaussian,

$$\mathcal{G}\big(\,\langle\boldsymbol{\epsilon}\rangle_\mathrm{sim}, \boldsymbol{\epsilon}, M_{ij}\,\big) = \frac{1}{(2\pi)^2\sqrt{\det M}} \exp\left(-\big(\boldsymbol{\epsilon} - \langle\boldsymbol{\epsilon}\rangle_\mathrm{sim}\big)^T \frac{M^{-1}}{2} \big(\boldsymbol{\epsilon} - \langle\boldsymbol{\epsilon}\rangle_\mathrm{sim}\big)\right) \tag{9.5}$$

where $\langle\boldsymbol{\epsilon}\rangle_\mathrm{sim}$ represents the vector of signal-event selection efficiencies predicted by the event simulation. The matrix M is defined as

$$M_{ij} = \sum_\alpha \Delta\epsilon_i(\alpha)\Delta\epsilon_j(\alpha), \quad i,j = \mathrm{A},\mathrm{B},\mathrm{C},\mathrm{D}. \tag{9.6}$$

Here $\Delta\epsilon_i(\alpha)$ denotes the shift in the selection efficiency in region i due to ±1 standard variation of some experimental quantity α, as discussed in Section 8.3. By this, the correlation of experimental uncertainties between the four regions is taken into account. In the case of asymmetric shifts, i.e. when the absolute value of the shift in ϵ_i is different for upwards and downwards variation of some quantity α, the magnitude of $\Delta\epsilon_i$ is chosen to be the larger of the two. The total likelihood function then reads:

$$\begin{aligned}\mathcal{L} \equiv\ & \mathrm{Poisson}\left(n_\mathrm{D} \,\middle|\, \kappa\frac{b_\mathrm{B} b_\mathrm{C}}{b_\mathrm{A}} + s_\mathrm{D}\right) \times \left(\prod_{i=\mathrm{A},\mathrm{B},\mathrm{C}} \mathrm{Poisson}(n_i \,|\, b_i + s_i)\right) \\ & \times \log\mathcal{N}\big(\hat{L}, L, \sigma_L\big) \times \log\mathcal{N}\big(\kappa_\mathrm{sim}, \kappa, \sigma_\kappa\big) \\ & \times \mathcal{G}\big(\,\langle\boldsymbol{\epsilon}\rangle_\mathrm{sim}, \boldsymbol{\epsilon}, M_{ij}\,\big)\,. \end{aligned} \tag{9.7}$$

The likelihood function does not model correlations between κ and the efficiencies ϵ_i. This is because the experimental systematic uncertainties on κ were found to be small compared to its total uncertainty.

9.2.2. Limit Setting

To obtain an upper limit s_{UL} on the signal strength parameter s, a frequentist approach using the CLs method [148, 149] is applied. For this purpose, a one-sided profile-likelihood ratio test statistic $\Lambda(s,\, n_i)$, is constructed,

$$\Lambda(s, n_i) = \begin{cases} \dfrac{\mathcal{L}(n_i,\, \widehat{\widehat{b}}_i(s),\, s)}{\mathcal{L}(n_i,\, \widehat{b}_i,\, \hat{s})}, & \text{if } \hat{s} < s \\ 1, & \text{otherwise} \end{cases} \tag{9.8}$$

where $\widehat{b}_i$ and $\widehat{s}$ denote the values of the nuisance parameters and the signal strength parameter, respectively, that maximize the likelihood function, and $\widehat{\widehat{b}}_i(s)$ that values of the nuisance parameters that maximize the likelihood function for a given value of s. In order to enforce positive background values, the minimum of the likelihood function is required to be obtained in the domain $b_i > 0$. Given the probability distributions for $\lambda \equiv -2 \ln \Lambda(s)$ in the model with signal, $p_{s+b}(\lambda)$, and in the background-only model, $p_b(\lambda)$, one can calculate confidence level (CL) values for the observed value λ_{obs} of the test statistic:

$$\mathrm{CL}_{s+b} = \int_{\lambda_{\mathrm{obs}}}^{\infty} d\lambda\, p_{s+b}(\lambda) \tag{9.9}$$

$$\mathrm{CL}_{b} = \int_{\lambda_{\mathrm{obs}}}^{\infty} d\lambda\, p_{b}(\lambda) \tag{9.10}$$

The signal model is then rejected at the 95% confidence level, if

$$\frac{\mathrm{CL}_{s+b}}{\mathrm{CL}_{b}} < 0.05\,. \tag{9.11}$$

The distributions $p_b(\lambda)$ and $p_{s+b}(\lambda)$ are produced with toy Monte Carlo experiments using the FrequentistCalculator class of RooStats [150].

9.3. Interpretation

Since no significant deviation from the Standard Model prediction is observed, the obtained results are used to set limits upon the parameters of the Constrained Supersymmetric Standard Model and a simplified model, as discussed in Sections 9.3.1 and 9.3.2.

9.3.1. CMSSM Interpretation

The soft SUSY-breaking Lagrangian of the CMSSM contains four free parameters, which are the masses of scalars and gauginos m_0 and $m_{1/2}$ at the GUT scale, the universal trilinear scalar interaction parameter A_0, and $\tan\beta$ (cf. Section 2.2.2). The sign of μ constitutes a fifth free parameter. For fixed parameters $\tan\beta = 10$, $A_0 = 0$ GeV, and $\mu > 0$, a scan in the m_0 - $m_{1/2}$ plane is performed. For each point in the scan, the signal-event selection efficiencies ϵ_{A}, ϵ_{B}, ϵ_{C}, and ϵ_{D} are calculated from simulated events. Next-to-leading-order and next-to-leading-logarithm (NLL) K factors [49, 111–114] on the LO cross sections of sparticle production are applied separately for each subprocess. For each point in the scan, the experimental systematic uncertainties are evaluated as described in Section 8.3. For the CMSSM limits, the inclusive 1-b-tag channel is used. The 95% CL limit using the CLs technique is presented in Fig. 9.2, where the solid red line represents the observed limit, including all experimental uncertainties. The region below this line is excluded. The dashed red lines show the observed limit with ± 1 standard variation on the signal event yields due to theoretical uncertainties on the cross sections of sparticle production arising from scale and PDF uncertainties. The dashed black line shows the median expected limit, which is calculated from simulated events only. The shaded area represents the experimental uncertainties on this limit.

As can be seen, the region with $m_0 < 800$ GeV and $m_{1/2} < 400$ GeV is excluded. For larger values of m_0, the limit on $m_{1/2}$ decreases with increasing m_0. Using the renormalization group equations, these limits can also be interpreted as limits on the masses of sparticles at the electroweak scale. For this purpose, contour lines that correspond to regions of constant squark and gluino masses are drawn in Fig. 9.2.

For gluino masses $m_{\tilde{g}}$ below 1 TeV, first- and second-generation squarks with masses $m_{\tilde{q}}$ smaller than about 1 TeV are excluded. With decreasing $m_{\tilde{g}}$, the upper limit on $m_{\tilde{q}}$ increases. This correlation mainly reflects the strong dependence of the gluino-production rate on the masses of first- and second-generation squarks in this region. As discussed in Sections 2.2.3.1 and 4.3.1, for $m_{\tilde{g}} < m_{\tilde{q}}$, the squark-associated gluino production ($\tilde{q}\tilde{g}$) and the pair production of first- and second-generation squarks ($\tilde{q}\tilde{q}^*$ and $\tilde{q}\tilde{q}$) strongly contribute to the gluino-induced production of third generation squarks, while the contribution of direct $\tilde{t}\tilde{t}^*$ and $\tilde{b}\tilde{b}^*$ production is small (for illustration see also Section 4.3.1, Fig. 4.2).

Moving towards smaller values of $m_{\tilde{q}}$, in contrast, the upper limit on $m_{\tilde{g}}$ saturates at about 1 TeV. This is basically due to the fact that the production rate of gluinos with masses around 1 TeV only slightly depends on the masses of first- and second generation squarks in this region. Consider for example benchmark scenario LM6 ($m_0 = 85$ GeV, $m_{1/2} = 400$ GeV), which is just excluded by this search. Since $m_{\tilde{g}} > m_{\tilde{q}}$, the gluino may not be produced from the decay of first and second generation squarks in this scenario.

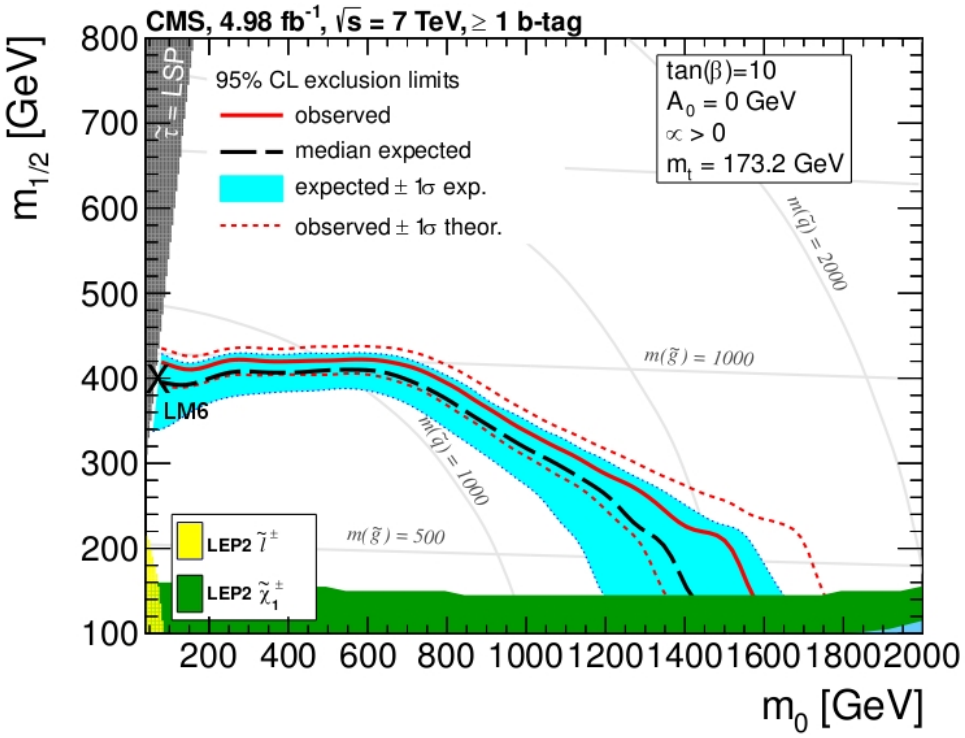

Figure 9.2.: The 95% CL limit for the CMSSM with $\tan\beta = 10$, $A_0 = 0$ GeV, and $\mu > 0$ in the inclusive 1-b-tag channel. The solid red line represents the observed limit, including all experimental uncertainties. The dashed red lines show the effect of ± 1 standard variation on the signal event yields due to theoretical uncertainties. The dashed black line shows the median expected limit with the shaded area representing the experimental uncertainties. Figure (modified) published in [7]

Moving for fixed parameter $m_{1/2} = 400$ GeV (which roughly corresponds to a gluino mass of 1 TeV) towards larger values of m_0, the masses of first- and second-generation squarks increase, which at first only slightly affects the contribution of the gluino-induced production of third generation squarks. However, the moment that $m_{\tilde{q}}$ gets larger than $m_{\tilde{g}}$, the contribution of the gluino-induced production becomes more dependent on $m_{\tilde{g}}$. Firstly, $\tilde{q}\tilde{q}^*$ and $\tilde{q}\tilde{q}$ production with the subsequent decay of at least one squark (antisquark) into a gluino and a quark (antiquark) additionally contribute. Secondly, the branching ratios for the decays $\tilde{g} \to t\tilde{t}^*$ and $\tilde{g} \to b\tilde{b}^*$ increase, because the gluino may not decay into quark-antisquark pairs of the first and second generations anymore. (Here, one would actually expect a slight increase of the limit, which is, however, hardly visible.) At further increased m_0, also the lighter top and bottom squarks become heavier than the gluino, such that the gluino may only decay in a three-body decay. Since this decay is largely independent

of the mass of the intermediate sparticle (which is produced off-shell) the branching ratios for the decays $\tilde{g} \to t\tilde{t}^*$ and $\tilde{g} \to b\tilde{b}^*$ drop off again.

To summarize, for models like the CMSSM with $\tan\beta = 10$, $A_0 = 0$ GeV, and $\mu > 0$, the sensitivity of the search presented in this thesis mainly arises from the gluino-induced production of third generation squarks, and, thus also depends on the masses of first- and second-generation squarks.

9.3.2. Simplified Model Interpretation

In order to facilitate the interpretation of results, simplified models are commonly used at the ATLAS and CMS experiments. In this thesis, limits are set upon the parameters $m_{\tilde{g}}$ and m_{LSP} of the four-top quark simplified model introduced in Section 2.2.4. Since it provides the best limit, the inclusive 3-b-tag channel is used. As in the CMSSM case, for each point in the parameter plane, the signal-event selection efficiencies are calculated from simulated events. The overall signal-event selection efficiencies (here labeled "$\mathbf{A} \times \boldsymbol{\varepsilon}$") are shown in Fig. 9.3.

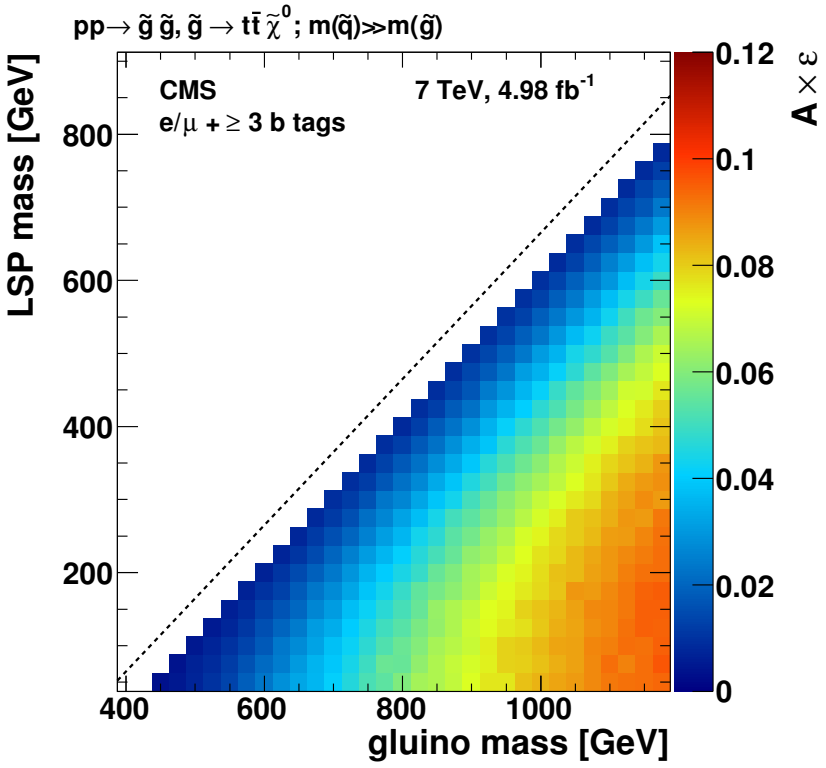

Figure 9.3.: Signal-event selection efficiency $\mathbf{A} \times \boldsymbol{\varepsilon}$ for the four-top quark simplified model in the inclusive 3-b-tag channel. Published in [7].

With increasing gluino mass, the signal-event selection efficiency becomes larger because all final-state objects carry larger transverse momenta on average. With increasing LSP mass, in contrast, the efficiency decreases. This is because the available phase spase of the final-state objects gets smaller. Close to the region where the decay $\tilde{g} \rightarrow t\bar{t}\chi_0^1$ is kinematically forbidden, indicated by the dashed line in Fig. 9.3, the gluinos' decay products may always be produced in rest. For each point in the scan, the experimental systematic uncertainties are calculated from simulated events. The 95% CL upper limit on the gluino-pair production cross section using the CLs technique is presented in Fig. 9.4.[2]

The solid red line shows the observed limit, including all experimental uncertainties. NLO and NLL K factors [49, 111–114] are applied. The effect of ± 1 standard variation of the signal event yields due to theoretical uncertainties on the $\tilde{g}\tilde{g}$-production cross section is represented by the dashed red lines. The thick black line shows the median expected limit with the thin black dashed lines representing the experimental uncertainties. As can be seen, for LSP masses below about 200 GeV, gluinos with masses between 600 and 900 GeV are excluded. For gluino masses between 700 and 850 GeV also larger LSP masses are excluded.

Since the four-top quark simplified model has no intermediate mass state, the obtained limits cannot be interpreted as limits on the top-squark mass. In order to derive upper limits on the masses of third-generation squarks, the simplified models that contain the direct pair production of top squarks ($\tilde{t}\tilde{t} \rightarrow t\bar{t}\tilde{\chi}_1^0\tilde{\chi}_1^0$) and bottom squarks ($\tilde{b}\tilde{b} \rightarrow t\bar{t}\tilde{\chi}_1^+\tilde{\chi}_1^- \rightarrow t\bar{t}W^-W^+\tilde{\chi}_1^0\tilde{\chi}_1^0$) (cf. Section 2.2.4) are examined. Despite higher signal-event selection efficiencies in these models, no limits can be obtained due to the low cross sections of direct $\tilde{t}\tilde{t}^*$ and $\tilde{b}\tilde{b}^*$ production (cf. Section 2.2.3.1).

In order to compare the sensitivity of this search with other searches that are based on the same data, the limits for the four-top quark simplified model are shown in Fig. 9.5. Besides the search presented in this thesis (labeled as "e/$\mu \geq$ 3b, $\mathrm{Y_{MET}}$"), another search in final states with a single lepton, b-jets, and missing transverse energy has been performed. In this search (labeled as "e/$\mu \geq 2\mathrm{b} + \not{E}_\mathrm{T}$"), the SM background in signal regions at large values of H_T and $\not{E}_\mathrm{T}$ is predicted by fitting $\not{E}_\mathrm{T}$ templates in normalization regions defined by lower values of $\not{E}_\mathrm{T}$ to the data. These templates are obtained from control regions defined by lower values of H_T. The limit shown in Fig. 9.5 is obtained in the inclusive 2-b-tag channel using a signal region defined by $H_\mathrm{T} > 750$ GeV and $\not{E}_\mathrm{T} > 250$ GeV [7]. While this limit covers a larger region along the $m_{\tilde{g}}$-axis compared to the limit obtained within this thesis, it has a slightly lower reach in m_LSP. However, the factorization method provides a better expected limit than the template method.

[2] Sometimes, such limits are interpreted as limits on the cross section of sparticle production times the branching ratio for a certain decay. However, if the Standard Model background is predicted by a data-driven method, such interpretations are very subtle. If the branching ratio for the considered decay does not equal one, other decays may in principle contaminate the control regions or control samples exploited (see also Section 2.2.4).

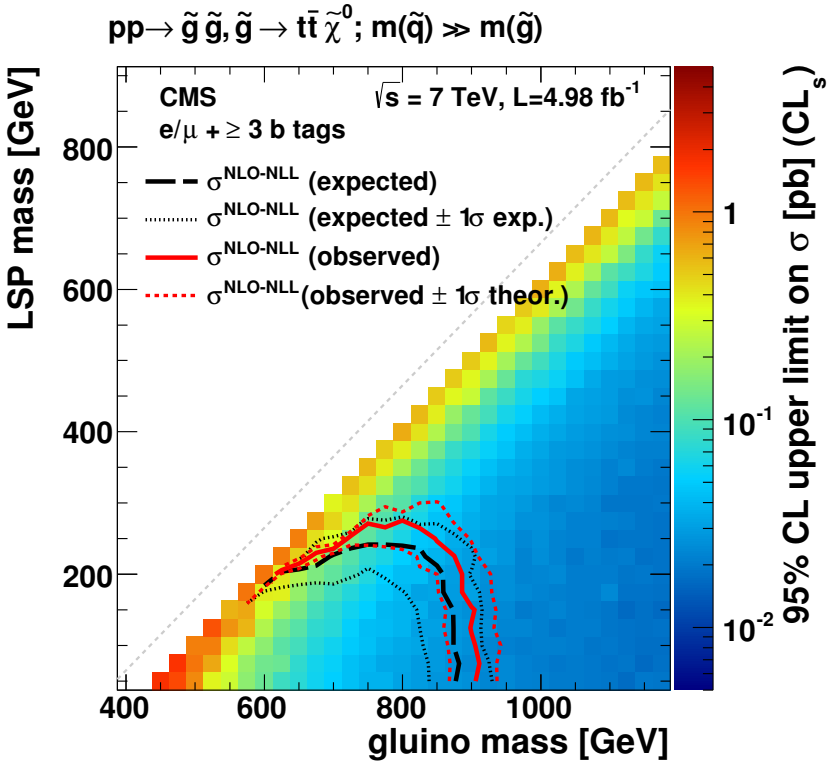

Figure 9.4.: The 95% CL upper limit for the four-top quark simplified model in the inclusive 3-b-tag channel. The solid red line represents the observed limit, including all experimental uncertainties. The dashed red lines show the effect of ± 1 standard variation on the signal event yields due to theoretical uncertainties. The thick black line shows the median expected limit with the thin black dashed lines representing the experimental uncertainties. The diagonal dashed line marks the lower kinematical limit on the LSP mass. Published in [7].

The reach of the single-lepton searches is complemented by a search in final states with same-sign dileptons and b-jets [151]. Since such final states will be less frequently produced, lower H_{T} and $\not\!\!E_{\mathrm{T}}$ requirements are applied. Associated therewith, this search has a lower reach in $m_{\tilde{g}}$, but covers a larger region in m_{LSP}.

Reflecting the large branching ratio for the four-top-quark system to decay into final states with at least one lepton, the limits obtained from leptonic searches are in general better than those obtained from all-hadronic searches. In Fig. 9.5 limits obtained from searches in exclusive jet + $\not\!\!E_{\mathrm{T}}$ final states using a cut-based method [152], the α_{T}-variable [153], and m_{T2} [154] are shown.

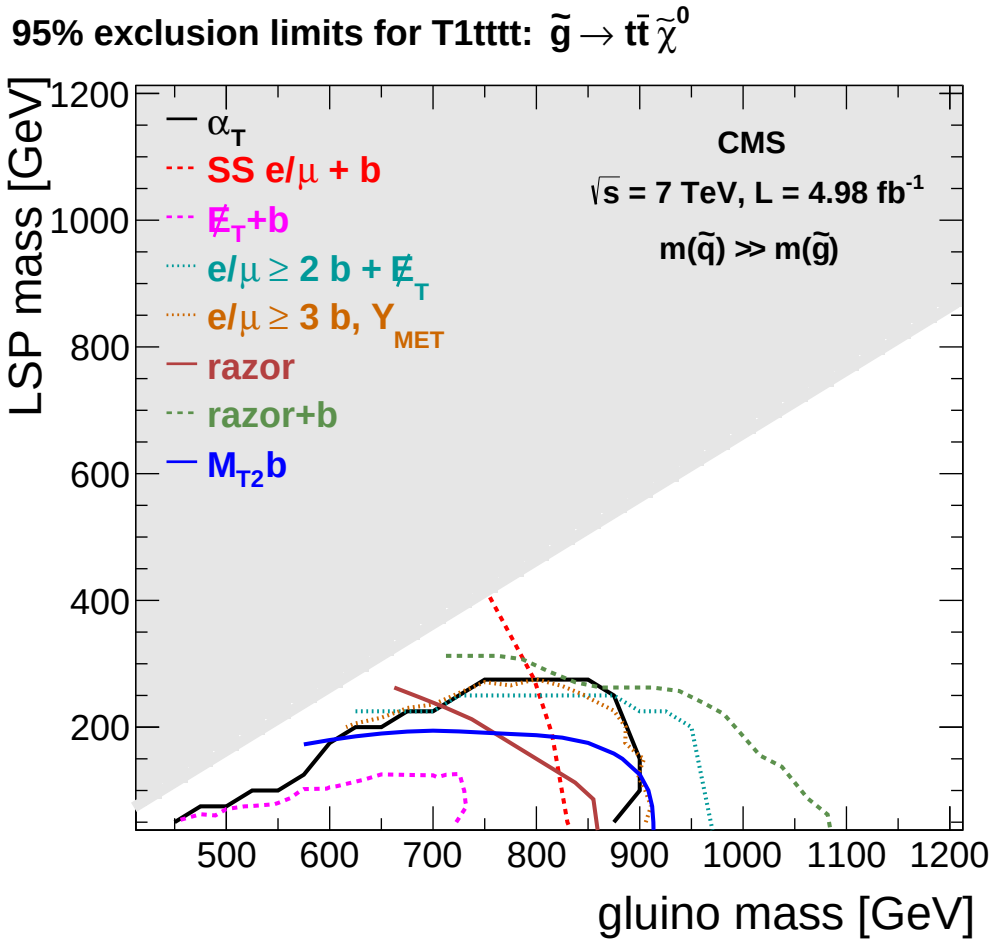

Figure 9.5.: The 95% CL limits for the four-top quark simplified model. The grey area represents the region where the decay $\tilde{g} \to t\bar{t}\chi_1^0$ is kinematically forbidden. All searches are based on data recorded at the CMS experiment at a center-of-mass energy of $\sqrt{s} = 7$ TeV during 2011, corresponding to an integrated luminosity of $4.98\,\mathrm{pb}^{-1}$. Published in [156].

Finally, the limits of an inclusive search that uses the razor variable [155] are illustrated. As can be seen, in combination with a b-tag requirement this search provides the best limit upon the parameters of the four-top quark simplified model.

Though motivated by supersymmetric models with light top and bottom squarks, the search presented in this thesis is expected to be sensitive to other types of physics beyond the Standard Model as well. For example, in models with universal extra dimensions, as outlined in Section 2.3.1, top and bottom quarks can be excited to quantized states in compact small extra dimensions. From our four-dimensional

point of view, these states (referred to as "Kaluze-Klein particles") appear as heavy top- and bottom-quark partner particles. In analogy to R-parity conservation in supersymmetric models, the conservation of momentum in the extra dimensions requires Kaluze-Klein particles to be produced in pairs and their decay chains to terminate with the lightest Kaluza-Klein particle. Hence, the signatures of universal extra dimensions may be very similar to those of Supersymmetry. The only intrinsic difference between unverisal extra dimensions and Supersymmetry, the different spin of Kaluza-Klein particles and sparticles, can be expected not to affect the performance of this search since variables that are sensitive to the spin of the initially produced new-physics particles are not exploited. Given that the limits for the four-top quark simplified model are provided in terms of upper limits on the cross section, the obtained results could in principle also be interpreted in a model that describes the pair production of Kaluza-Klein gluons, each of which decays into two top quarks and the lightest Kaluze-Klein particle.

Besides models with universal extra dimensions, various other extensions of the Standard Model predict new physics in states with top and bottom quarks at the Large Hadron Collider. In general, the sensitivity of the search presented in this thesis to such models essentially depends on the question whether final states will be characterized by a significant amount of missing transverse energy or not. For example, the production of fourth-generation quarks, as addressed in Section 2.3.3, may result in final states with similar multiplicities of isolated leptons and b-jets as Supersymmetry with light top and bottom squarks. However, the neutrino that is produced along with the single isolated lepton in a W-boson decay will not lead to a comparable amount of $\not\!\!E_{\mathrm{T}}$. This might be different in models that also predict a fourth lepton generation where a heavy neutrino constitutes a Dark Matter candidate. However, assuming this neutrino to be heavier than the W boson it needed to be produced from the decay of some heavy W-boson partner or similar.

10. Prospects for Parameter Determination at 14 TeV: Measuring Gluino Endpoints

Despite extensive searches in various production and decay channels, so far no significant deviation from the Standard Model prediction has been observed at the LHC. During the next data-taking periods, proton-proton collisions at envisaged center-of-mass energies of 13 and 14 TeV will open up new kinematic regions with a large discovery potential for physics beyond the Standard Model. If Supersymmetry is discovered, the next important task will be the measurement of sparticle properties. However, assuming R parity to be conserved, two lightest supersymmetric particles will escape detection, which makes any parameter determination non-trivial. Fortunately, many ideas have already been proposed to overcome this problem (see [157] for a review). The most traditional approach is to look for a kinematic edge or endpoint in the invariant mass distribution of the visible particles that result from the sparticle decay of interest. The position of such edge or endpoint allows to derive information about the masses of the involved sparticles. Other methods exploit M_{T2}-based variables, which often yield the event-by-event best lower bound on the mass of the unknown particle, or aim for the reconstruction of all four-momenta by solving the kinematic constraints inherent to the process of interest.

In this chapter, the possibility of extracting endpoints in invariant dijet-mass distributions originating from gluino three-body decays (gluino endpoints) is studied. This study is based on the simulation of proton-proton collisions at a center-of-mass energy of $\sqrt{s} = 14$ TeV, corresponding to an integrated luminosity of $\mathcal{L} = 300\,\mathrm{fb}^{-1}$, which is foreseen to be recorded during the next data-taking periods at the LHC. In absence of centrally provided samples for this center-of-mass energy, all simulated signal and background event samples are produced within this thesis. Three benchmark scenarios characterized by different masses of first- and second-generation squarks are investigated. Each of these scenarios inheres two kinematic endpoints, resulting from the decays $\tilde{g} \to q\bar{q}\tilde{B}$ and $\tilde{g} \to q\bar{q}\tilde{W}$, as discussed in Section 10.1. In order to disentangle these endpoints and to suppress the Standard Model background, dedicated event selection criteria are applied, which is described in Section 10.2. While the electric charge and the flavor of muons and electrons can be well identified, this is hardly possible for quarks of the first and second generations. In contrast to the reconstruction of dilepton-mass edges, combinatorial ambiguities therefore constitute a major issue. In order to minimize the impact of these, different kinematic variables are exploited. Endpoints are then determined from fits to the distributions of these variables, as described in Section 10.3. After a brief discussion of systematic uncertainties in Section 10.4, numerical results are presented in Section 10.5.

10.1. Benchmark Scenarios

Since the subject of this study is the gluino-three body decay, all squarks are assumed to be heavier than the gluino, whose mass is fixed to $m_{\tilde{g}} = 1200$ GeV. All slepton and higgsino states are assumed to be decoupled. Hence, the lightest neutralino is a purely composed bino state. Similarly, the second lightest neutralino and the lighter charginos are purely composed of wino states. In models with gravity-mediated and gauge-mediated Supersymmetry breaking, the gluino mass parameter M_3 at the TeV scale is roughly related to the bino and wino mass parameters $M1$ and $M2$ by the relation $M3 : M2 : M1 \approx 6 : 2 : 1$ [12]. Adopting this relation, the bino and wino masses are fixed to $m_{\tilde{B}} = 200$ GeV and $m_{\tilde{W}} = 400$ GeV. The gluino endpoints are then given by $m_{jj}^{\max} = m_{\tilde{g}} - m_{\tilde{B}} = 1000$ GeV for the decay $\tilde{g} \to q\bar{q}\tilde{B}$ and $m_{jj}^{\max} = m_{\tilde{g}} - m_{\tilde{W}} = 800$ GeV for the decay $\tilde{g} \to q\bar{q}\tilde{W}$. In the following, these endpoints are referred to as "bino endpoint" and "wino endpoint". Different assumptions about the masses of the first and second generation squarks define three benchmark scenarios, which are listed in Table 10.1 together with the numbers of generated events and the assumed cross sections. All samples are produced with Herwig++ and the CMS fast detector simulation, as described in Section 4.3.2.

Table 10.1.: Simulated 14 TeV signal samples, numbers of generated events, and assumed cross sections. All samples are produced within this thesis.

Sample	$\mathbf{m_{\tilde{g}}}$ **[GeV]**	$\mathbf{m_{\tilde{q}}}$ **[GeV]**	$\mathbf{m_{\tilde{B}}}$ **[GeV]**	$\mathbf{m_{\tilde{W}}}$ **[GeV]**	**No. events**	**Cross-sec. [pb]**
A	1200	1300	200	400	100,000	0.36 (LO)
B	1200	1900	200	400	100,000	0.092 (LO)
C	1200	10000	200	400	100,000	0.054 (LO)

In contrast to the search presented in the previous chapters, the third generation of squarks is explicitly decoupled. This does however not constitute any restriction with respect to the applicability of the presented method, which would similarly perform in the case that the gluino three-body decay to some extent resulted in states that include a quark-antiquark pair of the third-generation. If the gluino decayed into a $b\bar{b}$ pair and a bino, b-tagging would further help to minimize the impact of combinatorial backgrounds. If the gluino decay resulted in a state that includes a top quark, the reconstruction of endpoints would be highly non-trivial in any case: Leptonically decaying top quarks cannot be reconstructed because one decay product, the neutrino, escapes detection. In contrast to $t\bar{t}$ analyses, the total-momentum balance cannot be used as constraint on the neutrino momentum since two LSPs escape detection as well. Though in principle possible, the reconstruction of hadronically decaying top quarks strongly suffers from the large ambiguities that arise in events with many jets. In the case of $\tilde{g}\tilde{g}$ production with the subsequent decay

of each gluino into a $t\bar{t}$-like state and an LSP, the reconstruction of hadronically decaying top quarks is practically impossible at present center-of-mass energies.[1] However, this does not pose a problem for this study because events where the gluino decay resulted in a $t\bar{t}$-like state would anyhow be rejected by the event selection criteria that are applied to disentangle the two endpoints. Somehow astonishingly, though final states with a single lepton, b-jets, and $\not{E}_{\mathrm{T}}$ are most promising with respect to a potential discovery of Supersymmetry, this channel is not suited for the measurement of edges or endpoints that result from gluino decays.

In Fig. 10.1, the invariant-mass distribution of those quark pairs that arise from the gluino decays $\tilde{g} \to q\bar{q}\tilde{B}$ (a) and $\tilde{g} \to q\bar{q}\tilde{W}$ (b) in benchmark scenario A are shown. As can be seen, at the level of reconstructed jets that are matched to partonic objects, the endpoints are already smeared. For comparison, the corresponding distributions for the benchmark scenarios B and C are shown in Appendix E, Fig. E.1.

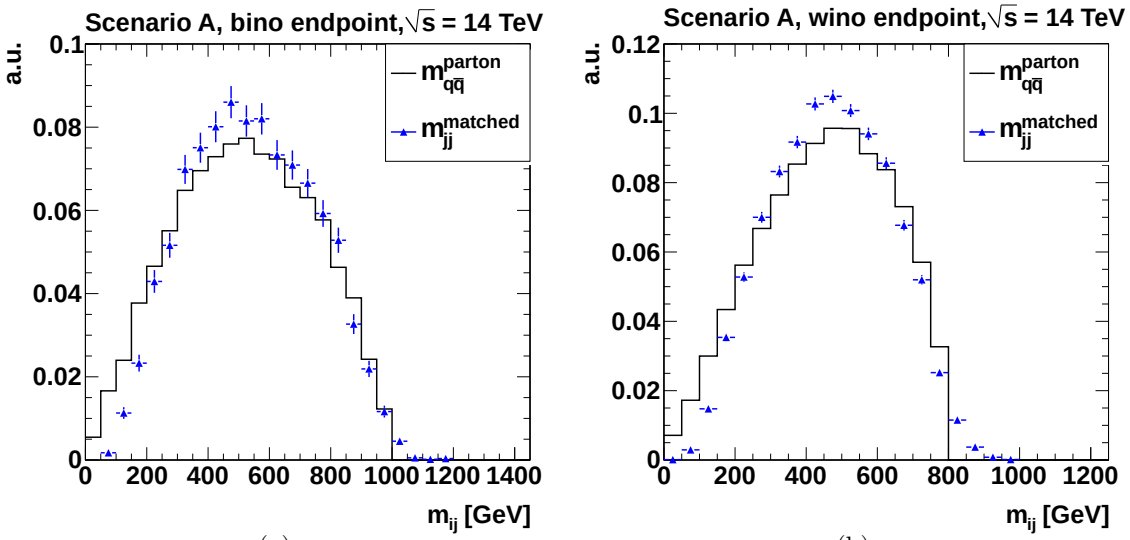

(a) (b)

Figure 10.1.: Invariant diquark-mass and invariant dijet-mass distributions resulting from the gluino three-body decays $\tilde{g} \to q\bar{q}\tilde{B}$ (a) and $\tilde{g} \to q\bar{q}\tilde{W}$ (b) in benchmark scenario A. Only jets that can be unambiguously matched to the quarks that result from the three-body decays are considered.

While all benchmark scenarios show the same two endpoints, they differ with respect to the dominant process of sparticle production. In scenario A, gluinos are mainly produced in association with a squark. Due to the small mass difference between the squarks and the gluino ($\Delta m \equiv m_{\tilde{q}} - m_{\tilde{g}} = 100$ GeV), the decay $\tilde{q} \to \tilde{g}q$

[1] At higher center-of-mass energies the situation might be different because top quarks produced in gluino-decay cascades may give rise to top-quark jets, which can be identified using dedicated jet reconstruction algorithms.

is kinematically suppressed. The squark predominantly decays into a quark and a bino or wino, resulting in final states with one potentially high-energetic jet that does not result from the gluino decay, as illustrated in Section 2.2.3.4, Fig 2.15, when replacing the top quarks by quarks of the first or second generation in that diagram. In scenario B, the squark-associated gluino production starts to be suppressed, but still has a sizable cross section. Reflecting the larger mass difference between the squarks and the gluino ($\Delta m = 700$ GeV), the squarks predominantly decay into a gluino and a quark. Thus, final states will be characterized by many jets, four of which are likely two result from two gluino three-body decays. In scenario C, the only strong-interaction process of sparticle production is the gluino-pair production. Since all squarks are decoupled in this scenario, to some extent also top and bottom quarks are produced from the gluino three-body decays.

10.2. Event Selection

In order to suppress the Standard Model background, H_{T} and $\not\!\!E_{\mathrm{T}}$ are required to be well beyond the parton-level cuts applied during the simulation of background events, as described in Section 10.2.1. Based on the discussion of event topologies, in Section 10.2.2, selection criteria are defined by which signal events that contain a gluino-decay cascade with a bino in the final state can be separated from signal events where the gluino decay results in a state with a wino. These criteria consist in different requirements on the first- and second-generation squarks and the number of selected jets and leptons and define two channels, which are referred to as "bino channel" and "wino channel" in the following. In order to further suppress the Standard Model background in each of these channels, event selection criteria that are commonly used in all-hadronic and single-lepton searches at the CMS experiment are applied, as discussed in Section 10.2.3 and Section 10.2.4.

All event selection criteria are based on the physics objects described in Section 5. The only difference with respect to the search at $\sqrt{s} = 7$ TeV is the tighter requirement on the jet p_{T}. Reflecting the higher center-of-mass energy (and potentially higher trigger thresholds), selected jets are required to have a transverse momentum larger than 50 GeV. By this, jets that originate from pile-up interactions are assumed to be sufficiently suppressed.

10.2.1. Preselection

During the simulation of Standard Model processes with MadGraph interfaced to Pythia, cuts on $H_{\mathrm{T}}^{\mathrm{parton}} > 700$ GeV, where $H_{\mathrm{T}}^{\mathrm{parton}}$ is calculated from all quarks and gluinos at parton level, and $\not\!\!E_{\mathrm{T}}^{\mathrm{parton}} > 100$ GeV, where $\not\!\!E_{\mathrm{T}}^{\mathrm{parton}}$ is defined as the sum

of all neutrino transverse momenta, are applied (cf. Section 4.3.2).[2] This is done to reduce the number of simulated events to an amount that can be locally produced and stored. In order to increase statistics at large H_{T}, during the simulation of QCD multijet events with PYTHIA a cross section that is flattened with respect to $\hat{p}_{\mathrm{T}}$ is assumed. Since missing transverse energy in QCD events exclusively results from jet energy mismeasurements (partly due to neutrinos produced in three-body decays of heavy-flavor quarks), no parton-level cut on $\not\!\!E_{\mathrm{T}}$ can be applied in this case.

In a sense, the applied parton-level cuts can be compared to potential trigger thresholds. Due to acceptance cuts and detector effects, H_{T} and $\not\!\!E_{\mathrm{T}}$ calculated at detector level will in general differ from $H_{\mathrm{T}}^{\mathrm{parton}}$ and $\not\!\!E_{\mathrm{T}}^{\mathrm{parton}}$, respectively. For this purpose, requirements on the offline reconstructed quantities of $H_{\mathrm{T}} > 1000$ GeV and $\not\!\!E_{\mathrm{T}} > 200$ GeV are applied. These requirements are found to be fully efficient with respect to the parton-level cuts and appropriate with respect to the rejection of Standard Model events. Assuming a total inelastic cross section of 10^{10} to 10^{11} pb at a center-of-mass of $\sqrt{s} = 14$ TeV, the number of Standard Model background events is reduced by ten to eleven orders of magnitude, while the signal event yield is only reduced by 25% in scenario A, 27% in scenario B, and 34% in scenario C. In Fig. 10.2 the H_{T} and $\not\!\!E_{\mathrm{T}}$ distributions of simulated Standard Model and signal events in the three benchmark scenarios are shown. It should be noted that, in contrast to the search in final states with a single lepton, the $Z/\gamma^* + \mathrm{Jets}$ sample also comprises the invisible decays $Z/\gamma^* \to \nu\bar{\nu}$, resulting in a partly significant amount of missing transverse energy.

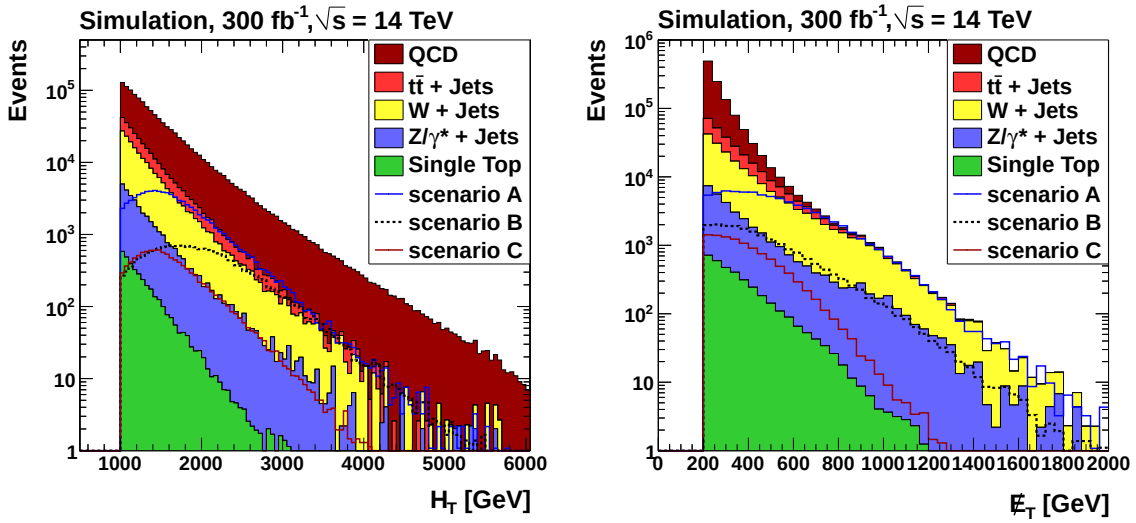

Figure 10.2.: H_{T} (left) and $\not\!\!E_{\mathrm{T}}$ (right) after the event preselection.

[2] In the case of $Z/\gamma^*(\to l^+l^-) + \mathrm{Jets}$ production, no cut on $\not\!\!E_{\mathrm{T}}^{\mathrm{parton}} > 100$ GeV is applied because in this process neutrinos are not produced at parton level.

Despite the $\not{E}_{\mathrm{T}}$ requirement by far the largest contribution to the simulated Standard Model background originates from QCD multijet production (74%). The bump in the $\not{E}_{\mathrm{T}}$ distribution around 1 TeV results from $W/Z + 1$-Jet events, where H_{T} necessarily equals $\not{H}_{\mathrm{T}}$, as already discussed in the 7 TeV case in Section 6.2.4. Finally, the number of selected jets and selected muons and electrons, which will serve as criteria for the separation of the two gluino endpoints, are shown in Fig. 10.3.

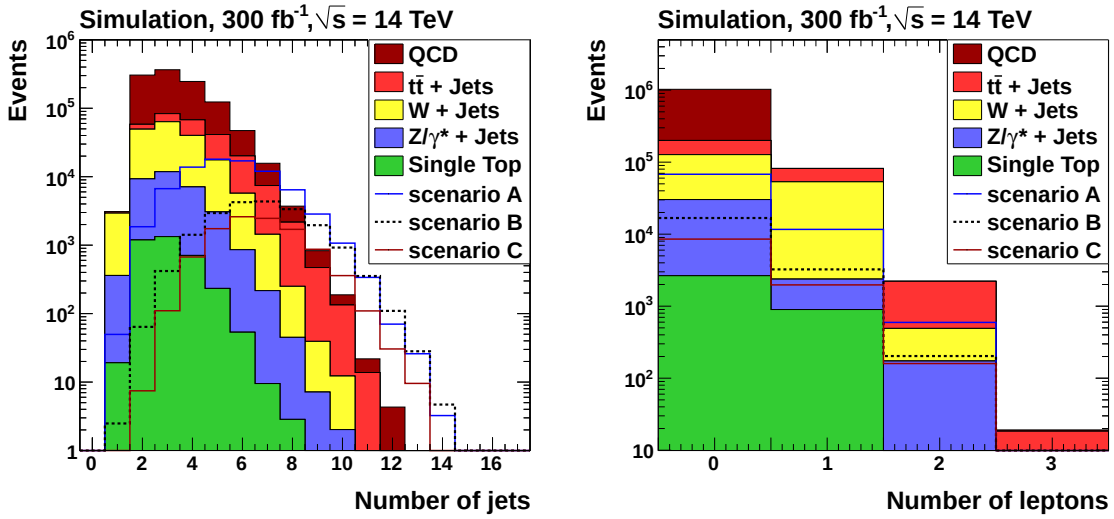

Figure 10.3.: Number of selected jets (left) and selected muons and electrons (right) after the event preselection.

10.2.2. Selection Criteria from Event Topologies

Many existing studies address the combinatorial issue of gluino edge and endpoint measurements in simplified-model scenarios that describe the pair production of gluinos, each of which subsequently decays into a quark-antiquark pair and a bino. Sometimes only $b\bar{b}$ pairs are assumed to be produced, which further simplifies the identification of those jet pairs that originate from the gluino decays because other jets can be rejected by means of b-tagging. However, in most of the interesting supersymmetric models, the gluino has at least one comparable decay mode, which is the decay into a quark-antiquark pair and a wino. Since the bino is lighter than the wino, the position of the bino endpoint is higher than that of the wino endpoint, resulting in a significant background for the wino endpoint measurement from the decay $\tilde{g} \to q\bar{q}\tilde{B}$. Because of the larger gauge coupling of the winos, the gluino decays more frequently into a $q\bar{q}$ pair and a wino than into a $q\bar{q}$ pair and a bino. Therefore, the decay $\tilde{g} \to q\bar{q}\tilde{W}$ will constitute a background for the bino edge measurements below the bino edge. Jets that are produced from squark decay cascades, as in the

case of scenarios A and B, initial and final state radiation, and the underlying event will result in further combinatorial ambiguities. Most challenging compared to e.g. the measurement of dilepton mass edges is therefore the combinatorial background. In order to disentangle the two gluino decay cascades, a detailed study of signal-event topologies is performed [8,158]. This study is based on the simulation of signal events with HERWIG++ and WHIZARD [159–161] interfaced to DELPHES [162] with CMS detector settings. The basic outcome of this study is that backgrounds from other gluino decays can be well suppressed by dedicated requirements on the number of selected leptons and jets. Following this approach, signal events in the bino channel are selected by requiring exactly four or five selected jets and no isolated muon or electron that fulfills the veto-criteria described in Sections 5.2 and 5.3. By these requirements, the ratio of events where at least one gluino decays into a wino and no gluino decays into a bino over events where at least one gluino decays into a bino and no gluino decays into a wino decreases by a factor of 2 to 4, depending on the scenario (cf. Appendix E, Tables E.2, E.3, and E.4). The decay $\tilde{g} \to q\bar{q}\tilde{W}$ still constitutes some background. However, since the position of the bino endpoint is higher than that of the wino endpoint, this is less worrying as it was the other way round. By requiring events to contain at least six selected jets and one isolated muon or electron, the ratio is increased by a factor of 6.5 in scenario A, 9.2 in scenario B, and 4.8 in scenario C. Hence, the background from the decay $\tilde{g} \to q\bar{q}\tilde{B}$ does not constitute a severe problem for the wino endpoint measurement anymore. However, in order to measure the gluino endpoints, the Standard Model background needs to be further suppressed, which is done separately for the two channels, as discussed in the following two sections.

10.2.3. Bino Channel Selection

The largest background after the preselection and the additional requirements of four to five jets and no isolated muon or electron fulfilling the veto-criteria described in Sections 5.2 and 5.3 originates from QCD multijet production (78%). In these events, large $\not{E}_{\mathrm{T}}$ is caused by single jet energy mismeasurements. In order to reject QCD mutlijet events, $\vec{\not{E}}_{\mathrm{T}}$ is therefore required not to direct along the transverse-momentum vectors of one of the three leading jets. Adopting the requirements applied in [163], the first two leading jets must fulfill $|\Delta\Phi(\vec{p}_{\mathrm{T}}^{\,\mathrm{jet1/2}}, \vec{\not{E}}_{\mathrm{T}})| > 0.5$ and the third jet has to satisfy $|\Delta\Phi(\vec{p}_{\mathrm{T}}^{\,\mathrm{jet3}}, \vec{\not{E}}_{\mathrm{T}})| > 0.3$. Figure 10.4 shows the $\Delta\Phi$ distributions before the successively applied requirements on $|\Delta\Phi(\vec{p}_{\mathrm{T}}^{\,\mathrm{jet}}, \vec{\not{E}}_{\mathrm{T}})|$ (as indicated by the dashed black lines) are applied. In total, the QCD multijet background is reduced by a factor of 34 by these requirements. Since the Standard Model background still dominates the signal, a tighter requirement on the missing transverse energy of $\not{E}_{\mathrm{T}} > 600$ GeV is applied in addition.

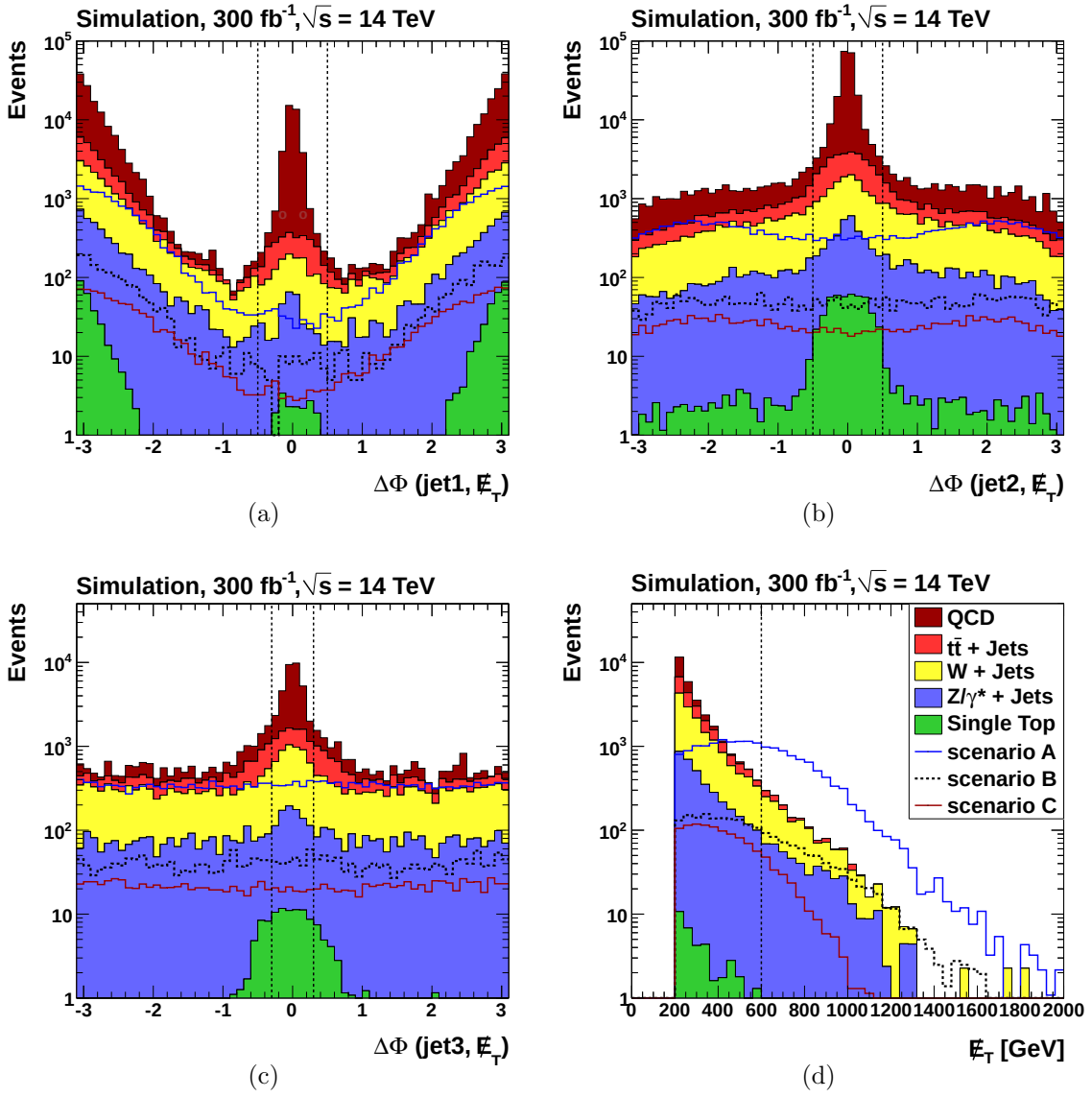

Figure 10.4.: $\Delta\Phi$ between $\not\!\!E_{\mathrm{T}}$ and the transverse-momentum vector of the first (a), second (b), and third (c) leading jet, and $\not\!\!E_{\mathrm{T}}$ before the successively applied selection criteria in the bino channel, as indicated by the dashed black lines. All events have passed the event preselection and contain four to five jets and no isolated muon and electron in the final state.

As can be seen in Fig. 10.4(d), in scenarios A and B, the signal-to-background ratio is strongly increased by this criterion (see also Table 10.2). In scenario C, this does apply to a lesser extent, because the LSPs exclusively result from the gluino three-body decays $\tilde{g} \to q\bar{q}\tilde{B}$ and $\tilde{g} \to q\bar{q}\tilde{W}$ with the subsequent decay of the

wino into a bino and an electroweak gauge or a Higgs boson. On average, the LSPs in scenario C therefore carry smaller transverse momenta as in scenario A and B, where one LSP may also be produced from the decay of a heavy squark into a quark ($\tilde{q} \to q\tilde{B}$) or a boosted wino that results from the decay $\tilde{q} \to q\tilde{W}$. In Table 10.2 the numbers of simulated Standard Model and signal events after the successively applied event selection criteria in the bino channel are shown.

Table 10.2.: Number of simulated Standard Model and signal events after the successively applied event selection criteria in the bino channel. Uncertainties are only statistical.

Selection	all SM	scenario A	scenario B	scenario C
preselection	$1,073,835 \pm 3462$	$80,174 \pm 294$	$20,171 \pm 74$	$10,683 \pm 41$
$4 \leq n_{\text{Jets}} \leq 5$	$358,091 \pm 2385$	$31,821 \pm 185$	4361 ± 34	2413 ± 19
lepton veto	$314,726 \pm 2342$	$25,159 \pm 164$	3079 ± 29	1592 ± 16
$\lvert\Delta\Phi(\text{jet1}, \not{E}_{\text{T}})\rvert > 0.5$	$277,157 \pm 2116$	$24,849 \pm 163$	3005 ± 28	1557 ± 15
$\lvert\Delta\Phi(\text{jet2}, \not{E}_{\text{T}})\rvert > 0.5$	$68,118 \pm 1080$	$21,665 \pm 152$	2530 ± 26	1350 ± 14
$\lvert\Delta\Phi(\text{jet3}, \not{E}_{\text{T}})\rvert > 0.3$	$29,917 \pm 598$	$18,045 \pm 139$	2080 ± 23	1146 ± 13
$\not{E}_{\text{T}} > 600$ GeV	1577 ± 60	7519 ± 90	731 ± 14	190 ± 5

10.2.4. Wino Channel Selection

The baseline selection in the wino channel consists of the requirements of at least six selected jets and one isolated muon or electron fulfilling the selection criteria described in Sections 5.2 and 5.3. To suppress the background from dileptonic $t\bar{t}$ decays, events with a second isolated muon or electron that passes the looser veto criteria are rejected. By these requirements the Standard Model background is reduced by more than two orders of magnitude. To further suppress the Standard Model background, a requirement on the transverse W-boson mass, which has been introduced in Section 6.5, of $m_{\text{T}} > 120$ GeV is applied. The dominant background after this selection criterion originates from semileptonic $t\bar{t}$ decays and dileptonic $t\bar{t}$ decays where one lepton, in many cases a hadronically decaying tau, does not pass the lepton veto criteria. As can be seen in Fig. 10.5(a), by applying the m_{T} requirement (marked by the dashed black line), the signal starts to dominate the Standard Model background. However, with respect to the wino-endpoint determination the event selection in this channel can still be optimized by requiring events to contain at most one b-jet, where the b-discriminator is defined as described in Section 5.6. As shown in Fig. 10.5(b), by this requirement the Standard Model background is

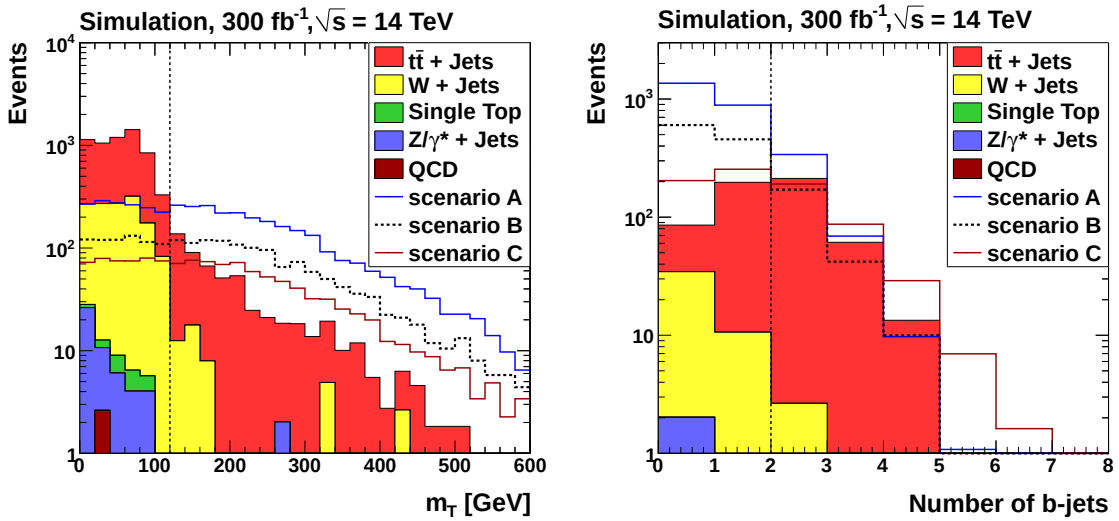

(a) (b)

Figure 10.5.: Transverse W-boson mass (a) and number of b-jets for the requirement $m_{\mathrm{T}} > 120$ GeV (b). All events have passed the event preselection and contain at least six jets and exactly one isolated muon or electron. The dashed black lines mark the selection criteria that are applied in the wino channel.

further reduced without rejecting too many signal events. Though it would result in a larger signal-to-background ratio, the requirement of exactly zero b-jets is found to be less suited because the endpoint extraction suffers from small statistics in this case. In Table 10.2, the numbers of simulated Standard Model and signal events after the successively applied event selection criteria in the wino channel are shown.

For both the bino channel and the wino channel, the numbers of simulated events after the successively applied event selection criteria are provided separately for each of the contributing Standard Model and signal subprocesses in Appendix E, Tables E.1, E.2, E.3, and E.4.

10.3. Endpoint Determination

Though the two gluino-decay cascades of interest are largely disentangled on an event-by-event basis by means of event selection criteria, combinatorial ambiguities remain. Selected events contain four or five jets in the bino channel and at least six jets in the wino channel. In order to minimize the impact of combinatorial backgrounds, dedicated kinematic variables, which are in Section 10.3.1, are used. Endpoints are then determined adopting the edge-to-bump method proposed in [164], as discussed in section 10.3.2.

Table 10.3.: Number of simulated Standard Model and signal events after the successively applied event selection criteria in the wino channel. Uncertainties are only statistical.

Selection	all SM	scenario A	scenario B	scenario C
no cuts	$1,073,835 \pm 3462$	$80,174 \pm 294$	$20,171 \pm 74$	$10,683 \pm 41$
preselection	$1,073,835 \pm 3462$	$80,174 \pm 294$	$20,171 \pm 74$	$10,683 \pm 41$
$n_{\text{Jets}} \geq 6$	$66,005 \pm 1009$	$39,825 \pm 207$	$15,319 \pm 65$	8150 ± 36
exactly 1 lepton	6554 ± 122	4232 ± 67	2000 ± 23	1230 ± 14
$m_T \geq 120$ GeV	570 ± 26	2667 ± 53	1283 ± 18	773 ± 11
$n_{\text{Bjets}} \leq 1$	282 ± 19	2248 ± 49	1051 ± 17	458 ± 8

10.3.1. Endpoint Variables

In order to determine how to select gluino dijet pairs out of the large number of possible jet pairings, the abundances of jets that are produced in gluino decays, jets that originate from squark decays, and jets that arise from wino decays as a function of the i-th hardest jet are studied. For this purpose detector-level jets are matched to particles at parton-level by a standard ΔR criterion. Based on this study [8, 158] the following variables are proposed:

$$min_{3j} = \min_{k=1,2} (m_{3k}) \tag{10.1}$$

$$min_{123} = \min_{i,j=1,2,3} (m_{ij}), \quad i \neq j \tag{10.2}$$

$$min_{234} = \min_{i,j=234} (m_{ij}), \quad i \neq j, \tag{10.3}$$

with m_{ij} the invariant mass of jets i and j, where jets are ordered by decreasing p_{T}. The variables min_{3j} and min_{123} are motivated by the observation that in scenarios A and C the three hardest jets are likely to arise from a gluino decay. The endpoint of min_{3j} is therefore expected to be the same as the gluino endpoint as long as one of the first hardest jets and the third hardest jet are coming from the gluino decay. As long as two of the third three hardest jets arise from the gluino decay, this does also apply for min_{123}. Reflecting the large branching ratio for the decay $\tilde{q} \to q\tilde{g}$ in scenario B (cf. Section 10.1), it is reasonable to explicitly exclude the hardest jet in this scenario, which motivates the definition of min_{234}. The distributions of min_{123} after the event selection in the bino channel and min_{234} after the event selection in the bino channel are shown in Fig. 10.6.

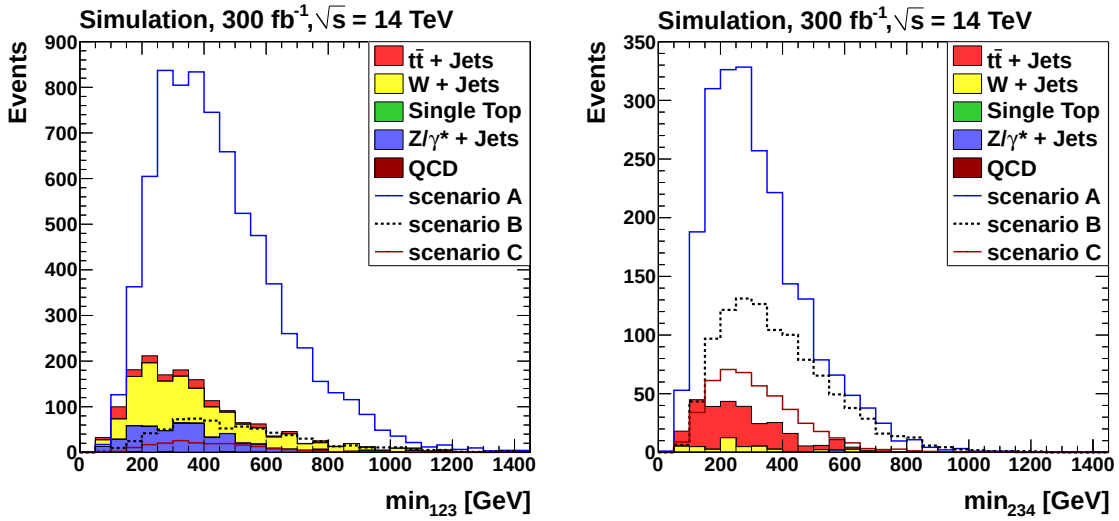

Figure 10.6.: Endpoint Variables min_{123} after the event selection in the bino channel (a) and min_{234} after the event selection in the wino channel (b).

In addition to these newly proposed variables, several existing variables that address the problem of combinatorics in gluino endpoint and edge measurements are used. Among these are F_3 and F_4, which have been proposed in [165]. F_3 is designed for event topologies where three jets come from the same decay chain and one jet originates from the other one. It is defined as the invariant dijet mass opposite to the maximum of all possible dijet masses,

$$F_3(p_1, p_2, p_3, p_4) = m_{kl}, \qquad \text{for} \quad \epsilon_{ijkl} \neq 0 \quad \text{and} \quad m_{ij} = \max_{r,s=1,\ldots,4} m_{rs}, \tag{10.4}$$

where ϵ_{ijkl} denotes the totally antisymmetric epsilon tensor. This variable has the same endpoint as the largest dijet-mass endpoint originating from the cascade chain that produces the three jets. F_4, in contrast, is designed for event topologies where both decay chains produce two jets. F_4 is defined as

$$F_4(p_1, p_2, p_3, p_4) = \min_{i,j=1,\ldots,4} \left(\max(m_{ij}, m_{kl})\right), \quad \epsilon_{ijkl} \neq 0, \tag{10.5}$$

which is the minimum of the larger dijet-mass pair out of three possible combinations. It has the same endpoint as the dijets coming from the same cascade chain each. Although these variables have originally been defined to address exclusive $4\,\text{jets} + \not{E}_\text{T}$ final states, they are used in this study by applying them to the four leading highest p_T jets only. In Fig. 10.7, F_4 after the event selection in the bino channel and F_3 after the event selection in the wino channel are shown.

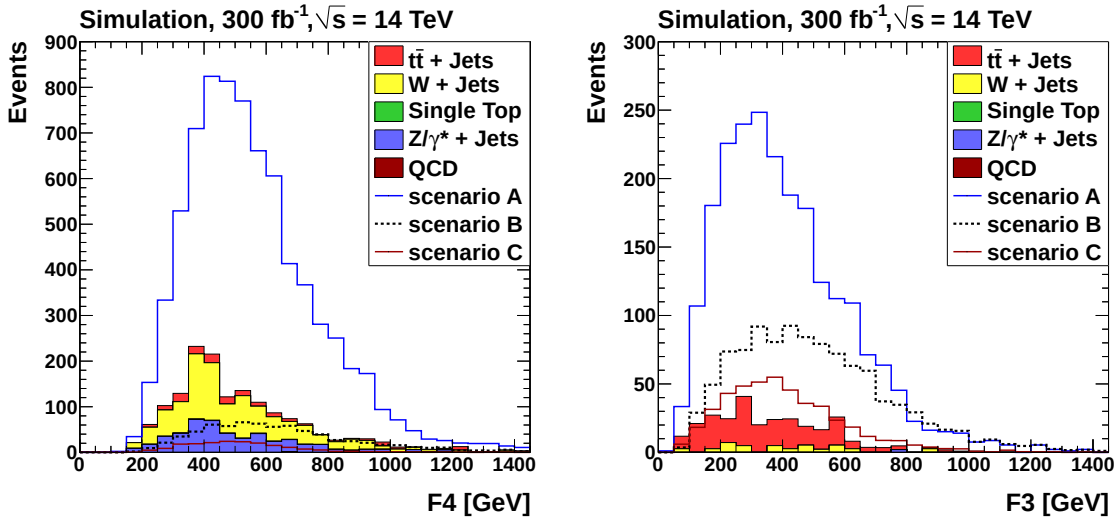

(a) (b)

Figure 10.7.: Endpoint Variables $F4$ after the event selection in the bino channel (left) and F_3 after the event selection in the wino channel (right).

10.3.2. Fitting Procedure

In order to quantitatively determine the position of the endpoints, a linear kink function, which consists of two joined lines with different gradients, is fitted to the signal+background distributions of the variables introduced in Section 10.3. For the distribution of min_{123} after the event selection in the bino channel and the distribution of F_3 after the event selection in the wino channel, the fit is exemplified in Figs. 10.8(a) and 10.9(a). As can be seen, the positions of the kinks obtained from the fits are located in the vicinity of the theoretically expected endpoints of $m_{jj}^{\max} = 1000$ GeV in the bino channel and $m_{jj}^{\max} = 800$ GeV in the wino channel.

However, usually the resulting fit values suffer from a non-negligible correlation of the fitting range set by hand. To minimize this artifact, the edge-to-bump method proposed in [164] is adopted. In that method, "kinky" features of distributions that could originate from underlying kinematic features are turned into bumps, which are easier accessible to data analysis methods. Roughly speaking, the edge-to-bump method fits the change in the slope of a distribution and translates it into a peak. The more distinct a peak is, the more likely it is that there is a true kinematic kink in the original distribution. For this purpose, 1000 kink fits with randomly generated fitting ranges are carried out. In this study, these fitting ranges are restricted to the interval (min_{fit}, max_{fit}), where min_{fit} is defined as that value where the distribution has its maximum, and max_{fit} is set to that value that corresponds to that bin that is located next-to-next-to-next-to the first empty bin. This is done to avoid a bias that may arise from large tails.

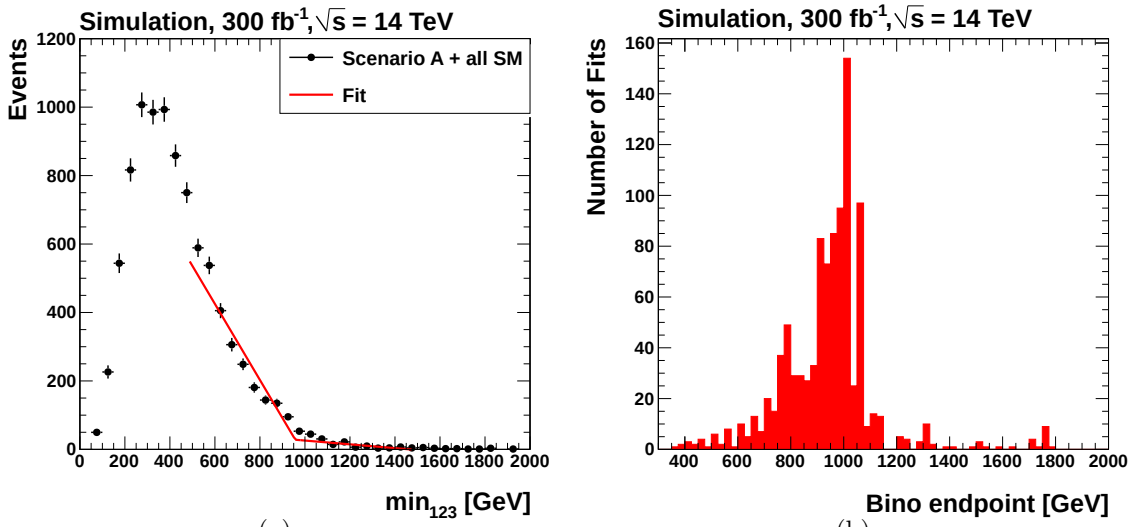

(a) (b)

Figure 10.8.: Example for a fit to the min_{123} distribution of signal+background events in scenario A (a) and distribution of 1000 endpoint fits to this distribution (b) after the event selection in the bino channel.

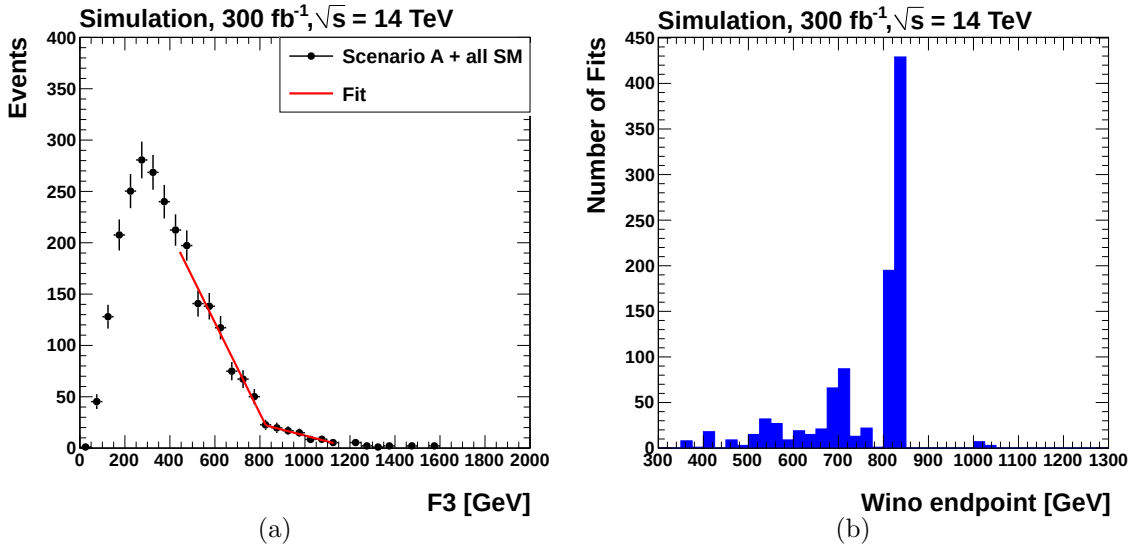

(a) (b)

Figure 10.9.: Example for a fit to the F_3 distribution of signal+background events in scenario A (a) and distribution of 1000 endpoint fits to this distribution (b) after the event selection in the wino channel.

Furthermore, the fitting ranges are required to contain at least five bins. As a first estimate, one might give the mean value of the endpoint distribution and the corresponding standard deviation as associated error. However, smaller peaks and non-negligible contributions far off the main peak lead to shifted mean values and considerably larger errors. Hence, to quantitatively estimate the actual endpoint position and reject contributions far away from the main peak, the following procedure is applied. First, the mean value $\hat{m}_0$ and the associated standard deviation σ_0 of the complete distribution are calculated. Secondly, the range of the endpoint distribution is set to $\hat{m}_0 \pm 2\sigma_0$. For this range, a new mean value $\hat{m}_i$ and standard and a new standard deviation σ_i are calculated. Finally, $\hat{m}_i$ and σ_i are taken as new seeds and the procedure is repeated from step two on. Iterating this procedure three to six times, $\hat{m}_i$ and σ_i are found to converge. In Fig. 10.8(b) and 10.9(b), the endpoint distributions obtained from applying this procedure to the min_{123} distribution after the event selection in bino channel and the F_3 distribution after the event selection in the wino channel are shown. The adapted mean values of $m_{jj}^{\max} = 985 \pm 51$ GeV in the bino channel and $m_{jj}^{\max} = 827 \pm 7$ GeV are well in agreement with the theoretically expected values of 1000 GeV and 800 GeV.

Up to now, simulated events have been used to predict the distribution of Standard Model and signal events. For this purpose, high statistics are desirable. During the fitting procedure, simulated events are treated as pseudo-data. Where possible, the number of processed signal events is chosen such that events have an event weight of one. Except for dileptonic $t\bar{t}$ events, the weight of simulated background events is larger than one. No restriction to the number of events is applied in this case.

10.4. Systematic Uncertainties

Possible sources of systematic uncertainties have already been discussed in the context of the search at $\sqrt{s} = 7$ TeV in Section 8. Of course, a detailed study of their impact on measurements of dijet-mass endpoints at a center-of-mass energy of 14 TeV is not possible at the moment. The experimental systematic uncertainties, provided e.g. in terms of data-to-simulation scale factors (cf. Section 8.3), strongly depend on the experimental environment. An accurate study of these will be possible after the first data at $\sqrt{s} = 13$ TeV or $\sqrt{s} = 14$ TeV have been analyzed. Similarly, a detailed study of the theoretical systematic uncertainties using dedicated simulated event samples is hardly feasible at the moment as it would require the local production of much more simulated events.[3] However, even though a precise estimation of systematic uncertainties is not possible, a rough estimate can be obtained. The gluino endpoint measurement described in the previous section es-

[3] Only the impact of the choice of the matching scale is checked using dedicated W + Jets event samples as described in Section 4.3.2. Reflecting the thigh phase space cuts at matrix-element level, the distributions of control variables are found not to depend on the matching scale.

sentially depends on the contribution of Standard Model background events in the fitting region and the reconstruction of invariant dijet masses. The largest impact on the endpoint measurement is therefore expected to result from the uncertainties on the cross sections of Standard Model processes, the jet energy scale, and the jet energy resolution, as investigated in the following.

Cross Sections

The largest contribution to the Standard Model background after the event selection in the wino channel originates from $t\bar{t}+\text{Jets}$ events (84%) and $W+\text{Jets}$ events (15%). In the bino channel also the production of neutrino-antineutrino pairs from Drell-Yan processes in association with hard jets contributes. This background amounts to 30%, while the background from $t\bar{t}+\text{Jets}$ production and $W+\text{Jets}$ production constitute 10% and 58%, respectively, of the simulated Standard Model background. The impact of the uncertainties on these cross section is studied by separately varying each cross section up and down by a factor of 50%.

Jet Energy Scale

The impact of the uncertainty on the jet energy scale is investigated by shifting the four-momenta of simulated jets with $p_{\text{T}} > 10$ GeV and $|\eta| < 4.7$ up and down by the uncertainties determined for the data-taking period in 2011, as described in Section 8.3.2. Of course, due to the different experimental environment during the next data-taking periods, resulting e.g. from a higher proton-bunch-crossing rate and a fourth layer of silicon pixel sensors, the uncertainty on the jet energy scale might increase or decrease. Nevertheless, to get an idea of how the jet energy scale will affect the endpoint measurement, it is totally sufficient to apply the uncertainties estimated for the run in 2011.

Jet Energy Resolution

The uncertainty on jet energy resolution is investigated as described in Section 8.3.3 with the difference that the scale factor is varied up and down by 10% independently of the jet pseudorapidity.

10.5. Results

The edge-to-bump method with a linear kink fit, as described in Section 10.3.2, is applied to the distributions of all variables introduced in Section 10.3.1. In order to obtain a rough estimate for the systematic uncertainties, each cross section, the jet energy scale, and the jet energy resolution are separately varied up and down by the assumed uncertainties and the fitting procedure is repeated each time. The

systematic uncertainties are summed up in quadrature. The results obtained in the bino and the wino channel in scenario A and the wino channel in scenario B are shown in Table 10.4, where the first uncertainties represent the standard deviation of the adapted mean values and the second the systematic uncertainties discussed in Section 10.4. In addition, the positions of the maximum values are given. Here, the uncertainties only reflects the systematic uncertainties.

Table 10.4.: Mean and maximum values of the endpoint distributions. The first uncertainties on the mean values represent the standard deviations, the second the systematic uncertainties. The uncertainties on the maximum values are only systematical. The values closest to the true values are printed in bold face. All values are given in GeV.

	Scenario A				Scenario B	
	Bino endpoint		Wino endpoint		Wino endpoint	
	mean	max	mean	max	mean	max
min_{123}	$\mathbf{985 \pm 51^{+25}_{-30}}$	$\mathbf{1000 + 50}$	$877 \pm 33^{+41}_{-41}$	$900 - 100$	$839 \pm 139^{+82}_{-30}$	1025^{+71}_{-35}
min_{3j}	$1024 \pm 84^{+37}_{-8}$	$975 + 125$	$892 \pm 18^{+32}_{-10}$	$900 - 35$	$944 \pm 97^{+94}_{-15}$	1025^{+43}_{-50}
min_{234}	$641 \pm 101^{+53}_{-19}$	725^{+50}_{-320}	$687 \pm 90^{+30}_{-67}$	750^{+35}_{-180}	$683 \pm 15^{+28}_{-50}$	$650 + 61$
F_3	$759 \pm 63^{+27}_{-4}$	725^{+106}_{-50}	$\mathbf{827 \pm 7^{+21}_{-19}}$	$\mathbf{825 + 25}$	$\mathbf{772 \pm 69^{+69}_{-10}}$	$\mathbf{725 + 117}$
F_4	$1085 \pm 35^{+34}_{-12}$	$1075 + 50$	$1048 \pm 44^{+12}_{-36}$	$1075 - 132$	$1004 \pm 54^{+66}_{-14}$	$1050 - 115$

In scenario A, min_{123} serves the best estimate of the bino endpoint. The determined value of $985 \pm 51^{+25}_{-30}$ GeV does well agree with the theoretically expected value of 1000 GeV. Also min_{j3} provides an estimate that is consistent with the theoretically expected value, while min_{234} does not allow for the reconstruction of the bino endpoint. This reflects the fact that the leading jet is likely to come from the gluino decay (cf. Section 10.3.1). In scenario B, the signal in the bino channel is dominated by the background. Fitting only the signal distributions, it is found that the endpoint could be well measured in the absence of Standard Model events. Thus, the measurement of the bino endpoint in this channel would require a precise modeling of the Standard Model background, e.g. with some data-driven method. In scenario C, the endpoint measurement additionally suffers from the poor statistics due to the low cross section of sparticle production and the tight $\not\!\!E_{\mathrm{T}}$ requirement, which is designed to suppress the Standard Model background in scenarios A and B (cf. Section 10.2.3).

In scenarios A and B, the best estimate for the wino endpoint is provided by F_3. The determined values of $827 \pm 7^{+21}_{-19}$ GeV and $772 \pm 69^{+69}_{-10}$ GeV are in good agreement with the expected value of 800 GeV. Also min_{123} provides an estimate that is close to or consistent with the theoretically expected endpoint. In scenario C, the small cross section of sparticle production does not allow for the reconstruction of the wino endpoint. However, when artificially increasing the statistics of signal events by a factor of five and requiring events to contain exactly zero b-jets to further suppress the Standard Model background, the wino endpoint can be similarly well determined as in scenario B. Hence, the wino endpoint in scenario C would be well in the reach of the High-Luminosity LHC, which is, according to the current planning of upgrades [166], foreseen to deliver proton-proton collisions with an integrated luminosity of $3000\,\mathrm{fb}^{-1}$ at a center-of-mass energy of 14 TeV.

11. Summary and Outlook

Supersymmetry constitutes an attractive extension of the Standard Model. It can resolve the hierarchy problem, may provide a Dark Matter candidate, and allows for the unification of gauge coupling strengths. In order for quadratic divergences to the squared Higgs-boson mass to cancel in a way that no further hierarchy is introduced, the top and the bottom squark must be relatively light. To a lesser extent this does also apply for the gluino. At the Large Hadron Collider top and bottom squarks may therefore be copiously produced. If R parity is conserved, this will happen by direct pair production or the production of gluinos that subsequently decay into a $t\tilde{t}^*$ or a $b\tilde{b}^*$ pair. Assuming at least one of the decays $\tilde{b}_1 \to t\tilde{\chi}_1^{\pm}$ and $\tilde{b}_1 \to \tilde{t}_1 W^-$ to be kinematically allowed and quark-flavor transitions between the first two generations and the third generation to be strongly suppressed, the production of third-generation squarks can be expected to result in states with a large multiplicity of isolated leptons, jets, some of which can be tagged as b-jet, and a significant amount of missing transverse energy.

In this thesis, the first search for Superysmmetry in final states with a single lepton, bottom-quark jets, and missing transverse energy at the Compact Muon Solenoid experiment is performed. This search is one of the worldwide first analyses that directly probes natural Supersymmetry. The search is based on proton-proton collision data recorded at a center-of-mass energy of 7 TeV during 2011, corresponding to an integrated luminosity of 4.98 fb^{-1}. By selecting events with a single isolated lepton, four jets, $H_{\mathrm{T}} > 375$ GeV, and $\not\!\!E_{\mathrm{T}} > 60$ GeV, the Standard Model background is reduced by a factor of approximately $5 \cdot 10^{10}$ in the inclusive 1-b-tag channel and a factor of about $9 \cdot 10^{11}$ in the inclusive 3-b-tag channel. Since the Standard Model prediction from the event simulation suffers especially in those regions of the phase space where a potential signal is expected from large systematic uncertainties, a data-driven background estimation method is applied. In simulated Standard Model events, H_{T} and $Y_{\mathrm{MET}} \equiv \not\!\!E_{\mathrm{T}}/\sqrt{H_{\mathrm{T}}}$ are largely uncorrelated, which suggests to predict the background in a potentially signal-enhanced region at large H_{T} and Y_{MET} by a factorization method from three background dominated control regions at low H_{T} and/or Y_{MET}. This data-driven method has the advantage that the systematic uncertainties largely cancel out. The observed number of events is found to be consistent with the predicted number of Standard Model events. The obtained results are therefore used to set 95% C.L. exclusion limits upon the parameters of several supersymmetric models. For the Constrained Minimal Supersymmetric Standard Model with $\tan\beta = 10$, $A_0 = 0$, and $\mu > 0$, limits are set

in the m_0 - $m_{1/2}$ parameter plane. Values of $m_{1/2}$ below 400 GeV are excluded for m_0 smaller than about 800 GeV. Limits are also set in the parameter plane of the gluino and LSP masses of a simplified model that describes the pair production of gluinos each of which decays into a $t\bar{t}$ pair and an LSP. For LSP masses below about 200 GeV, gluinos with masses between 600 and 900 GeV are excluded. For gluino masses between 700 and 850 GeV even larger LSP masses can be excluded. Due the large branching ratio for the four-top-quark system to decay into final states with at least one lepton, the limit obtained for the four-top-quark model is better than the limits obtained from all-hadronic searches. The range of the obtained limit is complemented by a search in final states with same-sign dileptons, which has a lower reach in $m_{\tilde{g}}$, but covers a larger region along the m_{LSP} axis. Despite the partly higher signal-event selection efficiency in simplified models that describe the direct $\tilde{t}\tilde{t}^*$ production and the direct $\tilde{b}\tilde{b}^*$ production, no exclusion limits are obtained in these models due to the low production cross section.

Though motivated by supersymmetric models with light top and bottom squarks, the search presented in this thesis can be expected to be sensitive to other types of physics beyond the Standard Model as well. For example, in models with universal extra dimensions, the excitation of pairs of third-generation quarks or gluons to states in small compact extra dimensions may result in similar final states as considered in this thesis. Given that the limits for the four-top-quark simplified model are provided in terms of upper limits on the cross section, the obtained results could in principle also be interpreted in a model that describes the pair production of Kaluza-Klein gluons each of which decays into a $t\bar{t}$ pair and the lightest Kaluza-Klein particle.[1] In general, the sensitivity of the presented search to other models for physics beyond the Standard Model essentially depends on the question whether final states will be characterized by a significant amount of missing transverse energy or not.

Reflecting the higher center-of-mass energy of 8 TeV and the larger integrated luminosity of $21.8\,\mathrm{fb}^{-1}$ in 2012, recent searches for Supersymmetry in states with third-generation squarks became more dedicated. While the search presented in this thesis can be regarded as generic in that it exploits a common signature of third-generation squark production and decay, searches that are based on 2012 data rather focus on specific processes. In the single-lepton channel, a search in final states with six jets at least two of which are identified as b-jet [167] extends the range of the exclusion limit in the four-top-quark simplified model. Using variables that show a kinematic endpoint that is specific either for the signal process or the main background process, in different simplified models upper limits on the cross

[1] The only intrinsic difference between universal extra dimensions and Supersymmetry, the different spin of Kaluza-Klein particles and sparticles, can be expected not to affect the performance of this search since variables that are sensitive to the spin of the initially produced new-physics particles are not exploited.

section of direct $\tilde{t}\tilde{t}^*$ production are obtained [168]. Finally, the results of several searches are interpreted in the context of simplified models that describe the direct pair production of bottom squarks [169–171].

Despite extensive searches in various channels, no significant deviation from the Standard Model prediction has been observed at the Large Hadron Collider. During the next data-taking periods, proton-proton collisions at envisaged center-of-mass energies of 13 and 14 TeV will open up new kinematic regions with a large discovery potential for physics beyond the Standard Model. With an integrated luminosity of $300\,\mathrm{fb}^{-1}$, which is foreseen to be recorded at these energies, large parts of the supersymmetric phase space that are of interest from naturalness arguments can be probed. After a possible discovery of Supersymmetry, the next important task will be the measurement of sparticle properties. In this thesis, prospects of measuring dijet-mass endpoints resulting from the gluino three-body decays $\tilde{g} \to q\bar{q}\tilde{B}$ and $\tilde{g} \to q\bar{q}\tilde{W}$ are investigated. Based on the simulation of proton-proton collisions at a center-of-mass energy of $\sqrt{s} = 14$ TeV, corresponding to an integrated luminosity of $300\,\mathrm{fb}^{-1}$, three benchmark scenarios defined by different masses of first- and second generation squarks are studied. The masses of the gluino, bino, and wino are fixed to $m_{\tilde{g}} = 1200$ GeV, $m_{\tilde{B}} = 200$ GeV, and $m_{\tilde{W}} = 400$ GeV, resulting in kinematic endpoints at $m_{jj}^{\max} = m_{\tilde{g}} - m_{\tilde{B}} = 1000$ GeV and $m_{jj}^{\max} = m_{\tilde{g}} - m_{\tilde{W}} = 800$ GeV. For a squark mass of $m_{\tilde{q}} = 1300$ GeV, it seems possible to measure both endpoints at the Large Hadron Collider during the next data-taking periods. The estimated values of $985 \pm 51^{+25}_{-30}$ GeV in the bino channel and $827 \pm 7^{+21}_{-19}$ GeV in the wino channel do well agree with the theoretically expected values. For a squark mass of 1900 GeV, the signal in the bino channel is dominated by the Standard Model background. In this case, the endpoint measurement with the described method would require a more precise modeling of the Standard Model background, e.g. with some data-driven method. In the wino channel, the measurement of endpoints seems to be possible also for a squark mass of 1900 GeV. In the case that all squarks are decoupled, the endpoint measurement in the wino channel would require an integrated luminosity that is about five times larger. Thus, it would be well possible at the High-Luminosity LHC, which is, according to the current planning of upgrades, foreseen to deliver an integrated luminosity of $3000\,\mathrm{fb}^{-1}$.

A. Theoretical Framework Appendix

Gamma Matrices

$$\gamma^0 = \begin{pmatrix} 1 & 0 & 0 & 0 \\ 0 & 1 & 0 & 0 \\ 0 & 0 & -1 & 0 \\ 0 & 0 & 0 & -1 \end{pmatrix} \quad \gamma^1 = \begin{pmatrix} 0 & 0 & 0 & 1 \\ 0 & 0 & 1 & 0 \\ 0 & -1 & 0 & 0 \\ -1 & 0 & 0 & 0 \end{pmatrix} \quad \gamma^2 = \begin{pmatrix} 0 & 0 & 0 & -i \\ 0 & 0 & i & 0 \\ 0 & i & 0 & 0 \\ -i & 0 & 0 & 0 \end{pmatrix}$$

$$\gamma^3 = \begin{pmatrix} 0 & 0 & 1 & 0 \\ 0 & 0 & 0 & -1 \\ -1 & 0 & 0 & 0 \\ 0 & 1 & 0 & 0 \end{pmatrix} \quad \gamma^5 = \begin{pmatrix} 0 & 0 & 1 & 0 \\ 0 & 0 & 0 & 1 \\ 1 & 0 & 0 & 0 \\ 0 & 1 & 0 & 0 \end{pmatrix}$$

Dirac Spinors

$$u_1(p) = \sqrt{E+m} \begin{pmatrix} 1 \\ 0 \\ \frac{p_z}{E+m} \\ \frac{p_x+ip_y}{E+m} \end{pmatrix} e^{-iEt}\, e^{+i\vec{p}\vec{x}}, \qquad u_2(p) = \sqrt{E+m} \begin{pmatrix} 0 \\ 1 \\ \frac{p_x-ip_y}{E+m} \\ \frac{-p_z}{E+m} \end{pmatrix} e^{-iEt}\, e^{+i\vec{p}\vec{x}},$$

$$v_1(p) = \sqrt{E+m} \begin{pmatrix} \frac{p_x-ip_y}{E+m} \\ \frac{-p_z}{E+m} \\ 0 \\ 1 \end{pmatrix} e^{+iEt}\, e^{-i\vec{p}\vec{x}}, \qquad v_2(p) = \sqrt{E+m} \begin{pmatrix} \frac{p_z}{E+m} \\ \frac{p_x+ip_y}{E+m} \\ 0 \\ 1 \end{pmatrix} e^{+iEt}\, e^{-i\vec{p}\vec{x}}$$

Formally, solutions of the Dirac equation (2.1) with positive (negative) energy are transformed into solutions with negative (positive) energy by the charge conjugation operation $\Psi \rightarrow i\gamma^2\Psi^*$. For example, $v_1 = i\gamma^2 u_1^*$ and $v_2 = i\gamma^2 u_2^*$. The spinors u_1 and v_2 describe fermions with a positive helicity, the spinors u_2 and v_1 correspond to fermions with a negative helicity. In this regard, the antiparticles of leptons and quarks might be referred to as having opposite helicity. However, in general, fermions are described by superpositions of u_1 and u_2 and v_1 and v_2, respectively, and hence not eigenstates of the helicity operator.

Euler-Lagrange Equations

$$\frac{\partial \mathcal{L}}{\partial \Phi(x)} - \partial^{\mu}\left(\frac{\partial \mathcal{L}}{\partial(\partial^{\mu}\Phi(x))}\right) = 0.$$

Pauli Matrices

$$\tau^1 = \begin{pmatrix} 0 & 1 \\ 1 & 0 \end{pmatrix} \quad \tau^2 = \begin{pmatrix} 0 & -i \\ i & 0 \end{pmatrix} \quad \tau^3 = \begin{pmatrix} 1 & 0 \\ 0 & -1 \end{pmatrix}$$

Epsilon Tensor

$$\epsilon_{ijk} = \begin{cases} +1 \text{ for even permutations of (1,2,3)} \\ -1 \text{ for odd permutations of (1,2,3)} \\ \ \ 0 \text{ if any index is repeated} \end{cases}$$

CKM Matrix

$$\begin{pmatrix} \text{d'} \\ \text{s'} \\ \text{b'} \end{pmatrix} = \begin{pmatrix} 0.97427 \pm 0.00015 & 0.22534 \pm 0.00065 & 0.00351^{+0.00015}_{-0.00014} \\ 0.22520 \pm 0.00065 & 0.97344 \pm 0.00016 & 0.0412^{+0.0011}_{-0.0005} \\ 0.00867^{+0.00029}_{-0.00031} & 0.0404^{+0.0011}_{-0.0005} & 0.999146^{+0.000021}_{-0.000046} \end{pmatrix} \begin{pmatrix} \text{d} \\ \text{s} \\ \text{b} \end{pmatrix}$$

Taken from [20].

Gellmann Matrices

$$\lambda^1 = \begin{pmatrix} 0 & 1 & 0 \\ 1 & 0 & 0 \\ 0 & 0 & 0 \end{pmatrix} \quad \lambda^2 = \begin{pmatrix} 0 & -i & 0 \\ i & 0 & 0 \\ 0 & 0 & 0 \end{pmatrix} \quad \lambda^3 = \begin{pmatrix} 1 & 0 & 0 \\ 0 & -1 & 0 \\ 0 & 0 & 0 \end{pmatrix} \quad \lambda^4 = \begin{pmatrix} 0 & 0 & 1 \\ 0 & 0 & 0 \\ 1 & 0 & 0 \end{pmatrix}$$

$$\lambda^5 = \begin{pmatrix} 0 & 0 & -i \\ 0 & 0 & 0 \\ i & 0 & 0 \end{pmatrix} \quad \lambda^6 = \begin{pmatrix} 0 & 0 & 0 \\ 0 & 0 & 1 \\ 0 & 1 & 0 \end{pmatrix} \quad \lambda^7 = \begin{pmatrix} 0 & 0 & 0 \\ 0 & 0 & -i \\ 0 & 1 & 0 \end{pmatrix} \quad \lambda^8 = \frac{1}{\sqrt{3}} \begin{pmatrix} 1 & 0 & 0 \\ 0 & 1 & 0 \\ 0 & 0 & -2 \end{pmatrix}$$

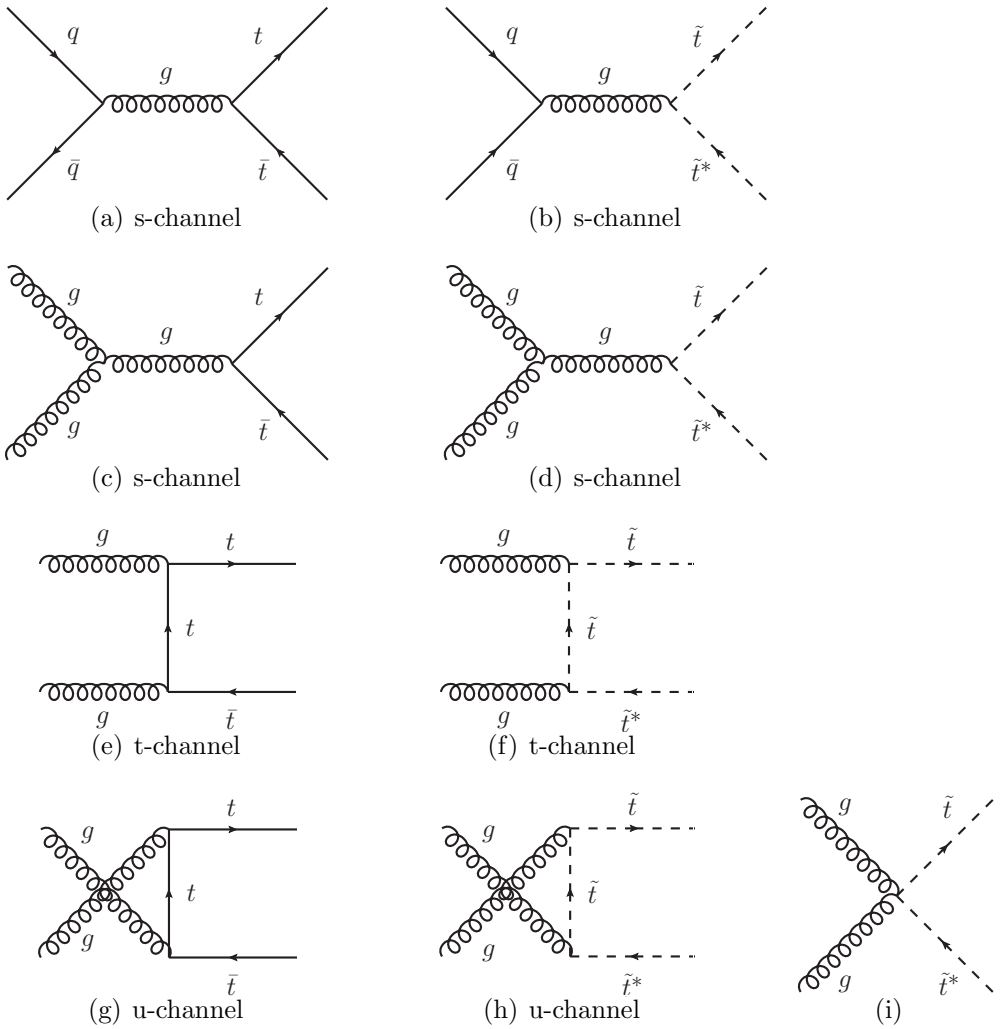

Figure A.1.: Direct pair production of top quarks (left) and squarks (right) in the s-, the t-, and the u-channel. The direct production of top squark pairs may in addition be induced by four-boson interaction, as illustrated in Fig. A.1(i). Diagrams for the direct pair production of quarks/squarks of any other flavor can be obtained by replacing all particles with top flavor accordingly. At LO (NLO), these diagrams represent the only possible strong interaction processes of direct top and bottom quark (squark) pair production that are not flavor-suppressed.

Direct Pair Production of First and Second Generation Quarks and Squarks

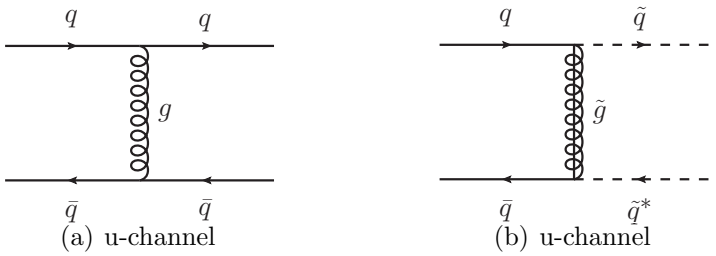

(a) u-channel (b) u-channel

Figure A.2.: Quark pair production induced by gluon exchange (a) and squark pair production induced by gluino exchange (b) in the t-channel. Since it requires the occurance of a $t\bar{t}$ or $b\bar{b}$ pair in the initial state, these channels do not contribute to the production of third generation quarks and squarks in proton-proton collisions.

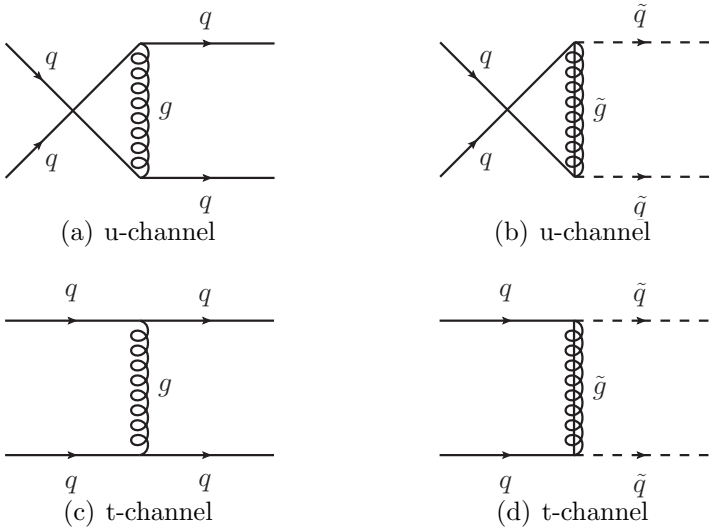

(a) u-channel (b) u-channel

(c) t-channel (d) t-channel

Figure A.3.: Pair production same-sign quarks (left) and squarks (right) in the u-channel. Since it requires the occurance of a tt or bb pair in the initial state, this channel do not contribute to the production of third generation quarks and squarks in proton-proton collisions

B. Event Simulation Appendix

B.1. CMSSM Mass Spectra

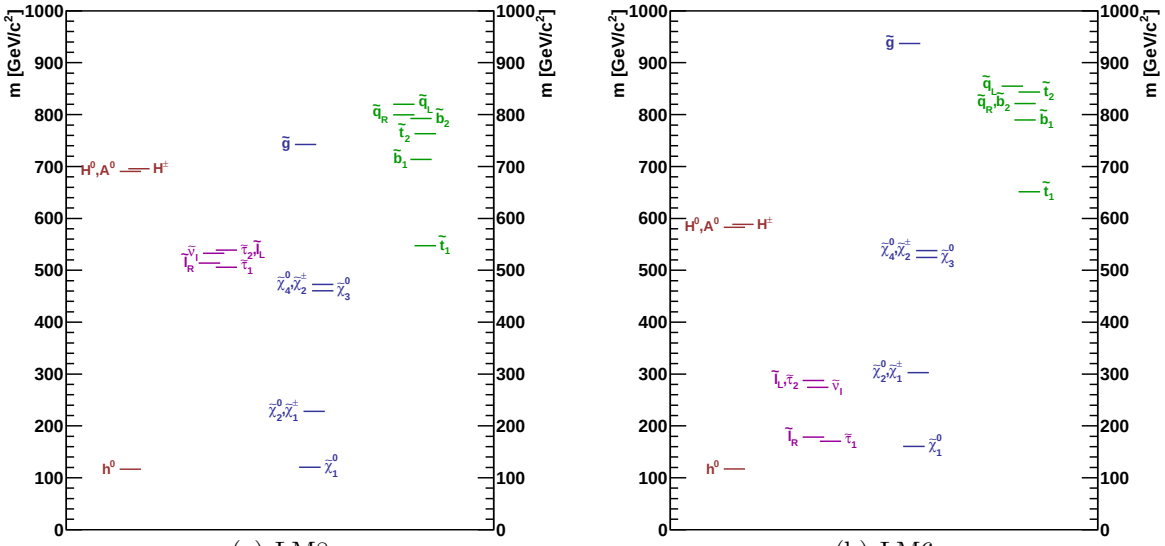

(a) LM8 (b) LM6

Figure B.1.: Mass spectra of the CMSSM low mass scenarios LM8 (a) and LM6 (b).

B.2. Pile-Up Reweighting

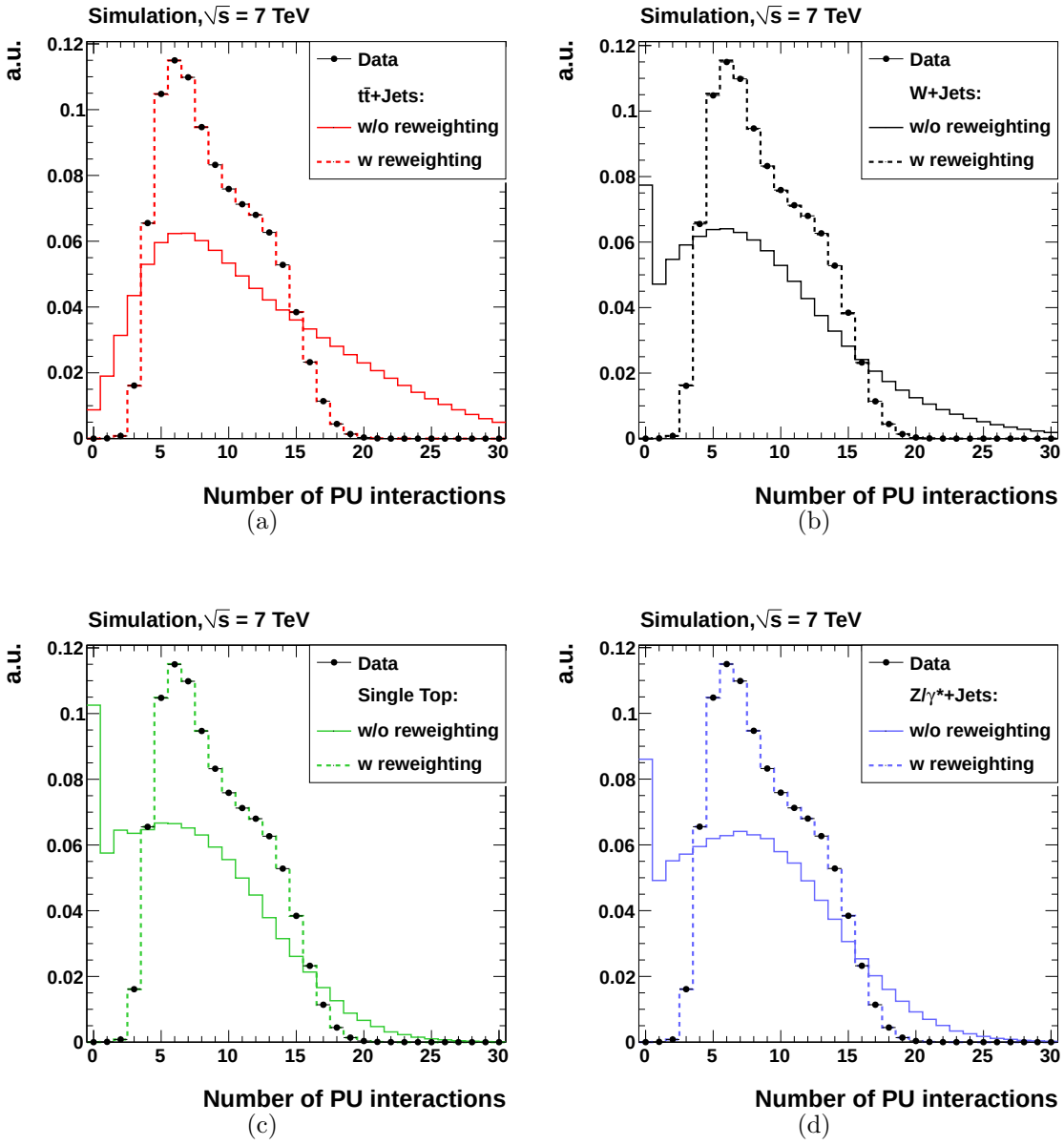

Figure B.2.: Number of pileup interactions in simulated $t\bar{t}$+Jets (a), W+Jets (b), single top (c), and Z+Jets (d) events before and after the pileup reweighting and in data. All distributions are normalized to unit area.

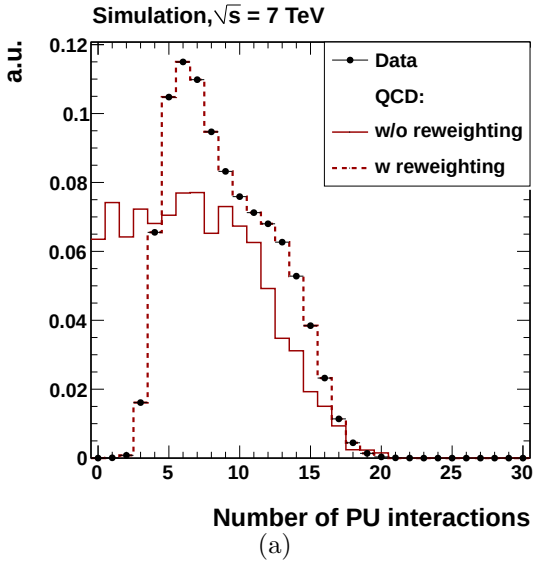

(a)

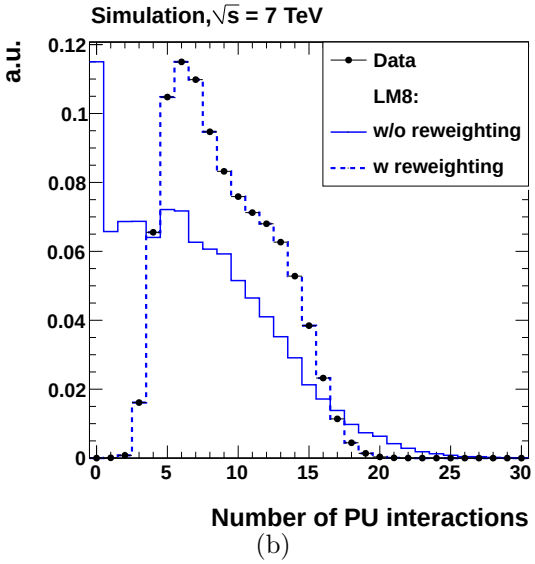

(b)

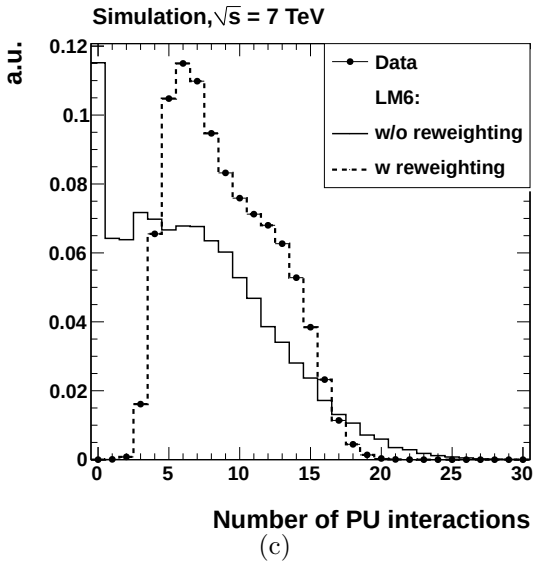

(c)

Figure B.3.: Number of pileup interactions in simulated QCD (a), LM8 (b), and LM6 (c) events before and after the pileup reweighting and in data. All distributions are normalized to unit area.

C. Event Selection Appendix

C.1. Further Control Plots

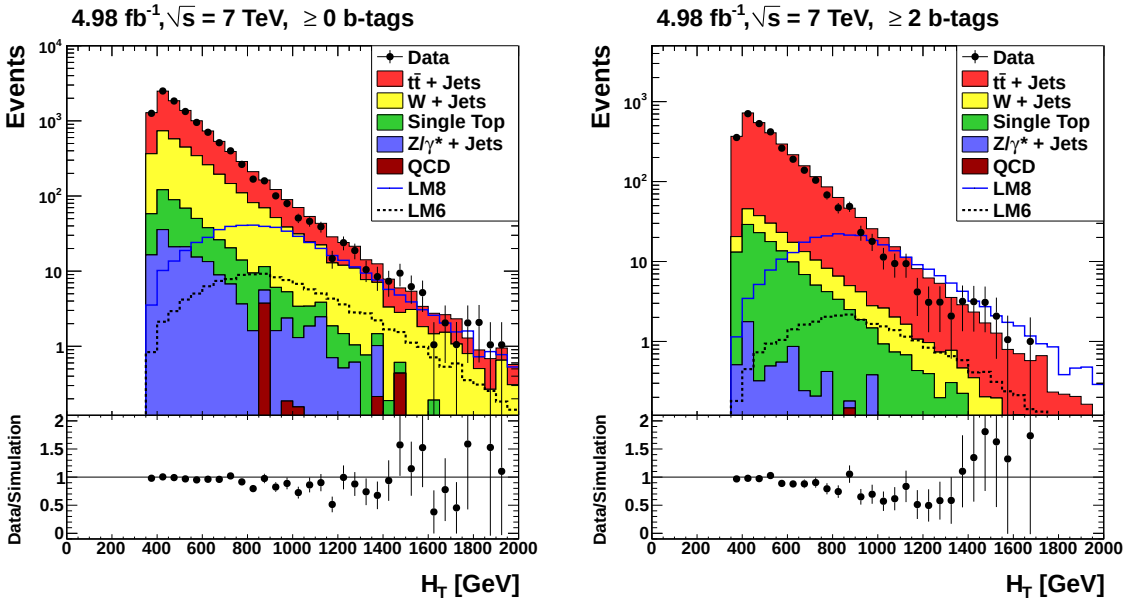

(a) (b)

Figure C.1.: H_T after the event selection with the requirement of at least zero b-jets (left) and at least two b-jets (right).

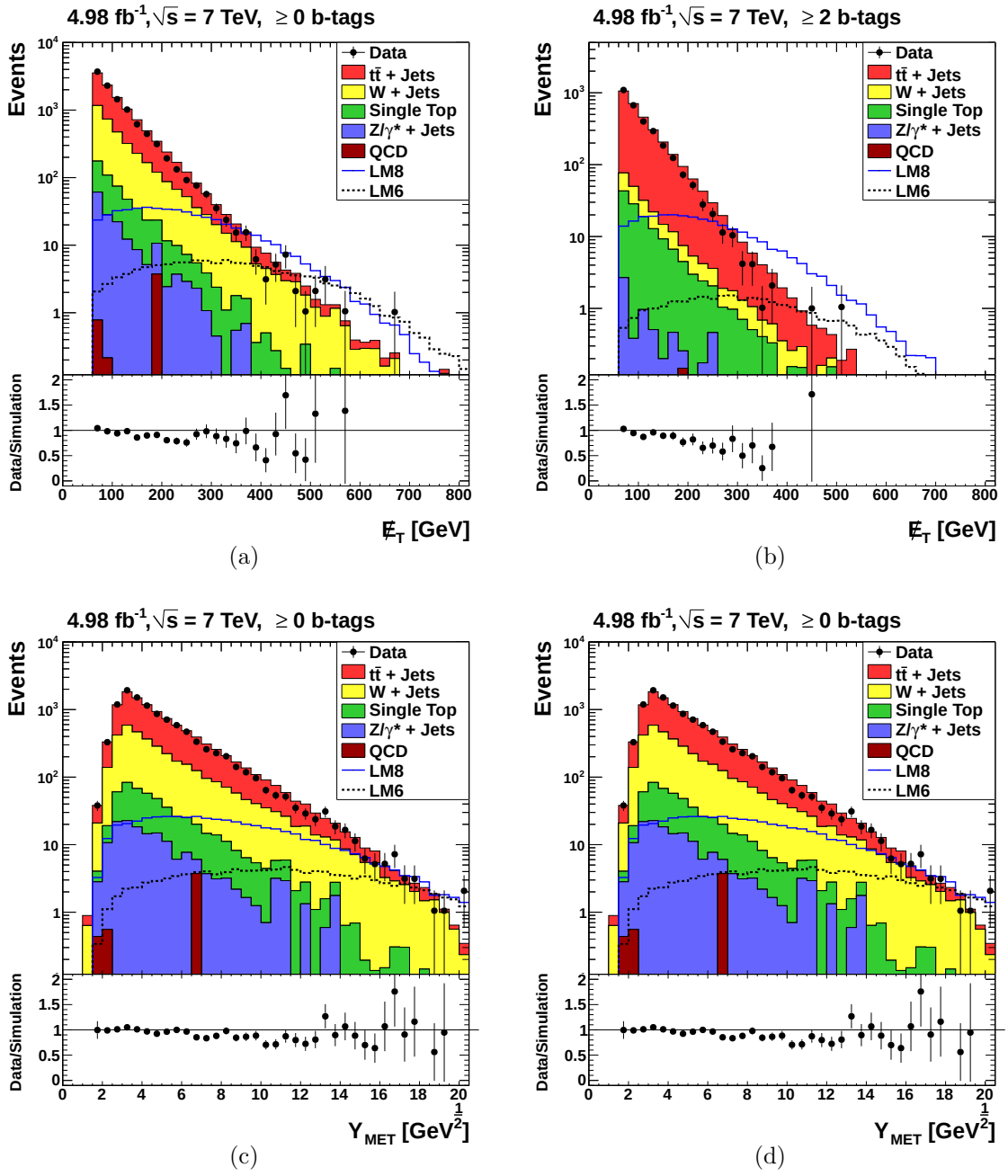

Figure C.2.: $\not\!\!E_T$ (top) and Y_{MET} (bottom) after the event selection with the requirement of at least zero b-jets (left) and at least two b-jets (right).

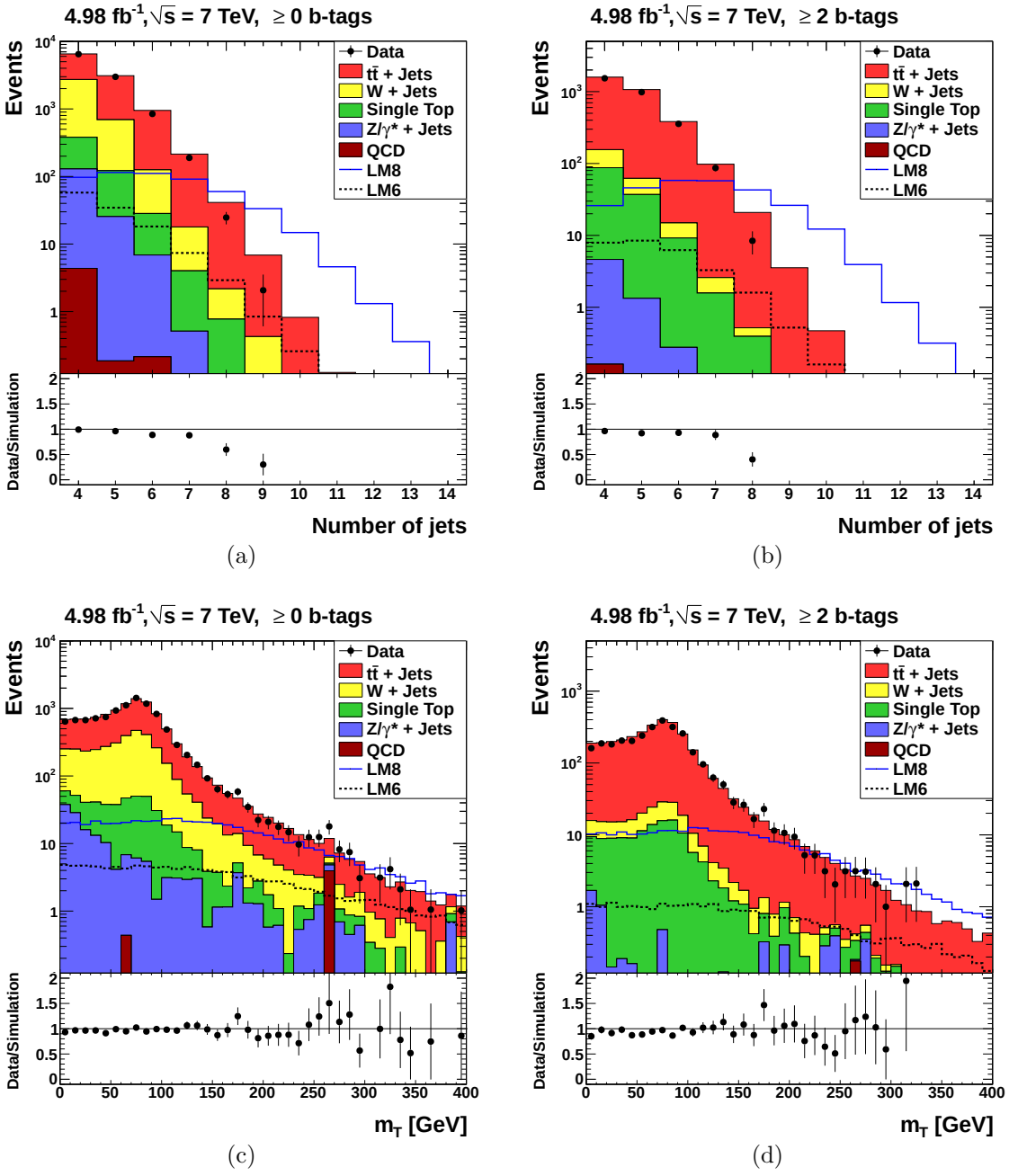

Figure C.3.: Multiplicity of selected jets (top) and tranverse W-boson mass m_T (bottom) after the event selection with the requirement of at least zero b-jets (left) and at least two b-jets (right).

C.2. B-tag Efficiency Weighting

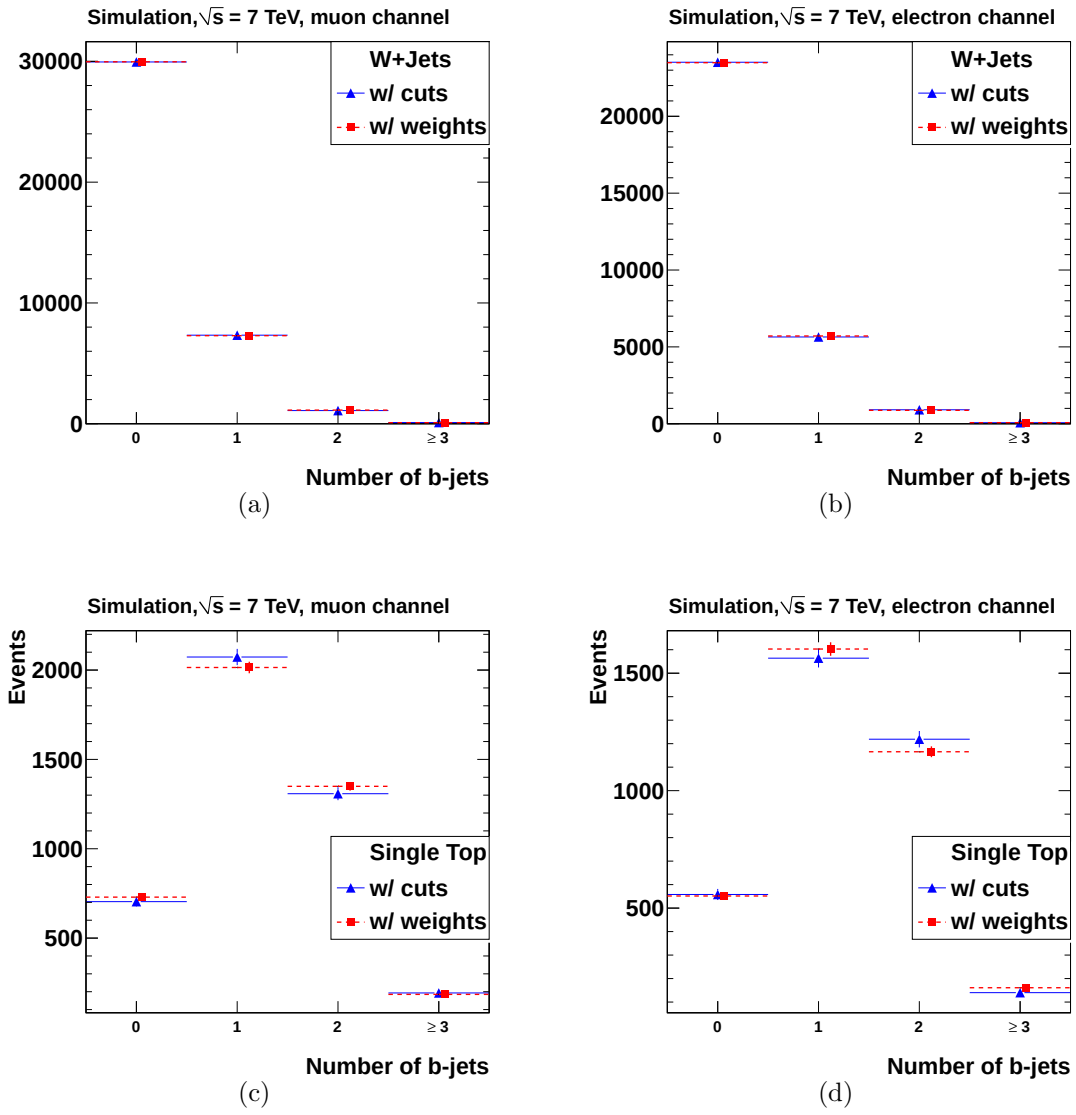

Figure C.4.: Number of b-jets in simulated W+Jets (top) and single top (bottom) events that pass the jet selection in the muon left and the electron (right) channel. The distributions obtained when applying weights are represented by the red markers, those obtained when applying cuts are indictaed by the blue markers. For better visibility, the markers are slightly shifted from one another in x direction. All scale factors are set to one and no cross section and pile-up weighting is applied.

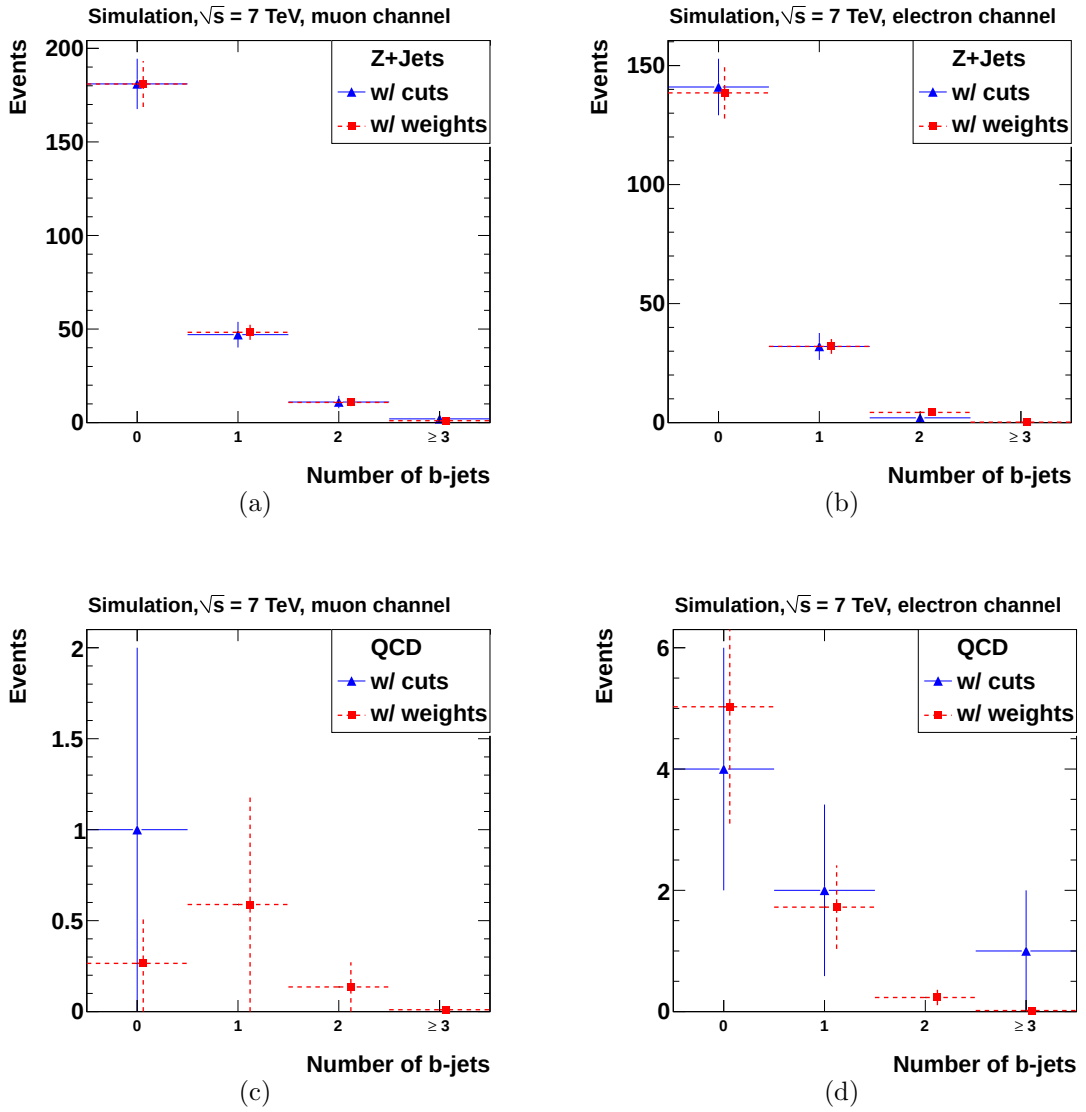

Figure C.5.: Number of b-jets in simulated Z+Jets (top) and QCD (bottom) events that pass the jet selection in the muon left and the electron (right) channel. The distributions obtained when applying weights are represented by the red markers, those obtained when applying cuts are indictaed by the blue markers. For better visibility, the markers are slightly shifted from one another in x direction. All scale factors are set to one and no cross section and pile-up weighting is applied. Because of limited statistics Z+Jets and QCD events are weighted according to the tagging effieciencies obtained from simulaetd W+Jets events

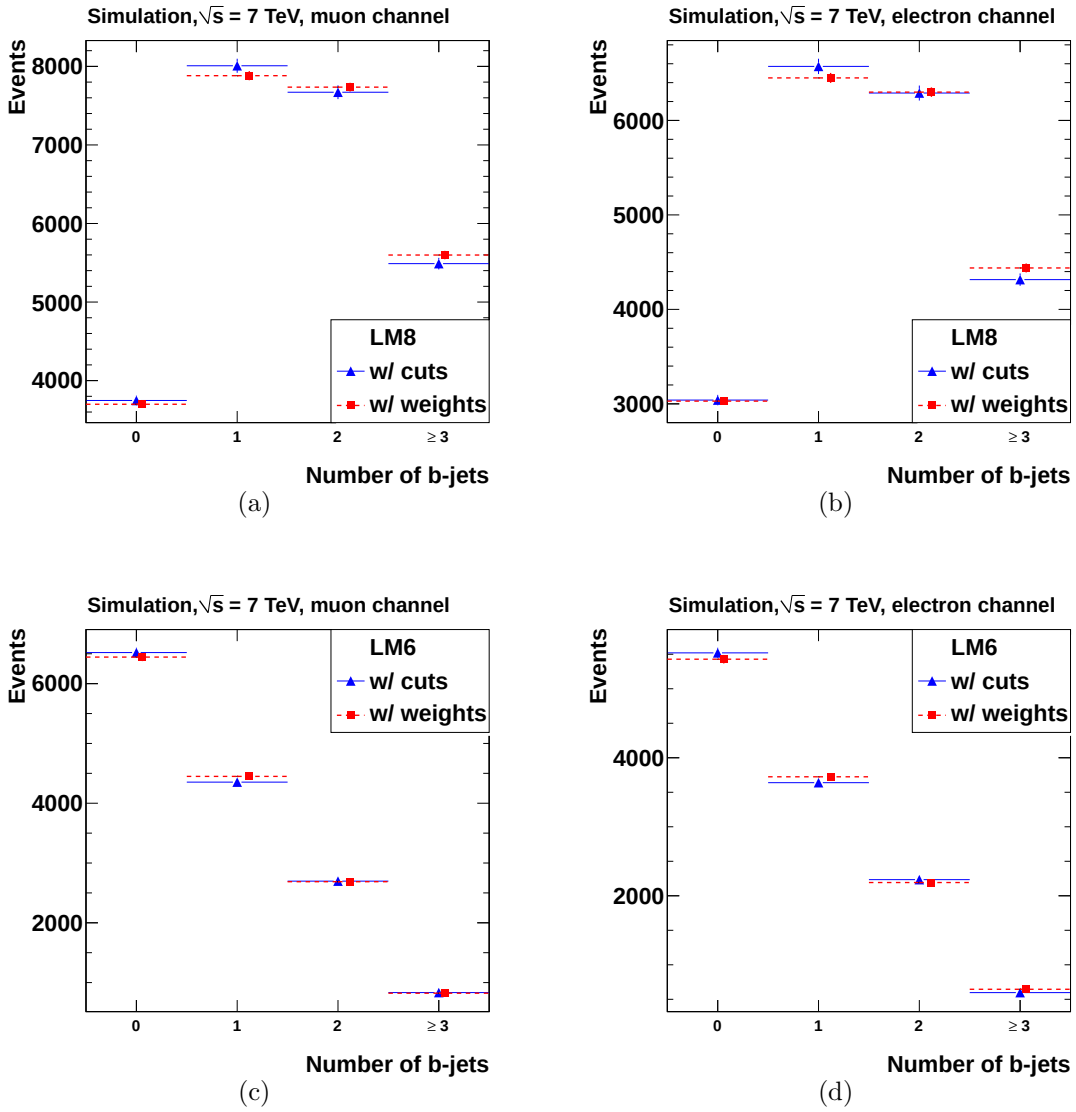

Figure C.6.: Number of b-jets in simulated signal events in the LM8 (top) and the LM6 (bottom) scenario that pass the jet selection in the muon (left) and the electron (right) channel. The distributions obtained when applying weights are represented by the red markers, those obtained when applying cuts are indictaed by the blue markers. For better visibility, the markers are slightly shifted from one another in x direction. All scale factors are set to one and no cross section and pile-up weighting is applied. Events in the LM8 and the LM6 scenario are weighted based on the efficiencies calculated from simulated $t\bar{t}$ events.

C.3. Further Event Yields

Table C.1.: Numbers of selected data events and simulated Standard Model events and data-to-simulation ratios after the successively applied event selection steps in the muon channel. Only statisical uncertainties are shown.

Selection	Data	All SM	Data/All SM
preselection	14586 ± 124	15322 ± 31	0.95 ± 0.01
jet selection	5822 ± 79	6005 ± 16	0.97 ± 0.01
$\geqq 1$ b-tags	3797 ± 63	3987 ± 9	0.95 ± 0.02
$\geqq 2$ b-tags	1660 ± 42	1750 ± 4	0.95 ± 0.02
$\geqq 3$ b-tags	212 ± 15	244 ± 1	0.87 ± 0.06

Table C.2.: Numbers of selected data events and simulated Standard Model events and data-to-simulation ratios after the successively applied event selection steps in the electron channel. Only statisical uncertainties are shown.

Selection	Data	All SM	Data/All SM
preselection	11985 ± 111	12749 ± 100	0.94 ± 0.01
jet selection	4703 ± 70	4840 ± 15	0.97 ± 0.01
$\geqq 1$ b-tags	3003 ± 56	3213 ± 8	0.93 ± 0.02
$\geqq 2$ b-tags	1309 ± 37	1416 ± 4	0.92 ± 0.03
$\geqq 3$ b-tags	160 ± 13	198 ± 1	0.81 ± 0.07

Table C.3.: Numbers of simulated $t\bar{t}$+Jets events for the individual subprocesses after the successively applied event selection steps.

Selection	All $t\bar{t}$+Jets	Semilep. e/μ	Semilep. τ	Dilep.	Fullhad.
preselection	10234	7827	875	1531	0.8
jet selection	7280	5779	641	861	0.7
$\geqq 1$ b-tags	6147	4873	539	735	0.5
$\geqq 2$ b-tags	2930	2321	256	353	0.2
$\geqq 3$ b-tags	418	338	37	43	< 0.1

Table C.4.: Numbers of simulated single top events for the individual subprocesses after the successively applied event selection steps.

Selection	All single top	$t + b$ (s-channel)	$t + q$ (t-channel)	$t + W$
preselection	853	42	318	492
jet selection	374	10	85	278
$\geqq 1$ b-tags	305	9.2	73	223
$\geqq 2$ b-tags	129	4.6	34	91
$\geqq 3$ b-tags	16	0.5	3.4	12

Table C.5.: Numbers of simulated signal events in the SUSY benchmark scenarios LM8 and LM6 and the resulting signal-to-background ratios after the event selection with the additional requirement of $m_T > 120$ GeV in the inclusive 0-b-tag channel ("$m_T > 120$ GeV"), the inclusive 1-b-tag channel, and the inclusive 3-b-tag channel.

Selection	LM8	LM6	LM8/All SM	LM6/All SM
$m_T > 120$	276	68	0.337 ± 0.004	0.083 ± 0.001
$\geqq 1$ b-tags	233	37	0.398 ± 0.004	0.064 ± 0.001
$\geqq 3$ b-tags	57	3.6	1.541 ± 0.024	0.096 ± 0.003

Table C.6.: Numbers of selected data and simulated Standard Model events and data-to-simulation ratios after the event selection with the additional requirement of $m_T > 120$ GeV in the inclusive 0-b-tag channel ("$m_T > 120$ GeV"), the inclusive 1-b-tag channel, and the inclusive 3-b-tag channel. Only statisical uncertainties are shown.

Selection	Data	All SM	Data/All SM
$m_T > 120$	821 ± 29	817 ± 7	1.00 ± 0.05
$\geqq 1$ b-tags	568 ± 24	586 ± 4	0.97 ± 0.06
$\geqq 3$ b-tags	35 ± 6	37 ± 0	0.94 ± 0.23

D. Background Prediction From Data Appendix

D.1. Factorization Method

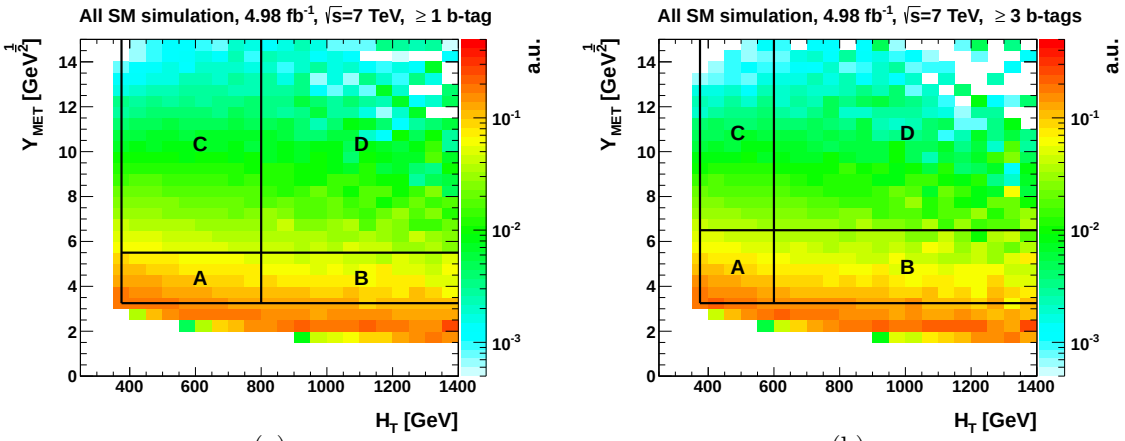

Figure D.1.: Distribution of simulated Standard Model events in the H_{T} - Y_{MET} plane after the event selection in the inclusive 1-b-tag channel (left) and the inclusive 3-b-tag channel (right). For each bin in Y_{MET} the distribution is normalized to unit area in the region of $H_{\mathrm{T}} > 375$ GeV.

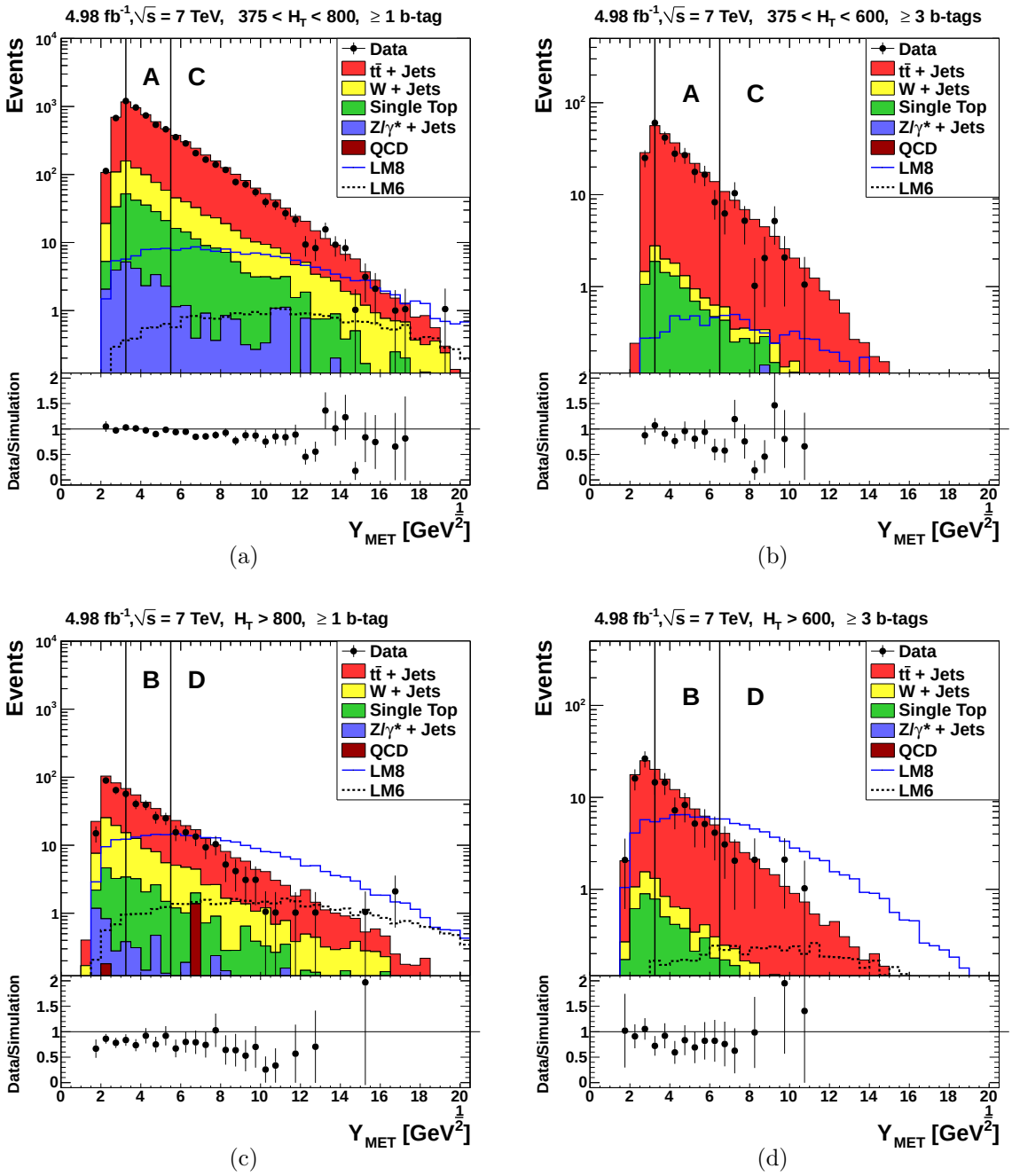

Figure D.2.: Y_{MET} of selected events after the event selection in the inclusive 1-b-tag channel (left) and the inclusive 3-b-tag channel (right) in the different control and signal regions, as indicated by the vertical black lines.

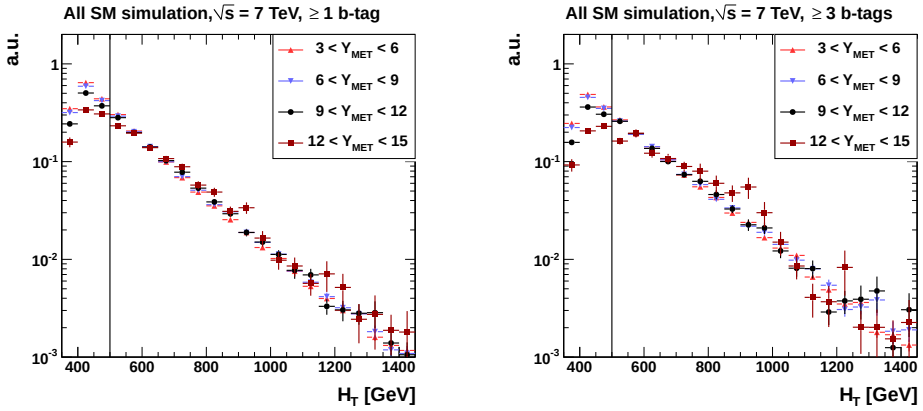

(a)

(b)

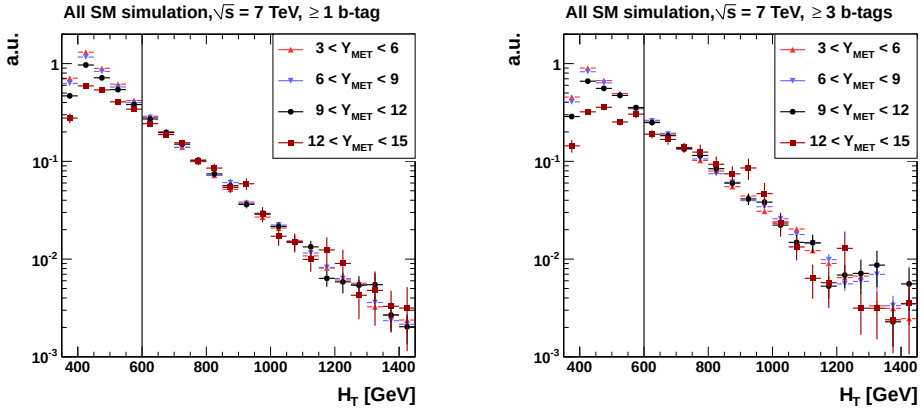

(c)

(d)

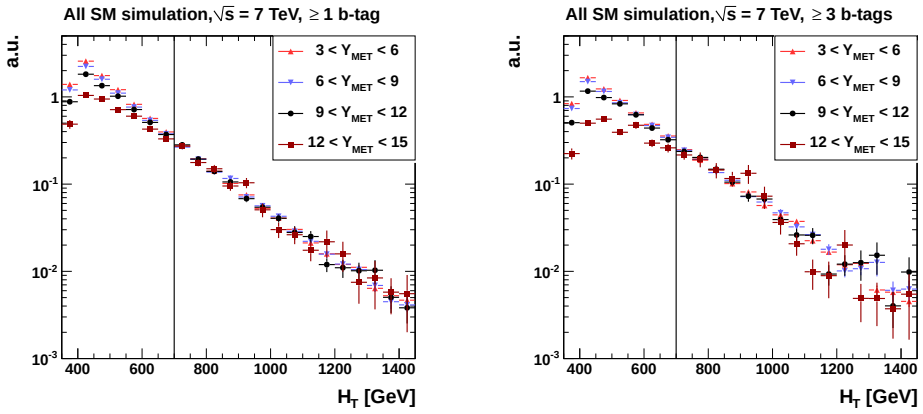

(e)

(f)

Figure D.3.: H_{T} of Standard Model events after the event selection with at least one b-jet (left) and at least two b-jets (right) for different Y_{MET} requirements. The distributions are normalized to unit area in the regions $H_{\mathrm{T}} > 500$ GeV (top), $H_{\mathrm{T}} > 600$ GeV (middle), and $H_{\mathrm{T}} > 700$ GeV (bottom), as marked by the vertical black lines.

D.2. Background From Semileptonic $t\bar{t}$ Decays

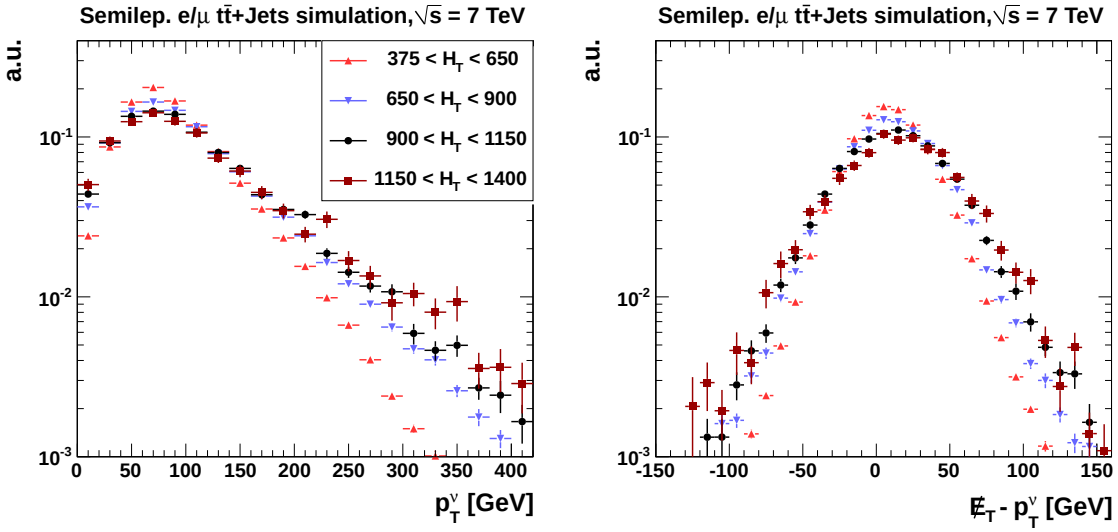

(a) $\geqq 3$ b-jets (b) $\geqq 3$ b-jets

Figure D.4.: p_{T}^{ν} (left) and $\not{E}_T - p_T^{\nu}$ (right) of simulated events after the event selection in the inclusive 1-b-tag channel with the additional requirement of $Y_{\mathrm{MET}} > 3.25\ \mathrm{GeV}^{\frac{1}{2}}$ in exclusive bins of H_{T}. A preselection on events that contain a semileptonically decaying $t\bar{t}$ pair with a muon or electron at generator level is applied. All distributions are normalized to unit area.

Correlation between H_T and p_T^ν

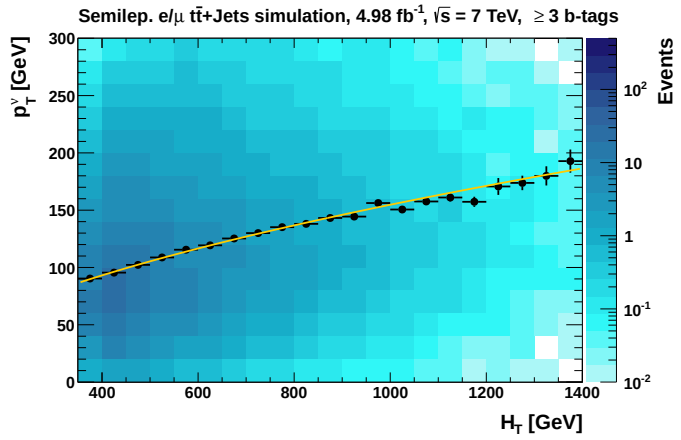

Figure D.5.: Distribution of simulated $t\bar{t}$+Jets events in the p_T^ν - H_T plane after the event selection in the inclusive 3-b-tag channel with the additional requirement of $Y_{\mathrm{MET}} > 3.25\ \mathrm{GeV}^{\frac{1}{2}}$. A preselection on events that contain a semileptonically decaying $t\bar{t}$ pair with a muon or electron at generator level is applied. The black markers represent the mean p_T^ν as a function of H_T. The yellow line represents the best fit.

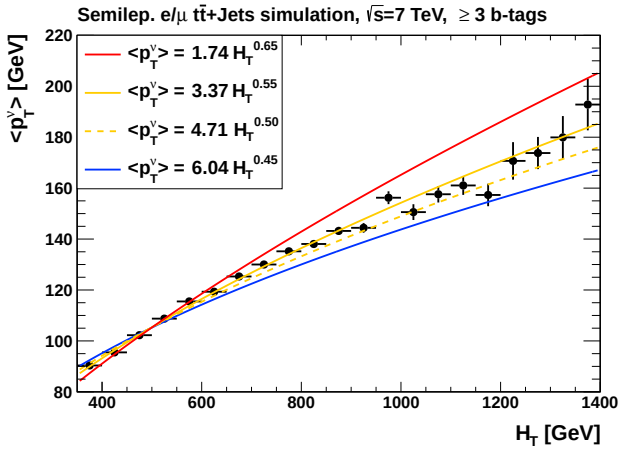

Figure D.6.: Mean p_T^ν as a function of H_T in simulated $t\bar{t}$+Jets events after the event selection in the inclusive 3-b-tag channel with the additional requirement of $Y_{\mathrm{MET}} > 3.25\ \mathrm{GeV}^{\frac{1}{2}}$. A preselection on events that contain a semileptonically decaying $t\bar{t}$ pair with a muon or electron at generator level is applied. The best fit with floating exponent is marked by the yellow line. The solid red, the solid blue, and the dashed yellow line represent fits with fixed exponent.

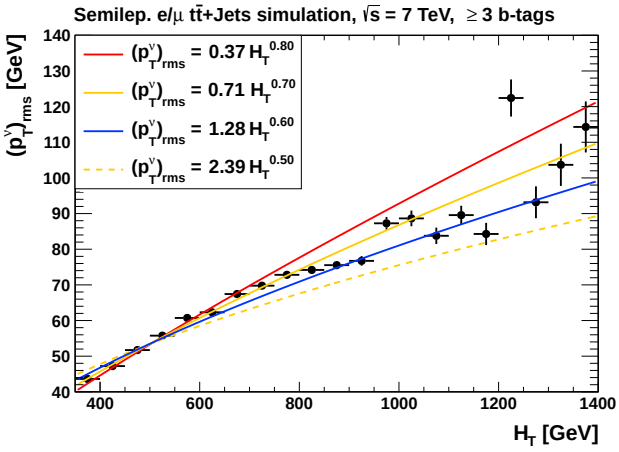

Figure D.7.: Root mean square of p_{T}^{ν} as a function of H_{T} in simulated $t\bar{t}$+Jets events after the event selection in the inclusive 1-b-tag channel with the additional requirement of $Y_{\mathrm{MET}} > 3.25\ \mathrm{GeV}^{\frac{1}{2}}$. A preselection on events that contain a semileptonically decaying $t\bar{t}$ pair with a muon or electron at generator level is applied. The best fit with floating exponent is marked by the yellow line. The solid red, the solid blue, and the dashed yellow line represent fits with fixed exponent.

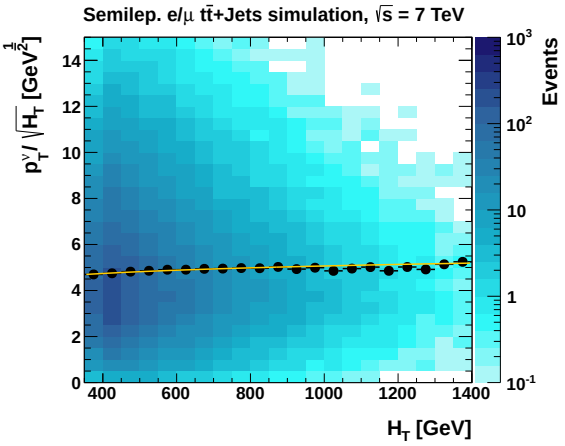

Figure D.8.: Distribution of simulated $t\bar{t}$+Jets events in the $p_{\mathrm{T}}^{\nu}/\sqrt{H_{\mathrm{T}}}$ - H_{T} plane after the event selection in the inclusive 3-b-tag channel with the additional requirement of $Y_{\mathrm{MET}} > 3.25\ \mathrm{GeV}^{\frac{1}{2}}$. A preselection on events that contain a semileptonically decaying $t\bar{t}$ pair with a muon or electron at generator level is applied. The black markers represent the mean $p_{\mathrm{T}}^{\nu}/\sqrt{H_{\mathrm{T}}}$ as a function of H_{T}. The yellow line represents the best fit.

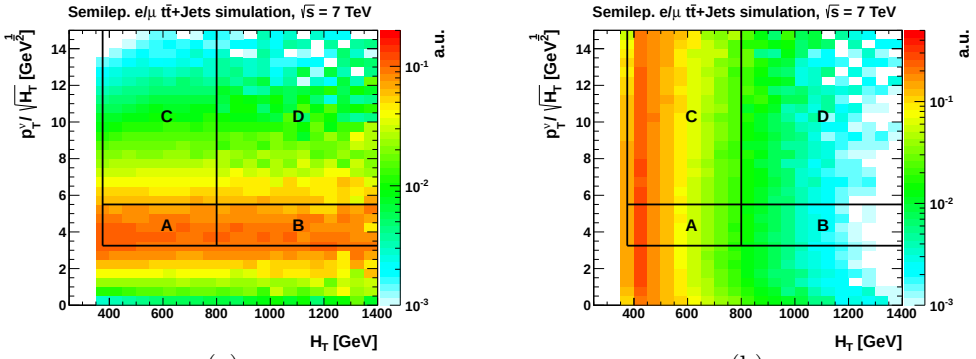

(a) (b)

Figure D.9.: Distribution of simulated events in the $p_{\mathrm{T}}^{\nu}/\sqrt{H_{\mathrm{T}}}$ - H_{T} plane after the event selection in the inclusive 3-b-tag channel with the additional requirement of $Y_{\mathrm{MET}} > 3.25$ GeV$^{\frac{1}{2}}$. A preselection on events that contain a semileptonically decaying $t\bar{t}$ pair with a muon or electron at generator level is applied. In Fig. (a), for each bin in H_{T} the distribution is normalized to unit area in the region of $p_{\mathrm{T}}^{\nu}/\sqrt{H_{\mathrm{T}}} > 0$ GeV$^{\frac{1}{2}}$. In Fig. (b), for each bin in $p_{\mathrm{T}}^{\nu}/\sqrt{H_{\mathrm{T}}}$ the distribution is normalized to unit area in the region $H_{\mathrm{T}} > 375$ GeV.

Correlation between H_{T} and $\not{E}_{\mathrm{T}} - p_{\mathrm{T}}^{\nu}$

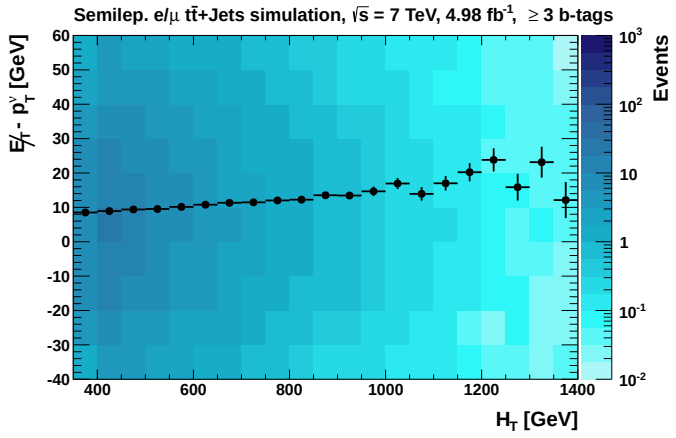

Figure D.10.: Distribution of simulated $t\bar{t}$+Jets events in the H_{T} - $(\not{E}_{\mathrm{T}} - p_{\mathrm{T}}^{\nu})$ plane after the event selection in the inclusive 1-b-tag channel with the additional requirement of $Y_{\mathrm{MET}} > 3.25$ GeV$^{\frac{1}{2}}$. level is applied. The black markers represent the mean $(\not{E}_{\mathrm{T}} - p_{\mathrm{T}}^{\nu})$ as a function of H_{T}.

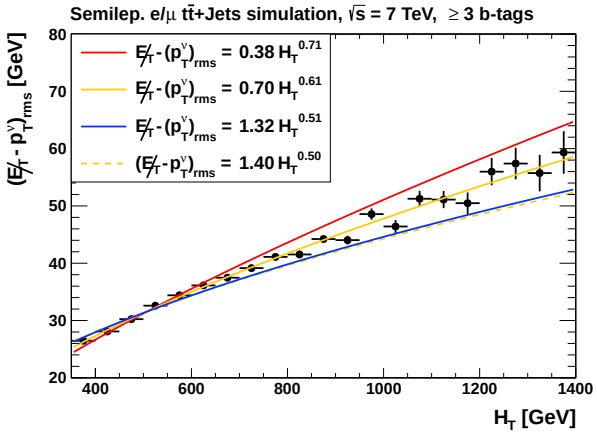

Figure D.11.: Root mean square of $(\not\!\!E_{\mathrm{T}} - p_{\mathrm{T}}^{\nu})$ as a function of H_{T} in simulated $t\bar{t}$+Jets events after the event selection in the inclusive 1-b-tag channel with the additional requirement of $Y_{\mathrm{MET}} > 3.25\ \mathrm{GeV}^{\frac{1}{2}}$. The best fit with floating exponent is marked by the yellow line. The solid red, the solid blue, and the dashed yellow line represent fits with fixed exponent.

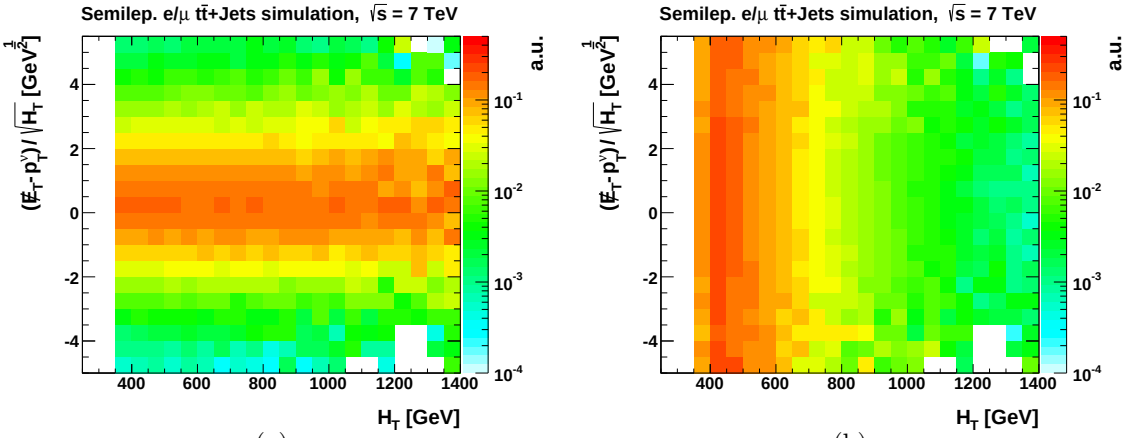

(a) (b)

Figure D.12.: Distribution of simulated events in the $(\not\!\!E_{\mathrm{T}} - p_{\mathrm{T}}^{\nu})/\sqrt{H_{\mathrm{T}}}$ - H_{T} plane after the event selection in the inclusive 3-b-tag channel with the additional requirement of $Y_{\mathrm{MET}} > 3.25\ \mathrm{GeV}^{\frac{1}{2}}$. A preselection on events that contain a semileptonically decaying $t\bar{t}$ pair with a muon or electron at generator level is applied. In Fig. (a), for each bin in H_{T} the distribution is normalized to unit area in the whole region of $(\not\!\!E_{\mathrm{T}} - p_{\mathrm{T}}^{\nu})/\sqrt{H_{\mathrm{T}}}$. In Fig. (b), for each bin in $(\not\!\!E_{\mathrm{T}} - p_{\mathrm{T}}^{\nu})/\sqrt{H_{\mathrm{T}}}$ the distribution is normalized to unit area in the region $H_{\mathrm{T}} > 375$ GeV.

Influence of the Event Selection

Table D.1.: Best fit values and χ^2 divided by the number of degrees of freedom. A preselection on events that contain a semileptonically decaying $t\bar{t}$ pair with a muon or electron at generator level is applied.

Selection	$\langle p_{\mathrm{T}}^{\nu} \rangle = b \cdot {H_{\mathrm{T}}}^{c}$	χ^2/n_{dof}	$\langle p_{\mathrm{T}}^{\nu} \rangle = a + b \cdot {H_{\mathrm{T}}}^{c}$	χ^2/n_{dof}
no cuts	$4.65 \cdot {H_{\mathrm{T}}}^{0.52}$	6.12	$18.39\,\mathrm{GeV} + 2.20 \cdot {H_{\mathrm{T}}}^{0.61}$	5.97
preselection	$4.19 \cdot {H_{\mathrm{T}}}^{0.53}$	4.95	$-2.32\,\mathrm{GeV} + 4.55 \cdot {H_{\mathrm{T}}}^{0.52}$	5.22
jet selection	$3.51 \cdot {H_{\mathrm{T}}}^{0.55}$	4.40	$-3.09\,\mathrm{GeV} + 3.95 \cdot {H_{\mathrm{T}}}^{0.54}$	4.64
$\geqq$ **1 b-tags**	$3.37 \cdot {H_{\mathrm{T}}}^{0.56}$	4.37	$-8.14\,\mathrm{GeV} + 4.57 \cdot {H_{\mathrm{T}}}^{0.52}$	4.56
$\geqq$ **3 b-tags**	$3.37 \cdot {H_{\mathrm{T}}}^{0.55}$	2.84	$-33.36\,\mathrm{GeV} + 9.73 \cdot {H_{\mathrm{T}}}^{0.43}$	2.70

Table D.2.: Best fit values and χ^2 divided by the number of degrees of freedom. A preselection on events that contain a semileptonically decaying $t\bar{t}$ pair with a muon or electron at generator level is applied.

Selection	$\langle p_{\mathrm{T}}^{\nu} \rangle_{\mathrm{rms}} = b \cdot {H_{\mathrm{T}}}^{c}$	χ^2/n_{dof}	$\langle p_{\mathrm{T}}^{\nu} \rangle_{\mathrm{rms}} = a + b \cdot {H_{\mathrm{T}}}^{c}$	χ^2/n_{dof}
no cuts	$1.29 \cdot {H_{\mathrm{T}}}^{0.62}$	5.96	$9.74\,\mathrm{GeV} + 0.55 \cdot {H_{\mathrm{T}}}^{0.73}$	11.44
preselection	$1.19 \cdot {H_{\mathrm{T}}}^{0.63}$	4.99	$-9.91\,\mathrm{GeV} + 2.33 \cdot {H_{\mathrm{T}}}^{0.55}$	5.02
jet selection	$0.77 \cdot {H_{\mathrm{T}}}^{0.69}$	4.23	$-16.66\,\mathrm{GeV} + 2.56 \cdot {H_{\mathrm{T}}}^{0.54}$	3.75
$\geqq$ **1 b-tags**	$0.73 \cdot {H_{\mathrm{T}}}^{0.69}$	4.36	$-22.17\,\mathrm{GeV} + 3.31 \cdot {H_{\mathrm{T}}}^{0.51}$	3.40
$\geqq$ **3 b-tags**	$0.71 \cdot {H_{\mathrm{T}}}^{0.70}$	7.08	$-56.20\,\mathrm{GeV} + 12.10 \cdot {H_{\mathrm{T}}}^{0.36}$	5.66

Table D.3.: Best fit values and χ^2 divided by the number of degrees of freedom. A preselection on events that contain a semileptonically decaying $t\bar{t}$ pair with a muon or electron at generator level is applied.

Selection	$\langle p_{\mathrm{T}}^{\nu} - \not{E}_{\mathrm{T}}^{\mathrm{fake}} \rangle_{\mathrm{rms}} = b \cdot {H_{\mathrm{T}}}^{c}$	χ^2/n_{dof}	$\langle p_{\mathrm{T}}^{\nu} - \not{E}_{\mathrm{T}}^{\mathrm{fake}} \rangle_{\mathrm{rms}} = a + b \cdot {H_{\mathrm{T}}}^{c}$	χ^2/n_{dof}
no cuts	$0.76 \cdot {H_{\mathrm{T}}}^{0.60}$	7.03	$9.74\,\mathrm{GeV} + 0.55 \cdot {H_{\mathrm{T}}}^{0.73}$	11.44
preselection	$0.82 \cdot {H_{\mathrm{T}}}^{0.59}$	5.87	$6.51\,\mathrm{GeV} + 0.27 \cdot {H_{\mathrm{T}}}^{0.73}$	5.55
jet selection	$0.72 \cdot {H_{\mathrm{T}}}^{0.61}$	3.12	$6.55\,\mathrm{GeV} + 0.22 \cdot {H_{\mathrm{T}}}^{0.76}$	2.73
$\geqq$ **1 b-tags**	$0.70 \cdot {H_{\mathrm{T}}}^{0.61}$	2.82	$5.04\,\mathrm{GeV} + 0.30 \cdot {H_{\mathrm{T}}}^{0.72}$	2.67
$\geqq$ **3 b-tags**	$0.70 \cdot {H_{\mathrm{T}}}^{0.61}$	1.96	$-3.12\,\mathrm{GeV} + 1.07 \cdot {H_{\mathrm{T}}}^{0.56}$	2.04

Influence of the Control and Signal Region Definition

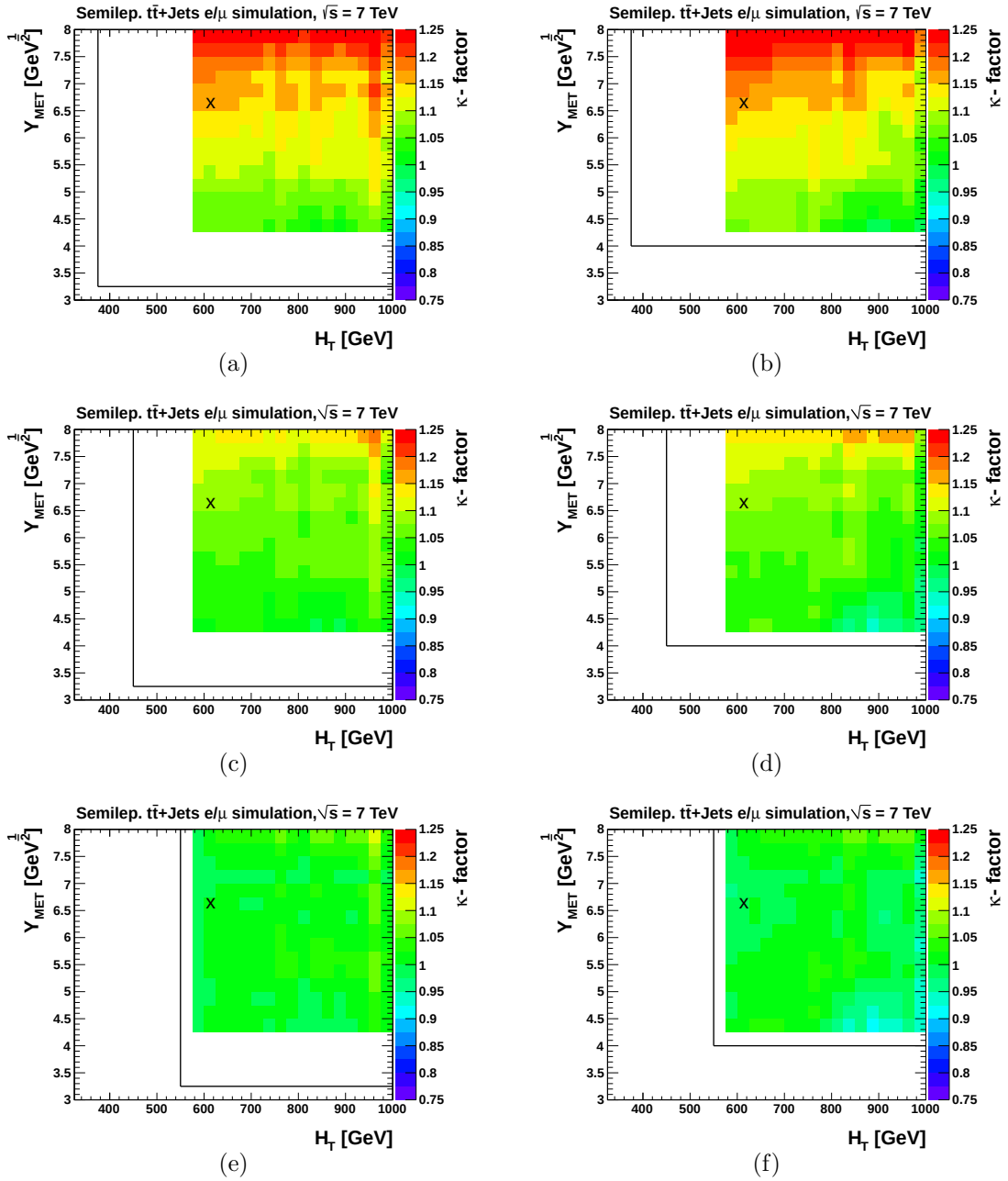

Figure D.13.: Influence of the definition of control and signal regions on the correlation factor κ in simulated events after the event selection in the inclusive 3-b-tag channel. A preselection on events that contain a semileptonically decaying $t\bar{t}$ pair with a muon or electron at generator level is applied. The κ-scan is performed for different lower H_{T} and Y_{MET} requirements, as marked by the solid black lines. The black cross indicates the H_{T} and Y_{MET} requirements by which the control and signal regions are separated from each other in this channel.

E. Gluino Endpoint Measurement Appendix

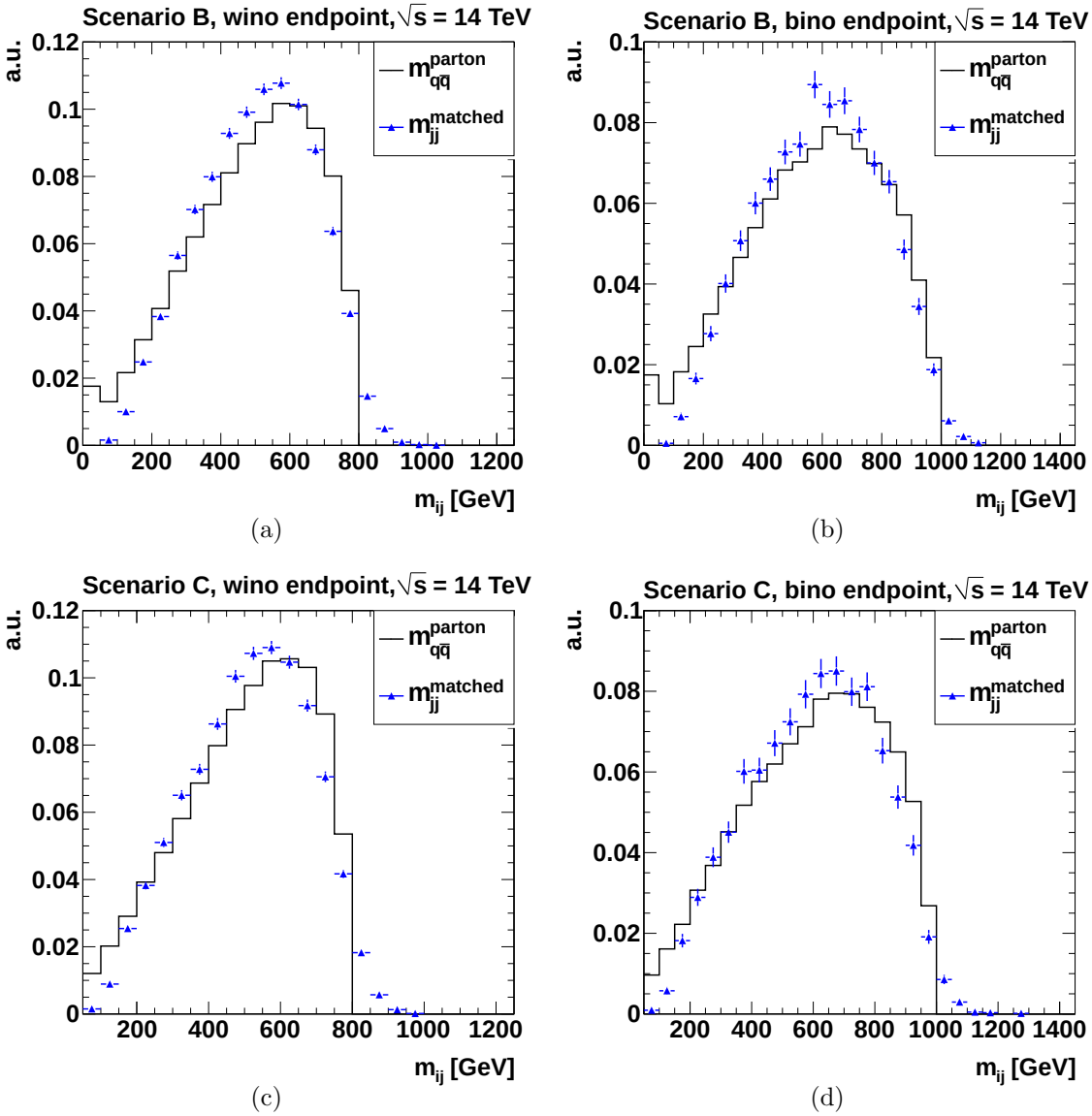

Figure E.1.: Invariant diquark-mass and invariant dijet-mass distributions resulting from the gluino three-body decays $\tilde{g} \to q\bar{q}\tilde{B}$ (left) and $\tilde{g} \to q\bar{q}\tilde{W}$ (right) in benchmark scenarios B (top) and C (bottom). Only jets that can be unambiguously matched to the quarks that result from the three-body decays are considered.

Table E.1.: Numbers of the simulated Standard Model events for the individual subprocesses after the successively applied event selection criteria in the bino and the wino channel. Uncertainties are only statistical.

Selection	QCD	$t\bar{t}$+Jets	W+Jets	Z+Jets	Single Top
preselection	$789,679 \pm 3365$	$103,110 \pm 480$	$14,8264 \pm 603$	$29,230 \pm 250$	3550 ± 25
Bino Selection					
$4 \leq n_{\text{Jets}} \leq 5$	$249,065 \pm 2332$	$51,365 \pm 338$	$47,496 \pm 341$	9222 ± 140	941 ± 12
lepton veto	$246,292 \pm 2307$	$30,298 \pm 267$	$29,290 \pm 268$	8230 ± 133	614 ± 10
$\lvert\Delta\Phi(\text{jet}^1, \not{E}_{\text{T}})\rvert > 0.5$	$211,427 \pm 2079$	$28,912 \pm 260$	$28,284 \pm 263$	7936 ± 130	595 ± 10
$\lvert\Delta\Phi(\text{jet}^2, \not{E}_{\text{T}})\rvert > 0.5$	$32,857 \pm 1041$	$12,142 \pm 167$	$17,890 \pm 209$	5092 ± 105	134 ± 4
$\lvert\Delta\Phi(\text{jet}^3, \not{E}_{\text{T}})\rvert > 0.3$	7253 ± 552	6519 ± 122	$12,188 \pm 173$	3914 ± 92	41 ± 2
$\not{E}_{\text{T}} > 600$ GeV	6.7 ± 2.5	156 ± 19	927 ± 47	480 ± 32	5.1 ± 0.7
Wino Selection					
$n_{\text{Jets}} \geq 6$	$35,664 \pm 973$	$22,869 \pm 230$	6343 ± 124	1062 ± 47	66 ± 3
one lepton	2.5 ± 2.5	5115 ± 106	1374 ± 58	50 ± 10	11 ± 1
$m_T \geq 120$ GeV	-	522 ± 24	45 ± 10	2.0 ± 2.0	-
$n_{\text{Bjets}} \leq 1$	-	237 ± 16	43 ± 10	2.0 ± 2.0	-

Table E.2.: Numbers of the simulated signal events in benchmark scenario A for the individual subprocesses after the successively applied event selection criteria in the bino and the wino channel. "$\tilde{B}$" and "$\tilde{W}$" denote initially produced gluinos that decay into a $q\bar{q}$ pair and a bino and a $q\bar{q}$ pair and a wino, respectively. Uncertainties are only statistical.

	$\tilde{B}+\tilde{B}$	$\tilde{B}+\tilde{q}$	$\tilde{B}+\tilde{W}$	$\tilde{W}+\tilde{W}$	$\tilde{W}+\tilde{q}$	$\tilde{q}+\tilde{q}$
no cuts	627 ± 26	9140 ± 99	6952 ± 86	18892 ± 142	49206 ± 230	23157 ± 158
preselection	487 ± 22	6877 ± 86	5428 ± 76	13087 ± 118	37402 ± 200	16968 ± 135
Bino Selection						
$4 \leq n_{\text{Jets}} \leq 5$	209 ± 15	3765 ± 63	1481 ± 40	1932 ± 45	16075 ± 131	8355 ± 94
lepton veto	207 ± 14	3404 ± 60	1175 ± 35	1135 ± 35	12221 ± 114	7014 ± 87
$\lvert\Delta\Phi(\text{jet}^1, \not{E}_{\text{T}})\rvert > 0.5$	207 ± 14	3367 ± 60	1158 ± 35	1112 ± 34	12051 ± 114	6951 ± 86
$\lvert\Delta\Phi(\text{jet}^2, \not{E}_{\text{T}})\rvert > 0.5$	195 ± 14	2991 ± 56	1004 ± 32	949 ± 32	10417 ± 106	6106 ± 81
$\lvert\Delta\Phi(\text{jet}^3, \not{E}_{\text{T}})\rvert > 0.3$	170 ± 13	2554 ± 52	852 ± 30	797 ± 29	8713 ± 97	4957 ± 73
$\not{E}_{\text{T}} > 600$ GeV	69 ± 8	1189 ± 35	230 ± 15	118 ± 11	3608 ± 62	2303 ± 49
Wino Selection						
$n_{\text{Jets}} \geq 6$	265 ± 16	2083 ± 47	3869 ± 64	11082 ± 109	19121 ± 143	3414 ± 60
one lepton	-	82 ± 9	249 ± 16	1715 ± 43	1919 ± 46	267 ± 17
$m_T \geq 120$ GeV	-	57 ± 8	172 ± 14	1054 ± 34	1219 ± 36	165 ± 13
$n_{\text{Bjets}} \leq 1$	-	53 ± 8	156 ± 13	887 ± 31	1027 ± 33	126 ± 12

Table E.3.: Numbers of the simulated signal events in benchmark scenario B for the individual subprocesses after the successively applied event selection criteria in the bino and the wino channel. "$\tilde{B}$" and "$\tilde{W}$" denote initially produced gluinos that decay into a $q\bar{q}$ pair and a bino and a $q\bar{q}$ pair and a wino, respectively. Uncertainties are only statistical.

	$\tilde{B}+\tilde{B}$	$\tilde{B}+\tilde{q}$	$\tilde{B}+\tilde{W}$	$\tilde{W}+\tilde{W}$	$\tilde{W}+\tilde{q}$	$\tilde{q}+\tilde{q}$
no cuts	609 ± 12	1053 ± 17	5958 ± 40	14349 ± 62	5264 ± 38	366 ± 10
preselection	503 ± 11	772 ± 14	4677 ± 35	9951 ± 52	3946 ± 33	319 ± 9
Bino Selection						
$4 \leq n_{\text{Jets}} \leq 5$	181 ± 7	369 ± 10	1007 ± 16	1174 ± 18	1465 ± 20	162 ± 6
lepton veto	178 ± 7	318 ± 9	765 ± 14	642 ± 13	1048 ± 17	126 ± 5
$\lvert\Delta\Phi(\text{jet}^1, \not{E}_{\text{T}})\rvert > 0.5$	174 ± 6	311 ± 9	748 ± 14	622 ± 13	1025 ± 16	123 ± 5
$\lvert\Delta\Phi(\text{jet}^2, \not{E}_{\text{T}})\rvert > 0.5$	150 ± 6	258 ± 8	656 ± 13	538 ± 12	826 ± 15	98 ± 5
$\lvert\Delta\Phi(\text{jet}^3, \not{E}_{\text{T}})\rvert > 0.3$	133 ± 6	203 ± 7	564 ± 12	455 ± 11	653 ± 13	69 ± 4
$\not{E}_{\text{T}} > 600$ GeV	47 ± 3	106 ± 5	133 ± 6	55 ± 3	347 ± 9	41 ± 3
Wino Selection						
$n_{\text{Jets}} \geq 6$	309 ± 9	298 ± 9	3630 ± 31	8743 ± 49	2260 ± 24	79 ± 4
one lepton	1.7 ± 0.7	15 ± 2.0	292 ± 9	1418 ± 20	265 ± 9	8.8 ± 1.6
$m_T \geq 120$ GeV	1.7 ± 0.7	8.0 ± 1.5	199 ± 7	895 ± 16	173 ± 7	6.6 ± 1.4
$n_{\text{Bjets}} \leq 1$	0.27 ± 0.27	7.5 ± 1.4	175 ± 7	722 ± 14	141 ± 6	5.2 ± 1.2

Table E.4.: Numbers of the simulated signal events in benchmark scenario C for the individual subprocesses after the successively applied event selection criteria in the bino and the wino channel. "$\tilde{B}$" and "$\tilde{W}$" denote initially produced gluinos that decay into a $q\bar{q}$ pair and a bino and a $q\bar{q}$ pair and a wino, respectively. Uncertainties are only statistical.

Selection	$\tilde{B}+\tilde{B}$	$\tilde{B}+\tilde{W}$	$\tilde{W}+\tilde{W}$
no cuts	523 ± 9	4689 ± 27	10982 ± 42
preselection	381 ± 7	3339 ± 23	6956 ± 33
Bino Selection			
$4 \leq n_{\text{Jets}} \leq 5$	174 ± 5	1008 ± 12	1228 ± 14
lepton veto	160 ± 5	749 ± 11	681 ± 10
$\lvert\Delta\Phi(\text{jet}^1, \not{E}_{\text{T}})\rvert > 0.5$	157 ± 5	733 ± 10	665 ± 10
$\lvert\Delta\Phi(\text{jet}^2, \not{E}_{\text{T}})\rvert > 0.5$	141 ± 4	637 ± 10	571 ± 9
$\lvert\Delta\Phi(\text{jet}^3, \not{E}_{\text{T}})\rvert > 0.3$	125 ± 4	545 ± 9	474 ± 8
$\not{E}_{\text{T}} > 600$ GeV	39 ± 2	104 ± 4	45 ± 2
Wino Selection			
$n_{\text{Jets}} \geq 6$	186 ± 5	2276 ± 19	5684 ± 30
one lepton	11 ± 1	244 ± 6	974 ± 12
$m_T \geq 120$ GeV	8.4 ± 1.2	167 ± 5	599 ± 10
$n_{\text{Bjets}} \leq 1$	4.2 ± 0.8	100 ± 4	354 ± 8

Bibliography

[1] Duhem, P., "La théorie physique: son objet, et sa structure". Chevalier & Riviére, Paris, 1906.

[2] W. V. O. Quine, "Two dogmas of empiricism", *Phil.Rev.* **60** (1951) 20–43.

[3] E. Noether, "Invarianten beliebiger Differentialausdrücke", *Gött. Nachr.* (1918) 37–44.

[4] R. Haag, J. T. Lopuszanski, and M. Sohnius, "All Possible Generators of Supersymmetries of the s Matrix", *Nucl.Phys.* **B88** (1975) 257. doi:10.1016/0550-3213(75)90279-5.

[5] M. Papucci, J. T. Ruderman, and A. Weiler, "Natural SUSY Endures", *JHEP* **1209** (2012) 035, arXiv:1110.6926. doi:10.1007/JHEP09(2012)035.

[6] Planck Collaboration Collaboration, "Planck 2013 results. I. Overview of products and scientific results", arXiv:1303.5062. doi:10.1051/0004-6361/201321529.

[7] CMS Collaboration, "Search for supersymmetry in final states with a single lepton, b-quark jets, and missing transverse energy in proton-proton collisions at $\sqrt{s} = 7$ TeV", *Phys.Rev.* **D87** (2013), no. 5, 052006, arXiv:1211.3143. doi:10.1103/PhysRevD.87.052006.

[8] N. Pietsch, J. Reuter, K. Sakurai et al., "Extracting Gluino Endpoints with Event Topology Patterns", *JHEP* **1207** (2012) 148, arXiv:1206.2146. doi:10.1007/JHEP07(2012)148.

[9] V. D. Barger and R. J. N. Phillips, "Collider Physics". Frontiers in Physics. Westview Press, Boulder, Colorado, 1996. ISBN 978-0201149456.

[10] D. Griffiths, "Introduction to elementary particles". Wiley-VCH Verlag Gmbh & Co KGaA, Weinheim, 1988. ISBN 978-3-527-40601-2.

[11] P. Schmüser, "Feynman-Graphen und Eichtheorien für Experimentalphysiker". Lecture Notes in Physics. Springer, Berlin, Heidelberg, New York, London, Paris, Tokyo, 1995. ISBN 3-540-58486-2.

[12] S. P. Martin, "A Supersymmetry primer", arXiv:hep-ph/9709356.

[13] J. Wess and B. Zumino, "Supergauge transformations in four dimensions", *Nucl. Phys. B* **70** (1974) 39. doi:10.1016/0550-3213(74)90355-1.

[14] E. C. G. Stückelberg, "Un noveau modèle de l'électron ponctuel en théorie classique", *Helvetica Physica Acta* **14** (1941) 51–80. doi:http://dx.doi.org/10.5169/seals-111170.

[15] S. L. Glashow, "Partial Symmetries of Weak Interactions", *Nucl.Phys.* **22** (1961) 579–588. doi:10.1016/0029-5582(61)90469-2.

[16] S. Weinberg, "A Model of Leptons", *Phys.Rev.Lett.* **19** (1967) 1264–1266. doi:10.1103/PhysRevLett.19.1264.

[17] A. Salam, "Weak and Electromagnetic Interactions", *Conf.Proc.* **C680519** (1968) 367–377.

[18] N. Cabibbo, "Unitary Symmetry and Leptonic Decays", *Phys. Rev. Lett.* **10** (Jun, 1963) 531 – 533. doi:10.1103/PhysRevLett.10.531.

[19] M. Kobayashi and T. Maskawa, "CP violation in the renormalizable theory of weak interaction", *Prog. Theor. Phys.* **49** (1973) 652–657.

[20] Particle Data Group Collaboration, "Review of particle physics", *Phys. Rev.* **D86** (2012) 010001.

[21] ATLAS and CMS Collaboration, "Combination of ATLAS and CMS results on the mass of the top quark using up to 4.9 fb^{-1} of data", *ATLAS Conference Note* **ATLAS-CONF-2013-037** (2012).

[22] P. W. Higgs, "Broken Symmetries and the Masses of Gauge Bosons", *Phys. Rev. Lett.* **13** (1964) 508 – 509. doi:10.1103/PhysRevLett.13.508.

[23] F. Englert and R. Brout, "Broken Symmetry and the Mass of Gauge Vector Mesons", *Phys. Rev. Lett.* **13** (1964) 321 – 323. doi:10.1103/PhysRevLett.13.321.

[24] G. S. Guralnik, C. R. Hagen, and T. W. B. Kibble, "Global Conservation Laws and Massless Particles", *Phys. Rev. Lett.* **13** (1964) 585 – 587. doi:10.1103/PhysRevLett.13.585.

[25] J. Goldstone, A. Salam, and S. Weinberg, "Broken Symmetries", *Phys. Rev.* **127** (1962) 965 – 970. doi:10.1103/PhysRev.127.965.

[26] J. Baglio and A. Djouadi, "Higgs production at the lHC", *JHEP* **1103** (2011) 055, arXiv:1012.0530. doi:10.1007/JHEP03(2011)055.

[27] S. Actis, G. Passarino, C. Sturm et al., "{NNLO} computational techniques: The cases and", *Nuclear Physics B* **811** (2009), no. 1–2, 182–273. doi:http://dx.doi.org/10.1016/j.nuclphysb.2008.11.024.

[28] ATLAS Collaboration, "Measurements of the properties of the Higgs-like boson in the two photon decay channel with the ATLAS detector using 25 fb^{-1} of proton-proton collision data", *ATLAS Conference Note* **ATLAS-CONF-2013-012** (2013).

[29] CMS Collaboration, "Combination of standard model Higgs boson searches and measurements of the properties of the new boson with a mass near 125 GeV", *CMS Physics Analysis Summary* **CMS-PAS-HIG-13-005** (2013).

[30] CMS Collaboration, "Properties of the Higgs-like boson in the decay H to ZZ to 4l in pp collisions at $\sqrt{s}$=7 and 8 TeV", *CMS Physics Analysis Summary* **CMS-PAS-HIG-13-002** (2013).

[31] ATLAS Collaboration, "Measurements of the properties of the Higgs-like boson in the $WW^* \to l\nu l\nu$ decay channel with the ATLAS detector using 25 fb^{-1} of proton-proton collision data", *ATLAS Conference Note* **ATLAS-CONF-2013-030** (2013).

[32] ATLAS Collaboration, "Combined coupling measurements of the Higgs-like boson with the ATLAS detector using up to 25 fb^{-1} of proton-proton collision data", *ATLAS Conference Note* **ATLAS-CONF-2013-034** (2013).

[33] CMS Collaboration, "Probing the heavy flavor content of the ttbar dilepton channel in proton-proton collisions at $\sqrt{s} = 10\,\text{TeV}$", *CMS Physics Analysis Summary* **CMS-PAS-TOP-09-001** (2009).

[34] CMS Collaboration, "Measurement of masses in the $t\bar{t}$ system by kinematic endpoints in pp collisions at $\sqrt{s}$=7 TeV", arXiv:1304.5783. Submitted to the European Physical Journal C.

[35] CMS Collaboration, "Search for the Standard-Model Higgs boson decaying to tau pairs in proton-proton collisions at sqrt(s) = 7 and 8 TeV", *CMS Physics Analysis Summary* **CMS-PAS-HIG-13-004** (2013).

[36] ATLAS Collaboration, "Search for direct top squark pair production in final states with one isolated lepton, jets, and missing transverse momentum in $\sqrt{s} = 8\,\text{TeV}$ pp collisions using 21 fb^{-1} of ATLAS data", *ATLAS Conference Note* **ATLAS-CONF-2013-037** (2013).

[37] CMS Collaboration, "Search for Supersymmetry in pp collisions at 8 TeV in events with a single lepton, multiple jets and b-tags", *CMS Physics Analysis Summary* **CMS-PAS-SUS-13-007** (2013).

[38] H1 and ZEUS Collaboration Collaboration, "Combined Measurement and QCD Analysis of the Inclusive e+- p Scattering Cross Sections at HERA", *JHEP* **1001** (2010) 109, arXiv:0911.0884. doi:10.1007/JHEP01(2010)109.

[39] H1 and ZEUS Collaboration, "HERAPDF1.5LO PDF Set with Experimental Uncertainties", **http://www-h1.desy.de/publications** (2013).

[40] G. 't Hooft and M. J. G. Veltman, "Regularization and Renormalization of Gauge Fields", *Nucl. Phys.* **B44** (1972) 189–213. doi:10.1016/0550-3213(72)90279-9.

[41] N. Jarosik, C. Bennett, J. Dunkley et al., "Seven-Year Wilkinson Microwave Anisotropy Probe (WMAP) Observations: Sky Maps, Systematic Errors, and Basic Results", *Astrophys.J.Suppl.* **192** (2011) 14, arXiv:1001.4744. doi:10.1088/0067-0049/192/2/14.

[42] WMAP Collaboration, "Seven-Year Wilkinson Microwave Anisotropy Probe (WMAP) Observations: Cosmological Interpretation", *Astrophys.J.Suppl.* **192** (2011) 18, arXiv:1001.4538. doi:10.1088/0067-0049/192/2/18.

[43] D. Clowe, M. Bradac, A. H. Gonzalez et al., "A direct empirical proof of the existence of dark matter", *Astrophys.J.* **648** (2006) L109–L113, arXiv:astro-ph/0608407. doi:10.1086/508162.

[44] Super-Kamiokande Collaboration Collaboration, "Evidence for oscillation of atmospheric neutrinos", *Phys.Rev.Lett.* **81** (1998) 1562–1567, arXiv:hep-ex/9807003. doi:10.1103/PhysRevLett.81.1562.

[45] D. Chung, L. Everett, G. Kane et al., "The Soft supersymmetry breaking Lagrangian: Theory and applications", *Phys.Rept.* **407** (2005) 1–203, arXiv:hep-ph/0312378. doi:10.1016/j.physrep.2004.08.032.

[46] R. Kitano and Y. Nomura, "Supersymmetry, naturalness, and signatures at the LHC", *Phys.Rev.* **D73** (2006) 095004, arXiv:hep-ph/0602096. doi:10.1103/PhysRevD.73.095004.

[47] G. L. Kane, E. Kuflik, R. Lu et al., "Top Channel for Early SUSY Discovery at the LHC", *Phys.Rev.* **D84** (2011) 095004, arXiv:1101.1963. doi:10.1103/PhysRevD.84.095004.

[48] T. Gregoire, E. Katz, and V. Sanz, "Four top quarks in extensions of the standard model", *Phys.Rev.* **D85** (2012) 055024, arXiv:1101.1294. doi:10.1103/PhysRevD.85.055024.

[49] W. Beenakker, R. Hopker, M. Spira et al., "Squark and gluino production at hadron colliders", *Nucl.Phys.* **B492** (1997) 51–103, arXiv:hep-ph/9610490. doi:10.1016/S0550-3213(97)80027-2.

[50] W. Beenakker, M. Kramer, T. Plehn et al., "Stop production at hadron colliders", *Nucl.Phys.* **B515** (1998) 3–14, arXiv:hep-ph/9710451. doi:10.1016/S0550-3213(98)00014-5.

[51] M. Spira, "Higgs and SUSY particle production at hadron colliders", arXiv:hep-ph/0211145.

[52] T. Plehn, "Measuring the MSSM Lagrangian", *Czech.J.Phys.* **55** (2005) B213–B220, arXiv:hep-ph/0410063.

[53] W. Beenakker, M. Klasen, M. Kramer et al., "The Production of charginos / neutralinos and sleptons at hadron colliders", *Phys.Rev.Lett.* **83** (1999) 3780–3783, arXiv:hep-ph/9906298. doi:10.1103/PhysRevLett.100.029901, 10.1103/PhysRevLett.83.3780.

[54] W. Beenakker, R. Hopker, and M. Spira, "PROSPINO: A Program for the production of supersymmetric particles in next-to-leading order QCD", arXiv:hep-ph/9611232.

[55] J. Alwall, P. Schuster, and N. Toro, "Simplified Models for a First Characterization of New Physics at the LHC", *Phys.Rev.* **D79** (2009) 075020, arXiv:0810.3921. doi:10.1103/PhysRevD.79.075020.

[56] LHC New Physics Working Group Collaboration, "Simplified Models for LHC New Physics Searches", *J.Phys.* **G39** (2012) 105005, arXiv:1105.2838. doi:10.1088/0954-3899/39/10/105005.

[57] M. Papucci, K. Sakurai, A. Weiler et al., "Fastlim: a fast LHC limit calculator", arXiv:1402.0492.

[58] D. Kazakov, "Beyond the standard model", arXiv:hep-ph/0411064.

[59] V. A. Rubakov, "Large and infinite extra dimensions: An introduction", *Phys. Usp.* **44** (2001) 871–893, arXiv:hep-ph/0104152.

[60] T. Kaluza, "Zum Unitaritäetsproblem der Physik", *Sitzungsbericht der Preussischen Akademie der Wissenschaften* (1921) 966–972.

[61] O. Klein, "Quantum Theory and Five-Dimensional Theory of Relativity.", *Z.Phys.* **37** (1926) 895–906. doi:10.1007/BF01397481.

[62] T. Appelquist, H.-C. Cheng, and B. A. Dobrescu, "Bounds on universal extra dimensions", *Phys.Rev.* **D64** (2001) 035002, arXiv:hep-ph/0012100. doi:10.1103/PhysRevD.64.035002.

[63] N. Arkani-Hamed, S. Dimopoulos, and G. R. Dvali, "The hierarchy problem and new dimensions at a millimeter", *Phys. Lett.* **B429** (1998) 263–272, arXiv:hep-ph/9803315. doi:10.1016/S0370-2693(98)00466-3.

[64] M. Mohammadi Najafabadi and S. Paktinat Mehdiabadi, "Top Production from Black Holes at the LHC", *JHEP* **0807** (2008) 011, arXiv:0803.1287. doi:10.1088/1126-6708/2008/07/011.

[65] L. Randall and R. Sundrum, "A Large mass hierarchy from a small extra dimension", *Phys.Rev.Lett.* **83** (1999) 3370–3373, arXiv:hep-ph/9905221. doi:10.1103/PhysRevLett.83.3370.

[66] L. Randall and R. Sundrum, "An Alternative to compactification", *Phys.Rev.Lett.* **83** (1999) 4690–4693, arXiv:hep-th/9906064. doi:10.1103/PhysRevLett.83.4690.

[67] ATLAS Collaboration, "A search for $t\bar{t}$ resonances in the lepton plus jets final state with ATLAS using 14 fb^{-1} of pp collisions at $\sqrt{s} = 8$ TeV", *ATLAS Conference Note* **ATLAS-CONF-2013-052** (2013).

[68] ATLAS Collaboration Collaboration, "Search for resonances decaying into top-quark pairs using fully hadronic decays in *pp* collisions with ATLAS at $\sqrt{s} = 7$ TeV", *JHEP* **1301** (2013) 116, arXiv:1211.2202. doi:10.1007/JHEP01(2013)116.

[69] ATLAS Collaboration Collaboration, "Search for resonant top plus jet production in $t\bar{t}$ + jets events with the ATLAS detector in pp collisions at $\sqrt{s} = 7$ TeV", *Phys.Rev.* **D86** (2012) 091103, arXiv:1209.6593. doi:10.1103/PhysRevD.86.091103.

[70] CMS Collaboration, "Search for ttbar resonances in semileptonic final state", *CMS Physics Analysis Summary* **CMS-PAS-B2G-12-006** (2013).

[71] CMS Collaboration, "Search for Z ' resonances decaying to $t\bar{t}$ in dilepton+jets final states in *pp* collisions at $\sqrt{s} = 7$ TeV", *Phys.Rev.* **D87** (2013) 072002, arXiv:1211.3338. doi:10.1103/PhysRevD.87.072002.

[72] CMS Collaboration, "Search for resonant $t\bar{t}$ production in lepton+jets events in *pp* collisions at $\sqrt{s} = 7$ TeV", *JHEP* **1212** (2012) 015, arXiv:1209.4397. doi:10.1007/JHEP12(2012)015.

[73] T. Plehn and T. M. Tait, "Seeking Sgluons", *J.Phys.* **G36** (2009) 075001, arXiv:0810.3919. doi:10.1088/0954-3899/36/7/075001.

[74] T. G. Rizzo, "Z' phenomenology and the LHC", arXiv:hep-ph/0610104.

[75] P. H. Frampton, P. Hung, and M. Sher, "Quarks and leptons beyond the third generation", *Phys.Rept.* **330** (2000) 263, arXiv:hep-ph/9903387. doi:10.1016/S0370-1573(99)00095-2.

[76] O. Eberhardt, G. Herbert, H. Lacker et al., "Impact of a Higgs Boson at a Mass of 126 GeV on the Standard Model with Three and Four Fermion Generations", *Phys. Rev. Lett.* **109** (Dec, 2012) 241802. doi:10.1103/PhysRevLett.109.241802.

[77] Brüning, Oliver Sim and Collier, Paul and Lebrun, P and Myers, Stephen and Ostojic, Ranko and Poole, John and Proudlock, Paul, "LHC Design Report". CERN, Geneva, 2004.

[78] ATLAS Collaboration, "The ATLAS Experiment at the CERN Large Hadron Collider", *JINST* **3** (2008) S08003. doi:10.1088/1748-0221/3/08/S08003.

[79] CMS Collaboration, "The CMS experiment at the CERN LHC", *JINST* **3** (2008) S08004. doi:10.1088/1748-0221/3/08/S08004.

[80] LHCb Collaboration, "The LHCb Detector at the LHC", *JINST* **3** (2008) S08005. doi:10.1088/1748-0221/3/08/S08005.

[81] ALICE Collaboration, "The ALICE experiment at the CERN LHC", *JINST* **3** (2008) S08002. doi:10.1088/1748-0221/3/08/S08002.

[82] CMS Collaboration, "Public CMS Luminosity Information", *Public CMS Wiki* (2012). https://twiki.cern.ch/twiki/bin/view/CMSPublic/LumiPublicResults.

[83] CMS Collaboration, "CMS Detector Performance and Software",. CMS-TDR-008-1. CERN-LHCC-2006-001.

[84] CMS Collaboration, "CMS Tracking Performance Results from early LHC Operation", *Eur.Phys.J.* **C70** (2010) 1165–1192, arXiv:1007.1988. doi:10.1140/epjc/s10052-010-1491-3.

[85] CMS Collaboration, "Measurement of Tracking Efficiency", *CMS Physics Analysis Summary* **CMS-PAS-TRK-10-002** (2010).

[86] CMS Collaboration, "CMS technical design report, volume II: Physics performance", *J.Phys.* **G34** (2007) 995–1579. doi:10.1088/0954-3899/34/6/S01.

[87] CMS Collaboration Collaboration, G. L. Bayatyan, M. Della Negra, A. Hervé et al., "CMS computing: Technical Design Report". Technical Design Report CMS. CERN, Geneva, 2005. Submitted on 31 May 2005.

[88] C. Eck, J. Knobloch, L. Robertson et al., "LHC computing Grid: Technical Design Report. Version 1.06 (20 Jun 2005)". Technical Design Report LCG. CERN, Geneva, 2005.

[89] W. Adam, V. Adler, B. Hegner et al., "PAT: The CMS physics analysis toolkit", *J.Phys.Conf.Ser.* **219** (2010) 032017. doi:10.1088/1742-6596/219/3/032017.

[90] S. Drell and T.-M. Yan, "Partons and their Applications at High-Energies", *Annals Phys.* **66** (1971) 578. doi:10.1016/0003-4916(71)90071-6.

[91] J. C. Collins and D. E. Soper, "The Theorems of Perturbative QCD", *Ann.Rev.Nucl.Part.Sci.* **37** (1987) 383–409. doi:10.1146/annurev.ns.37.120187.002123.

[92] T. Gleisberg, S. Hoeche, F. Krauss et al., "Event generation with SHERPA 1.1", *JHEP* **0902** (2009) 007, arXiv:0811.4622. doi:10.1088/1126-6708/2009/02/007.

[93] Y. L. Dokshitzer, "Calculation of the Structure Functions for Deep Inelastic Scattering and e+ e- Annihilation by Perturbation Theory in Quantum Chromodynamics.", *Sov.Phys.JETP* **46** (1977) 641–653.

[94] V. Gribov and L. Lipatov, "Deep inelastic e p scattering in perturbation theory", *Sov.J.Nucl.Phys.* **15** (1972) 438–450.

[95] G. Altarelli and G. Parisi, "Asymptotic Freedom in Parton Language", *Nucl.Phys.* **B126** (1977) 298. doi:10.1016/0550-3213(77)90384-4.

[96] V. Sudakov, "Vertex parts at very high-energies in quantum electrodynamics", *Sov.Phys.JETP* **3** (1956) 65–71.

[97] M. L. Mangano, M. Moretti, F. Piccinini et al., "Matching matrix elements and shower evolution for top-quark production in hadronic collisions", *JHEP* **0701** (2007) 013, arXiv:hep-ph/0611129. doi:10.1088/1126-6708/2007/01/013.

[98] GEANT4 Collaboration, "GEANT4: A Simulation toolkit", *Nucl.Instrum.Meth.* **A506** (2003) 250–303. doi:10.1016/S0168-9002(03)01368-8.

[99] CMS Collaboration, "The fast simulation of the CMS detector at LHC", *J.Phys.Conf.Ser.* **331** (2011) 032049. doi:10.1088/1742-6596/331/3/032049.

[100] T. Sjostrand, S. Mrenna, and P. Z. Skands, "PYTHIA 6.4 Physics and Manual", *JHEP* **0605** (2006) 026, arXiv:hep-ph/0603175. doi:10.1088/1126-6708/2006/05/026.

[101] R. Field, "Early LHC Underlying Event Data - Findings and Surprises", arXiv:1010.3558.

[102] J. Pumplin, D. Stump, J. Huston et al., "New generation of parton distributions with uncertainties from global QCD analysis", *JHEP* **0207** (2002) 012, arXiv:hep-ph/0201195.

[103] Z. Was, "TAUOLA the library for tau lepton decay, and KKMC / KORALB / KORALZ /... status report", *Nucl.Phys.Proc.Suppl.* **98** (2001) 96–102, arXiv:hep-ph/0011305. doi:10.1016/S0920-5632(01)01200-2.

[104] M. Bahr, S. Gieseke, M. Gigg et al., "Herwig++ Physics and Manual", *Eur.Phys.J.* **C58** (2008) 639–707, arXiv:0803.0883. doi:10.1140/epjc/s10052-008-0798-9.

[105] A. Martin, R. Roberts, W. Stirling et al., "Parton distributions incorporating QED contributions", *Eur.Phys.J.* **C39** (2005) 155–161, arXiv:hep-ph/0411040. doi:10.1140/epjc/s2004-02088-7.

[106] J. Alwall, P. Demin, S. de Visscher et al., "MadGraph/MadEvent v4: The New Web Generation", *JHEP* **0709** (2007) 028, arXiv:0706.2334. doi:10.1088/1126-6708/2007/09/028.

[107] P. Nason, "A New method for combining NLO QCD with shower Monte Carlo algorithms", *JHEP* **0411** (2004) 040, arXiv:hep-ph/0409146. doi:10.1088/1126-6708/2004/11/040.

[108] S. Frixione, P. Nason, and C. Oleari, "Matching NLO QCD computations with Parton Shower simulations: the POWHEG method", *JHEP* **0711** (2007) 070, arXiv:0709.2092. doi:10.1088/1126-6708/2007/11/070.

[109] S. Alioli, P. Nason, C. Oleari et al., "NLO single-top production matched with shower in POWHEG: s- and t-channel contributions", *JHEP* **0909** (2009) 111, arXiv:0907.4076. doi:10.1007/JHEP02(2010)011, 10.1088/1126-6708/2009/09/111.

[110] B. Allanach, "SOFTSUSY: a program for calculating supersymmetric spectra", *Comput.Phys.Commun.* **143** (2002) 305–331, arXiv:hep-ph/0104145. doi:10.1016/S0010-4655(01)00460-X.

[111] A. Kulesza and L. Motyka, "Threshold resummation for squark-antisquark and gluino-pair production at the LHC", *Phys.Rev.Lett.* **102** (2009) 111802, arXiv:0807.2405. doi:10.1103/PhysRevLett.102.111802.

[112] A. Kulesza and L. Motyka, "Soft gluon resummation for the production of gluino-gluino and squark-antisquark pairs at the LHC", *Phys.Rev.* **D80** (2009) 095004, arXiv:0905.4749. doi:10.1103/PhysRevD.80.095004.

[113] W. Beenakker, S. Brensing, M. Kramer et al., "Soft-gluon resummation for squark and gluino hadroproduction", *JHEP* **0912** (2009) 041, arXiv:0909.4418. doi:10.1088/1126-6708/2009/12/041.

[114] W. Beenakker, S. Brensing, M. Kramer et al., "Squark and Gluino Hadroproduction", *Int.J.Mod.Phys.* **A26** (2011) 2637–2664, arXiv:1105.1110. doi:10.1142/S0217751X11053560.

[115] CMS Collaboration, "Standard Model Cross Sections for CMS at 7 TeV", *Internal CMS Wiki* (2012). https://twiki.cern.ch/twiki/bin/viewauth/CMS/StandardModelCrossSections.

[116] CMS Collaboration, "Tracking and Primary Vertex Results in First 7 TeV Collisions", *CMS Physics Analysis Summary* **CMS-PAS-TRK-10-005** (2010).

[117] Frühwirth, R. and Waltenberger, W. and Vanlaer, P., "Adaptive vertex fitting", *J.Phys.* **G34** (2007) N343. doi:10.1088/0954-3899/34/12/N01.

[118] Frühwirth, R., "Application of Kalman filtering to track and vertex fitting", *Nucl.Instrum.Meth.* **A262** (1987) 444–450. doi:10.1016/0168-9002(87)90887-4.

[119] CMS Collaboration Collaboration, "Performance of CMS muon reconstruction in pp collision events at $\sqrt{s} = 7$ TeV", *JINST* **7** (2012) P10002, arXiv:1206.4071. doi:10.1088/1748-0221/7/10/P10002.

[120] J. M. Campbell, J. Huston, and W. Stirling, "Hard Interactions of Quarks and Gluons: A Primer for LHC Physics", *Rept.Prog.Phys.* **70** (2007) 89, arXiv:hep-ph/0611148. doi:10.1088/0034-4885/70/1/R02.

[121] CMS Collaboration, "Muon Identification", *Internal CMS Wiki* (2012). https://twiki.cern.ch/twiki/bin/view/CMSPublic/SWGuideMuonIdta.

[122] CMS Collaboration, "Measuring Electron Efficiencies at CMS with Early Data", *CMS Physics Analysis Summary* **CMS-PAS-EGM-07-001** (2008).

[123] W. Adam, O. Buchmueller, T. Danielson et al., "Reconstruction, identification, and trigger efficiencies for SUSY searches in the single lepton channel in 2011", *CMS Analysis Note* **CMS-AN-11-536** (2012). Internal documentation.

[124] CMS Collaboration, "Electron reconstruction and identification at sqrt(s) = 7 TeV", *CMS Physics Analysis Summary* **CMS-PAS-EGM-10-004** (2010).

[125] Adam, Wolfgang and Frühwirth, R. and Strandlie, Are and Todor, T., "Reconstruction of Electrons with the Gaussian-Sum Filter in the CMS Tracker at the LHC", *CERN-CMS-NOTE* **CERN-CMS-NOTE-2005-001** (2005).

[126] CMS Collaboration, "Electron Identification", *Internal CMS Wiki* (2012). https://twiki.cern.ch/twiki/bin/viewauth/CMS/SimpleCutBasedEleID.

[127] CMS Collaboration, "Particle-Flow Event Reconstruction in CMS and Performance for Jets, Taus, and MET", *CMS Physics Analysis Summary* **CMS-PAS-PFT-09-001** (2009).

[128] M. Cacciari, G. P. Salam, and G. Soyez, "The Anti-k(t) jet clustering algorithm", *JHEP* **0804** (2008) 063, arXiv:0802.1189. doi:10.1088/1126-6708/2008/04/063.

[129] CMS Collaboration, "Determination of Jet Energy Calibration and Transverse Momentum Resolution in CMS", *Journal of Instrumentation* **6** (2011) P11002, arXiv:1107.4277. doi:10.1088/1748-0221/6/11/P11002.

[130] CMS Collaboration, "Jet Performance in pp Collisions at 7 TeV", *CMS-PAS-JME-10-003* **CMS-PAS-JME-10-003** (2010).

[131] J. Gallicchio and M. D. Schwartz, "Quark and Gluon Tagging at the LHC", *Phys.Rev.Lett.* **107** (2011) 172001, arXiv:1106.3076. doi:10.1103/PhysRevLett.107.172001.

[132] CMS Collaboration, "Performance of quark/gluon discrimination in 8 TeV pp data", *CMS Physics Analysis Summary* **CMS-PAS-JME-13-002** (2013).

[133] CMS Collaboration, "Identification of b-quark jets with the CMS experiment", *JINST* **8** (2013) P04013, arXiv:1211.4462. doi:10.1088/1748-0221/8/04/P04013.

[134] CMS Collaboration, "B-Tag and Vertexing Working Group", *Internal CMS Wiki* (2011). https://twiki.cern.ch/twiki/bin/view/CMS/BtagPOG.

[135] M. Kramer, A. Kulesza, R. van der Leeuw et al., "Supersymmetry production cross sections in pp collisions at $\sqrt{s} = 7$ TeV", arXiv:1206.2892.

[136] CMS Collaboration Collaboration, "Missing transverse energy performance of the CMS detector", *JINST* **6** (2011) P09001, arXiv:1106.5048. doi:10.1088/1748-0221/6/09/P09001.

[137] J. Lange, "Differential Top-Quark-Pair Cross Sections in pp Collisions at $\sqrt{s}$=7 TeV and Charge Multiplication in Highly-Irradiated Silicon Sensors". PhD thesis, Universität Hamburg, Hamburg, Germany, 2013. DESY-THESIS-2013-042.

[138] W. Behrenhoff, "Measurement of Differential $t\bar{t}$ Cross Sections in the Dilepton Decay Channels with the CSM Detector at 7 TeV Centre-of-Mass Energy". PhD thesis, Universität Hamburg, Hamburg, Germany, 2012. DESY-THESIS-2012-037.

[139] G. Antchev, P. Aspell, I. Atanassov et al., "First measurement of the total proton-proton cross section at the LHC energy of $\sqrt{s}$ =7 TeV", *Europhys.Lett.* **96** (2011) 21002, arXiv:1110.1395. doi:10.1209/0295-5075/96/21002.

[140] A. Czarnecki, J. G. Korner, and J. H. Piclum, "Helicity fractions of W bosons from top quark decays at NNLO in QCD", *Phys.Rev.* **D81** (2010) 111503, arXiv:1005.2625. doi:10.1103/PhysRevD.81.111503.

[141] J. M. Campbell and R. K. Ellis, "Top-quark processes at NLO in production and decay", arXiv:1204.1513.

[142] CMS Collaboration, "Search for new physics with single-leptons at the LHC", *CMS Physics Analysis Summary* **CMS-PAS-SUS-11-015** (2011).

[143] CMS Collaboration, "Search for supersymmetry in pp collisions at $\sqrt{s} = 7$ TeV in events with a single lepton, jets, and missing transverse momentum", *Eur.Phys.J.* **C73** (2013) 2404, arXiv:1212.6428. doi:10.1140/epjc/s10052-013-2404-z.

[144] CMS Collaboration, "Prescription for calculating uncertainties on Missing Transverse Energy", *Internal CMS Wiki* (2012). https://twiki.cern.ch/twiki/bin/view/CMS/MissingETUncertaintyPrescription.

[145] CMS Collaboration, "Jet Energy Resoultion", *Internal CMS Wiki* (2012). https://twiki.cern.ch/twiki/bin/view/CMS/JetResolution.

[146] CMS Collaboration, "Pile-up Uncertianty", *Internal CMS Wiki* (2012). https://twiki.cern.ch/twiki/bin/viewauth/CMS/PileupSystematicErrors.

[147] CMS Collaboration, "Absolute Calibration of the Luminosity Measurement at CMS: Winter 2012 Update", *CMS-PAS-SMP-12-008* **CMS-PAS-SMP-12-008** (2012).

[148] A. L. Read, "Presentation of search results: the CLs technique", *Nucl.Part.Phys.* **28** (2002) 2693–2704. doi:10.1088/0954-3899/28/10/313.

[149] T. Junk, "Confidence level computation for combining searches with small statistics", *Nucl.Instrum.Meth.* **A434** (1999) 435–443, arXiv:hep-ex/9902006. doi:10.1016/S0168-9002(99)00498-2.

[150] L. Moneta, K. Belasco, K. S. Cranmer et al., "The RooStats Project", *PoS* **ACAT2010** (2010) 057, arXiv:1009.1003.

[151] CMS Collaboration Collaboration, "Search for new physics in events with same-sign dileptons and b-tagged jets in pp collisions at $\sqrt{s} = 7$ TeV", *JHEP* **1208** (2012) 110, arXiv:1205.3933. doi:10.1007/JHEP08(2012)110.

[152] CMS Collaboration Collaboration, "Search for supersymmetry in events with b-quark jets and missing transverse energy in pp collisions at 7 TeV", *Phys.Rev.* **D86** (2012) 072010, arXiv:1208.4859. doi:10.1103/PhysRevD.86.072010.

[153] CMS Collaboration Collaboration, "Search for supersymmetry in final states with missing transverse energy and 0, 1, 2, or at least 3 b-quark jets in 7 TeV pp collisions using the variable alphaT", *JHEP* **1301** (2013) 077, arXiv:1210.8115. doi:10.1007/JHEP01(2013)077.

[154] CMS Collaboration Collaboration, "Search for supersymmetry in hadronic final states using MT2 in pp collisions at $\sqrt{s} = 7$ TeV", *JHEP* **1210** (2012) 018, arXiv:1207.1798. doi:10.1007/JHEP10(2012)018.

[155] CMS Collaboration Collaboration, "Inclusive search for supersymmetry using the razor variables in pp collisions at $\sqrt{s} = 7$ TeV", *Phys.Rev.Lett.* **111** (2013), no. 8, 081802, arXiv:1212.6961. doi:10.1103/PhysRevLett.111.081802.

[156] CMS Collaboration Collaboration, "Interpretation of Searches for Supersymmetry with simplified Models", *Phys.Rev.* **D88** (2013), no. 5, 052017, arXiv:1301.2175. doi:10.1103/PhysRevD.88.052017.

[157] A. J. Barr and C. G. Lester, "A Review of the Mass Measurement Techniques proposed for the Large Hadron Collider", *J.Phys.* **G37** (2010) 123001, arXiv:1004.2732. doi:10.1088/0954-3899/37/12/123001.

[158] D. Wiesler, "Combinatorial and Off-Shell Effects in New Physics Cascades". PhD thesis, Universität Hamburg, Hamburg, Germany, 2012. DESY-THESIS-2012-048.

[159] W. Kilian, T. Ohl, and J. Reuter, "WHIZARD: Simulating Multi-Particle Processes at LHC and ILC", *Eur.Phys.J.* **C71** (2011) 1742, arXiv:0708.4233. doi:10.1140/epjc/s10052-011-1742-y.

[160] M. Moretti, T. Ohl, and J. Reuter, "O'Mega: An Optimizing matrix element generator", arXiv:hep-ph/0102195.

[161] W. Kilian, J. Reuter, S. Schmidt et al., "An Analytic Initial-State Parton Shower", *JHEP* **1204** (2012) 013, arXiv:1112.1039. doi:10.1007/JHEP04(2012)013.

[162] S. Ovyn, X. Rouby, and V. Lemaitre, "DELPHES, a framework for fast simulation of a generic collider experiment", arXiv:0903.2225.

[163] CMS Collaboration Collaboration, "Search for new physics in the multijet and missing transverse momentum final state in proton-proton collisions at $\sqrt{s}$= 8 TeV", *JHEP* **1406** (2014) 055, arXiv:1402.4770. doi:10.1007/JHEP06(2014)055.

[164] D. Curtin, "Mixing It Up With MT2: Unbiased Mass Measurements at Hadron Colliders", *Phys.Rev.* **D85** (2012) 075004, arXiv:1112.1095. doi:10.1103/PhysRevD.85.075004.

[165] Y. Bai and H.-C. Cheng, "Identifying Dark Matter Event Topologies at the LHC", *JHEP* **1106** (2011) 021, arXiv:1012.1863. doi:10.1007/JHEP06(2011)021.

[166] D. Abbaneo, M. Abbrescia, P. P. Allport et al., "ECFA High Luminosity LHC Experiments Workshop: Physics and Technology Challenges. 94th Plenary ECFA meeting", *Report submitted to ECFA* **ECFA-13-284** (2013).

[167] CMS Collaboration Collaboration, "Search for supersymmetry in pp collisions at $\sqrt{s}$=8 TeV in events with a single lepton, large jet multiplicity, and multiple b jets", *Phys.Lett.* **B733** (2014) 328–353, arXiv:1311.4937. doi:10.1016/j.physletb.2014.04.023.

[168] CMS Collaboration Collaboration, "Search for top-squark pair production in the single-lepton final state in pp collisions at $\sqrt{s} = 8$ TeV", *Eur.Phys.J.* **C73** (2013) 2677, arXiv:1308.1586. doi:10.1140/epjc/s10052-013-2677-2.

[169] CMS Collaboration Collaboration, "Search for supersymmetry in hadronic final states with missing transverse energy using the variables α_T and b-quark multiplicity in pp collisions at $\sqrt{s} = 8$ TeV", *Eur.Phys.J.* **C73** (2013) 2568, arXiv:1303.2985. doi:10.1140/epjc/s10052-013-2568-6.

[170] CMS Collaboration Collaboration, "Search for new physics in events with same-sign dileptons and b jets in pp collisions at $\sqrt{s} = 8$ TeV", *JHEP* **1303** (2013) 037, arXiv:1212.6194. doi:10.1007/JHEP03(2013)037, 10.1007/JHEP07(2013)041.

[171] CMS Collaboration, "Search for anomalous production of events with three or more leptons in pp collisions at $\sqrt{s} = 8$", *CMS Physics Analysis Summary* **CMS-PAS-SUS-13-002** (2014).

Danksagung

Abschliessend möchte ich mich bei allen bedanken, die zum Gelingen dieser Doktorarbeit beigetragen haben.

Zunächst will ich mich bei Dr. Isabell Melzer-Pellmann für die große Geduld, mit der sie diese Doktorarbeit betreut hat, die stete Diskussionsbereitschaft, sowie den freundschaftlichen Umgang bedanken. Dann bedanke ich mich bei Prof. Dr. Peter Schleper für die Motivation, die ich in Gesprächen und Diskussionen mit ihm stets erfahren habe. Für die Gastfreundschaftlichkeit meiner Kollegen der Universität Hamburg in Gebäude 68 und in Saint-Genis möchte ich mich stellvertretend bei Jun.-Prof. Dr. Christian Sander bedanken. Vielen Dank an Dr. Andreas Meyer für die Betreuung meiner DQM-Tätigkeit am CERN.

Herzlich bedanken möchte ich mich bei Matthias Schröder und Holger Enderle, die durch ihre stete Hilfsbereitschaft und Verläßlichkeit sehr zum Gelingen dieser Arbeit beigetragen haben. Vielen Dank an Roger Wolf, Dean Horton, Dirk Krücker und Martijn Gosselink für die Hilfe in vielen technischen Fragen. Für die Möglichkeit, ein Stück weit über meinen Tellerrand hinauszublicken, möchte ich mich bei Daniel Wiesler, Kazuki Sakurai und Jürgen Reuter bedanken. Mir hat die Zusammenarbeit viel Spass gemacht.

Für die gute Arbeitsatmosphäre bedanke ich mich bei Matthias Stein, Hannes Schettler, Jakob Salfeld, Francesco Costanza, Ozgur Sahin, Artur Lobanov, Karim Trippkewitz, Arne Dräger, Annika Vanhöfer, Daniele Marconi, Malte Hoffmann und Simon Kurz.

Für die Unterstützung während der letzten Jahre möchte ich mich ganz herzlich bei meinen Freunden und meiner Familie bedanken.